Ion beam deposited optical mirror coatings for next generation gravitational wave detectors

PhD Thesis

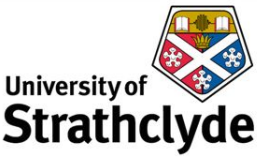

Gavin S. Wallace

Precision Measurement Group
Department of Biomedical Engineering
University of Strathclyde, Glasgow

May 11, 2023

This thesis is the result of the author's original research. It has been composed by the author and has not been previously submitted for examination which has led to the award of a degree.

Contents

List of Figures

List of Tables

Abbreviations

AlGaAs - Aluminium Gallium Arsenide

AlGaP - Aluminium Gallium Phosphide

aLIGO - Advanced Laser Interferometric Gravitational wave Observatory

AR - Anti-Reflection

a-Si - Amorphous Silicon

aLIGO+/A+ - Advanced Laser Interferometric Gravitational wave Observatory Plus

BBH - Binary Black Hole

BCA - Binary Collision Approximation

BE - Binding Energy

BNS - Binary Neutron Star

CAD - Computer Aided Design

CE - Cosmic Explorer

CGW - Continuous Gravitational Wave

CIT - California Institute of Technology

CTN - Coating Thermal Noise

DAQ - Data Acquisition

EBE - Electron Beam Evaporation

ECR - Electron-Cyclotron Resonance

EDS - Energy Dispersive X-ray Spectroscopy

EFI - Electric Field Intensity

EM - Electro-Magnetic

ESA - European Space Agency

ET - Einstein Telescope

ETM - End Test Mass

FEA - Finite Element Analysis

FFT - Fast Fourier Transform

GaAs - Gallium Arsenide

GaP - Gallium Phosphide

GeNS - Gentle Nodal Suspension

GIXRD - Grazing Incidence X-ray Diffraction

GRB - Gamma-Ray Burst

GW - Gravitational Wave

GWD - Gravitational Wave Detector

GWINC - Gravitational Wave Interferometer Noise Calculator

He:Ne - Helium Neon

HR - Highly Reflective

IBSD - Ion Beam Sputtered Deposition

IMC - Input Mode Cleaner

IPA - Iso-propyl Alcohol

IR - Infrared

ITM - Input Test Mass

$\boldsymbol{k}$ - Extinction Coefficient

KAGRA - Kamioka Gravitational Wave Detector

KE - Kinetic Energy

KKR - Kramers-Kronig Relation

Kr-C - Krypton-Carbon

LISA - Laser Interferometric Space Antenna

LMA - Laboratoire des Matériaux Avancés

LMXB - Low Mass X-ray Binary

MBE - Molecular Beam Epitaxy

MC - Monte Carlo

MD - Molecular Dynamics

MS - Magnetron Sputtering

$\boldsymbol{n}$ - Refractive Index

NASA - National Aeronautics and Space Administration

NEMO - Neutron star Extreme Matter Observatory

NS - Neutron Star

OJL - O'Leary, Johnson and Lim

OMC - Output Mode Cleaner

PCI - Photothermal Common-Path Interferometry

PECVD - Plasma Enhanced Chemical Vapour Deposition

ppm - Parts Per Million

PVD - Physical Vapour Deposition

QPD - Quadrant Photodiode

RF - Radio Frequency

RFN - Radio Frequency Neutraliser

RHEED - Reflection High Energy Electron Diffraction

ROC - Radius Of Curvature

SDTrimSP - Static and Dynamic Transport Range of Ions in Matter Serial Parallel

SEM - Scanning Electron Microscope

Si_3N_4 - Silicon Nitride

SiN_x - Silicon Nitride (Non-stoichiometric)

SiO_2 - Silicon Dioxide

SiO_xN_y - Silicon Oxynitride

SNR - Signal-to-Noise Ratio

SQL - Standard Quantum Limit

SRIM - Stopping and Range of Ions in Matter

TEM - Transmission Electron Microscope

TEM_{00} - Transverse Electromagnetic 00 mode

TiO_2:Ta_2O_5 - Titania doped Tantalum Pentoxide

TLS - Two Level System

TRIM - Transport Range of Ions in Matter

UHV - Ultra-High Vacuum

UV - Ultraviolet

Vis - Visible

XPS - X-ray Photoelectron Spectroscopy

XRD - X-ray Diffraction

ZBL - Ziegler Biersack and Littmark

ZrO_2 - Zirconia

Acknowledgements

Firstly I would like to thank my supervisor Prof Stuart Reid for providing me with the opportunity to complete a PhD in addition to giving me guidance and support throughout the course of my studies.

I would also like to acknowledge Dr Marwa Ben Yaala, Dr Paul Hill and Dr Kieran Craig for additional support and guidance plus having to put up with all the stupid questions I have asked over the years. You have all taught me a lot about research and I am indebted to you for this.

I would like to say thank you to my PhD compadres, Chalisa Gier and Callum Wiseman, for their advice on various topics over the years and making this all a lot of fun.

I must acknowledge Thomas McCanny for his technical support in addition to putting up with me "borrowing" parts from his stores. The SCAPA facilities and equipment would never have been running without your help.

For her assistance and incredible patience in setting up EDS and XRD measurements a huge thank you to Dr Maider Olasolo.

I am extremely grateful to my colleague and good friend at Glasgow University Dr Simon Tait for always being there to provide assistance to my research in addition to being more than happy to attend the pub and talk nonsense frequently.

I would like to thank my parents for supporting me throughout the last 4 years, putting up with me still being in their house after so long and occasionally coming home in a bad mood.

Last but by no means least I'd like to thank my amazing fiancé Laura Findlay (soon to be Wallace) for all her support, encouragement and love. When things have been

good you were always there to celebrate with me and when things went badly you have been the one who has pulled me up, brushed me off and told me to keep going. For that I am eternally grateful, I love you very much and cannot wait to be your husband.

Summary

Gravitational waves are a form of radiation, generated from the largest astrophysical bodies in the Universe, which were first postulated by Albert Einstein in 1915 as part of his general theory of relativity. A century after this the gravitational waves from a binary black hole merger were measured on the 14th of September 2015, by the LIGO scientific community. This was the first measurement of its kind and has heralded a new form of astronomy.

Gravitational waves are measured by laser interferometry, where light is reflected from a mirror over two 4 km arm cavities, in the case of aLIGO, and combined to form an interference condition. As the displacement caused by a gravitational wave passing through the Earth are so small ($\approx 10^{-18}$ m) the detectors can be subject to strict sensor noise budgets, with sources of such noise ranging from earthquakes on the other side of the planet to thermal fluctuations of the very molecules in the detector.

The thermal fluctuations in the detector associated with the highly reflective coatings used on the interferometry mirrors, can be characterised as coating Brownian thermal noise. This source of noise is at its highest between 50 Hz - 150 Hz, the most sensitive band of the detector. As such there is a large effort in the community to reduce this noise source significantly for the next generation of gravitational wave detectors.

This thesis focuses on the use of ion beam sputtering deposition, the current method used to produce gravitational wave detector mirrors, to create low optical and mechanical loss coatings for the next generation of gravitational wave detector. The materials chosen to be studied optically, mechanically, compositionally and structurally were amorphous silicon and silicon nitride due to their desirable optical and mechanical properties for gravitational wave detectors.

Chapter 1 describes the nature of gravitational waves, confirmed and unconfirmed Cosmic sources of such waves and methods used, both historically and currently, to detect them. Fundamental limits to the detectors are discussed with an explanation to the methods used to mitigate such limits. Notable gravitational wave detections are explained in addition to the current generation of detectors. Finally an overview is given of the next generation of detectors.

Chapter 2 describes Brownian thermal noise, both its origins and methods currently used by gravitational wave detectors to mitigate its effects on observational reach.

Chapter 3 details the coating techniques which have been used, either as part of research or production, for optical mirror coatings of gravitational wave observatories. Specifically ion beam deposition is described in more detail, both from a theoretical and experimental standpoint.

Chapter 4 describes the metrology used in this research to characterise the thin film coatings optically, mechanically, compositionally and structurally.

Chapter 5 and 6 details the research conducted on amorphous silicon and silicon nitride coatings and the evaluation of such coating use for gravitational wave detectors both as deposited and after heat treating at increasing temperatures.

Preface

This thesis is a record of research carried out on optical coatings deposited by ion beam sputtering between October 2018 and December 2022. The application of these coatings are for next generation gravitational wave detectors. Research was mainly carried out in University of Strathclyde with additional experimentation conducted at the University of Glasgow and the California Institute of Technology.

In Chapter 1 the nature of gravitational radiation is explained, in addition to sources of such radiation and methods by which to detect them. Fundamental limits to the detectors are discussed with an explanation to the methods used to mitigate such limits. Notable gravitational wave detections are explained in addition to the current generation of detectors. Finally an overview is given of the next generation of detectors.

In Chapter 2 the origins of Brownian coating thermal noise in a gravitational wave detector is explained with attention to specific sources of such noise. Methods by which to minimise the effect of this source are also described.

In Chapter 3 the coating techniques used in gravitational wave detector research are is described. Particular attention is given to ion beam sputtering and the RF ion source used in this research. Additionally methods to computationally simulate the ion beam sputtering process are described. Finally a description of the ion beam deposition used in this research is given, built and operated by the author.

In Chapter 4 the measurements techniques used to analyse the coatings produced in this research are described. Attention is given to the Gentle Nodal Support measurement system built and operated by the author.

In Chapter 5 research into amorphous silicon films produced by the author is discussed. All spectrophotometry measurements and SCOUT fittings were conducted by

the author at the University of Strathclyde. PCI absorption measurements and analysis were carried out by Dr Simon Tait in the Institute for Gravitational Research at the University of Glasgow with input from the author. Mechanical loss measurements and analysis of the coating was conducted by the author. EDS, XRD measurements and analysis were conducted by the author with assistance from Dr Maider Olasolo.

In Chapter 6 research into non-stoichiometric silicon nitride films produced by the author is discussed. All spectrophotometry measurements and SCOUT fittings were conducted by the author at the University of Strathclyde. PCI absorption measurements and analysis were carried out by Dr Simon Tait in the Institute for Gravitational Research at the University of Glasgow with input from the author. Mechanical loss measurements and analysis of the coatings was conducted by Dr Gabriele Vajente in the LIGO Laboratory at the California Institute of Technology with input from the author. XPS measurements and analysis were carried out by Dr Stephen Francis at the University of St Andrews with input from the author. EDS and XRD measurements and analysis were conducted by the author at the Advance Materials Research Laboratory in the University of Strathclyde with assistance from Dr Maider Olasolo.

In Appendix A XRD results are shown to confirm the amorphous nature of the films measured in this work, using a multitude of configurations: grazing incidence and Bragg Brentano, longer and shorter scan lengths and changing angle of the grazing incidence scan. The XRD measurements and analysis were conducted by the author at the Advance Materials Research Laboratory in the University of Strathclyde with assistance from Dr Maider Olasolo.

In Appendix B ANSYS APDL code is given which was written by the author to calculate the coating elastic energy ratio for a coated disk in ANSYS Workbench.

In Appendix C both simulated elastic energy ratios and measured mechanical loss results conducted by the author are shown which were published in Optica peer-reviewed journal.

Chapter 1

Gravitational Waves and Detectors

1.1 Introduction

Predicted in 1915 by Albert Einstein in his General Theory of Relativity [1], gravitational waves are a consequence of asymmetric acceleration of matter and therefore the largest signals would be expected from large cosmic interactions in the Universe. First indirectly measured by Hulse and Taylor from a binary pulsar system [2, 3] they have since been an elusive form of radiation to measure. Over the last half century many scientist have developed methods by which to capture data showing the existence of these waveforms, the most recent and successful effort by use of laser interferometry.

Observed directly for the first time in 2015 [4] gravitational waves have heralded a new era of astronomy. New experimental techniques have been developed along the way to enable increased detector sensitivity. This has resulted in a both a multitude of Cosmic events being observed in addition to new understanding of experimental technologies for use on *terra firma*.

In this section gravitational waves (GWs) will be described in addition to the various interstellar phenomena that create them. The historical attempts to detect GWs and more modern methods will also be discussed including the limiting factors to detector sensitivity. Finally the current experimental observations of GWs will be discussed in

addition to the next generation of detectors.

1.2 Gravitational Waves

A gravitational wave (GW) will be produced by the acceleration of mass in much the same way as electromagnetic (EM) radiation is produced by the acceleration of charge. The caveat to this is EM radiation can be created from a magnetic dipole (from a positive and negative charge) however a GW cannot be produced by a dipole due to the conservation of momentum [5]. Conservation of energy prevents mono-polar gravitational radiation therefore GWs can only be quadrupolar in nature, produced from non-axisymmetric acceleration of mass.

GWs can be observed in two distinct polarisation states h_+ and $h_\times$ where h is the strain amplitude of the GW, resulting from the differing contraction and elongation that propagate at the speed of light. An example of these wave polarisation states effect on a ring of free falling particles is shown in Fig [1.1].

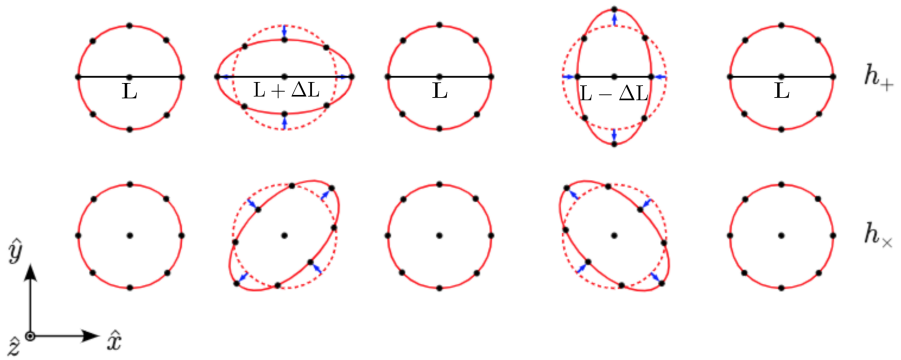

Figure 1.1: Effect of h_+ and $h_\times$ gravitational waves on a ring of free falling particles. The wave propagation direction is perpendicular to the page. Image from [6].

For the h_+ polarisation state the wave will contracts and elongates along the y and x axis and for the $h_\times$ along the $y = x$ and $y = -x$ axis. The strain amplitude of the wave can be characterised by the following equation [6],

$$h = \frac{2\Delta L}{L}, \tag{1.1}$$

where ΔL is the differential separation of the particles due to contraction and elongation relative to the original spacing from the axis centre L. A GW passing through a detector with an arm length on the scale of a few kilometres will cause a differential length change of the order 10^{-18} m [6].

1.3 Sources of Gravitational Waves

As the masses required to generate such measurable strains can only come from large astrophysical sources there are many different varieties of signal that can be produced, depending on the event that caused them. The main sources of gravitational waves are described with reference to the signal characteristics they would generate.

1.3.1 Continuous Sources

A source of continuous gravitational waves (CGW) is defined as sources which last a few weeks in length with constant amplitude and slow variation in frequency over time of observation [7]. An example of such a source are fast spinning neutron stars (pulsars), densely packed stellar objects created from the core collapse of a massive star ($> 8M_{\odot}$ [8]) which emit high energy EM radiation as they rotate [9].

A pulsar produces gravitational waves from deformities on its surface (due to surface instability or a magnetic field not aligned to the axis of spin) which cause non-axisymmetry as it spins [10]. This will lead to the production of GWs through the asymmetrical acceleration of the neutron matter with an expected frequency twice that of its spin [11] (current observed limit is 700 Hz [10]). A CGW of this kind is expected to have a strain amplitude of $h \approx 10^{-25}$ [10].

Another example of a CGW signal is a binary system where a neutron star strips material from a companion star to emit x-rays from the accretion disk, designated a Low Mass X-ray Binary (LMXB). A CGW from this source is expected to have a strain amplitude of the order $h \approx 10^{-27}$ [10].

1.3.2 Burst Sources

Burst sources or GW transients are short GW signals (< 1 s) created by the rapid acceleration of mass from a short energetic cosmic event. This is thought to be from a Type II supernovae explosion [5] or from compact binary mergers [12]. In the case of the latter source the merging of two large objects such as neutron stars or black holes can cause a large gravitational wave signal amplitude over a short time scale. This is discussed further in Section [1.3.4]. The strain amplitude of supernovae explosions are expected to be on the order of $h \approx 10^{-21}$ [13].

1.3.3 Stochastic Sources

A stochastic source of gravitational waves is very different from continuous, burst or inspiral sources as they are not produced from one location but from all directions [14]. Thought to be isotropic this waveform would appear as noise in a single gravitational wave detector therefore two separate detectors in different locations would be necessary to correlate the signals [14].

Sources of these waves include all the binary black hole (BBH) systems, binary neutron star (BNS) systems, supernovae, kilonovae and asymmetrically rotating neutron stars that have or do exist in the Universe [14]. Additionally primordial stochastic gravitational waves from the inflation period after the Big Bang (10^{-36} s - 10^{-32} s) can also be considered as a possible signal source [15]. The strain amplitude of the stochastic GW background is thought to be $10^{-23} - 10^{-21}$ near 1 kHz [5].

1.3.4 Inspiral Sources

Inspiral sources of gravitational waves are created by the decaying orbit and merger of massive cosmic objects such as black holes or neutron stars. Currently this kind of event has proven to be the most observable as no less than 90 events have been detected by the current detector configuration [16].

As the two objects orbital period decay, more energy is lost to gravitational waves causing an increase in signal amplitude. The strain of such a signal is classified by the so called chirp mass ($\mathcal{M}$) defined as [4],

$$\mathcal{M} = \frac{(m_1 m_2)^{3/5}}{(m_1 + m_2)^{1/5}}, \tag{1.2}$$

where m_1 and m_2 are the masses of the two orbiting objects. As the objects merge, they produce a signal with increasing frequency before finally decreasing in frequency as they merge creating a so called "ringdown". From the signal frequency and amplitude characteristics the mass and therefore classification of the objects can be determined.

1.4 Detectors

Although the current iteration of gravitational wave detector (GWD) use the principles of Michelson interferometry, this was not the first conceived idea to measure gravitational wave strain. A brief overview of other techniques used to attempt to measure GWs, in addition to a discussion of the operational principles and techniques employed in current GWDs, is provided below.

1.4.1 Resonant bar detectors

The resonant mass or "bar" detector was conceptualised and designed by Joseph Weber in 1960 [17]. As one of the first practical methods to detect GWs the idea was a weak gravitational perturbation would interact with a long cylindrical mass by stretching and squeezing the mass, exciting a resonant mode which could be monitored with the aid of an electrical signal from multiple piezoelectric transducers [5]. The "bars" were placed 1000 km apart so if a gravitational wave passed through the Earth it could be verified [18]. Due to the resonant frequency of the bars being around 1660 Hz [18] only certain astrophysical events such as supernovae (and later discovery of neutron star binaries) were theorised to be observable using this apparatus [5].

The first bar detector was fabricated from aluminium and was thought to have detected coincidental gravitational radiation in 1969 [18]. These results were later disproved however and thought to be a thermal fluctuation in the mass (thermal noise) which caused the "event" signal [5, 19]. Further efforts were employed to increase the detector sensitivity to this noise source principally by the use of cryogenics [20].

Due to a lack of plausible event detection in addition to the limited bandwidth of these detectors, they have all since been put out of commission in favour of interferometric GWDs [21].

1.4.2 Laser Interferometry

In 1963 Gertsenshtein and Pustovoit proposed a using a interferometer to detect gravitational waves [22]. The idea was to use a set up similar to a Michelson-Morley interferometer [23] where two cylindrical test masses, Input Test Mass (ITM) and End Test Mass (ETM), would be separated down two arms to form an L shape. The motion of the test masses would be monitored by a laser beam, divided in two by a beam splitter, which would reflect of the end mirror masses and create a dark fringe interference condition at the signal output (shown in Figure [1.2]).

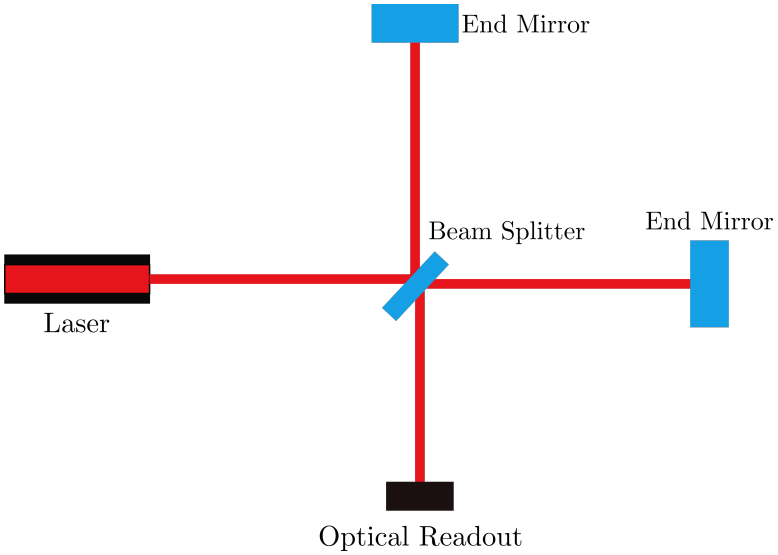

Figure 1.2: Layout of Michelson-Morley Interferometer showing how light is split into two beam arms and measured at an optical readout. Recreated from [24] and [23].

A gravitational wave passing through the Earth would cause differential motion to the arms (by the stretching and squeezing effect) which would change the phase of the light in the interferometer arms (in high vacuum) and show a shift from the dark fringe condition from the readout. The first prototype of this system was created by Forward *et al.* in 1978 [25] however this was limited in bandwidth and sensitivity due to small

arm length (2 m) and the low power of the He:Ne laser used. Since then a number of interferometer test beds have been built (e.g. a 10 m interferometer at Glasgow University [26] and the 40 m prototype at the California Institute of Technology [27]) in order to develop the technologies needed to operate a large km scale interferometer which would give the capability of detecting gravitational waves.

1.5 Noise Sources in Detectors

As the displacement caused by a gravitational wave is extremely small ($\approx 10^{-18}$ m over km-scale arm lengths) the sensitivity of the detectors is paramount to successful operation. Fig [1.3] shows the noise budget for aLIGO outlining the noise contributions from various sources which influence the overall detector sensitivity. This was created using the Gravitational Wave Interferometer Noise Calculator (GWINC) [28]. These sources will be outlined in the subsequent section in addition to measures taken to mitigate their effects.

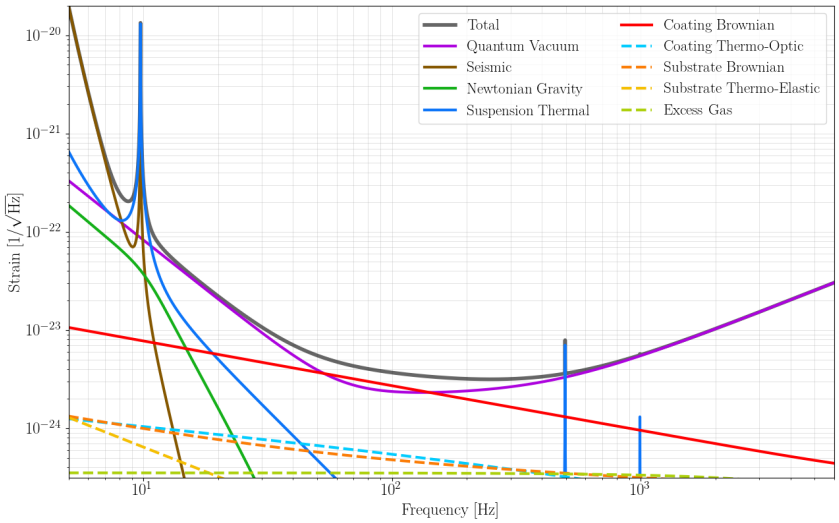

Figure 1.3: Noise budget for aLIGO showing contributions of all noise sources to detector sensitivity. Created using pyGWINC [29].

1.5.1 Seismic Noise

Displacements from within the Earth and on the surface can lead to seismic noise. The displacements are usually on the micrometre level but can contribute to significant noise levels (with value of $10^7 f^{-2}\mathrm{m/Hz}^{1/2}$ in all three dimensions [30]) from 0.1-10 Hz . Noise created up to 1 Hz originates from ocean waves propagating to the ocean bottom creating motion within the Earth's crust, known as the microseism background [31]. Earthquakes can also contribute to noise in this frequency band however are present over a shorter time period. Noise between 1-10 Hz is typically created by man made activity on the Earth. The method currently employed to mitigate this noise source is the use of multi stage suspension systems which can isolate the test mass mirrors. These systems use passive and active components to filter ground motion in 6 degrees of freedom thereby leaving the test masses as isolated as possible [32].

1.5.2 Quantum Noise

Quantum noise is one of the most limiting noise sources to GWD sensitivity. Covering the entire detector bandwidth it consists of two components, radiation pressure noise and shot noise. These noise sources are described in the subsequent sections.

Shot Noise

In order to measure a gravitational wave strain a detector should monitor the position of the test masses using a dark fringe interference condition. The uncertainty in this measurement partially depends on the statistical fluctuation of photons produced by the laser and measured at the photodiode, more commonly know as shot noise [30]. The strain amplitude of this effect can be described as [33],

$$h(f) = \frac{1}{L}\sqrt{\frac{\hbar c\lambda}{2\pi P}}, \tag{1.3}$$

where f the frequency, L is the arm length of the GWD, c is the speed of light, λ the laser wavelength, and P is the optical power in the interferometer arms. Eq[1.3] shows that the method to reduce this noise contribution is to increase the power inside

the arm cavity. Fabry Pérot cavities are currently employed in GWDs to reduce shot noise as the circulating power in each arm cavity is held at ≈ 750 kW [34].

Radiation Pressure Noise

While increasing the power inside the arm cavities of a GWD will reduce the shot noise contribution it will additionally create a higher photon count impingent on the test mass. The caveat is that this will create a momentum transfer from the photons causing pressure on the face. This transfer displaces the test mass and creates another noise contribution, known as radiation pressure noise. This can be described by [33],

$$h(f) = \frac{1}{mf^2L}\sqrt{\frac{\hbar P}{2\pi^3 c\lambda}}, \tag{1.4}$$

where m is GWD mirror mass. It can be seen from Eq [1.4] that increasing the mirror mass will reduce the radiation pressure noise contribution in a GWD. This is due to the increase mass alleviating the effects of photon momentum transfer. Additionally Eq [1.4] shows that shot noise and radiation pressure are inversely related regarding laser beam power. Therefore a careful balance is needed to minimise the contributions of the two noise sources. The maximum sensitivity that can be obtained by balancing these noise contributions is known as the standard quantum limit (SQL) [35]. In order to surpass this limit optical squeezing can be employed to further increase sensitivity [30]. This is discussed more in Section [1.6.4].

1.5.3 Newtonian Gravity Noise

Surface waves caused by the Earth's seismic activity will produce density fluctuations which create localised gravity gradients near a GWD test mass [30]. This produces a noise source commonly known as gravity gradient noise or Newtonian gravity noise. This effect produces significant noise < 20 Hz [36].

There are methods to mitigate this noise contribution, one of which is to monitor the signal using seismometers to create a subtraction signal to the detector baseline [30, 37]. Another method is to construct the detector underground (~ 150 m where

the surface wave amplitude is suitably reduced [30]) or to operate a detector in space. These options are described further in Section [1.9].

1.5.4 Excess Gas Noise

Even though the main optical components of a GWD are under ultra high vacuum ($< 10^{-7}$ mbar) any residual gas particles in the beam path will cause a refractive index change to the cavity medium [34]. While this is a statistical process with no direct mitigation to remove the effect, maintaining suitably low vacuum reduces this noise source far below the detector sensitivity.

1.5.5 Thermal Noise

Thermally induced vibrational motion is a fundamentally limiting factor to the sensitivity of a GWD. As such the materials which a detector test mass and suspension is manufactured from are vitally important in addition to the design of the suspension system itself [38]. This noise contribution, known as thermal noise, can be shown to have two main contributions. These are suspension thermal noise and coating thermal noise.

Suspension thermal noise arises from thermal fluctuations of the suspension components, resulting in a noise peak around the bounce mode of the detector ($> 10^{-20} 1/\sqrt{\text{Hz}}$ at 10 Hz). As these thermally induced vibrations can excite resonant modes of the detector the current design of GWD suspensions keeps these eigenfrequencies outside the detection band. An addition method employed to mitigate this noise sources is to use fused silica fibres to suspend the test masses [39]. This material has low mechanical dissipation allowing the suspension thermal noise contribution to be minimised and attractive thermomechanical properties that allow a theoretical cancellation of thermoelastic thermal noise [40].

Coating thermal noise originates from both intrinsic thermally induced vibrations of the coating materials in addition to motion induced from interacting with the sensing laser. This is most significant at ≈ 100 Hz where the detector is most sensitive [30].

There are two methods which can be to reduce this noise contribution. The first is

to use materials with low internal friction, such as fused silica for detector construction. The test mass requires a highly reflective (HR) coating stack made from materials with low internal friction (currently TiO_2 doped Ta_2O_5 and SiO_2 for aLIGO) [30] to give high reflectivity at 1064 nm. The other method which will reduce this noise source is to reduce the overall temperature of the test mass itself.

A more throughout treatment of coating thermal noise source is given in the subsequent Chapter [2].

1.6 Detector Operation and Interferometric Techniques

Although modern GWDs have opted for Michelson interferometry to improve detector sensitivity (over resonant bar detectors) they require additional techniques, beyond a standard Michelson layout, in order to be sensitive enough for event detection. An overview of the aLIGO interferometer layout is shown in Figure [1.4]. Employed are a variety of techniques which further increase detector sensitivity, which are discussed in this section.

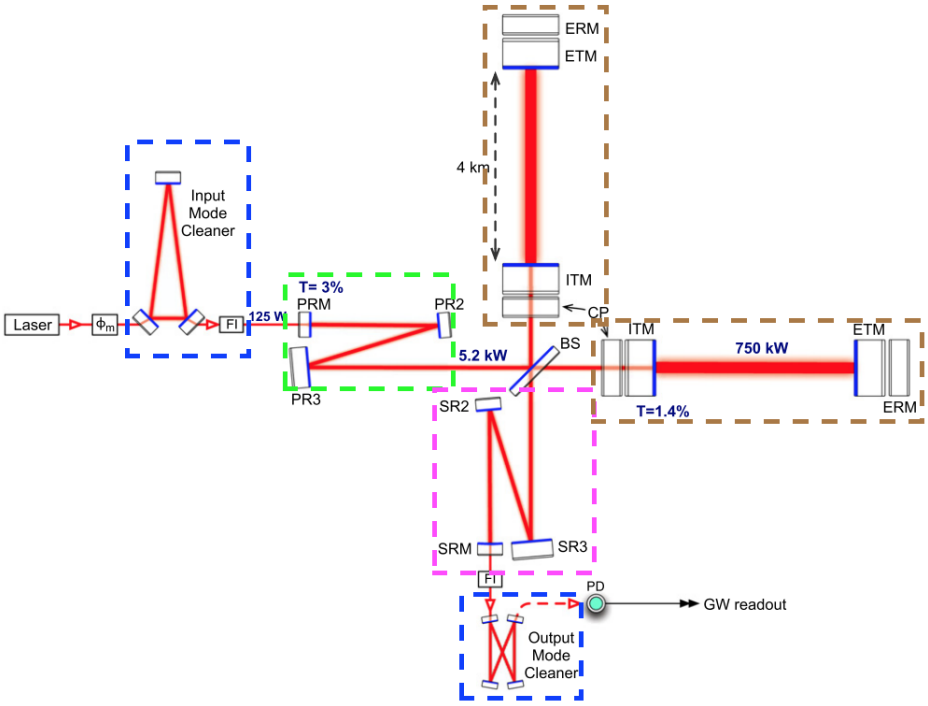

Figure 1.4: Layout of aLIGO showing the input mode cleaner (highlighted in blue), power recycling and signal recycling cavities (highlighted in green and pink respectively) in addition to the main Fabry-Pérot cavities (highlighted in brown). Main optical components are held under ultra high vacuum $< 1 \times 10^{-7}$ mbar. Taken from [34]

1.6.1 Input and Output Mode Cleaner

To measure the position of a GWD test mass to the accuracy required to measure GWs, a highly stable laser beam is required in the optical cavity. As such additional higher order modes should be rejected before light enters the main interferometer arms. For GWD this is through the input mode cleaner (IMC) which generates a pure transverse electromagnetic 00 mode (TEM_{00}) Gaussian beam and filters higher order modes which can be generated from various sources such as optical misalignment, surface distortions on optics or beam clipping from aperture sizing [41]. This is achieved by a curved and two flat mirrors with carefully chosen distances to maximise transmission of the TEM_{00} mode. This is highlighted in blue in Figure [1.4].

While a GWD is designed to reject all higher order modes from the signal cavity the output light will still contain higher order modes. If the power in these modes is low

enough they can be filtered from the main GW signal using an output mode cleaner (OMC) [41]. This is achieved by use of two flat and two curved mirrors with carefully chosen distances between each (similar to the IMC) to maximise the transmission of the GW signal. This is highlighted in blue in Figure [1.4]

1.6.2 Delay lines and Fabry Pérot Cavity

As described in Section [1.5.2] high circulating power is required in the main optical cavities to overcome the effects of shot noise. Additionally the storage time of light in a GWD cavity should be equal to half the period of the GW [42]. This can be difficult to generate over a fixed distance with a single reflection Michelson interferometer. In order to mitigate shot noise and increase the duration light spends in the cavity two types of configuration can be used. The first is to create extra reflections by either folding the cavity or shaping the mirrors to create extra bounces, therefore building up a higher circulating power [43]. This is known as a delay line and is shown in Figure [1.5]. The folded cavity technique is currently employed in the GEO600 GWD [44]. The other method to achieve high circulating laser power within the optical cavities is to introduce a resonant condition. This is achieved by focusing the light in the cavity to overlap each beam, also known as a Fabry Pérot cavity [45], shown in Figure [1.5]. This is the technique used by aLIGO, Advanced VIRGO and KAGRA to achieve high cavity power [34, 46, 47].

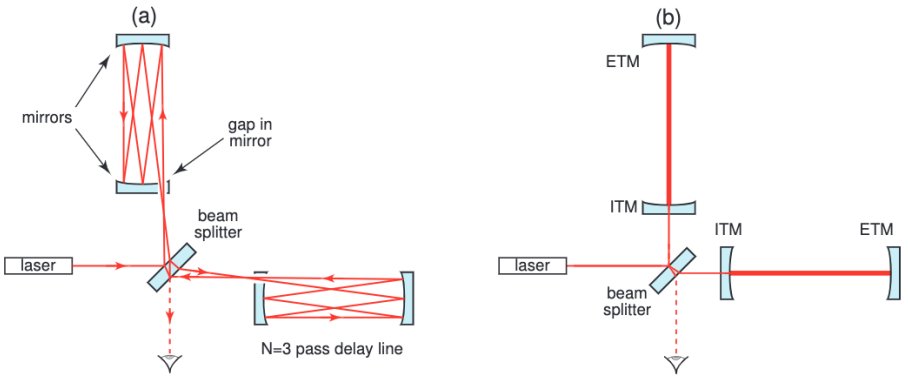

Figure 1.5: Diagram of optical layout for two interferometers with a) Delay line and b) Fabry Pérot cavity. Reprinted from [30].

1.6.3 Power and signal recycling

As the cavities in GWDs have low optical losses most of the laser light is reflected back towards the laser if the interferometer is held on a dark fringe. It was realised that if an additional mirror is placed between the incoming laser light and main arm cavities an additional optical cavity will be created giving increased arm power to the main interferometer [41]. This technique is known as power recycling (highlighted in green in Figure [1.4]) [48, 49].

Additionally placing a mirror between the main interferometer arms and the photodiode can be helpful to increase the signal seen at the output. This is known as signal recycling (highlighted in pink in Figure [1.4]) [50]. Specifically this increases the sidebands of the main GW signal by choosing a suitable reflectivity of the mirror used to reflect the signal back into the interferometer. To tune the frequency band in which the performance of the detector will peak requires positional changes to the signal recycling mirror [30].

1.6.4 Squeezed light

As described in Section [1.5.2] the fundamental limit to lowering the Quantum noise contribution to a GWD is the SQL. However this is not entirely the case when considering the light in the detector not a classical coherent EM field but as a series of quantised fields with an uncertainty associated with the phase and amplitude of the light [51]. Squeezed states are achieved by correlating light fluctuations usually by converting a single photon to two lower frequency photons with correlated phases [35]. The introduction of squeezed states into the dark port of a detector can reduce the uncertainty to one of these components (shown in Figure [1.6]) and thus improve the detector sensitivity at low (using amplitude squeezing) or high frequencies (using phase squeezing) [52].

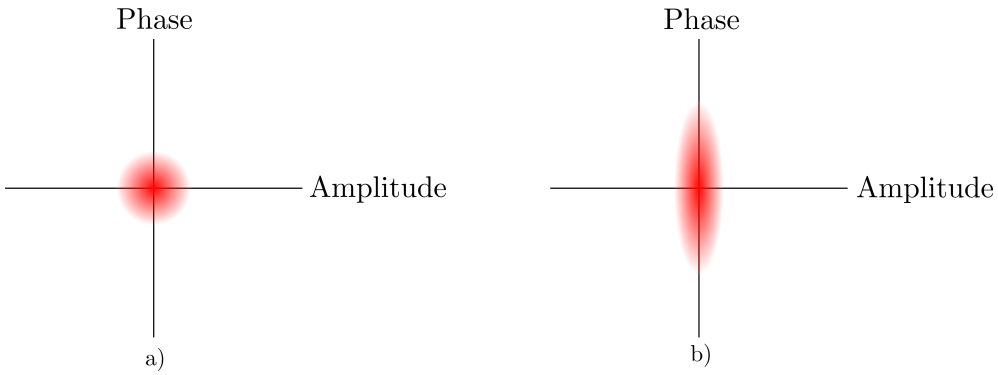

Figure 1.6: Probability distributions of light when in a) vacuum state and b) amplitude squeezing state. Modified from [24, 35]

1.7 Gravitational wave detections

Since 2015 the number of gravitational wave detections by the ground based detector network has continued to grow at a rapid rate. Having run for 3 operational periods, aLIGO currently has 90 candidate detections [16] where event rates will continue to increase with detector sensitivity enhancements, leading to many more anticipated detections in the years ahead. In this section a summary is given of some key cosmic events GWDs have witnessed over the last decade.

1.7.1 Black hole binary (GW150914)

The very first direct observation of GWs occurred on the 14^{th} of September 2015 [4]. The event was the merger of two black holes with solar masses ($M_\odot$) $36^{+5}_{-4}M_\odot$ and $29^{+4}_{-4}M_\odot$. When combined they formed a black with mass $62^{+4}_{-4}M_\odot$ calculated from a chirp mass (see Section [1.3.4]) of $\mathcal{M} \simeq 30M_\odot$. This was detected in the 10 Hz - 100 Hz range [4], the most sensitive band of the detector. This meant that $3.0^{+0.5}_{-0.5}M_\odot$ of energy was radiated away in the form of gravitational waves [4]. The signal was detected by both aLIGO sites, first in Washington and then in Louisiana 6.9 ms later. The signal was measured over the frequency band 35 Hz - 150 Hz showing a peak strain amplitude of 1×10^{-21} and a combined signal to noise ratio (SNR) of 24. The signal was localised to the southern hemisphere however with the use of detectors strategically placed over

the globe this could be narrowed down for preceding events [53].

This discovery was the first direct observation of a black hole and proved Einstein's general theory of relativity holds true for the generation of GWs from massive cosmic objects.

1.7.2 Neutron star binary (GW170817)

On the 17^{th} of August 2017 Advanced VIRGO (aVIRGO) detected a signal in the 10 Hz - 100 Hz sensitivity band followed 22 ms later by aLIGO Livingston and then after 3 ms aLIGO Hanford [54]. The objects mass were calculated to be between $1.17M_{\odot}-1.60M_{\odot}$, with a total merger mass of the system to be $2.74^{+0.04}_{-0.01}M_{\odot}$ and $\mathcal{M} = 1.188^{+0.004}_{-0.002}M_{\odot}$ [55]. A gamma-ray burst (GRB) was detected by the Fermi telescope 1.7 s after the merger allowing further localisation of the binary source [54, 55]. This discovery was therefore the first measured multi-messenger astrophysical event and to date the event which has been localised the greatest precision (to 28 deg^2, see Figure [1.7]) .

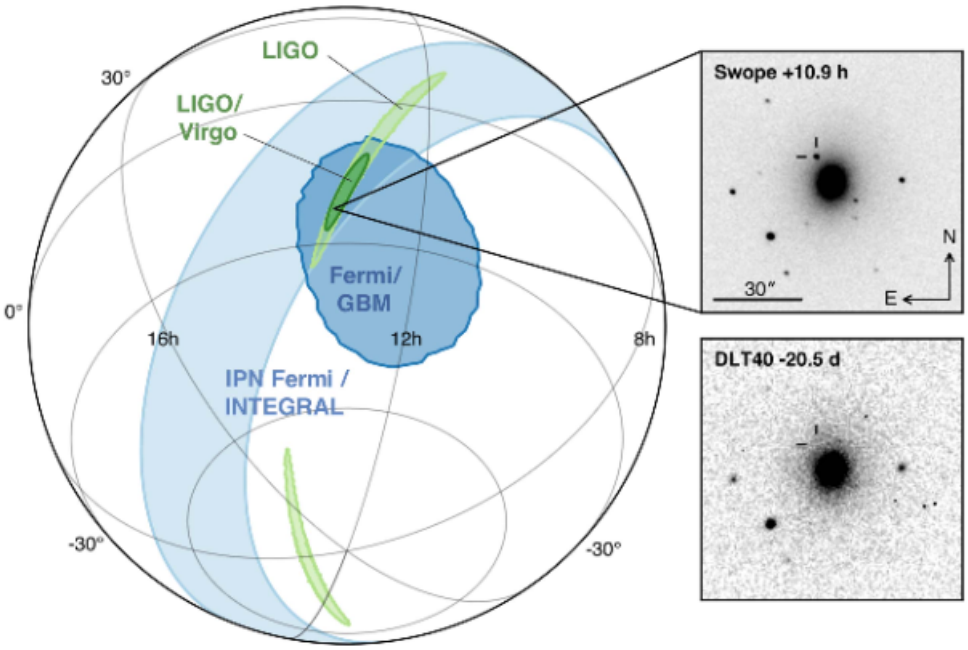

Figure 1.7: Localization of the gravitational-wave, gamma-ray, and optical signals. The left panel shows an orthographic projection of the 90% credible regions from LIGO (190 deg^2; light green), the initial LIGO-VIRGO localization (31 deg^2; dark green), IPN triangulation from the time delay between Fermi and INTEGRAL (light blue), and Fermi-GBM (dark blue). The inset shows the location of the apparent host galaxy NGC 4993 in the Swope optical discovery image at 10.9 hr after the merger (top right) and the DLT40 pre-discovery image from 20.5 days prior to merger (bottom right). The reticle marks the position of the transient in both images. Reprinted from [54].

1.7.3 Neutron star - black hole binary (GW200105 and GW200115)

On the 5$^{\text{th}}$ of January 2020 a signal, dubbed GW200105, was detected by both the LIGO and VIRGO detector networks. The signal showed the merger of a binary system thought to be a neutron star and black hole (with masses $8.9^{+1.2}_{-1.5}$ and $1.9^{+0.3}_{-0.2}M_\odot$ respectively) with chirp mass $\mathcal{M} = 3.41^{+0.08}_{-0.07}M_\odot$ [56]. This was followed by a second system 10 days later consisting of another binary system signal with similar masses involved ($5.7^{+1.8}_{-2.1}$ and $1.5^{+0.7}_{-0.3}M_\odot$ with chirp mass $\mathcal{M} = 2.42^{+0.05}_{-0.07}M_\odot$ respectively). The SNR was measured to be 13.9 and 11.6 for the two signal respectively which is above the noise floor of the current operational detectors but lower than other discoveries making the confidence intervals harder to define [56]. While it is thought that these

two events are two separate neutron star black hole binary systems, the given SNR calls the mass of the two objects into question. Some theorise that the smaller object is not a neutron star, as there was no EM counterpart measured however the mass is still within probability limits for neutron stars [56]. This event is yet another way GW observations can monitor dense matter in extreme cosmic conditions.

1.8 Current Detectors

From the first use of resonant bar detectors to the development of large scale laser interferometry, the GWD field has grown to be able to detect large cosmic events. Every additional detector added to the network, increases the localisation of event sources [57].

Currently there are five detectors in operation around the Earth (shown in Figure [1.8]), four of which are actively searching for gravitational wave signals. All of these projects will be discussed in the following section.

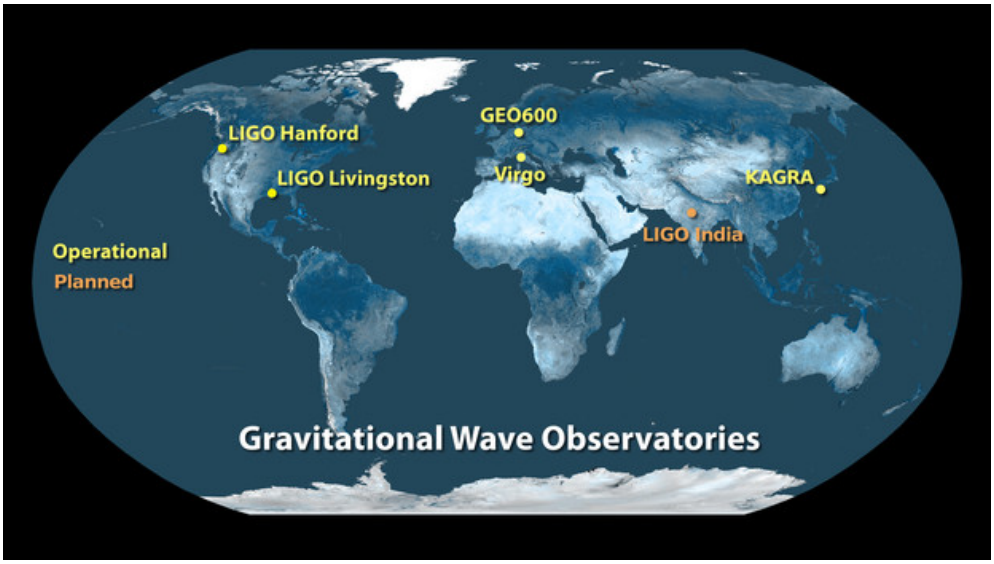

Figure 1.8: Map of the currently operational and planned GWD detector network sites across the Earth. LIGO India is discussed in Section [1.9.1]. Reprinted from [58]

1.8.1 Advanced Laser Interferometer Gravitational-wave Observatory (aLIGO)

The Advanced Laser Interferometer Gravitational-wave Observatory (aLIGO) is a GWD project in the US run as a joint venture by the Massachusetts Institute of Technology (MIT) and the California Institute of Technology (CIT). In its third instrumental iteration [59] the LIGO project was founded in the 1970s by Kip Thorne, Rainer Weiss and Ron Drever with the initial construction and commissioning extending from the early 1990s - early 2000s at two sites in Hanford, Washington and Livingston, Louisiana (shown in Figure [1.9]) [60].

Currently the aLIGO detectors consist of two 4 km long Fabry Pérot arm cavities which employ power recycling to achieve a total circulating power in each arm cavity of 750 kW [34]. The test masses used in the detectors (34 cm diameter, with a mass 40 kg) are fabricated from high grade fused silica attached to a monolithic suspension system consisting of fused silica fibres [34]. Each test mass is coated in a highly reflective (HR) mirror stack (formed of layers of TiO_2 doped Ta_2O_5 and SiO_2) to increase the reflectivity of the test mass to the laser beam at 1064 nm [34].

Figure 1.9: Images of the aLIGO Washington (left) and aLIGO Louisiana sites (right) in the U.S. Reprinted from [61]

During the last observing run of the detectors (O3b) both aLIGO sites were operation for 79% of the run duration. They additionally achieved a Binary Neutron Star (BNS) inspiral event detection range (for two $1.4M_{\odot}$ with SNR of 8) of 115 Mpc for aLIGO Hanford and 133 Mpc for aLIGO Livingston [16].

The current ongoing upgrade to aLIGO is aLIGO+ (A+) which is set to improve the noise floor of the detector at its most sensitive regime (100 Hz) by at least a factor of 4. Major improvements include the addition of frequency dependent squeezing [62], improved suspensions [63] and a new amorphous HR coating stack for the test masses [64–66].

1.8.2 Advanced VIRGO (aVIRGO)

The VIRGO project is a collaborative GWD venture in Europe, which has acted as a sister project to LIGO. Formed in 1987 by the scientists Adalberto Giazotto and Alain Brillet, the construction of a laser interferometer began in 1997 near Pisa in Italy and was completed in 2000 (shown in Figure [1.10]) [67].

In its current third iteration [59] the Advanced VIRGO (aVIRGO) detector consists of two 3 km Fabry Pérot arm cavities which can generate 700 kW of circulating arm power [68]. The test masses (35 cm diameter, with a mass of 42 kg) are made from high grade fused silica attached to four fused silica fibres. This is attached to the aVIRGO Superattenuator, a unique suspension system to capable of reducing seismic noise by ten orders of magnitude above 2 Hz [69]. Much like aLIGO as the SiO_2 are not reflective enough at the laser wavelength of 1064 nm to sustain low optical losses in the cavity they are coated with a HR stack. Like aLIGO this stack is comprised of layers of TiO_2 doped Ta_2O_5 and SiO_2 [69].

Although VIRGO was not observing during the first GW event discovery, it has since been involved in subsequent detections [53, 55, 56]. Being located on the other side of the Earth to the aLIGO project allowed further localisation of detections through the second and third observing runs [16]. During this time aVIRGO managed to achieve a BNS inspiral event detection range (for two $1.4M_{\odot}$ with SNR of 8) of 60 Mpc towards the end of the third observing run [70].

Figure 1.10: Image of the Advanced VIRGO site near Pisa, Italy. Reprinted from [71]

The planned upgrade to aVIRGO, designated aVIRGO+, will give even greater sensitivity to the detector. This overhaul to the detector will include reconfigurations to the signal recycler and much like A+ will include frequency dependent squeezing for a broadband increase to detector sensitivity [72]. Additionally new test masses of 104 kg are planned to be installed with a new suspension system [72]. The test masses will have new coatings, the current proposal is to replace the high index layer of TiO_2 doped Ta_2O_5 to Si_3N_4 for improved thermal noise performance [66, 73].

1.8.3 KAmioka Gravitational Wave Detector (KAGRA)

The KAmioka Gravitational Wave Detector (KAGRA) is a GWD operating under the Kamioka mines in Gifu Prefecture, Japan [74]. Having finished construction in 2019 it managed to join the third observing run of the global detector network [74].

KAGRA consists of 3 km Fabry Pérot cavities with signal and power recycling much like aLIGO and aVIRGO [74]. Being situated underground gives KAGRA better base seismic isolation, further improved by the use of a multi-stage seismic isolation system.

Additionally the main cavity in the interferometer is cryogenically cooled to < 22 K giving better thermal noise performance [74, 75]. Fused silica cannot be used as a test mass or suspension fibres in this case, due to a low temperature peak in thermal noise performance [76–78] therefore sapphire is employed instead (22 cm diameter, with mass of 22.8 kg [74]). The mirrors are coated with an HR stack of Ta_2O_5 and SiO_2 layers

[79]. The development of the cryogenic technologies at KAGRA will be paramount to the next generation of GWD, which plan to operate at such low temperatures [80, 81].

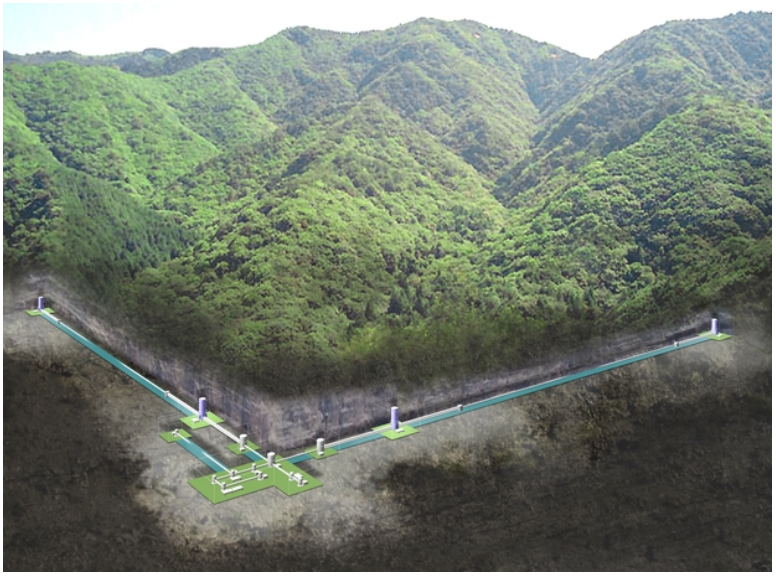

Figure 1.11: Image of KAGRA layout under the Kamioka mines in Japan. Reprinted from [82]

During the third observing run KAGRA managed to achieve a BNS inspiral event detection range (for two $1.4M_{\odot}$ with SNR of 8) of 600 kpc [74]. While not comparable to aLIGO or aVIRGO this is a promising step for a GWD operating in its infancy and an important trailblazer in the use of cryogenics.

1.8.4 GEO600

The GEO600 GWD is a European project which finished construction in 2002. It was based from two similar projects, the 10 m prototype at Glasgow University, UK [26] and the 30 m prototype interferometer at the Max Planck Institute near Munich, Germany [83].

The project consists of two folded 600 m cavities using power and signal recycling [83]. Initially GEO600 was used as an observational GWD, which would monitor for events when other detectors around the global network were shut down for maintenance or upgrade installation. Since then it has been used a test bed interferometer, developing technologies for the current and next generation of GWD [59] such as monolithic

suspension and optical squeezing [44, 84].

Currently GEO600 is focusing on increasing the sensitivity of the detector at higher frequencies (> 500 Hz) with the use of optical squeezing (see Section [1.6.4]) [44]. This technique will be particularly important in future upgrades to current detectors.

1.9 Future Planned Detectors

While not fully achieving the design sensitivity, the current generation of GWD (aLIGO, aVIRGO, *etc.*) have managed to detect GWs consistently since 2015. In order to push the limit of events that can be detected new techniques are needed which can mitigate the fundamental physical limits to their sensitivity. This section discusses future planned detectors, both on the ground or in space, which will either use these techniques to increase detector sensitivity or enhance the global GWD network .

1.9.1 Ground based

LIGO India

LIGO India is a joint collaborative GWD project between multiple instistutes in India to construct and operate a GWD. While awaiting construction this detector will use technologies, infrastructure and equipment from the already established aLIGO Hanford site to create a 4 km GWD [24]. When this GWD is online it has the potential to enhance the global detector network greatly and further increase sky localisation of GW events [57].

LIGO Voyager

LIGO Voyager is a potential upgrade to aLIGO after A+. If the project achieves design sensitivity it will improve the overall sensitivity of the detectors by a factor of 4-5 over aLIGO [80]. Modifications include larger test masses (45 cm diameter, 200kg) made of crystalline silicon with a new HR coating design (layers of amorphous silicon (aSi) and SiO_2) [80]. Additionally the laser wavelength will be changed to 2000 nm to decrease optical cavity losses and the main optics will be cryogenically cooled to 123

K to decrease thermal noise contributions [80]. The use of cryogenics will mean an entirely new suspension system will be needed, based from technologies in use at the KAGRA facility [80].

Cosmic Explorer (CE)

Cosmic Explorer (CE) is a proposed next generation GWD which will be operated in the US by the LIGO Collaboration. It aims to push the overall sensitivity of the current generation of GWD by over an order of magnitude [85]. The planned layout of the project is shown in Figure [1.12].

The main modification to CE over the current generation of detector will be the use of 40 km Fabry Pérot arm cavities to improve sensitivity, especially at lower frequencies (< 10 Hz) [85]. The core optics will include 70 cm diameter 320 kg test masses with a yet undefined HR coating scaled up from 34 cm diameter of A+ coatings [86]. Alongside these upgrades will be frequency dependant squeezing and a balance homodyne output for the GW signal. There are additional plans to upgrade CE to "Stage 2" which would use cryogenics if it proves successful to further lower the sensitivity [86].

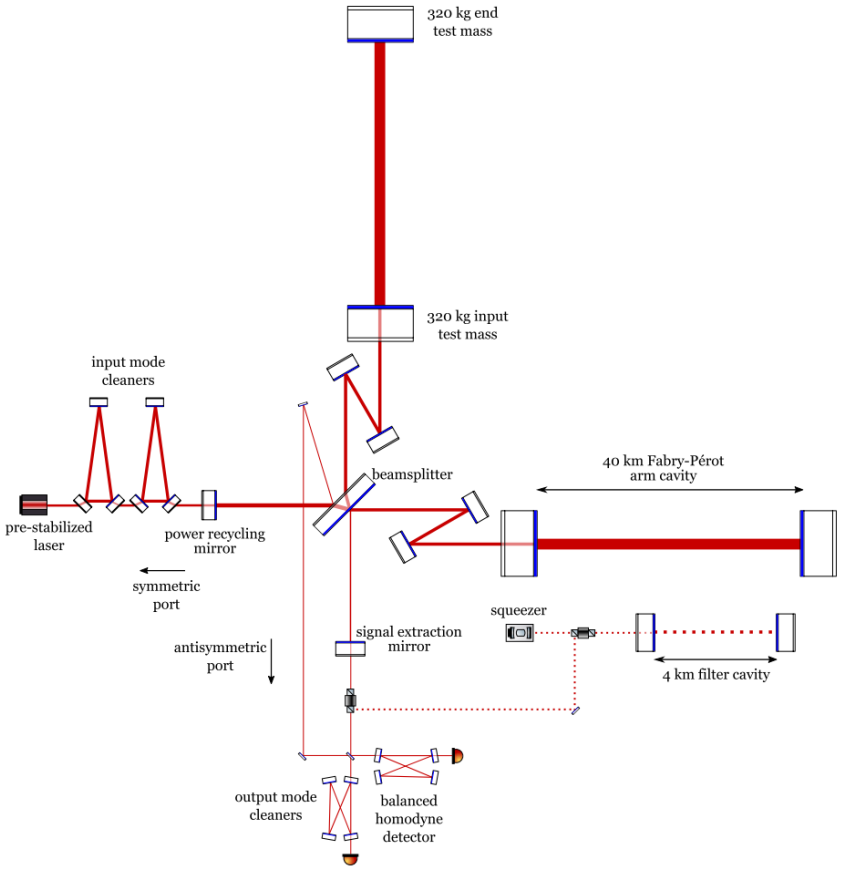

Figure 1.12: Simplified optical layout of Cosmic Explorer showing 40 km Fabry Pérot cavities with dual input mode cleaners, balance homodyne output and frequency dependant squeezer. Reprinted from [86].

Einstein Telescope (ET)

The Einstein Telescope (ET) is a planned European project to build a next generation GWD. It aims to achieve a sensitivity of a factor of 10 better than the current generation of GWD [81]. The planned layout of the detector is shown in Figure [1.13] with the site location still in the selection process.

ET will consist of three 10 km detectors, located underground to reduce seismic noise, with two interferometers each for low and high frequency monitoring in a xylophone design [87]. They are arranged in a 60° configuration which will enable slightly increased sensitivity to GWs than a 90° arm layout [87].

The high frequency interferometer (100 Hz - 10 kHz) will use room temperature

technology with 2 MW of cavity arm power (with laser wavelength of 1064 nm) and 62 cm diameter 200 kg test mass made of high grade fused silica [87].

The low frequency detector (2 Hz - 100 Hz) will use cryogenic technology to hold the detector at 123 K with 18 kW of cavity arm power (with laser wavelength of 1550 nm) and 45 cm diameter 211 kg test mass made of crystalline Si [87].

The HR coating design for ET has yet to be specified but possible options include multimaterial amorphous oxide and nitride designs (aSi, SiO_2, Si_3N_4 and Ta_2O_5) or crystalline coatings such as AlGaAs [87, 88].

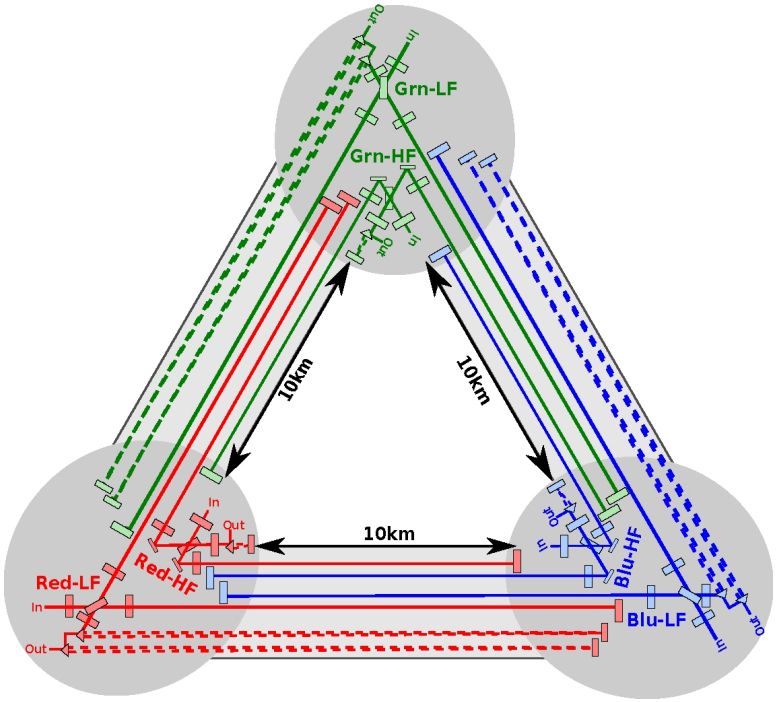

Figure 1.13: Simplified layout of the Einstein telescope showing three low and high frequency 10 km detectors arranged at 60° to one another. Reprinted from [7]

Neutron Star Extreme Matter Observatory (NEMO)

The Neutron Star Extreme Matter Observatory (NEMO) is a project between institutions in Europe and Australia designed to study high frequency GWs (1 kHz - 4 kHz). The main aim of the project is to probe the nuclear physics of neutron stars, particularly the equation of state which governs their constituent matter [89].

The project is currently designed as a 4km cryogenic interferometer (123 K) with

4.5 MW of arm power in Fabry Pérot cavities. This will be achieved by a 2000 nm, 500 W seed laser [89]. The test masses will be 45 cm diameter, 74.1 kg crystalline Si with an HR AlGaAs/GaAs coating[89]. Although in its early stages, this project plans to achieve the sensitivity of projects such as CE and ET at high frequencies (maximum sensitivity of $10^{-24}/\sqrt{\text{Hz}}$ at 2 kHz), with reduced costs [89].

1.9.2 Space based

Laser Interferometer Space Antennae (LISA)

The Laser Interferometer Space Antennae (LISA) is a planned collaboration between the European Space Agency (ESA) and the National Aeronautics and Space Administration (NASA) to build a GWD which can be operated in space. LISA consists of three interferometric spacecraft each containing a free floating test mass and optics [90]. They will be separated by more than a million km, greater than could ever be capable with ground based detectors. Additionally LISA would not subject to any seismic motion created by the Earth [91]. This will enable LISA to observe events in the mHz region (0.1 mHz - 1 Hz) of the GW source regime such as supermassive black holes and large compact binary systems [90].

The LISA pathfinder mission finished testing how free floating masses perform in a space interferometer test bed in 2016. The results show that the mass was subject to minimal fluctuations and proved a positive result for the LISA mission [92]. This has shown the space based GWD technology is promising, potentially opening new event sources to the field.

1.10 Conclusion

A century since Einstein first formulated his theory of General Relativity, gravitational waves were finally observed directly. Created from the acceleration of massive cosmic objects their detection has opened a new door in astronomy, providing the opportunity to directly observe black holes. In the time since the discover there have been 50 confirmed detections of inspiral sources of GWs [93].

The caveat to this is there are multiple noise sources which contribute to a detectors sensitivity and decrease the ability to detect events. Current detectors use multiple laser interferometric and seismic isolation techniques to increase the baseline sensitivity of detectors. To date the maximum detection range achieved is 133 Mpc with a strain sensitivity $< 10^{-23}/\sqrt{\text{Hz}}$ at 100 Hz [16].

In the years to come there are plans to upgrade current detectors (such as aLIGO and aVIRGO) in addition to building new ground and space based GWDs (CE, ET and LISA). This is set to increase event sensitivity and sky localisation greatly and allow us to peer further into the back in time to larger and more varied sources of gravitational waves that exist in the Cosmos.

Chapter 2

Coating Thermal Noise

2.1 Introduction

According to the equipartition theorem, every system above 0K has a mean thermal energy of $\frac{1}{2}k_{\mathrm{B}}T$ associated with each degree of freedom of the molecules in the mechanical system, resulting in random vibrations in the molecules at the microscopic and macroscopic level [5]. In the context of a gravitational wave detector where displacements measured can be on the order of magnitude 10^{-18} m, these vibrations will lead to motion of the test mass mirrors and subsequently create a noise source at the detectors most sensitive frequencies, the so called thermal noise.

With this source being the dominant noise contribution to aLIGO (50 - 150 Hz), Being able to reduce the magnitude of this source is therefore fundamental to improving the aLIGO detector and subsequently increasing the number of observable events. This can be done in a number of ways: by increasing the laser beam size; by reducing the temperature of the mirrors like in cryogenic detectors such as KAGRA and ET; by building the mirrors from materials with low mechanical loss.

The following chapter outlines how thermal noise impacts a gravitational wave detector's performance. It also shows how by reducing the so called "internal friction" or mechanical loss of the coating materials chosen can reduce the overall detector thermal noise contribution.

2.2 Brownian Noise

It was first observed by Robert Brown in 1828 that pollen grains exhibit random motion when suspended in water [94]. Einstein later formulated this motion in a 1905 paper showing that the motion is driven by stochastic collisions between the pollen and water molecules [**Einstein**]. This paper also showed how the pollen particles lost kinetic energy during the collisions showing the first example of a dissipative process from seemingly random fluctuations. J.B Johnson and H. Nyquist later found this process to be exhibited in conductors due to random fluctuations of electrons due to their thermal energy [95, 96].

2.2.1 Fluctuation-Dissipation Theorem

The random motion in systems first witnessed by Brown was explored further by a series of papers published by Callen *et al* [97, 98]. They show how any system in thermodynamic equilibrium will exhibit spontaneous fluctuations pertaining to the irreversible response of the system to an applied force. This response is referred to as the admittance function ($Y(\omega)$) given by,

$$Y(\omega) = \left(\frac{F(\omega)}{v(\omega)}\right)^{-1}, \tag{2.1}$$

where $F(\omega)$ and $v(\omega)$ are the force applied to the system and its resultant velocity respectively. The real part of the admittance function's inverse ($\Re[Y^{-1}(\omega)]$) characterises the magnitude of the thermally induced vibrations. The power spectral density ($S_x(\omega)$) of these vibrations can be described as,

$$S_x(\omega) = \frac{4k_BT}{\omega^2}\Re[Y(\omega)], \tag{2.2}$$

where k_B is Boltzmann's constant, T is the temperature of the object under consideration and ω is angular frequency. The mechanical impedance or damping associated with the test masses and suspensions in a GWD can be caused by internal and external factors. An external factor can be gas damping causing drag on the suspended mass

[5]. Gravitational wave detectors such as aLIGO typically operate at high vacuum ($\leq 1.33 \times 10^{-8}$ mbar) [99] in order to avoid such external damping. Internal damping arises from the anelasticity of the materials used for the detector assembly [100]. A measure of this in materials is the so called internal friction, defined as the phase lag between an applied stress and resulting strain [100].

2.2.2 Internal mechanical dissipation

In perfect elastic system an applied stress will lead to an instantaneous strain. However in an anelastic body an applied stress will have a delayed strain response [100]. A periodic stress (σ) applied to a material will take the form,

$$\sigma = \sigma_0 e^{i\omega t}, \tag{2.3}$$

where σ_0 is the stress amplitude and ω is the angular frequency of the oscillations. Applying this force to an anelastic system will lead to a periodic strain but with a phase lag respective to the applied stress described as,

$$\epsilon = \epsilon_0 e^{i(\omega t - \phi)}, \tag{2.4}$$

where ϵ_0 is the strain amplitude and ϕ is the phase lag or the so called mechanical loss.

From this definition it can be said that mechanical loss can also be defined as the fractional energy loss per cycle of oscillation,

$$\phi = \frac{1}{Q} = \frac{E_{\text{lost per cycle}}}{2\pi E_{\text{stored}}}, \tag{2.5}$$

where Q is the quality factor of the oscillator. A material exhibiting internal damping can be found to obey Hooke's law with a spring constant defined as,

$$F = -k[1 + i\phi]x, \tag{2.6}$$

where k is the spring constant and x is the displacement. Using the definitions for displacement and acceleration in terms of velocity ($x = \frac{\dot{x}}{i\omega}$ and $\ddot{x} = i\omega\dot{x}$ respectively)

[5] and substituting into Hooke's law ($F = m\ddot{x} + f\dot{x}$),

$$F = mi\omega\dot{x} + \frac{k[1 + i\phi]\dot{x}}{i\omega}, \tag{2.7}$$

Substituting in to Eq[2.1] and rationalising the denominator,

$$Y = \frac{i\omega(k - ki\phi - \omega^2 m)}{(k - \omega^2 m)^2 + \phi^2 k^2}, \tag{2.8}$$

The thermal noise power spectral density can then be calculated using Eq[2.2],

$$S_x(\omega) = \frac{4k_b T k\phi\omega}{\omega^2(k - \omega^2 m)^2 + \phi^2 k^2}, \tag{2.9}$$

using the equivalent relation for $k = m\omega_0^2$ where ω_0 is the angular resonant frequency gives,

$$S_x(\omega) = \frac{4k_b T m\omega_0^2\phi}{\omega^2(m\omega_0^2 - \omega^2 m)^2 + m^2\omega_0^4\phi^2}, \tag{2.10}$$

Fig [2.1] illustrates the effect of mechanical loss on the thermal noise spectral density of an oscillator. It can be seen that as the mechanical loss decreases in the oscillator the thermal noise is reduced off resonance. This is key in gravitational wave detectors as the resonant frequency of the test masses are much higher than the detection band therefore reducing off resonance thermal noise improves detector sensitivity [101].

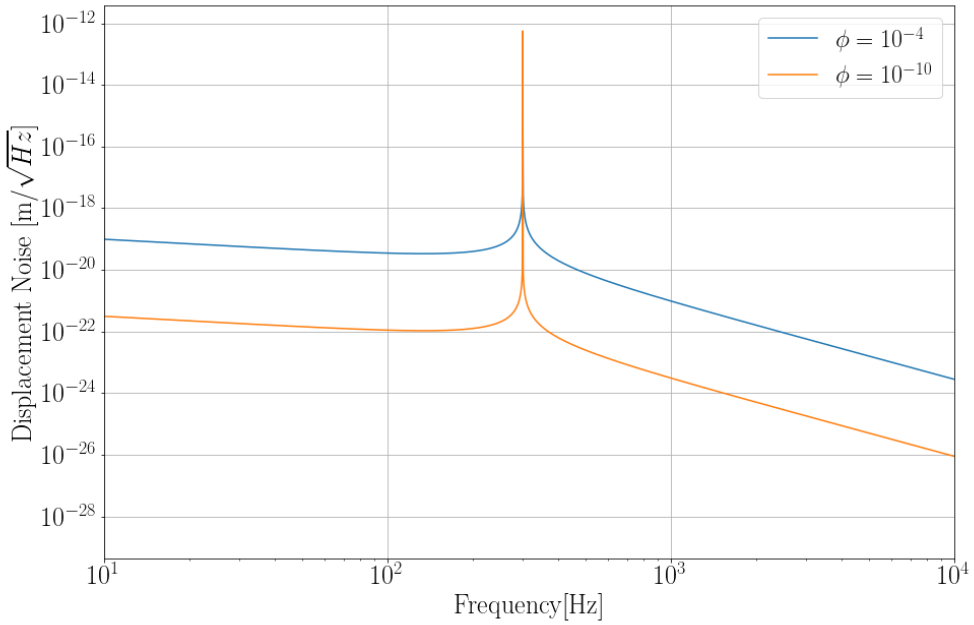

Figure 2.1: Plot of the thermal noise contribution for 2 masses with different mechanical losses using Eq[2.10]. For this case $m = 40$ kg, $f_0 = 300$ Hz and $T = 295$K.

2.3 Coating Brownian Thermal Noise

One of the first estimations of thermal noise in a gravitational wave detector was calculated by applying the fluctuation-dissipation theorem to each resonant mode of the test mass and summing over all modes [102]. This is described by,

$$S_x(f) \approx \sum_n \frac{4k_B T}{\alpha_n m \omega_n^2} \frac{\phi_n(\omega)}{\omega}, \tag{2.11}$$

where α_n, ω_n and ϕ_n are the effective mass coefficient, resonant frequency and mechanical loss of eigenmode n. α_n models optical and vibration resonance as a single dimension mass-spring system. This thermal noise estimation assumes the distribution of loss inside the test mass is spatially homogeneous. This breaks down in practice as the front face of the test mass has a highly reflective (HR) mirror stack coatings, made up of materials with higher loss than the fused silica test mass [103]. In the case of

aLIGO the stack consists of titania doped tantalum pentoxide (TiO_2:Ta_2O_5) and SiO_2 layers with a mechanical loss at least 3 orders of magnitude higher than the bulk SiO_2 [104]. Additionally both the coating and test mass can have inhomogeneity in losses associated with changes in the bulk properties through the medium (defects in material deviations from a purely crystalline structure) [105].

To account for the mechanical loss in the test mass caused by the HR coating a direct approach was formulated by Levin [105] and further studied by Nakagawa *et al.* [106] using methods other than modal expansion. In this case the test mass is considered to have a Gaussian force placed on it's surface, simulating the laser beam monitoring the test mass. The thermal noise power spectral density then takes the form,

$$S_x(f) = \frac{2k_BT}{\pi^2 f^2}\frac{W_{\text{diss}}}{F_0^2}, \tag{2.12}$$

where W_{diss} is the time-averaged power dissipation within the media (test mass) when the Gaussian oscillator is applied with peak force F_0. This can be described for an inhomogeneous media as [107],

$$W_{\text{diss}} = 2\pi f \int_{vol} \epsilon(x,y,z)\phi(x,y,z,f)dV, \tag{2.13}$$

where ϵ and ϕ are the energy density at maximum elastic deformation and mechanical loss inside the test mass respectively. If the mass is semi-infinite in comparison to the beam diameter the Brownian thermal noise power spectral density of the substrate can be described as [107],

$$S_x(f) = \frac{2k_BT}{\pi f}\frac{1-\sigma^2}{\sqrt{2\pi}Yr_0}\phi_{\text{substrate}}(f), \tag{2.14}$$

where r_0 is the radius of the beam at $1/e^2$ intensity, Y is the Young's modulus σ is the Poisson's ratio of the test mass and $\phi_{\text{substrate}}$ is the mechanical loss of the test mass (substrate). As the force is applied to the front of the mirror, displacements located at the front face will contribute more to thermal noise (from displacement) than the back face. It is therefore important to have a material of low loss on the front face of the

test mass in a gravitational wave detector.

Nakagawa *et al* [108] then calculated a thermal noise estimate on a non-uniform lossy test mass with a layer of high loss on its surface where a Gaussian beam profile is in contact.

Harry *et al* [109] described a method to estimate the thermal noise contribution of the test mass including the mirror coating. While this method was similar to the method used by Levin, the key difference was the introduction of elastic strain perpendicular ($\perp$) and parallel ($\parallel$) to the coating surface. This was to account for any potential anisotropy in mechanical loss of the coating layers. This gives thermal noise of the form,

$$\begin{aligned} S_x(f) = \frac{2k_BT}{\pi^{3/2}f}\frac{1-\sigma_{\rm sub}^2}{r_0 Y_{\rm sub}}\Bigg\{\phi_{\rm substrate} &+ \frac{1}{\sqrt{\pi}}\frac{d}{r_0}\frac{1}{Y_{\rm sub}Y_{\rm coat}\left(1-\sigma_{\rm coat}^2\right)\left(1-\sigma_{\rm sub}^2\right)} \\ &\times\Big[Y_{\rm coat}^2(1+\sigma_{\rm sub})^2(1-2\sigma_{\rm sub})^2\phi_{\parallel} \\ &+Y_{\rm sub}Y_{\rm coat}\sigma_{\rm coat}(1+\sigma_{\rm sub})\left(1+\sigma_{\rm coat}\right)\left(1-2\sigma_{\rm sub}\right)\left(\phi_{\parallel}-\phi_{\perp}\right) \\ &+Y_{\rm sub}^2\left(1+\sigma_{\rm coat}\right)^2\left(1-2\sigma_{\rm coat}\right)\phi_{\perp}\Big]\Bigg\} \end{aligned} \tag{2.15}$$

where d is the coating thickness. In this work Y_{coat} and σ_{coat} is calculated by averaging the Young's modulus and Poisson ratio of each material used in the HR stack over all layers of the coating. Additionally if the assumption is made that $\phi_{\perp} = \phi_{\parallel}$ and $\sigma_{\rm sub} = \sigma_{\rm coat} = 0$ the following expression is derived,

$$S_x(f) = \frac{2k_BT}{\pi^{3/2}f}\frac{1}{r_0 Y}\left\{\phi_{\rm substrate} + \frac{1}{\sqrt{\pi}}\frac{d}{r_0}\left(\frac{Y_{\rm coat}}{Y}\phi_{\parallel}+\frac{Y}{Y_{\rm coat}}\phi_{\perp}\right)\right\}, \tag{2.16}$$

This assumption regarding mechanical losses of the coating was made due to there being no direct way to measure both parameters. This theorem does however hold for a multilayer of TiO_2:Ta_2O_5 and SiO_2 assuming there is no friction generated at the interface between the coating and substrate [104]. An additional theorem is needed to account for differing losses within materials.

2.4 Bulk and Shear Loss

Although the assumption that $\phi_\perp = \phi_\parallel$ is so far agreeable by direct measurement of coating thermal noise there is no physical reason why this should be the case in any coating. With this in mind Hong *et al* [110] devised an approach to calculate thermal noise based on separate loss mechanisms arising from bulk and shear deformations in the coating. The total energy in the coating can be described as,

$$U_{\text{coating}} = U_{\text{B}} + U_{\text{S}}, \tag{2.17}$$

where the bulk (U_B) and shear (U_S) energy components of Eq[2.17] can be expressed as,

$$U_B = \int_{\text{coating}} \frac{K}{2} \Theta^2 dV, \tag{2.18}$$

$$U_S = \int_{\text{coating}} \mu \Sigma_{ij} \Sigma_{ij} dV, \tag{2.19}$$

Taking the Levin approach to the thermal noise problem the authors calculated the bulk and shear elastic energy components with respect to a Gaussian force applied to the surface of the test mass (F_0) gives,

$$\begin{aligned} \frac{U_B}{F_0^2} =& \frac{(1-2\sigma_{coat})\,d}{3} \left[\frac{Y_{coat}}{Y_{sub}^2} \frac{(1-2\sigma_{sub})^2 (1+\sigma_{sub})^2}{(1-\sigma_{coat})^2} \right. \\ &+ \frac{1}{Y_{sub}} \frac{2(1-2\sigma_{sub})(1+\sigma_{sub})(1+\sigma_{coat})}{(1-\sigma_{coat})^2} + \left. \frac{1}{Y_{coat}} \frac{(1+\sigma_{coat})^2}{(1-\sigma_{coat})^2} \right] \\ &\times \frac{1}{\mathcal{A}_{\text{eff}}} \end{aligned} \tag{2.20}$$

$$\begin{aligned}\frac{U_S}{F_0^2} =& \frac{2d}{3}\left[\frac{Y_{coat}}{Y_{sub}^2}\frac{\left(1-\sigma_{coat}+\sigma_{coat}^2\right)\left(1+\sigma_{sub}\right)^2\left(1-2\sigma_{sub}\right)^2}{\left(1-\sigma_{coat}\right)^2\left(1+\sigma_{coat}\right)}\right. \\ & -\frac{\left(1+\sigma_{coat}\right)\left(1-2\sigma_{coat}\right)\left(1-2\sigma_{sub}\right)\left(1+\sigma_{sub}\right)}{Y_{sub}\left(1-\sigma_{coat}\right)^2} \\ & \left.+\frac{\left(1-2\sigma_{coat}\right)^2\left(1+\sigma_{coat}\right)}{Y_{coat}\left(1-\sigma_{coat}\right)^2}\right]\frac{1}{\mathcal{A}_{\text{eff}}}\end{aligned} \tag{2.21}$$

where $\mathcal{A}_{\text{eff}} = \pi r_0^2$. Assuming no light penetration into the coating and assuming that the coating thickness (d) $\ll$ substrate thickness (d_{sub}) and beam spot size (r_0), the power spectral density of thermal noise for a single layer coating takes the form,

$$S_{\bar{\xi}} = \frac{4k_BT}{\pi f}\left[\phi_B\frac{U_B}{F_0^2} + \phi_S\frac{U_S}{F_0^2}\right], \tag{2.22}$$

This method while included in this thesis for completeness, is not used in any analysis of data by the author in the following chapters. This is due to there being no direct method to measuring ϕ_B or ϕ_S therefore any inferred values will increase the error in a thermal noise evaluation for the material in question [111].

2.5 Thermoelastic noise

Thermoelastic noise arises in a gravitational wave detector from temperature gradients leading to thermal fluctuations. These fluctuations create a motion on the mirror surface of the detector thereby creating a measurable cavity length change. This was first quantified by Braginsky *et al.* [112] for a substrate and later adapted by Fejer *et al.* [113] for a multilayer coating to be,

$$S_x(f) = \frac{8\sqrt{2}k_BT^2}{\pi\sqrt{\omega}}\frac{l^2}{w^2}\left(1+\sigma_s\right)^2\frac{C_f^2}{C_s^2}\frac{\alpha_s^2}{\sqrt{k_sC_s}}\tilde{\Delta}^2, \tag{2.23}$$

where C_s is the specific heat capacity of the substrate. In this approach the multilayer coating properties are averaged over the entire thickness therefore C_f is the averaged specific heat capacity of the coating and $\tilde{\Delta}^2$ is a dimensionless combination of material constants defined as,

$$\tilde{\Delta}^2 \equiv \left\{ \frac{C_s}{2\alpha_s C_f} \frac{\alpha}{1-\sigma} \left[\frac{1+\sigma}{1+\sigma_s} + (1-2\sigma_s)\frac{Y}{Y_s} \right] - 1 \right\}^2, \tag{2.24}$$

where Y, Y_s and σ, σ_s are the Young's modulus and Poisson ratio of the coating and substrate respectively. It is important to note that the thermoelastic noise contribution will differ depending on the material selected for a gravitational wave detector substrate and HR mirror stack. This noise contribution can therefore be reduced by selecting materials with similar properties to the substrate used.

2.6 Thermoelastic dissipation

In addition to thermoelastic noise, thermoelastic dissipation is also a prominent constraint on material choice for a GW detector. Considering a small beam as in Fig[2.2] when the system is under compression the beam will be slightly hotter and when the beam is expanding it will be slightly cooler. This gives rise to a temperature gradient across the beam which will have a corresponding mechanical dissipation related to the resulting heat flow, given by [114, 115],

$$\phi_{\text{therm}} = \frac{Y\alpha^2 T}{\rho C} \frac{\omega\tau}{1+\omega^2\tau^2}, \tag{2.25}$$

where τ is defined as the thermal relaxation time which is the related to the time taken for the thermal gradient across the beam to relax. This quantity is geometry dependant, for a simple rectangular beam is given as [116],

$$\tau = \frac{\rho C t^2}{\pi^2 \kappa}, \tag{2.26}$$

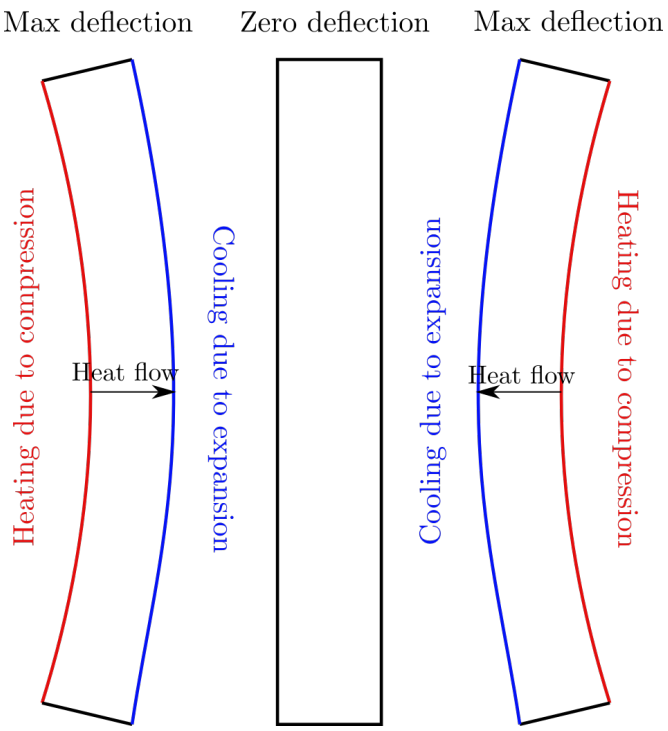

Figure 2.2: Diagram of thermoelastic damping showing how expansion and contraction of a beams surface will cause a heat flow across the bulk.

2.7 Thermo-refractive noise

Thermo-refractive noise is caused by thermal fluctuations creating a phase shift in the reflected light from the detector mirror surface. This arises from a change in the refractive index of the mirror materials with respect to temperature which will cause fluctuations in the optical thickness of the coating (with the penetration depth of the light being of the order of optical thickness of bilayers in a HR stack). This factor, known as the thermo-refractive factor ($\beta = \frac{dn}{dT}$) can be much greater than α for gravitational wave detector's mirror materials (30 times larger for fused SiO_2 [117]). The power spectral density of this effect was calculated by Braginsky *et al.* [117] described as,

$$S_{x,\beta}^{TD}(\omega) = \frac{\sqrt{2}\beta_{\text{eff}}^2 \lambda^2 k_B T^2}{\pi r_0^2 \sqrt{\omega \rho C \kappa}}, \tag{2.27}$$

where λ is the wavelength, κ is the thermal conductivity, ρ is the density, C is the specific heat capacity and β_{eff} is th effective thermo-refractive factor of the whole multilayer coating (consisting of quarter wavelength layers only) given by,

$$\beta_{\text{eff}} = \frac{n_2^2\beta_1 + n_1^2\beta_2}{4\left(n_1^2 - n_2^2\right)}, \tag{2.28}$$

where n_1 and n_2 are the refractive indices of odd and even layers of the multilayer coating respectively.

2.8 Thermo-optic noise

Thermoelastic and thermo-refractive noise both arise from thermally driven random fluctuations in the temperature. These effects would lead to a change in the sensing position of the test mass. Evans *et al* [118] related these two noise sources coherently by describing both effects as thermo-optic noise. In this treatment the power spectrum of thermal fluctuations in the coating responsible for thermo-optic noise as seen by a Gaussian beam profile is given by,

$$S_{\text{TO}}^{\Delta T} = \frac{2\sqrt{2}}{\pi}\frac{k_B T^2}{r_0^2\sqrt{\kappa C\omega}}, \tag{2.29}$$

where κ is the thermal conductivity of the mirror and C is the heat capacity per volume. By considering the substrate as semi-infinite and assuming the coating elastic coefficients are similar to the substrate material an expression can be derived for thermo-optic noise of a test mass mirror with a thick coating,

$$S_{\text{TO}}^{\Delta z} = S_{\text{TO}}^{\Delta T}\Gamma_{tc}\left(\Delta\bar{\alpha}_{fsm}d - \bar{\beta}\lambda\right)^2, \tag{2.30}$$

where d is the coating thickness, Γ_{tc} is the correction factor of the thermo-optic noise related to a thin coating, α_{fsm} is a correction factor for the thermoelastic medium derived from the mirror beam size and $\bar{\beta}$ is the thermo-refractive coefficient given for a multilayer HR stack (of 1/4 wavelength doublets with a 1/2 wavelength cap layer) by,

$$\bar{\beta} \simeq \frac{B_H + B_L \left(2\left(n_H/n_L\right)^2 - 1\right)}{4\left(n_H^2 - n_L^2\right)}, \tag{2.31}$$

where B_X is the fractional change in optical path length for the high or low index layer and n_X is the refractive index of the high or low index layer.

It can be seen in Eq [2.30] that thermoelastic and thermo-refractive contributions are two terms separated by a negative sign. This result shows that the two effects reduce the overall thermo-optic noise contribution (as the test mass is displaced thermoelastic effects the sensing position is changed in the opposite direction due to thermo-refractive change in reflection phase). For the current materials used for aLIGO this effect is of an insignificant magnitude [118] however for future upgrades careful material selection will be necessary to further mitigate this source of noise.

2.9 Conclusions

In summary, random thermal fluctuations can cause a variety of noise sources which can impede the operational sensitivity of a gravitational wave detector. Furthermore the noise sources are highly correlated to the materials used in the detector, particularly of the substrate and coating. Another way to reduce these noise sources is to lower the temperature of the detector, such as what has been used in KAGRA and the proposed ET. However a cryogenic upgrade to any detector requires a wealth of additional complex requirements. In the case of aLIGO this noise source is larger and therefore more prominent around 50 - 150 Hz, the most sensitive band of the detector. Therefore the choice of mirror materials for the next upgrade, aLIGO + (A+), is vitally important in improving the overall detector sensitivity.

Chapter 3

Coating Deposition

3.1 Introduction

As described in Section 1.5.2, to suitably reduce the shot noise within the bandwidth of interferometric GW detectors, large levels of circulating optical power are required. Current and future GW observatories plan to use MW-levels of power within their optical cavities, which sets stringent requirements on the required reflectivities and optical losses [41]. The typical route to achieve these mirror performances is to use optical interference from multilayer coatings, however the thermal noise associated with typical mirror coatings creates an additional challenge to be overcome, as described in Section 1.5.5 (and [105]). Current GW mirrors use physical vapour deposition (PVD), which is capable of producing highly dense, low absorption thin film coatings [119]. The current preferred PVD technique used to produce the coatings for a gravitational wave detector (GWD) is ion beam sputtered deposition (IBSD), as one of the only methods verified to produce coatings with low absorption and scatter (ppm and sub-ppm) over large area (10s cm to approaching metre-scale) [120]. In addition to low optical absorption films, the technique has also shown to produce coating mechanical loss over large area substrates ($>$ 20 cm) which can get close to the requirements for a GWD [121, 122]. As discussed in Chapter 2, this is key to reducing the thermal noise contribution within GW detectors, and therefore improve their sensitivity and astrophysical reach.

Outlined in this chapter is a brief summary of common coating deposition methods that have been utilised for research into improving gravitational wave detector coating thermal noise performance including chemical and physical vapour deposition techniques. In addition, the theory of ion beam deposition and ion sources used to produce highly reflective coatings is discussed. Also introduced are simulation packages used to model IBSD and the relevance to the studies presented. Finally outlined is how this applies to gravitational wave detector coatings, specifically the design and construction of a large RF-IBSD 1200 system, a custom built deposition chamber specially designed for researching low loss coating materials relevant for gravitational wave detectors.

3.2 Deposition Methods

3.2.1 Plasma-enhanced chemical vapour deposition (PECVD)

Plasma-enhanced chemical vapour deposition (PECVD) has been used to deposit silicon nitride coatings of various stoichiometry (SiN_x) for the application of room temperature and cryogenic GW detectors [123] in addition to amorphous silicon (a-Si) [124] and silica (SiO_2) [125]. The deposition occurs by the introduction chemical vapour precursors to heated substrates under vacuum (typically $< 10^{-3}$ mbar). The chemical reaction between the heated substrates and precursors in vapour phase forms a coating on the substrates. By creating a plasma in this environment the precursors are more thermally energetic and partially decompose before reaching the substrates [126]. The plasma is created by injecting radio frequency (RF) power (usually at 13.56 MHz) into a carrier gas [123]. The introduction of a plasma into this process allows the deposition to occur at lower temperatures (250 - 350 ^{o}C [126]) than conventional chemical vapour deposition (800 - 1000 ^{o}C [127]) meaning no additional components are required to decompose the precursor gas [126].

The mechanical losses of SiN_x fabricated by PECVD have been shown to reach 1.3 $\times 10^{-5}$ [123] however further developments are required to understand the optical absorption and uniformity of materials deposited by this method [128].

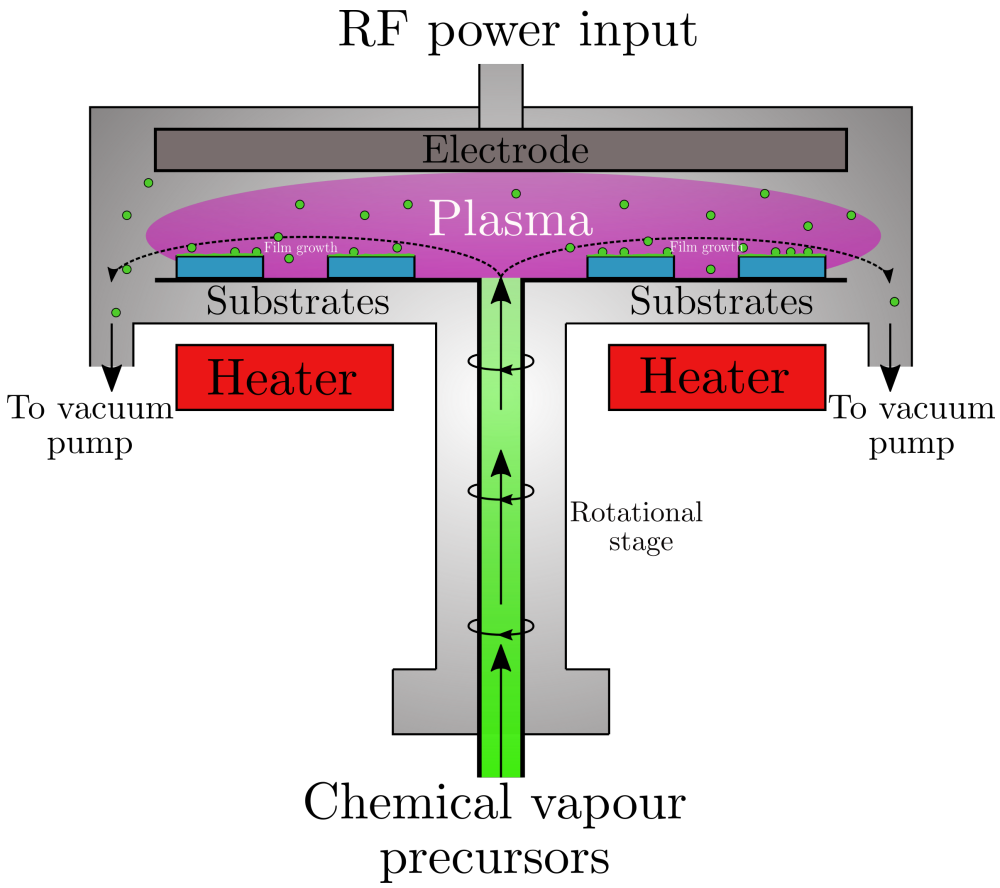

Figure 3.1: Schematic diagram of conventional PECVD deposition process. Modified from [126]

3.2.2 Magnetron Sputtering (MS)

Magnetron sputtering (MS) using an radio frequency (RF) supply has been used in the past to create amorphous Si (a-Si) and ZrO_2 doped Ta_2O_5 coatings for GW detector research [129, 130]. This process utilises a plasma situated in front of a target material under vacuum (typically $< 10^{-3}$ mbar) to bombard and sputter material via biasing of the target [131]. The plasma is created via glow discharge, where current is passed through a gas from an anode (substrate) to a cathode (target material). In passing high voltage through the sputtering gas, from either an RF or pulsed DC supply, electrons are accelerated away from the cathode causing ionising collisions with additional gas atoms [132]. This causes a cascade of high energy ions to be produced which are accelerated towards the target (cathode) to sputter material from the surface. By having a magnetic

field confine the plasma (one pole at the centre of the target material and the other formed around the edge by a ring of magnets) the secondary electron emission can be confined to the target [131], further controlling the sputtering process. This process is outlined in Figure [3.2]. The plasma is neutralised by secondary electron emitted from the target which circulate the plasma to keep the net $q = 0$.

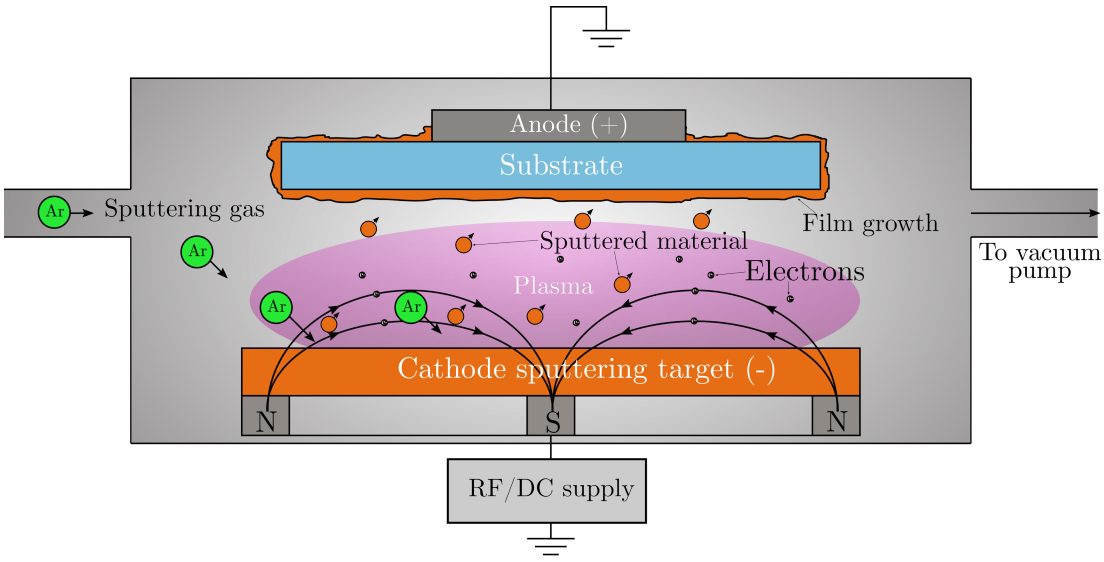

Figure 3.2: Schematic diagram of conventional magnetron sputtering process outlining magnetic field distribution and coating deposition using Ar as the sputtering gas. Modified from [133] and [131]

.

3.2.3 Electron beam evaporation (EBE)

Electron beam evaporation (EBE) is a PVD technique utilising the thermionic emission of electrons from a filament to evaporate material from a target [134]. This process is illustrated in Figure[3.3]. Typically a tungsten filament is used to generate the electrons which are directed via electrostatic optics and an additional static magnetic field towards a material. The filament is usually located behind the target material to avoid damage from the evaporated plume [134]. This process is conducted in high vacuum ($\approx 10^{-4}$ mbar) to allow the mean free path of electrons to be longer than the distance between the filament and substrate as EBE is a low thermal energy process

[134]. This method has shown to produce low thermal noise coatings both at cryogenic and room temperature with conventional EBE methods and ion plating (EBE with ion assist directed at the vapour plume) [135–137]. Furthermore it has also proven to coatings with high uniformity over large areas (99.5% over 0.75 m) [138, 139]. Currently however this method has not proved empirically that both the level of uniformity and low thermal noise performance can be achieved simultaneously.

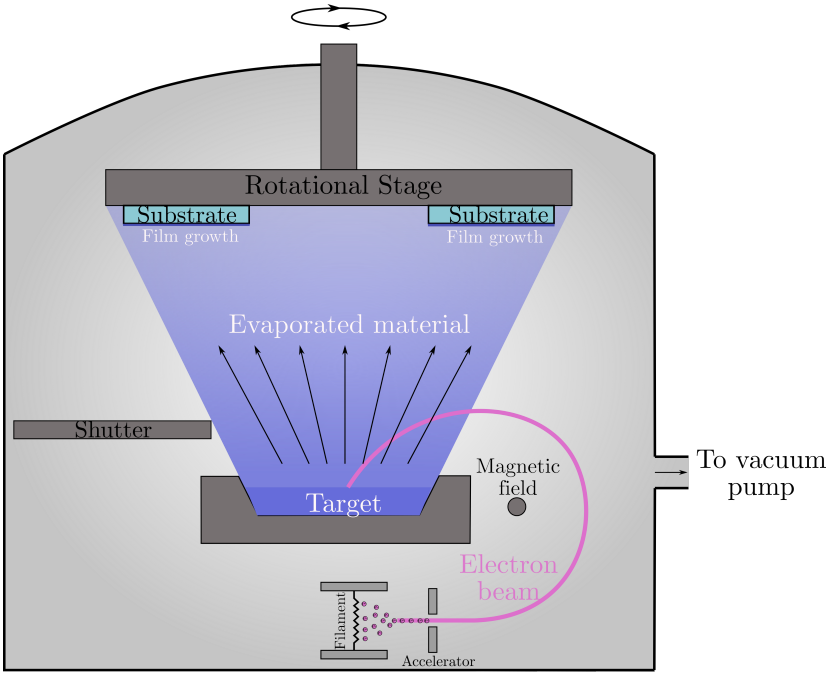

Figure 3.3: Diagram of conventional electron-beam evaporation deposition process showing cathodic electron generation and material deposition on substrates (Modified from [134]).

3.2.4 Molecular Beam Epitaxy (MBE)

Molecular beam epitaxy (MBE) is a PVD technique largely used to grow novel microwave and optoelectronic devices [140]. It has however been studied for use in gravitational wave coatings research by producing crystalline coatings of GaAs, GaP, AlGaAs and AlGaP [141, 142]. The process consists of beams of material being projected onto a heated substrate surface under ultra high vacuum (UHV) of $< 10^{-7}$ mbar [140]. The beams are created by effusion cells mounted on flanges with moveable shutters to control the beam flow. The effusion cell itself consists of a crucible of material surrounded

by heater. As the temperature increases in the cell the material vaporises allowing it to be deposited onto an adjacent substrate [143]. The process is monitored using reflection high energy electron diffraction (RHEED) and phosphor fluorescent screen. Electrons strike the sample at a glancing angle and the resulting diffraction pattern shown on the screen allows the thickness and crystal structure of the growth to be monitored [143]. The beam flux is calibrated by an ion gauge, monitoring beam density. Liquid nitrogen panels surround the process to both cool the material sources and prevent any cross contamination between materials by trapping stray molecules [143].

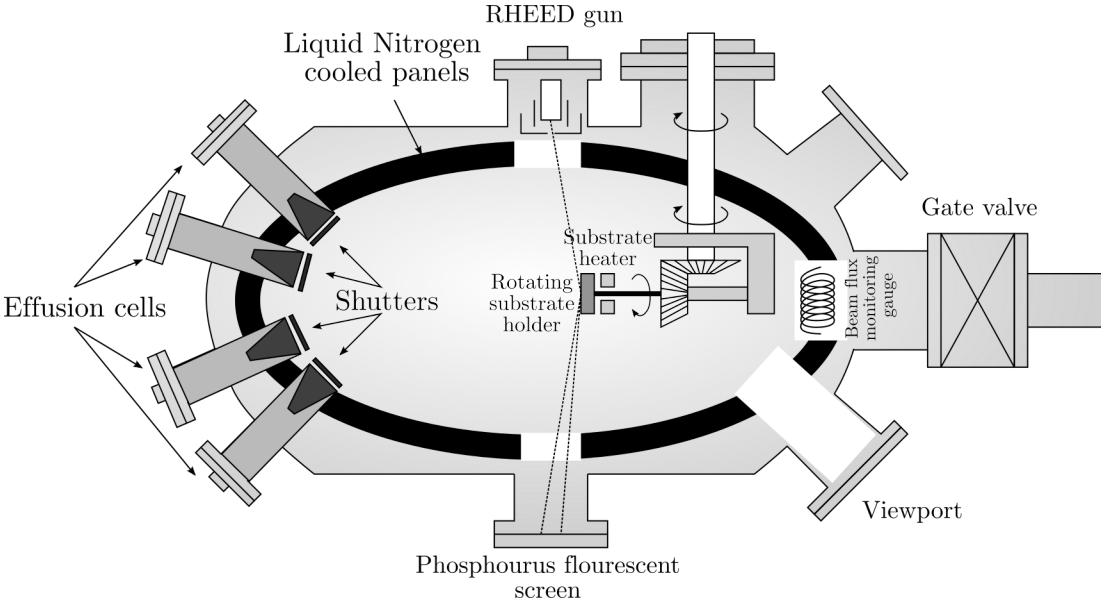

Figure 3.4: Schematic of Molecular Beam Epitaxy system. Highlighted are effusion cells for molecular beam production, RHEED and fluorescent screen for sample monitoring and rotating substrate holder. Modified from [143]

The substrate is usually fed into the chamber via a load-lock system, to avoid having to fully vent the MBE process chamber when coating. The substrate holder both rotates and is heated, the former to smooth out any uniformity issues generated from the localised beam direction and the latter to increase surface diffusion in the process, so the molecular species can find appropriate lattice sites in the structure by which to match with [143]. The process has been able to produce coatings which meet the requirements for aLIGO + however as yet has been unable to manufacture these coatings on substrates larger than 20 cm [144, 145]. This is due to the process of

transferring the crystalline coating to an appropriate size and optical quality substrate.

AlGaAs coatings are grown on GaAs wafers due to lattice matching properties of the substrate. This substrate is not suitable for a GWD due to the optical characteristics, therefore it needs to be transferred to a more appropriate substrate, such as SiO_2, using specific etching and bonding techniques [141]. However currently both the scale up and growth of this method have not been proven [144]. AlGaP has however been grown directly on Si substrates due to the appropriate lattice matching being achieved, making it a promising candidate for a cryogenic GWD [142]. In its current state however more material development is required to achieve better optical quality [146].

3.2.5 Ion Beam Sputtered Deposition (IBSD)

IBSD belongs to a class of deposition methods known as physical vapour deposition [119]. This coating process (shown in Figure[3.7]) uses a beam of positively charged gas particles, generated through methods such as radio frequency (see Section [3.3]) or electron cyclotron resonance, to sputter material from a target surface towards an adjacent substrate. The current coatings for gravitational wave detectors are produced through this deposition method as it is currently the only process capable of meeting the detector design requirements over a large area [103]. A comparison of this method to the other deposition methods outlined is given in Table[3.1]. This process is described in more detail in Section [3.4]

Coating property	PECVD	MS	EBE	MBE	IBSD
High reflection	✓[147]	✓[148]	✓[149]	✓[150]	✓[151]
Low optical losses	✓[147]	×[152]	✓[149]	✓[150]	✓[151]
Low absorption	✓[147]	✓[153]	✓[149]	✓[150]	✓[151]
Low scatter	✓[124]	×[152]	✓[149]	✓[150]	✓[151]
High uniformity over large area	× [154]	×[152]	✓[139]	Untested[144]	✓[122]
Low thermal noise performance	× [123]	× [129]	× [155]	✓[144]	✓[122]

Table 3.1: Comparison of coating properties from chemical and physical vapour deposition methods where × = not suitable, ✓= suitable [156].

3.3 Ion generation using a radio frequency (RF) source

Radio frequency (RF) power supplies have been used to generate ion beam plasmas since the 1940s [157]. The main operation of these sources revolves around the extraction of positively charged atoms from a discharge cavity. By use of a hot filament (Kaufman source [157]) or a quartz discharge cavity (inductively coupled RF source [157]) as a cathode, ions can be generated inside the source by injection of a gas. Due to the filament in a Kaufman source only inert gas should be used, such as Argon, to avoid damaging the filament and contaminating the process [157]. However in a inductively coupled RF source, reactive and inert gas mixtures can be injected into the discharge cavity via a high voltage antenna [158]. This is however not enough to create cascading ionisation of a gas and in the case of an RF ion source a time varying magnetic field is applied parallel to the gas flow using an RF generator at 13.56 MHz [159]. This causes the ions created by the discharge to collide with additional gas atoms and produce more ions inside the cavity, their motion governed by the Lorentz force [160],

$$\mathbf{F} = Q[\mathbf{E} + (\mathbf{v} \times \mathbf{B})], \tag{3.1}$$

where Q is the charge, E is the electric field, v is the velocity in a magnetic field B. Eq[3.1] is fundamental to all ion and electron beam generation as this defines the scale and confinement of the beam.

In order to generate the B field condition necessary to confine the plasma an inductor coil is used to enclose the entire cavity. By use of electrostatic optics in the form of gridded plates with an applied negative potential the ions can be extracted from the cavity towards a target material. This process is illustrated in Figure [3.5]

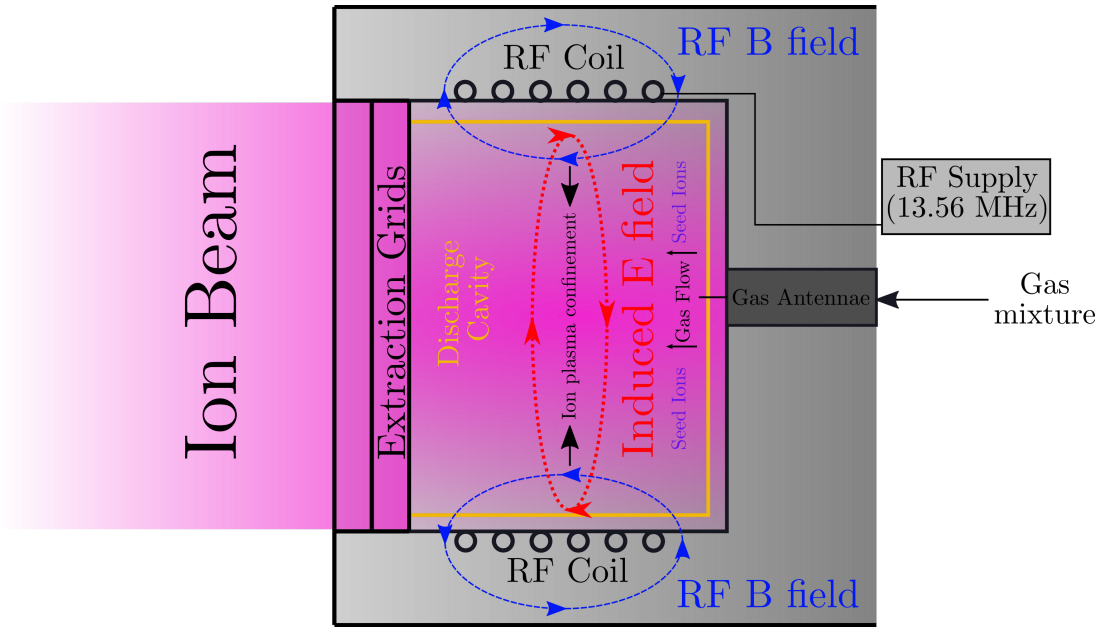

Figure 3.5: Diagram of an inductively coupled RF Source showing motion of ions in source relative to the electric and magnetic field generated (Modified from [161] and [162]).

The electric field strength inside the cavity is strongest nearest the coil and can be described as [159],

$$E \approx \frac{\mu_0 \pi N_t I r f}{L}, \tag{3.2}$$

where μ_0 is the permeability of free space, N_t is the number of turns in the induction coil, I is the peak current flowing in the coil, r is the radius of the coil and f is the frequency and L is the coil length. The magnetic field generated by the coil induces a perpendicular electric field inside the cavity which compresses the ion plasma. When a voltage is applied to the accelerator grids the plasma is extracted from the cavity through the grid aperture [163]. The design of the cavity in addition to the voltage and current applied in an RF ion source is therefore paramount in changing the energy of the ion beam and subsequently, the properties of sputtered coatings produced by such a source. Beam current and beam energy are key parameters which have been studied through this work in relation to their impact on coating morphology. The RF source used in this work can extract a large beam current from the cavity (100 - 500

mA) but with a lower beam energy (0.2 - 1.5 keV) [164] than other ion sources used in such processes like an Electron Cyclotron Resonance (ECR) source [165], which can generate ion beam energies of up 400 keV with beam currents in the range of 700 μA [166]. The beam parameters are a key part of the work in this thesis.

3.4 IBSD Process

Fundamental to the IBSD process is the ion-solid interaction. When a particle collides with a solid target material the energy transfer between particles can cause one of three processes to occur (illustrated in Figure [3.6]). If the primary particle has a low potential in comparison to the surface binding energy of the target it can recoil or scatter from the target surface. If the primary particle has a higher potential than the surface binding energy it can sputter material from the target surface or implant itself into the material ejecting further material [161]. The primary particle will then either remain stationary in the target or scatter from the target surface [161].

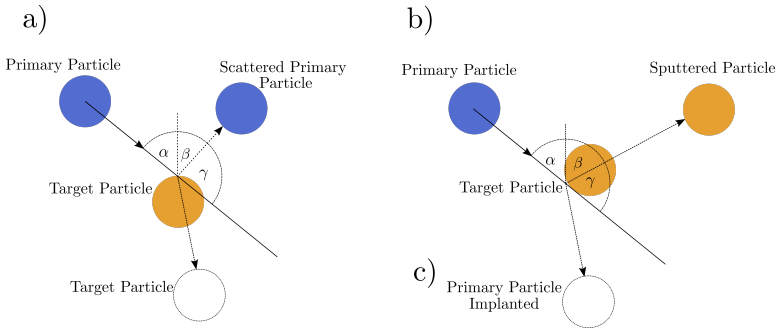

Figure 3.6: Diagram of the ion-solid interaction processes showing a) direct scattering, b) direct sputtering and c) implantation [161]

In the case of IBSD the primary particles are ions typically created from an inert gas (such as Ar) and are directed towards a high purity target. The sputtered material then forms a coating on substrates placed at an angle to the target as shown in Figure[3.7]. This process differs from such methods as magnetron sputtering and pulsed laser deposition by using a high energy ion beam (0.2 - 30 keV depending on the source used see Section [3.3]) with a low working pressure (typically $< 10^{-2}$ mbar). Importantly all geometric and ion beam parameters are spatially separated stopping

unwanted interaction between the plasma, target and substrates [161]. This allows the thin film properties to be highly customisable when all parameters are taken into consideration.

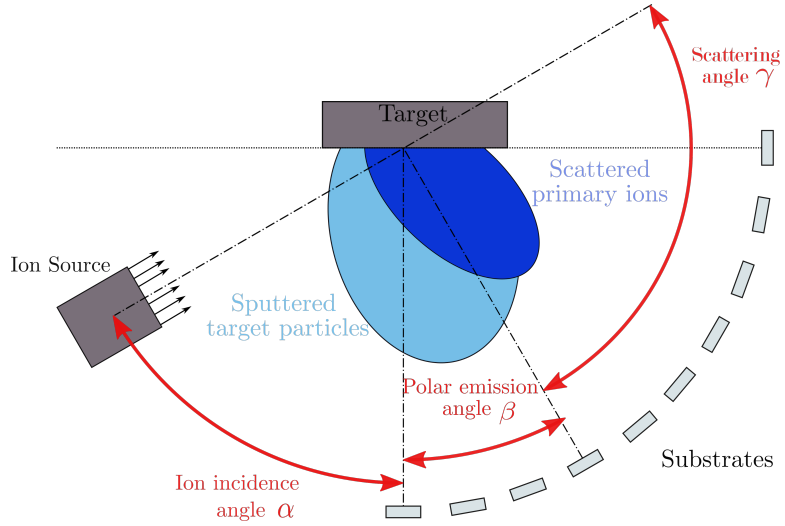

Figure 3.7: Schematic diagram of the IBSD process outlining geometric factors which can contribute to differing sputter plume distributions (ion incidence angle α, polar emission angle β and scattering angle γ) [167].

Geometric parameters that are integral to the properties of IBSD coatings include the beam angle of incidence (α), polar emission angle (β) and scattering angle (γ) given by,

$$\gamma = 180^{\circ} - (\alpha + \beta), \tag{3.3}$$

This has been quantified recently, as when $60^{\circ} < \alpha < 85^{\circ}$ the largest sputtering yield is gained from the target material [161]. Additionally target distance to the source also has a key role in the process, due to target heating constraints in addition to the beam energy profiles contribution to sputtered material distribution.

The energy of sputtered material is also vitally important in tailoring thin film properties using IBSD. Typically the energy of a sputtered particle can be given by,

$$E_{\mathrm{Spu}} = E_{\mathrm{Ion}} \frac{4 M_{\mathrm{Ion}} M_{\mathrm{Target}}}{(M_{\mathrm{Ion}} + M_{\mathrm{Target}})^2} \cos^2(\gamma), \tag{3.4}$$

where $M_{\text{Ion/Target}}$ is the mass of the target or ion and E_{Ion} is the mass of the primary ion defined by,

$$E_{\text{kinetic, ion}} = qeU_{\text{total}}, \tag{3.5}$$

where q is the charge state of the ion, e is the electron charge and U_{total} is the total potential applied to accelerate the ion. As there is only a single ionisation to the gas in this process $q = 1$ the voltage applied to ions in the source is equal to their energy in electron volts [168].

As a consequence of Eq[3.4] deposition properties, such as the sputtering yield, will change as a function of the ion energy and angle of incidence. Furthermore this will change the properties of the thin film produced and therefore allows tailoring of specific coating properties with reference to these parameters.

3.5 Simulation of the IBSD Process

Simulations of the ion beam process are useful in calculating quantities which can normally only be determined by lengthy and expensive measurements such as mass spectroscopy. As such it is a good method to approximate ion energy, sputtering yield and material plume distribution using computational means. There are a number of ways to simulate the ion beam sputtering process. Typically the two methods chosen are Monte Carlo (MC) simulation based from binary collision approximation (BCA) or molecular dynamic (MD) programs.

MD simulations directly apply Newton's equations of motion to all particles in the system and using a suitable chosen interatomic potential can model the ion beam sputtering process thoroughly [169]. While a more rigorous approach to simulating the process this does however come at a high computational cost and therefore simulations can take long durations to complete [161].

BCA simulations consider the interaction potential of the ions to track the particles. Assuming binary elastic collisions of each particle multiple quantities such as the sputtering yield and ion energy can be extracted [161].

MC programs based on the BCA approximation balance accuracy with computational time allowing extraction of ion energy and plume distribution parameters of the ion beam process from minimal computational power [161]. Two of the popular choices of programs used are Stopping and Range of Ions in Matter (SRIM) [170] and Static and Dynamic version of TRIM.SP (SDTrimSP)[171] which are outlined in the following section. Data from the two programs is outputted in spherical coordinates as illustrated in Figure [3.8].

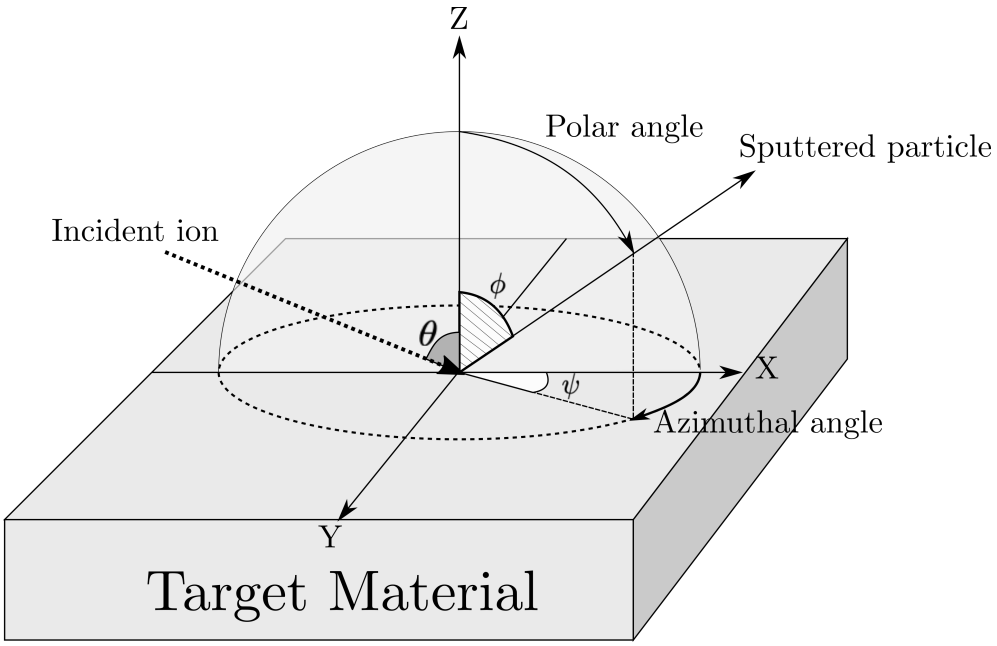

Figure 3.8: Coordinate system for MC simulation programs SRIM and SDTrimSP [172].

3.5.1 Stopping and Range of Ions in Matter (SRIM)

SRIM is a program developed in the early 2000s to simulate and model the ion solid interaction. Based from earlier Transport Ions in Matter (TRIM)[173] code this allows the extraction of parameters such as material plume orientation and sputtering yield from a simulated ion beam process. The software uses the Ziegler, Biersack and Littmark (ZBL) interaction potential [170]. Determined by measurements of over 500 different ion-target interactions this potential can be applied to a variety of simulated experiments [170]. This governs the entirety of the simulation as it defines the radial potential gradient and therefore distance at which one particle will interact with

another and is defined as,

$$a_{\mathrm{ZBL}} = \frac{0.8853 a_0}{(Z_1^{2/3} + Z_2^{2/3})}, \tag{3.6}$$

where a_{ZBL} is the ZBL screening length, Z_1 and Z_2 are the atomic numbers of the incident and target particle respectively and a_0 is the Bohr radius.

TRIM and therefore by extension SRIM operates using a number of approximations, of which two can be considered important. The first is uses the so called "Magic Formula" derived by Biersack [174, 175] for scattering angle defined as,

$$\cos\frac{\Theta}{2} = \frac{B + R_C + \Delta}{R_0 + R_C}, \tag{3.7}$$

where Θ is the scattering angle of a particle (not to be confused with θ in Figure [3.8]) and B, R_C, R_0 and Δ are the impact parameter, radius of curvature of the centre-of-mass system, radius of closest approach of the particle and the correction factor in terms of the ZBL potential screening length a_{ZBL} as,

$$B = \tfrac{p}{a_{\mathrm{ZBL}}}, \tag{3.8}$$

$$R_0 = \tfrac{r_0}{a_{\mathrm{ZBL}}}, \tag{3.9}$$

$$R_C = \tfrac{\rho}{a_{\mathrm{ZBL}}}, \tag{3.10}$$

$$\Delta = \tfrac{\delta}{a_{\mathrm{ZBL}}}, \tag{3.11}$$

$$\tag{3.12}$$

where p is the impact parameter (perpendicular distance between the particle and the potential field centre [170]), r_0 is the radius of curvature of the particle trajectory, ρ is the radius of curvature of the centre-of-mass system and δ is the correction term for the particle motion.

Eq [3.7] decreases computational time of calculation because it allows a highly precise solution to scattering angle without having to fully integrate over the entire simulation space [170].

The second approximation which is important to the computational efficiency and accuracy of TRIM is removing interactions in the simulation which involve a negligible transfer of energy and cause negligible deflection angles in the ion flight path. Negligible is here defined in TRIM as any random quantity which has $< 0.1\%$ effect on the final result [170]. An example of this would be a high energy proton (> 10 MeV) colliding with a target material can skip thousands of monolayers between collision calculations. The energy loss into each layer can still be computed however this requires less computational time [170]. This so called "free flight path" is not constant throughout the simulation as once the maximum jump length is determined (the maximum distance a particle can travel without a meaningful interaction) it is reduced by a distribution of random numbers between 0 and 1 to attain a more realistic prediction to the ion trajectory.

Simulation results showing the sputtering yield and ion energy distribution from a 0.6 keV Ar ion beam impingent on a Si target at 60° angle of incidence are show in Figure [3.9]. These are the default configuration parameters of the RF IBSD system used in the research of this thesis (discussed in Section[3.6]).

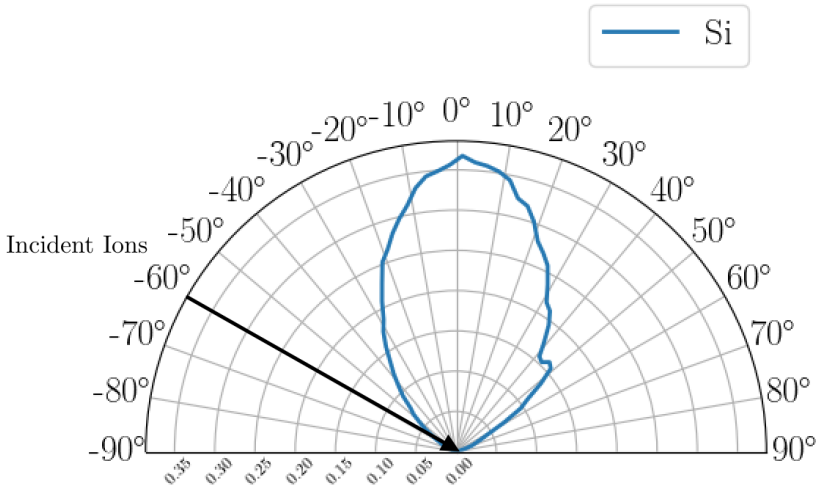

(a) Sputtered atoms as a function of polar angle.

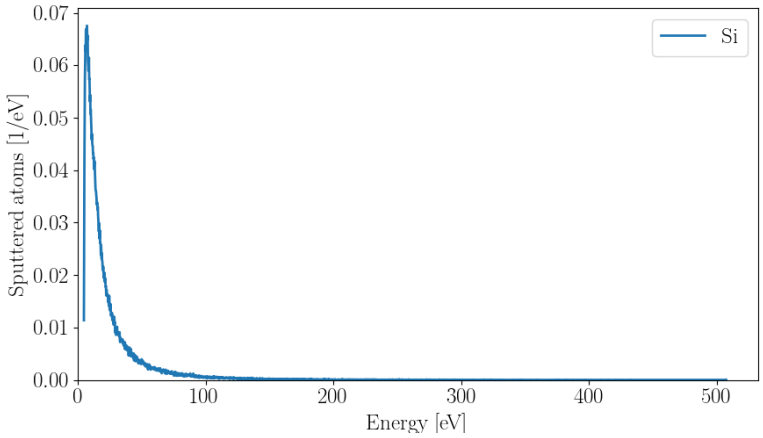

(b) Energy distribution of the sputtered atoms.

Figure 3.9: SRIM-2013 simulation output for 0.6 keV Ar beam incident on Si target at 60° angle of incidence.

The results show a sputtered atom distribution normal to the target surface (Fig [3.9a]. This is in line with results shown previously for SRIM results of Cs ion bombardment of a Si target at 60° [176] however Ar will lead to less sputtered atoms due to it being lighter than Cs. The energy distribution (Fig [3.9b]) shows this is a lower

energy process as the incident ions are at 0.6 keV and the vast majority of sputtered atoms are at energies <0.1 keV.

These results will be compared to results from the same simulation in SDTrimSP. By comparing both results to experimental data this will assess which program is best suited to give more realistic results which can be utilised as a benchmark to understanding the IBSD process further.

3.5.2 Static and Dynamic Transport Range of Ions in Matter Serial Parallel (SDTrimSP)

SDTrimSP is a similar MC program to SRIM written in Fortran 90 by the Max Planck Institute in Germany [177]. While being able to run the so called "static" ion beam process like SRIM simulates on sequential and parallel computer architectures this program models the so called "dynamic" case in the ion beam process, where the stoichiometry of the target material will change over time as the material's surface and volume is bombarded by high energy ions. This is important when dealing with mixed targets in addition to mixed gases being used in the sputtering process as SRIM can give false ion distributions for large angles of incidence ($> 60°$) and $Z_{\text{Target}} < 14$ due to the interaction potential used by the software not being compatible with these elements [176]. The main workflow of the program is shown in Figure[3.10]. This is shown in sequential mode as this was compatible with the computer architecture used in this work.

Firstly an input file must be generated specifying the simulations parameters (number of ions, ion species and energy, target composition, *etc*,) [177]. The programs then distribute this information to the simulation (having been pointed to the input file). In the projectile loop the specified number of incident ions are divided into smaller groups and followed around the simulation iteratively while undergoing collisions, in order to effectively manage computational power [177]. Any particles that recoil along the projectile trajectories are tracked in the separate recoil loop. If in static mode the data generated from the projectile and recoil loops is passed back to the program start to generate additional atoms until the specified ion quantity has been reached. In

dynamic mode before passing the data to the program start, target data is collected regarding the projectile and recoil interaction within the target (depth, energy, *etc.*) [177]. This is all relayed back to the start of the program. After the number of specified particles have been used in the simulation, the results are collated and outputted.

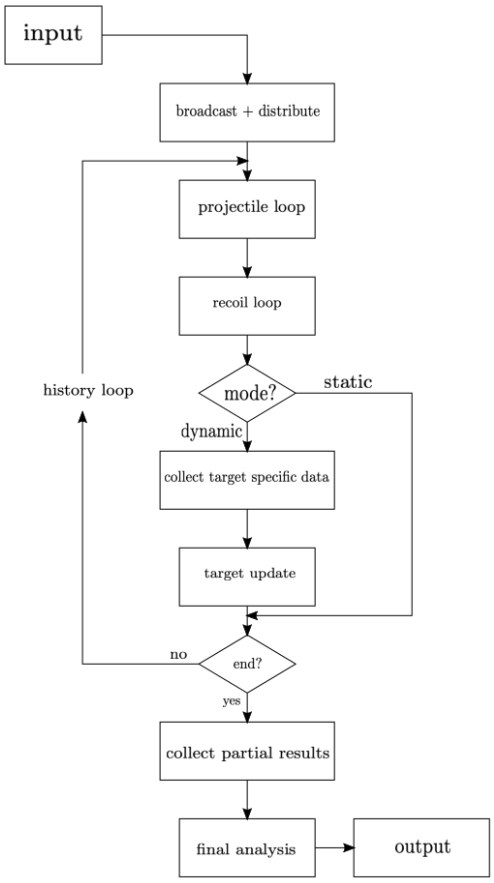

Figure 3.10: Main workflow for SDTrimSP in sequential mode [177].

The software also has the advantage of being more customisable than SRIM, with increased options for interaction potentials and integration methods for the scattering angle over the so called "Magic Formula" (Eq[3.7]). The additional integration methods available (Gauss-Legendre and Gauss-Mehler) can be less accurate than the

"Magic Formula" but can be used for all interaction potentials, this is not a physical constraint but a limitation of the software [177]. The interaction potential chosen for the simulations is the Krypton-Carbon (Kr-C) potential [178]. This has a screening function which is very similar to the ZBL potential at smaller interaction distances but has a stronger effect at larger interaction distances than the ZBL [176]. This gives the benefit to low energy collisions at larger distances, lending itself to model lighter elements ($Z_{\text{Target}} < 14$) [176]. Therefore SRIM cannot operate correctly for targets of Na, Mg, Al or all oxide, carbide, nitride and fluoride targets due to use of only the ZBL potential which cannot simulate low energy collisions accurately due to a slow decrease in the potential screening function at large atomic distances [176]. Results from SDTrimSP are shown in Figure[3.11] for the same sputtering configuration presented in Figure [3.9] (0.6 keV Ar on Si at 60° angle of incidence) using a mixture of hard coding in FORTRAN 90 [179] and a graphical user interface [180] based in Python [181].

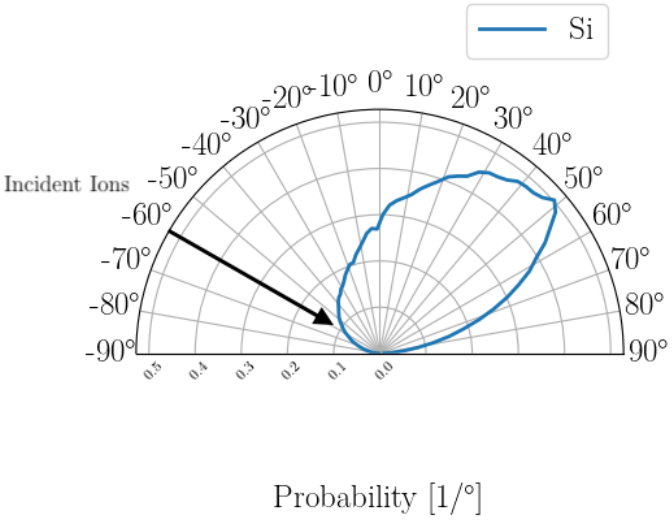

(a) Sputtered atoms as a function of polar angle.

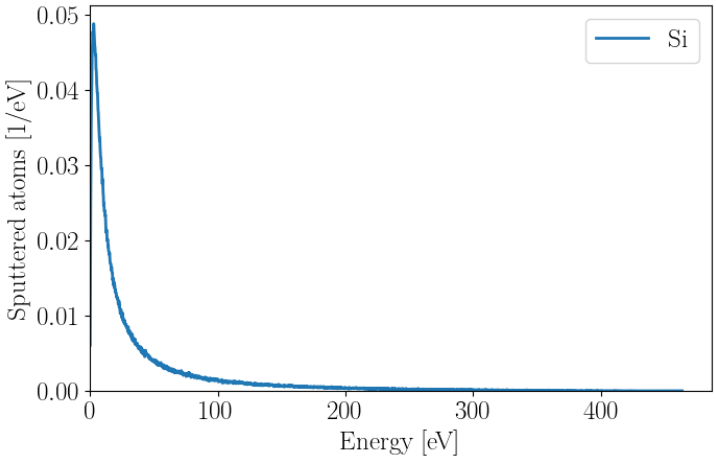

(b) Energy distribution of the sputtered atoms.

Figure 3.11: SDTrimSP output for 0.6 keV Ar beam incident on Si target at 60° angle of incidence.

In comparison to Figure [3.9a] it is clear to see the distribution of sputtered particles (Figure [3.11a]) is at approximately 40° - 50° to the target normal and not at the target normal direction. This highlights the shortcomings of the SRIM program as the distribution of sputtered particles should be in line with the results from Figure [3.11], this is confirmed by historical experimental data [176, 182] from similar simulations.

Regarding the energy distribution Figure [3.11b], the overall quantity of sputtered atoms is lower ($1/\text{eV} < 0.05$) however the energy of such atoms is comparable to SRIM (Figure [3.9b]) with the majority of atoms having energy <0.1 keV. This is however not the case at lower energy (< 50 eV) as the energy distribution from SRIM shows an increase in lower energy ions. This is likely a result of the change in sputtered distribution from the approximate interaction potential limitations of SRIM. It has been shown that SDTrimSP matches data with comparable agreement to the sputtering characteristic found from experiments not conducted by the author [176], therefore it can be assumed the ion characteristics modelled are also indicative of experimental processes.

In absence of experimental techniques to measure ion energy and species such as a Langmuir probe or mass spectrometer, ion beam characteristics in this work will be derived from simulations in SDTrimSP. The program will be used to understand how the IBSD process functions under variation of deposition parameters for specific materials. This will give an insight into how these parameters influence the properties of the coatings and how the process can be tuned to create thin films which can meet the aLIGO + design requirements.

3.6 Application of RF IBSD for gravitational wave detection

The current method of depositing coatings for the aLIGO detector is RF IBSD. This technology is incorporated into the "Grand Coater" at Laboratoire des Matériaux Avancés (LMA) [183]. This system uses dual Veeco 16cm inductively coupled RF ion sources to co-sputter materials [184] onto 40 kg fused silica substrates for gravitational wave detectors depending on the chosen coating design. In this work a custom IBSD system was built around the same ion source by the author. Figure 3.12 outlines this system, featuring a large 1.2 m x 1.2 m x 1.2 m Stainless Steel 316L vacuum chamber allowing full customisation of the IBSD process geometry to fully understand the coating properties produced by this process.

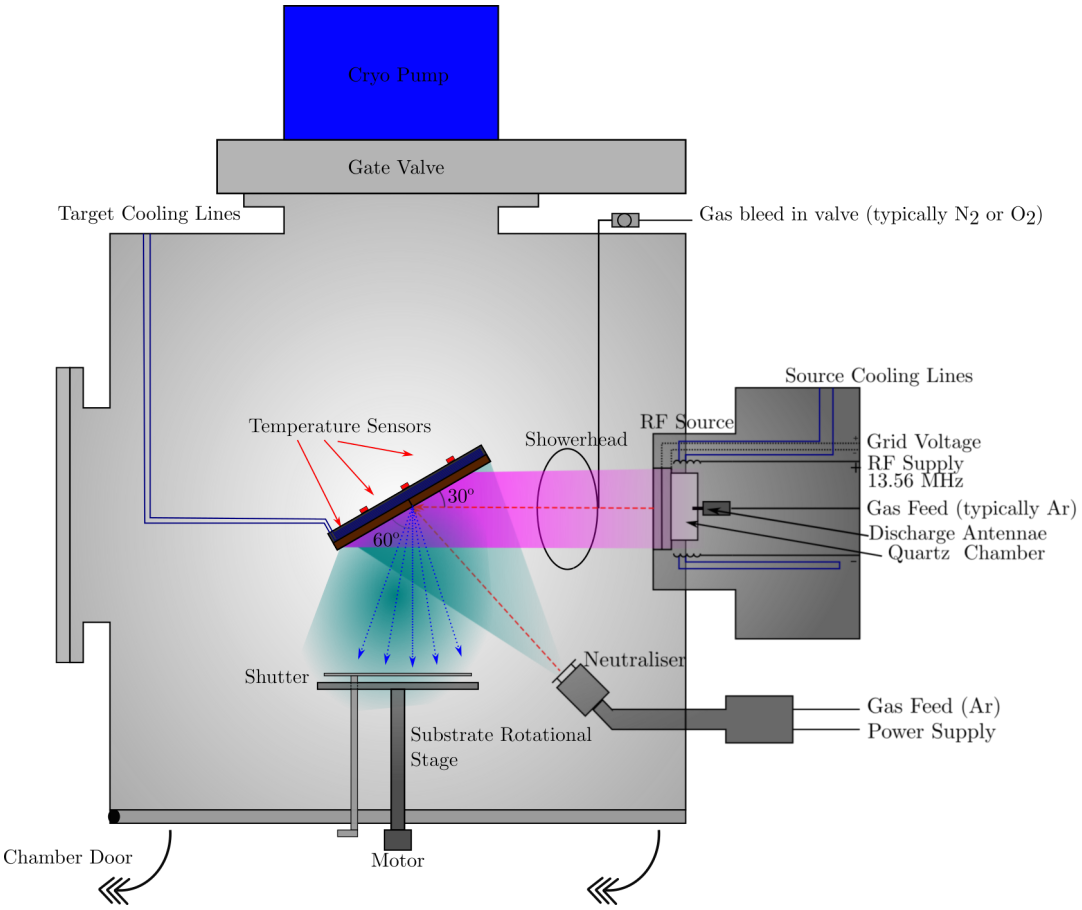

Figure 3.12: Top elevation of Strathclyde RF 1200 system detailing geometry and source operation. Gas can be introduced into the process by means of a shower head gas line in addition to directly through the source. Substrates are mounted on a rotational stage relative to the beam with a shutter to allow etching of a target material before deposition.

This system is able to obtain low vacuum pressure of 10^{-5} mbar using both a Ebara AAS10N dry roughing pump and Pfeiffer Vacuum HiPace^{TM}2400 MC turbo pump. Also used is a Sumitomo Marathon® CP-16 cryopump in order to remove background water in the chamber to achieve a lower vacuum pressure $< 10^{-6}$ mbar in absence of a Meissner trap or chamber baking due the overall size of the vacuum system and the design of the chamber being such to accommodate the cryopump. In addition to the geometry of the deposition being customisable so is the energy of ions produced by the source. The total applied potential to ions produced by the Veeco 16cm RF ion source can be described as [164],

$$U_{\text{total}} = (U_{\text{beam}} + U_{\text{accel}}), \tag{3.13}$$

where U_{beam} and U_{accel} are the voltages applied to the cavity coil and accelerator grid respectively. However as the accelerator provides a negative potential to the ions $E_{\text{ion}} \approx U_{\text{beam}}$ [164]. This is due to the downstream potential being approximately zero due to a decelerator grid voltage being applied ensuring the beam voltage is approximately the energy of the ions, regardless of the accelerator voltage [163]. The accelerator voltage applied and feedback current relates to the divergence of the beam. The source is controlled remotely using Veeco software, shown in Figure [3.13a]. An electron beam neutraliser is directed towards the ion beam and target during deposition to ensure no charge build up occurs on any surface the ion beam is impingent on. This stops any accumulation of charge build up on the target surface (particularly non conductive targets) and additionally stops discharging occurring from the ion source to a surface in the deposition chamber, therefore reducing unwanted containments in the coatings produced. Exact directional neutralisation of the beam is unnecessary due to the electrons low electrical potential and high mobility [164]. The neutraliser operates similarly to the RF ion source. An RF coil surrounds a discharge cavity where an inert gas (typically Ar) is fed into [185]. Only as inert gas is used to prevent contamination to the RFN as it is only used for beam management in the process [186]. The gas is ionised when discharged and the RF coil induces additional collisions to create and maintain a plasma [163]. A negatively charged plate, known as the collector, is used to draw ions in the cavity while a positive potential is applied to a plate at the front of the cavity, known as the keeper plate [185]. The electrons are attracted to the keeper plate and exit the cavity.

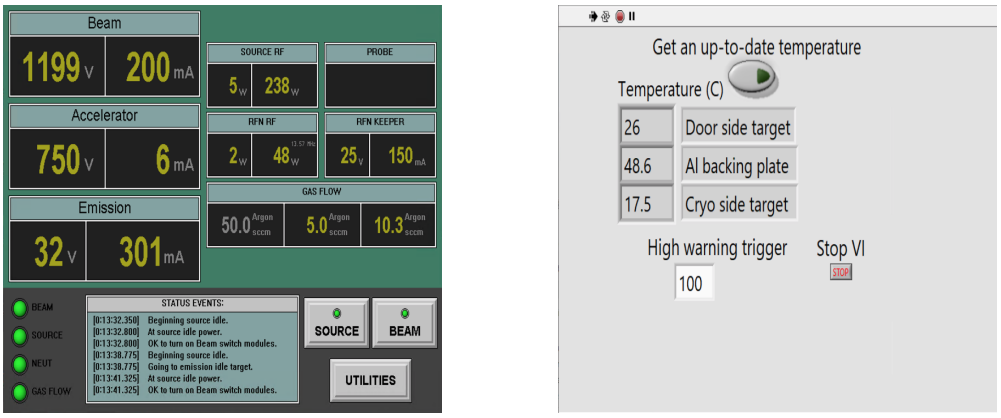

(a) Veeco software screenshot for remote control of ion source.

(b) Thermocouple monitoring software. High temperature warning is programmable.

Figure 3.13: Software for remote control of RF IBSD system.

The system target material is mounted on a custom stage (see Fig[3.14]) designed and built by the author. Three thermocouples are mounted between the stage and target to monitor any increase in temperature during deposition. This is important due to the target material being bonded to a aluminium backing plate using indium which has a melting point of 156°C [187]. The temperature is monitored remotely using custom Labview software, written by the author, shown in Figure [3.13b].

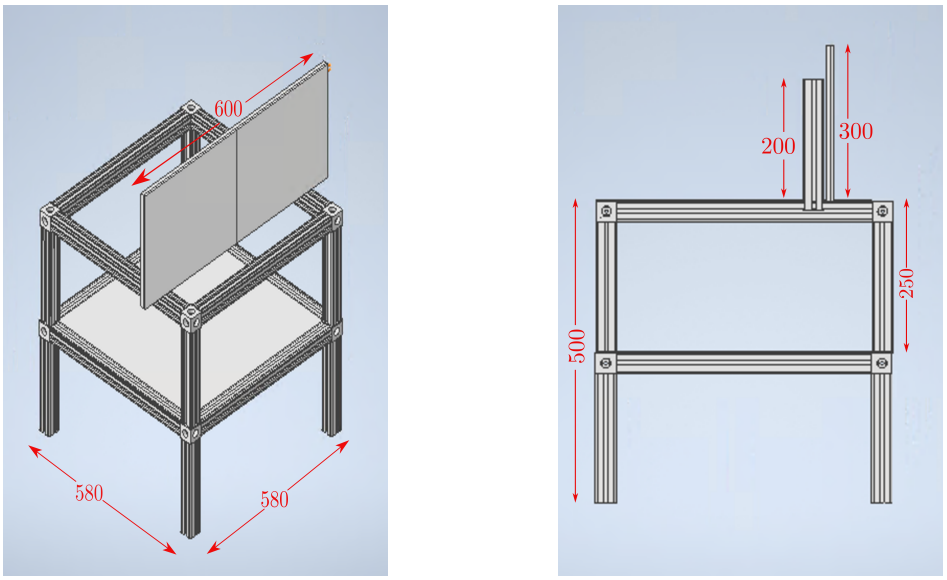

(a) Isometric view.

(b) Side view.

Figure 3.14: Computer aided design side and isometric views of target stage showing target mounting. All sizes shown are in mm.

Mounting the substrates to the rotational stage was conducted through custom holders (See Fig[3.15],[3.16] and [3.17]) made from Al 6061 designed by the author. Due to the holder not being vented virtual leaks would be possible but have not been observed during their operation. The holders were designed such that a substrate can be place inside with minimal surface area being left uncoated. They are then locked in place by a threaded cut-out ensuring they are secure inside. This is key in maintaining coating uniformity throughout the deposition as a non-uniform coating across a large area, such as a aLIGO optic of 20 cm, will lead to non-uniform absorption (heating) across the sensing surface [188] or small angle scattering of light ultimately reducing detector sensitivity [145]. It is therefore important to maintain this uniformity on smaller substrates to ensure the results are comparable.

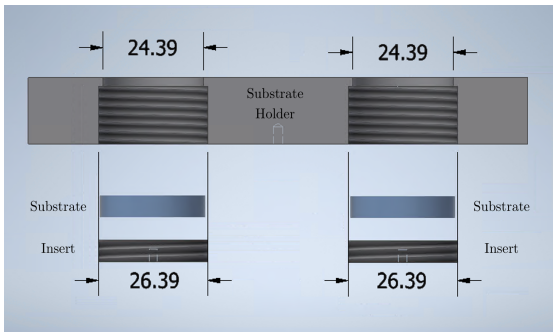

(a) 25.4 mm substrate holder cross section

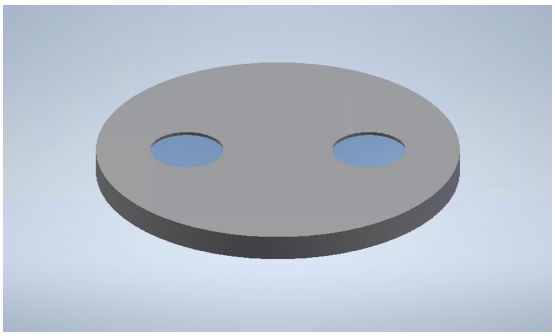

(b) 25.4 mm substrate holder isometric view

Figure 3.15: Computer aided design outline of substrate holders for 25.4 mm disks.

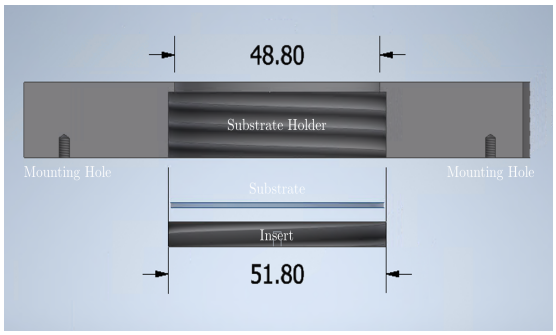

(a) 50 mm substrate holder cross section

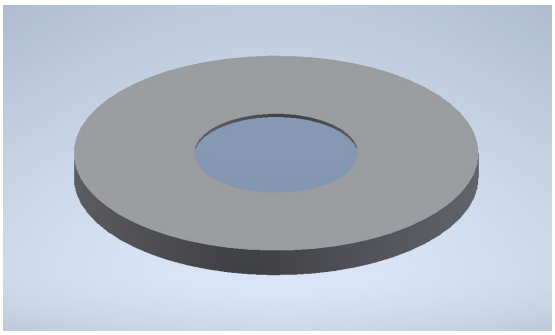

(b) 50 mm substrate holder isometric view

Figure 3.16: Computer aided design outline of substrate holders for 50mm disks.

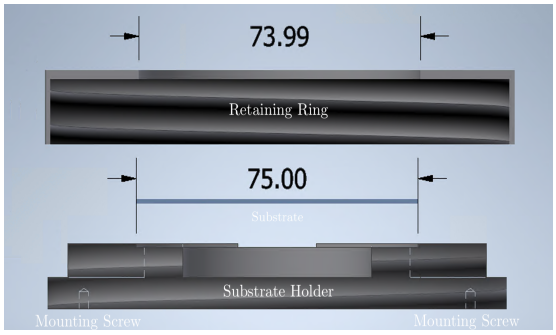

(a) 75 mm substrate holder cross section

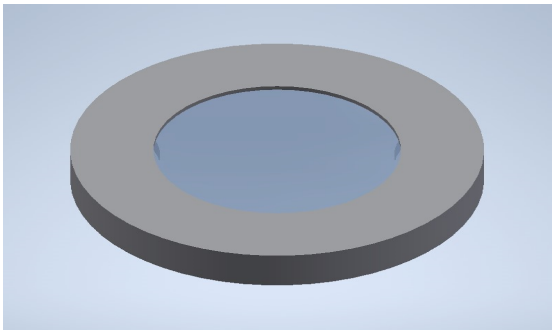

(b) 75 mm substrate holder isometric view

Figure 3.17: Computer aided design outline of substrate holders for 75mm disks.

3.7 Conclusions

In summary IBSD is one deposition processes which can be used to create tailored coatings by modification of the deposition parameters. This can be achieved by the unique spatial separation and customisable variability of the components in the process (ion beam energy, target angle, *etc*,). Furthermore this is the preferred deposition method for gravitational wave detector mirror coatings as it has so far been the only process to produce coatings close to the absorption, mechanical loss and scattering requirements for GWD large area coatings. Understanding how the process parameters effect the optical and mechanical properties of the coatings is therefore paramount in designing and fabricating the next generation of detector coatings, whether the systems are at room temperature in the case of aLIGO+ or at cryogenic temperatures such as LIGO Voyager.

Chapter 4

Metrology

4.1 Introduction

Characterisation of thin films started in the late 19^{th} century when Drude used the phase shift between orthogonal components of polarised light to measure the film thickness down to sub-nm levels [189, 190]. Since then a variety of techniques have developed which can measure a multitude of thin film properties such as optical, compositional and electrical characteristics.

In the case for gravitational wave detection the characterisation of thin film coatings is crucial in determining materials which could be used in the next generation of detectors. Optically the films for an A+ HR mirror require a sufficient contrast in refractive indices between high and low index materials, in addition to low absorption, at 1064nm to give 99.999% reflectivity [121]. Crucially the coatings must also exhibit low internal friction to not impede thermal noise performance of the detector.

Outlined in this chapter are techniques used throughout the work enclosed in this thesis to determine optical, compositional and mechanical properties of the films produced by IBSD. Particular attention is given to mechanical characterisation by means of the Gentle Nodal Suspension (GeNS) system. This method is used to measure the internal friction of coatings, the so called "mechanical loss" which is a key factor in determining materials which can improve a gravitational wave detector's thermal noise performance.

4.2 Optical Spectroscopy

Optical Spectroscopy is a method used the characterise optical coatings by measurement of the reflection and transmission intensity of light, at wavelengths in the ultraviolet to near infrared region [191]. This measurement allows the extraction of multiple properties of a thin film including refractive index (n), extinction coefficient (k), film thickness and band gap energy. From a simplistic view this is done through the use of a broadband light source, diffraction gratings and adjustable optical slits. The light is separated into constituent wavelengths through use of a grating and then selected using the optical slit before impinging on the sample [191]. A photodetector is then able to measure the reflected or transmitted light (depending on the geometrical configuration) at the varying wavelengths. This process is shown in Figure[4.1]. The system used in this work is a Photon RT UV-Vis-IR spectrophotometer [192] located within the University of Strathclyde, capable of measuring both reflectance (R) and transmittance (T) from a single calibration of T. The calibration is conducted by measuring the raw monochromator output on the photodetector with no sample between the light and detector at wavelengths of 185 - 5000 nm [192]. This range covers the UV-IR range in particular wavelengths of interest to next generation gravitational wave detectors (1064 nm, 1550 nm & 2000 nm). This technique was chosen over other optical measurement techniques such as ellipsometry for, in this equipments case, the ability to calibrate and measure samples very quickly to a wavelength resolution of (at its largest) 1.0 nm with no additional sample preparation after coating. The Photon RT can also be used to gather phase information from samples but this has additional requirements (silica wedge samples) not used in this work.

The substrates used for these measurements are 20 mm diameter 1 mm thick JGS1 and JGS3 grade silica in addition to 25.4 mm diameter 5 mm thick Corning 7979 grade silica due to their low absorption characteristics at the wavelengths mentioned previously [193–195]. This allows the coating properties to be extracted without intensive modelling of the substrate. Measurements were done post-deposition with the samples being transported to the measurement equipment in a sample container with a high

grade optical coating wipe used as protection for the coating.

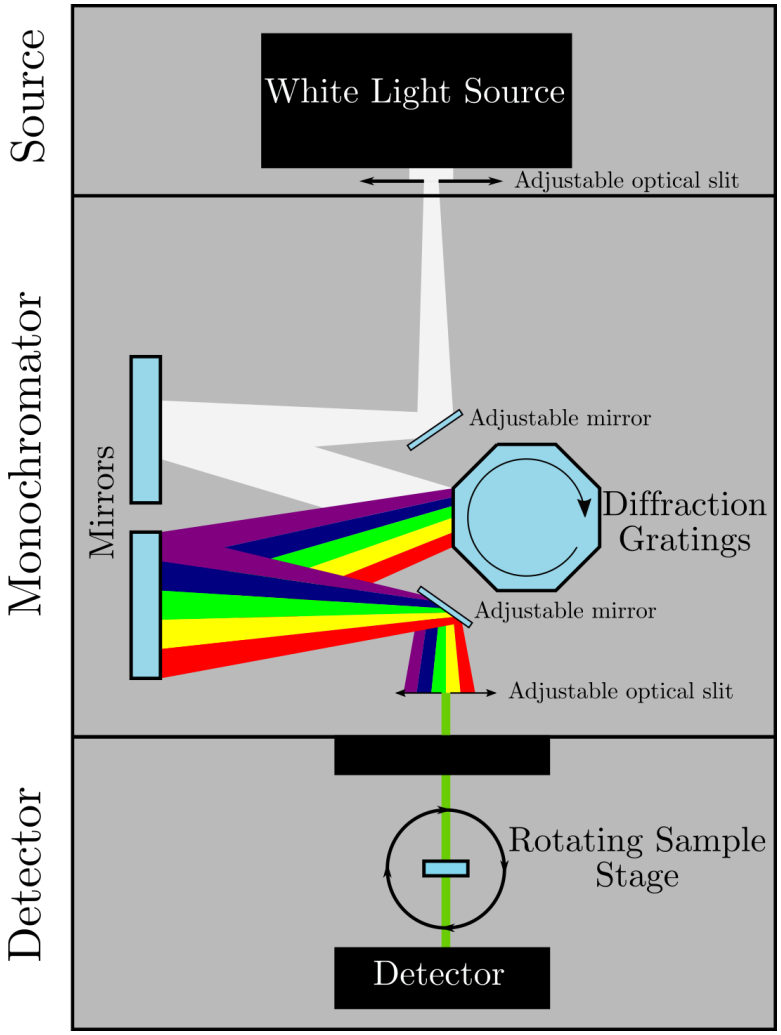

Figure 4.1: Diagram of Photon RT optical spectrophotometer showing light source, monochromator and sample stage. Light is shown in the visible however the full range of the Photon RT includes UV-Vis-IR. Recreated from internal images of system and [191].

4.2.1 SCOUT

SCOUT is a program used to model the values of n, k, film thickness and band gap energy (E_{gap}) from measured R and T values [196]. By modelling the optical structure of the coating materials it is possible to recreate the R and T spectra measured by the spectrophotometer. The model used for all SCOUT fittings in this work is based

from the O'Leary, Johnson, Lim (OJL) model [197]. Here expressions for the density of states are given for interband transitions of electrons between the conduction and valence band ($N_C(E)$ and $N_V(E)$ respectively) [197],

$$N_C(E) = \frac{\sqrt{2}m_C^*}{\pi^2\hbar^3}^{3/2} \begin{cases} \sqrt{E - E_C}, & E \geq E_C + \frac{\gamma_C}{2} \\ \sqrt{\frac{\gamma_C}{2}} exp(-\frac{1}{2}) exp(\frac{E-E_C}{\gamma_C}), & E < E_C + \frac{\gamma_C}{2} \end{cases} \tag{4.1}$$

$$N_V(E) = \frac{\sqrt{2}m_V^*}{\pi^2\hbar^3}^{3/2} \begin{cases} \sqrt{\frac{\gamma_V}{2}} exp(-\frac{1}{2}) exp(\frac{E_V-E}{\gamma_V}), & E < E_V - \frac{\gamma_V}{2} \\ \sqrt{E_V - E}, & E \geq E_V - \frac{\gamma_V}{2} \end{cases} \tag{4.2}$$

where $m^*_{C(V)}$, $E_{C(V)}$ and $\gamma_{C(V)}$ are the effective mass, band edge and tail state breath of the conduction or valence band.

The OJL model works well for coatings with high disorder such as the materials presented here [198] where tail states can exist between the conduction and valence band (so called "Urbach tails" [199]) which decrease exponentially into the band gap [200]. A diagram illustration the electronic density of states for the OJL model is shown in Figure [4.2]. SCOUT uses a number of terms in the OJL model: strength, gap energy, gamma and decay. The strength term is proportional to the slope of the conduction and valence band structure and represents m^*. A low strength value means a flat band and a high term a parabolic structure [200]. The gap energy (E_0) is a measure of the band gap in the material (E_V - E_C) with no tail states extended into the band gap structure. The gamma term (γ) is a measure of the damping constants associated with the Urbach tail extended into the band gap from the valence band. Finally the decay term is associated with the drop of the imaginary part of the dielectric function at high frequencies to zero. If this final term was not introduced the imaginary part of the dielectric function would tend to infinity with increasing energy and the real part could therefore not be calculated [201]. These terms are given user-defined boundary condition which, if possible, are taken from literature values.

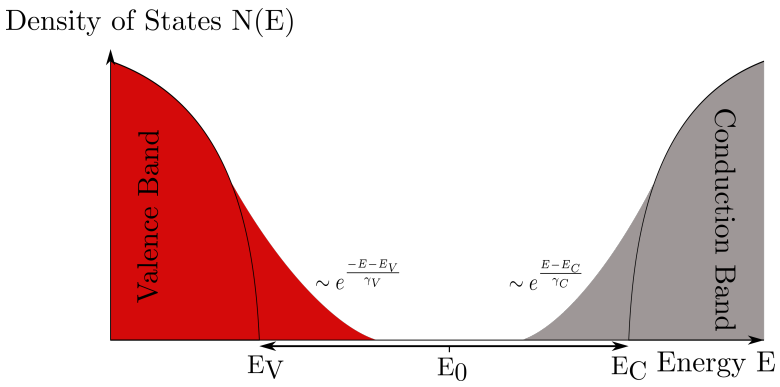

Figure 4.2: Density of states as a function of energy for the OJL model. Highlighted are the band gap and Urbach tails. Recreated from [200].

Additionally an oscillator is used at UV wavelengths (180-300 nm) to simulate O-H bond absorption characteristics that can be incorporated into coatings during the deposition process. Alternatively the so called "Extended Drude Model" can be used, this is an extension of the classical Drude model of electrical conductivity [202] where free carrier damping is dependent on frequency [201]. However for the work presented here an OJL term with a constant refractive index term and UV oscillator is what is typically used unless specified for complex R and T spectra. The real part of the dielectric function can be reconstructed from the imaginary part using the Kramers-Kronig relation (KKR) [200, 203] which describes the relation between real and complex susceptibility (the proportionality constant between induced electric fields and polarisation [160]). This requires sufficient data points for the Fast Fourier Transforms which convert the imaginary to real part of the susceptibility [201]. A thickness averaging term is used to account for any scatter or inhomogeneity within the coating layer [201]. The output screen for SCOUT for a 71 nm silicon nitride (Si_3N_4) film is shown in Figure [4.3]. The thickness of the film is determined by fitting the number of interference fringes from the film to the model. This can be difficult for films with a thickness < 1 nm however this is not the case of films used in this work. The substrate is also vitally important to the fitting routine and as such a measurement was also taken of blank JGS1 and JGS3 samples to create a appropriate models for fitting.

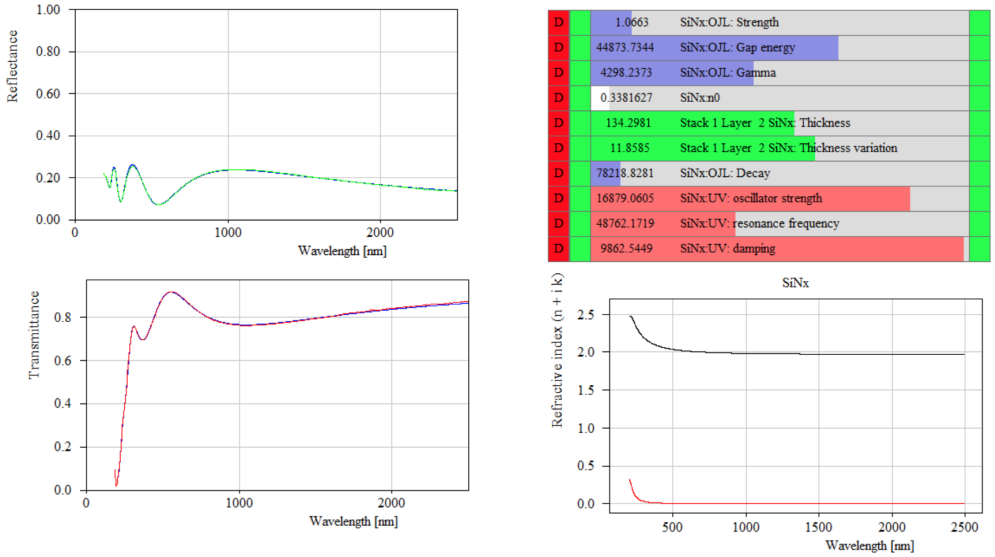

Figure 4.3: Example of SCOUT output window for a Si_3N_4 thin film on JGS3 glass with measurements taken at wavelengths between 180-2500 nm.

4.3 Photothermal Common-path Interferometry (PCI)

Photothermal Common-path Interferometry (PCI) is a technique which can be used to measure optical absorption of thin film coatings to very high-resolution in the parts per million regime (< 1 ppm) [204]. This is extremely important for gravitational wave detectors as they have a stringent requirement on levels of absorption in the test masses (< 0.3 ppm at 1064 nm for aLIGO [205]), a diagram of this technique is shown in Figure [4.4]. The technique functions using a high-intensity pump laser beam, in this case the wavelengths chosen are 1064nm, 1550nm or 2000 nm (wavelengths used and proposed for current and future gravitational wave detectors) focused on a sample to cause a heating effect.

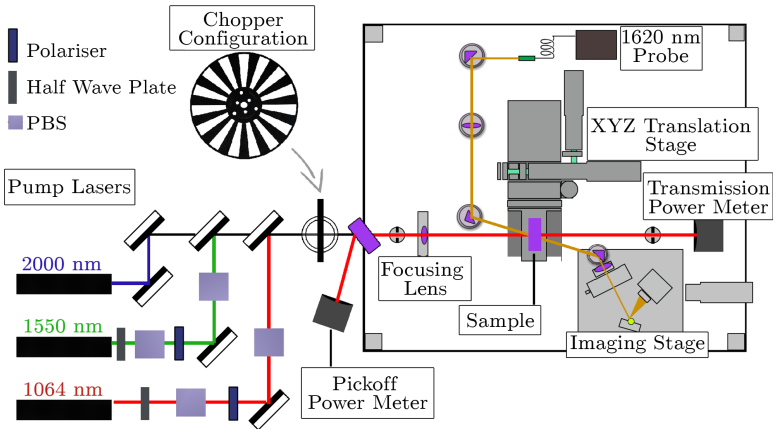

Figure 4.4: Diagram of Photothermal Common-path Interferometer highlighting key parts of configuration. Recreated from [24].

This will create a thermal lens due to the thermo-optic effect. By chopping this pump beam the sample is periodically heated and cooled create a periodic change in the refractive index characterised by,

$$\Delta n = \frac{dn}{dT}\Delta T, \tag{4.3}$$

where n is refractive index and T is temperature. A probe beam at 1620 nm with larger beam radius and differing wavelength than the pump beam is used to monitor the sample. Due to multiple factors arising from the heating effect such as a refractive index change and thermal expansion, the probe beams shape will distort and induce a phase change in its signal. As only part of the signal experiences a phase change the interference maximum (which depends on the absorption coefficient) can be extracted by use of a photodiode and lock in amplifier (Imaging stage) [204]. An XYZ translation stage is employed to measure the absorption at multiple points on a sample. This allows coating absorption as a function of distance across the whole optic to be measured to assess thickness uniformity. In addition any defects on the sample can be navigated if they pose a problem for measurement. The substrates used for PCI are 25.4 mm diameter 5 mm thick Corning 7979 grade SiO_2 due to there low absorption characteristics at 1064 nm and 1550 nm [195].

Measurements were done post-deposition using a pre-built system at the University

of Glasgow with the samples being transported to the measurement equipment in a sample container with a high grade optical coating wipe used as protection for the coating. The system was calibrated using a neutral density filter of fused silica which has a known absorption of 21.4% between 1000 nm and 2000 nm [24].

4.4 Scanning Electron Microscope/Energy Dispersive X-ray Spectroscopy (SEM/EDS)

Scanning electron microscopy (SEM) can produce high resolution images (nm scale) of the thin film coating surface. SEM creates an image by measuring the scattering of electrons from a surface. The electrons are produced via a tungsten filament and directed and focused using electrostatic optics towards a sample in high vacuum ($< 10^{-3}$ mbar). The electrons can be backscattered from the surface of the sample or remove additional electrons from the sample known as secondary electrons [206]. A diagram of this is shown in Fig [4.5].

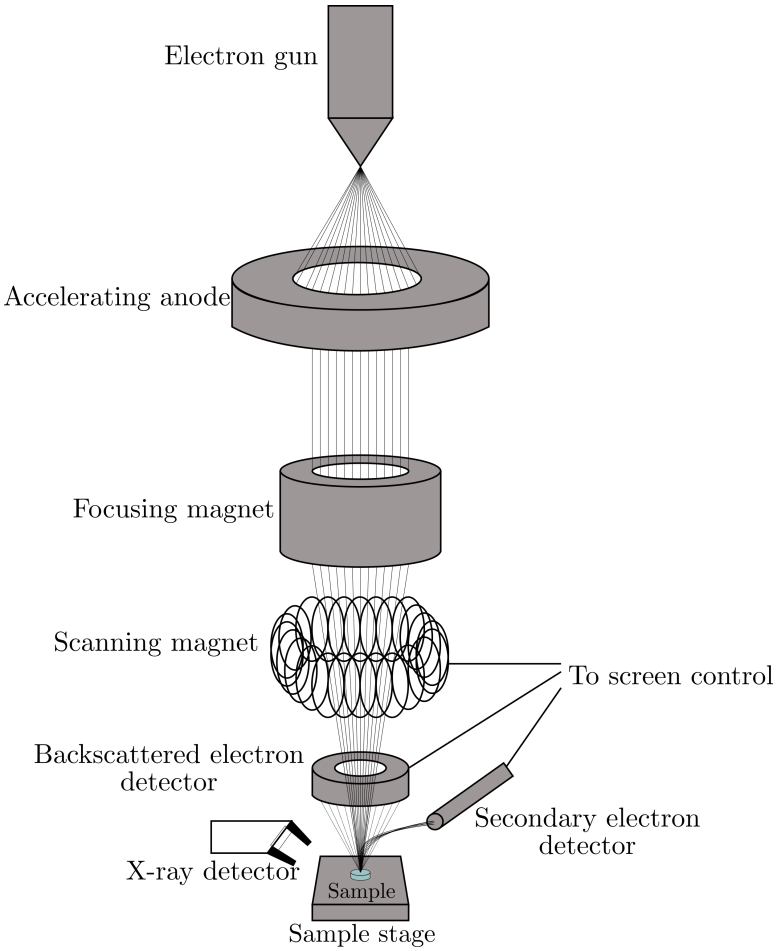

Figure 4.5: Diagram of Scanning electron microscope and electron dispersive X-ray equipment. Modified from [207].

Multiple detectors recognise these electrons and create a signal which can be reconstituted into an image. The equipment used in this work was a pre-built Hitachi S3700-N [208] with an Oxford Instruments X-Max 80 mm^2 EDS X-ray detector [209] attached for compositional analysis of films located in the Advance Material Research Laboratory (AMRL) at the University of Strathclyde. This system can accelerate electrons in the voltage range of 0.3 - 30 kV resulting in images with resolution of up to 30 nm [210].

The incident electrons additionally create vacancies in the atomic energy shells of the sample. This allows another electron from a higher energy shell to fill in the vacancy and in doing so emit an X-ray [211]. This is shown in Figure [4.6].

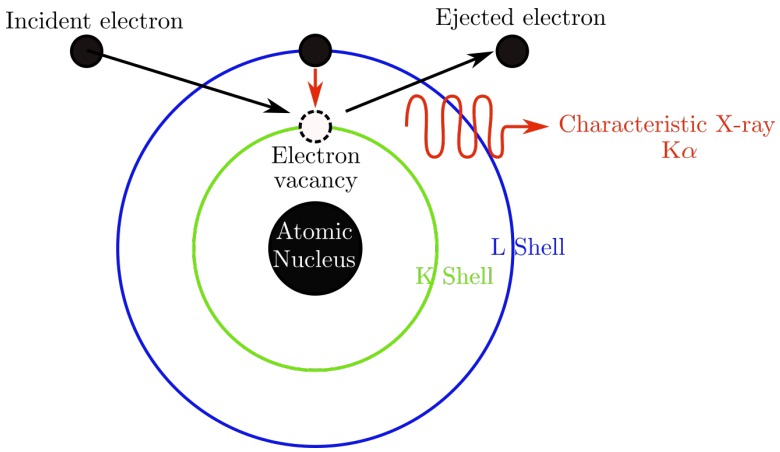

Figure 4.6: Diagrammatic of X-ray emission from an electron shell. Recreated from [212]

The X-rays emitted are characteristic of the electron that filled the shell vacancy in the atom. It is therefore possible to reconstruct the composition of sample elements due to their signature of X-ray energy corresponding to an electron shell transition in addition to quantity of the element from area under the peak [211]. This process is called Energy Dispersive X-ray Spectroscopy (EDS). As both SEM imaging and EDS require bombarding a sample with electrons there is a charge build-up therefore the sample should ideally be conductive to avoid this and maintain high resolution [213]. As such the substrates used for these measurements are 20 mm diameter 1 mm thick Si ($\langle 100 \rangle$ orientation).

Measurements were done post-deposition with the samples being transported to the measurement equipment in a sample container with a high grade optical coating wipe used as protection for the coating. The Si samples mounted on a carbon adhesive attached to a aluminium plate for greater conductance through the sample. The EDS system was previously calibrated using a reference sample of known composition.

4.5 X-ray Diffraction (XRD)

X-ray Diffraction (XRD) is a technique used to characterise the crystallinity of materials. This is important property to monitor for GWD coatings as crystalline oxides will

cause high scatter which will increase optical loss in a detector [103]. XRD functions under two fundamental principles. Firstly is the assumption Thomson scattering allows us to treat atomic planes as mirrors using the laws of specular reflection and the second is that the wavelength of X-rays is the same order of magnitude as the interatomic distances in crystals, allowing an interference condition to be created and therefore gives the ability to measure at these distances [214]. As an X-ray is incident on a crystal it is scattered depending on the incident angle and crystal plane it strikes. The equation governing this process and relates the angular position of diffracted X-rays to the lattice spacing of the crystal is the Bragg equation given by,

$$n\lambda = 2d_{hkl} \sin \theta_{\mathrm{B}}, \tag{4.4}$$

where n is an integer value, λ is the wavelength of the incident beam, d refers to the Miller indices of the crystallo-graphic plane (with interplanar spacing hkl) and θ_{B} is the Bragg angle. An XRD measurement system uses an X-ray source and detector mounted on a angular stage to measure the crystallinity and lattice spacing relative to a sample. A diagram illustrating this setup is shown in Figure [4.7]. The X-ray source consists of a tungsten filament cathode and a high purity metal anode. As thermionic emission ejects electrons from the filament when they strike the metal anode they ionise the target atoms and create the emission of X-rays due to electronic relaxation. The X-rays are characteristic of the excited and relaxed electrons [214], the strongest of which is the K set including $K_{\alpha 1}$, $K_{\alpha 2}$ and K_{β}. The X-rays can then be filtered depending on radiation lines required and focused depending on the emission window used in the X-ray tube [214].

Once the X-rays have struck the sample of interest the X-rays are then measured by a detector. These can either be proportionality counters, scintillation counters or solid-state detectors [214]. The proportionality counters or gas counter utilises a hollow metal tube with a thin metal wire anode within at high voltage (1.5 -2 kV) [215]. Electron and ions produced by X-ray interaction with an inert gas within the tube are accelerated towards the anode and cathode respectively. This is measured as a voltage which is proportional to the ratio between the energy of the X-ray and energy required to ionise

the inert gas [215]. Scintillation counters use a phosphor screen to produce a coating of thallium-doped sodium iodide crystals [216]. This produces photons (of wavelength 450-495 nm) which are converted to a voltage by a photomultiplier tube, the voltage being proportional to the original X-ray. Finally solid-state detectors, the most common of which is the Si(Li) detector diode, use doped materials to detect electron-hole pairs [215]. The detector is formed p-type silicon and n-type high concentration lithium to produce a p-i-n diode. When an X-ray enters the detector it produces electron-hole pairs in which the electron create a potential difference across the diode. This creates a measurable voltage which can be passed to a counting circuit in the detector[215].

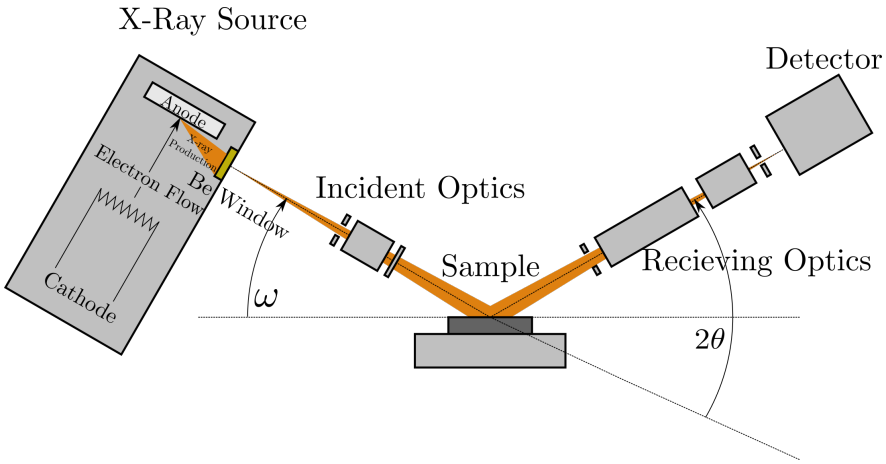

Figure 4.7: Diagram of X-ray diffraction equipment showing X-ray production and key angle parameters relative to the sample. Modified from [214].

In order to measure the crystallinity of different materials the XRD system needs to be able to measure the angle between the source, detector and sample surface [214]. Different crystal peaks will be aligned to the detector at different angles of X-ray incidence therefore a goniometer is employed to output this measurement. This is sample dependant as different materials will require additional configurations to measure the X-ray crystal peaks [214]. This includes coupled-theta or Bragg Brentano measurements where the source and detector always move simultaneously relative to the sample surface or grazing incidence measurements where the source is at a fixed angle close to parallel with the sample surface and the detector moves in varied theta relative to the source [214].

The XRD system used in this work is a Bruker D8 Advance [217] in both coupled-theta and grazing incidence XRD (GIXRD) mode at 0.5°. The 2θ scanning parameters were from 15-80° using a Ni window to filter the K_β lines and background radiation. This additionally omits doublet peaks from the measurements. At these values of 2θ all characteristic crystal peaks of the materials used in this work could be detected. Samples used were a mixture of 20mm diameter 1mm thick Si ($\langle 100 \rangle$ orientation) and JGS3 grade SiO_2. Measurements were done post-deposition with the samples being transported to the measurement equipment in a sample container with a high grade optical coating wipe used as protection for the coating. The equipment was calibrated at 0 degrees using a 1mm witness sample described above to establish the correct height for the mounting stage prior to measurement using Bragg Brentano or GIXRD.

The data from these measurements was analysed using Bruker DIFFRAC.EVA. This software can import XRD spectra for analysis and manipulation. Measurements conducted in this work had the background of the substrate structure removed by normalisation of the data. This allows any X-ray peaks to stand out clearly. This using databases within the Bruker software (Open Crystallography and International Centre fro Diffraction Data (ICDD) PDF database 2019) the peaks can be matched to know crystal structures in the database. A snapshot of the software layout is shown in Figure [4.8].

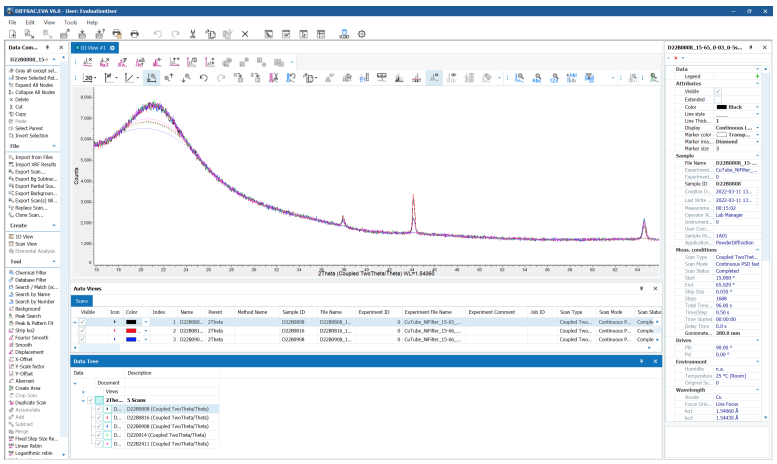

Figure 4.8: Snapshot of Bruker DIFFRAC.EVA software for XRD analysis.

4.6 X-ray Photoelectron Spectroscopy (XPS)

X-ray Photoelectron Spectroscopy (XPS) is a technique used to characterise thin film composition and in particular, the electronic and chemical structure of elements inside the coatings. These parameters are key to understanding morphology of the coating in relation to the deposition parameters used. The operational principle of this technique relies on the emission of electrons from an atom when struck by a high energy photon such as an X-ray [218]. The X-ray is annihilated in the process meaning the kinetic energy (KE) of the ejected electron, which is measured, is a function of the binding energy (BE) of the element in the material in addition to the material work function given by [219],

$$KE = h\nu - BE - \phi_{\mathrm{s}}, \tag{4.5}$$

where $h\nu$ is the X-ray energy and ϕ_{s} is the work function of the spectrometer. The BE corresponds to the particular elemental atomic shell the electron was emitted from, therefore enabling the composition to be calculable. Additionally this measurement gives a materials chemical state as the peak intensity of elemental photoelectrons as a function of binding energy corresponds to the different bond concentrations in the material [219]. A diagram of the XPS instrumentation is shown in Figure [4.9]. The process starts by the generation of X-rays, using a similar anode-cathode setup as in Section 4.5 with an electron gun emitting towards an Al mirror in a UHV ($< 10^{-7}$ mbar) [218]. The X-rays then enter a monochromator consisting of a quartz lens which seperate out the X-rays by energy according to Eq[4.4].

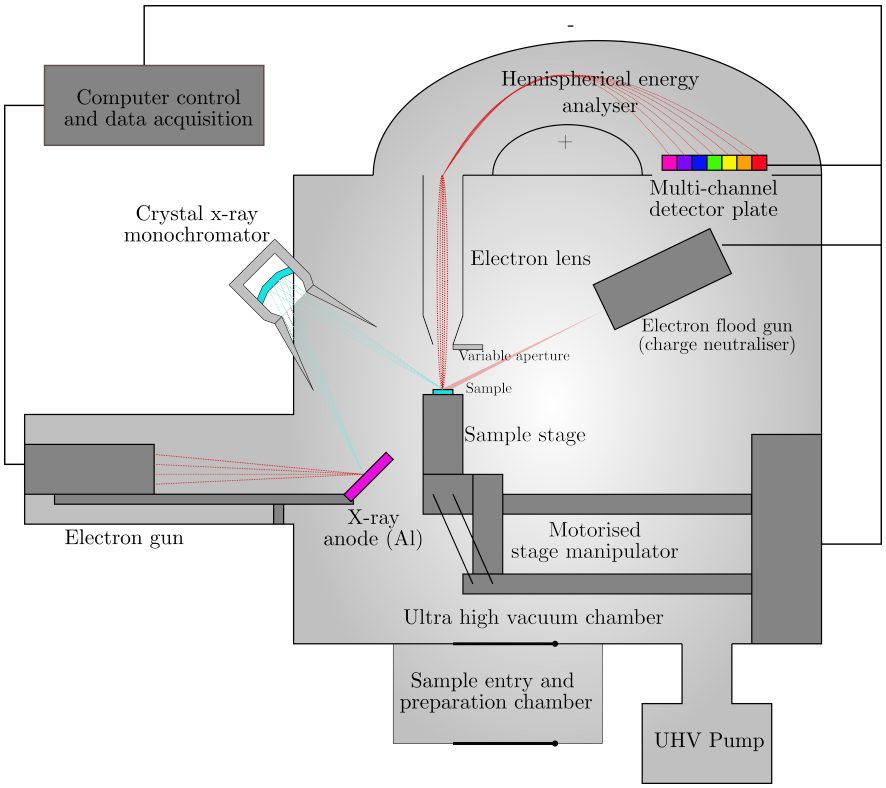

Figure 4.9: Diagram of X-ray Photoelectron Spectroscopy equipment showing X-ray generation and photoelectron detection from a sample. Modified from [220].

This ensures the beam can be focused without having to move the X-ray source in addition to the energy of the X-rays being a narrower peak [218]. Once the X-rays have struck the sample and electrons are emitted they are focused using a series of electrostatic lens before being passed to the energy analyser. This consists of two hemispheres with a potential applied across them. The path of the electrons across this potential is such that they are separated dependent on their incoming kinetic energy. This allows the separation of energies onto a multichannel detector therefore enabling binding structure to be determined [218].

The instrument used in this work is a Scienta 300 [221] located at the University of St Andrews, operating at or below $1x10^{-9}$ mbar. The X-ray source is an SPECS monochromated Al K_α source (X-ray energy 1486.6 eV) operating at approximately 12 kV and 200 W power. UNIFIT (version 2016) [222] and CASA XPS [223] Software was used to analyse the data produced by the instrument. This is peak fitting soft-

ware specifically designed for XPS measurements, allowing background smoothing and calculation of atomic concentration from peak area.

The instrument was calibrated to the C 1s peak before measurement using a Au reference sample. Measurements were done post-deposition with the samples being transported to the measurement equipment in a sample container with a high grade optical coating wipe used as protection for the coating.

4.7 Mechanical Loss

4.7.1 Introduction

Aside from optical properties such as absorption and scatter there is the additional coating thermal noise characteristics that need to meet the requirements for aLIGO+. This property can be measured directly for multilayer highly reflective (HR) stacks using cavity locked optical resonance [224] however this method cannot be applied to single layer coatings. To assess the mechanical loss properties of a single material methods are applied which give the internal friction of this material relative to the substrate. These methods include the cantilever resonant method [225], disk suspension [226] and the Gentle Nodal Suspension (GeNS) [227, 228].

4.7.2 Theory

Mechanical loss of materials can be characterised by the distribution of two level systems (TLS) in the material [229]. These are described as asymmetric double well potentials separated by an energy barrier and arise from the rearrangement of atomic clusters [230, 231]. Build up of TLS in a material will lead to a phase lag between applied stress and resulting strain from friction when a system eigenfrequency is excited [100]. In the context of a coated substrate with an oscillatory amplitude applied, the energy loss can be characterised by Eq[4.6],

$$E_{\text{lost,coated}} = E_{\text{lost,substrate}} + E_{\text{lost,coating}}, \tag{4.6}$$

By dividing by $2\pi E_{\text{stored,coated}}$ the resultant dissipation of energy in the coated

substrate can be described as,

$$\frac{E_{\text{lost,coated}}}{2\pi E_{\text{stored,coated}}} = \frac{E_{\text{lost,substrate}}}{2\pi E_{\text{stored,coated}}} + \frac{E_{\text{lost,coated}}}{2\pi E_{\text{stored,coating}}}, \tag{4.7}$$

When the coating is thin in comparison to the substrate, it can be approximated that $E_{\text{stored,substrate}} \approx E_{\text{stored,coated}}$. This in conjunction with the definition of mechanical loss from Eq [2.5] gives,

$$\phi_{\text{coated}} \simeq \phi_{\text{substrate}} + \frac{E_{\text{stored,coating}}}{E_{\text{stored, substrate}}}\phi_{\text{coating}}, \tag{4.8}$$

Eq [4.8] therefore gives the mechanical loss of the coating material by measurement of the substrates energy dissipation before and after the coating process,

$$\phi_{\text{coating}} \simeq \frac{E_{\text{stored, substrate}}}{E_{\text{stored, coating}}}(\phi_{\text{coated}} - \phi_{\text{substrate}}), \tag{4.9}$$

To calculate $\frac{E_{\text{stored, substrate}}}{E_{\text{stored, coating}}}$ for a coated disk two approaches can be used. This first involves using analytical expressions for the resonant frequencies and energy ratios of a coated disks using the thin plate approximation [232, 233].

This approximation assumes that the disk thickness is smaller than the radius of the disk in addition to motion in the middle surface being small and purely orthogonal to the disk. Transverse shear deformations and rotational inertia is ignored [233]. Calculation of the eigenvalues of the system can only be done numerically for all possible values and as such can be computationally expensive [233].

The other method by which to calculate the energy ratio between the coating and substrate of a disk is to use Finite Element Analysis (FEA) software. These packages (such as ANSYS [234] or COMSOL [235]) allow a 3D model to be constructed of the disk and coating with nodal points calculated for the model with an associated equation of motion [236]. This is solved numerically to give a solution at each resonant mode. Extraction of energy ratios between the substrate and coating based on inputted mechanical properties (Young's modulii, Poisson ratios, *etc.*) can then be performed. The ratio between elastic strain energy in the substrate and coating is calculated by summation of all elastic strain energies for all elements in the respective geometries.

This method has proven to show results with greater accuracy (on the order of 25%) than a purely analytical model [233] and therefore is the chosen route of energy ratio extraction in this work.

4.7.3 Measurement

The measurement of mechanical loss (ϕ) is characterised by a exponential decay of an oscillator after excitation at a resonant frequency. This decay can be characterised by,

$$A_i(t) = A_i(0)e^{-t/\tau_i}, \tag{4.10}$$

where $A_i(t)$, $A_i(0)$, t is the time and τ_i is the time constant (time taken for $A_i(t) = 1/e \cdot A_i(0)$) of a resonant mode i. ϕ is then extracted from the following equation,

$$\phi_i = \frac{1}{Q_i} = \frac{1}{\pi f_i \tau_i}, \tag{4.11}$$

where ϕ_i, Q_i and f_i are the mechanical loss , quality factor and frequency of resonant mode i. In this context the oscillator is a substrate, coated with a material of interest. There are many different experimental configurations that have been used to characterise coatings in this way. The first was using a cantilever measurement system [225]. Using a thin rectangular glass substrate as the oscillator and welding it to a thicker square piece of glass using an oxyhydrogen flame the thin substrate can be clamped to allow the oscillatory behaviour of the thin ribbon substrate to be measured [237]. Placing the cantilever in a vacuum to remove air damping effects and driving it with an external oscillation at the eigenfrequency of the cantilever will induced a mechanical excitation. The decay of this excitation gives a measurement of the mechanical loss of the cantilever.

4.7.4 Gentle Nodal Suspension (GeNS) and Multi Modal GeNS

The Gentle Nodal Suspension (GeNS) mechanical loss experiment was realised in 2000 by Numata [238] as a method to measure bulk loss of uncoated disks. It was later adapted to measure the mechanical loss of coated disks by Yamamoto [227] and Cesarini

[228] . A diagram is shown of the GeNS experimental set up built by the author in Figure [4.10]. A disk is suspended over a nodal point (a hemisphere such as a Si lens) in high vacuum ($< 10^{-6}$ mbar) by use of a custom designed suspension stage [24]. This allows the disk to be lowered on to the nodal support only in high vacuum and avoid being displaced by the lowering of pressure from the vacuum equipment. The stage is able to move in high vacuum by use of a vacuum compatible Newport TRA25PPV6 stepper motor which raises and lowers the disk insert stage via a controller and interface software [239]. Once lowered under vacuum an electrical signal at a eigenfrequency of the disk is either generated by a PC and sent through a National Instruments USB-6361 Data Acquisition (DAQ) or generated by an Agilent 33210A function generator and fed to a single sided printed circuit board with multiple branch electrodes known as a comb exciter [240], suspended over the disk. The DAQ is used for cases where testing multimodal measurement, using white noise to excite all eigenfrequencies of the disk simultaneously. The function generator white noise output produces more of a broadband signal than can be tailored by the PC and sent to the DAQ. The oscillating electric field drives resonant motion in the disk and the decay of the excitation is measured using a optical lever set up which consists of a laser (typically a HeNe laser with $\lambda \approx 633$ nm), quadrant photodiode (QPD) and mirrors. The laser is incident on the disk surface, if possible at a vibrational anti-node via an optical telescope. This is formed of two lenses (-75 mm and 150 mm focal length) which diverge and collimate the laser beam. This ensures a stable beam radius around the optical lever set up and therefore increases the differential signal strength from the QPD. The laser enters and exits the vacuum tank in the same window by use of a folded mirror cavity [241]. As the disk oscillates from mechanical excitation the laser spot will move over the QPD at the same frequency with an amplitude proportional to the disk motion. This will incur a measurable potential difference over the segments of the QPD which can be tracked as the oscillation decays. The signal is then passed through a preamplifier stage which high pass filters the signal (variable depending on the disks lowest measurable eigenfrequency) and amplifies the signal before it reaching the DAQ where is recorded by the PC. The process is controlled by custom Python software in addition to a

program written in Labview [242].

The benefit to this method over the cantilever or disk suspension set up is no prior modification is required to the substrate before measurement (dicing or welding). This has the added benefit of not introducing additional losses from welding or bonding that are not indicative of the substrate [228]. The drawback to this method is modes with significant displacement close to the centre of the disk (so called "drumhead" modes, shown in Fig [4.11b]) cannot be measured as they experience large contact loss with the suspension point of the disk [243].

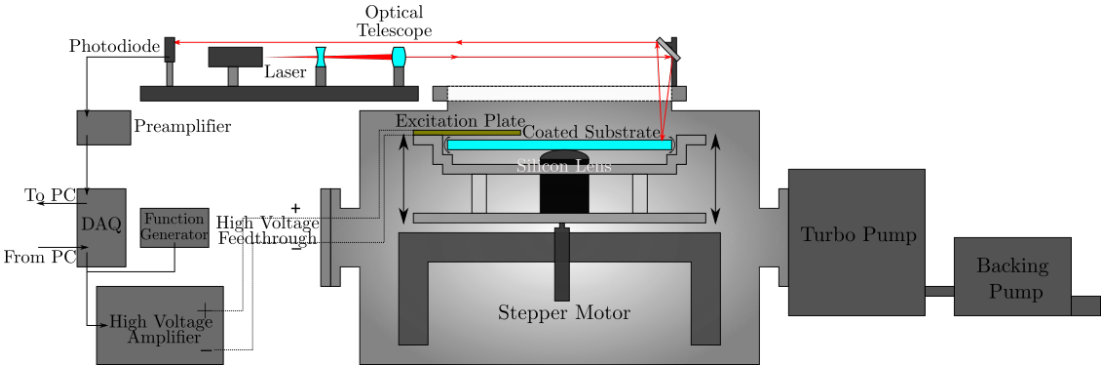

Figure 4.10: Side elevation of the GeNS system showing how a SiO_2 disk is excited by an electrical signal. Also shown is the optical lever system used to measure the ringdown decay. It should be noted that the disk fits perfectly inside the stage inset but for illustrative purposes is slightly smaller in the diagram.

The mechanical decay of a GeNS disk oscillator does not take the same form as Eq [4.10] as the eigenmodes of the disk are two separate decays spatially varied by 45° which can oscillate freely. An illustration of the degenerate mode pairs for a 50 mm diameter 0.5 mm thick Corning 7980 grade fused silica substrate calculated from the ANSYS Mechanical FEA package is shown in Figure [4.11]. Due to both spatially varied modes resonating close to the same frequency, the disk will have two separate exponential decays which are measure simultaneously. The decays are separated by a beat frequency (Δf) and take the form [243],

$$
\begin{aligned}
q_i^2(t) = &\left| A_{i,1} e^{2\pi i f_i t - t/\tau_{i,1}} + A_{i,2} e^{2\pi i \left(\int_i + \Delta f_i\right) t - t/\tau_{i,2} + \varphi_i} \right|^2 \\
= &A_{i,1}^2 e^{-2t\gamma_{i,1}} \left[1 + \frac{A_{i,2}^2}{A_{i,1}^2} e^{-2t\Delta y_i} + 2\frac{A_{i,2}}{A_{i,1}} e^{-t\Delta y_i} \times \cos\left(2\pi t \Delta f_i + \varphi_i\right) \right]
\end{aligned}
\tag{4.12}
$$

where $\gamma_{i,1} = 1/\tau_{i,1}$ and $\gamma_{i,2} = 1/\tau_{i,2}$ are the inverse of the time constant of the two modes, $f_{i,1}$ and $f_{i,2}$ are their frequencies, $A_{i,1}$ and $A_{i,2}$ are the initial amplitudes of the two modes and φ_i is the initial relative phase. The beat frequency is denoted with $\Delta f_i = f_{i,1} - f_{i,2}$ and the difference of inverse time constants between the two modes as $\Delta\gamma_i = \gamma_{i,1} - \gamma_{i,2}$.

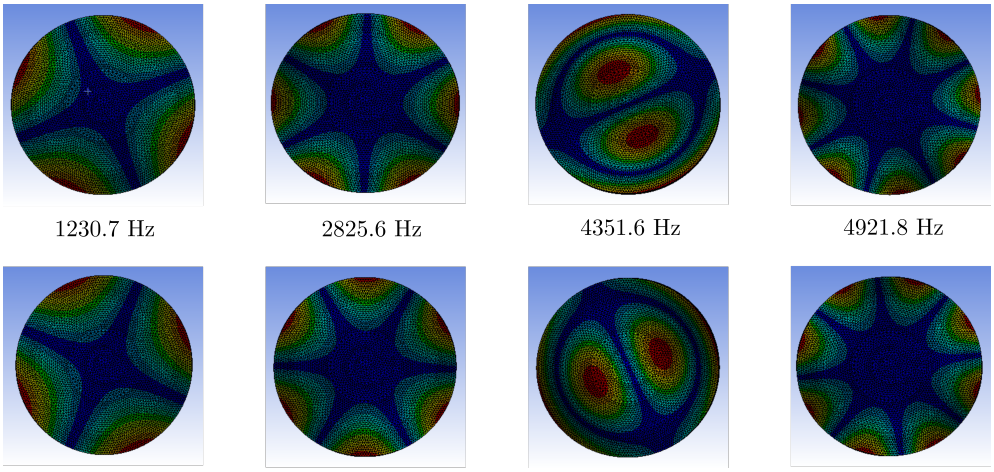

(a) First 4 mode pairs of the disk highlighting 45° rotation in deformation.

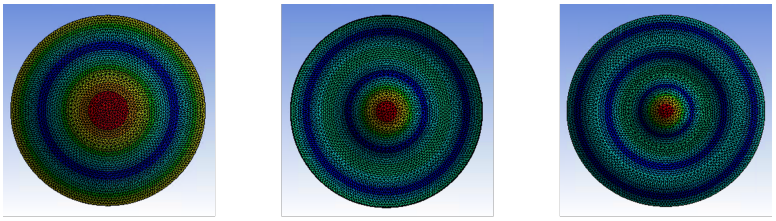

(b) First 3 drumhead modes of the disk highlighting deformation directly at the centre of the disk.

Figure 4.11: Mode shapes and frequencies of a 50 mm diameter 0.5 mm thick SiO_2 substrate, calculated using ANSYS FEA software.

The software required to analyse and fit this function to a degenerate ringdown decay was configured in Python and modified by the author from code written by

G.Vajente [244]. A flowchart of the software fitting routine is show in Fig [4.12]. Firstly the program will find and plot the ringdowns, having been pointed by the user to the folder where the data resides. User screening options are then given to analyse the entire dataset or select a portion (encase any part of the excitation was captured in the data).

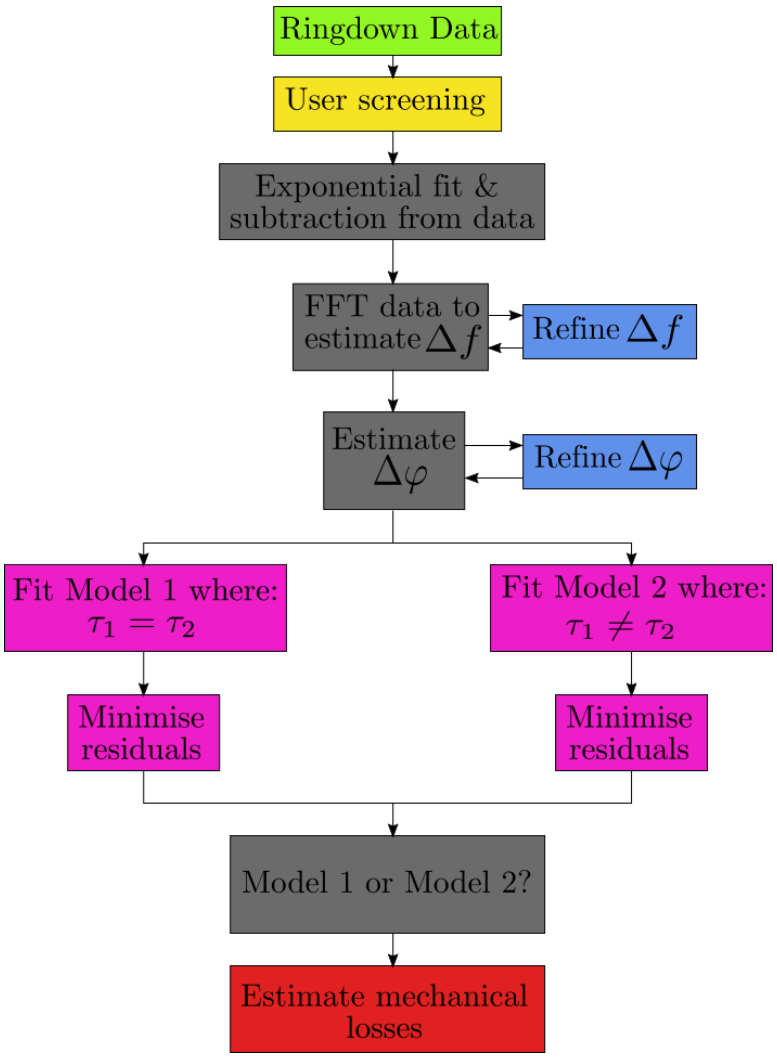

Figure 4.12: Flowchart of degenerate ringdown fitting program routine. Highlighted are the key stages of the process. Modified from [24]

After screening the dataset is "de-trended" by subtracting a decaying exponential from the data. This gives a flat oscillating signal so that the amplitude of the beat frequency peak can be estimated [24]. Then using the amplitude as a maxima and min-

ima of the oscillating signal, a Fast Fourier Transform (FFT) of this data for multiple periods gives an estimate of Δf_i. The program then estimates $\Delta\gamma_i$ by fitting a cosine function to the flat oscillatory signal of varying phase (0, $\pi/2$, π, $3\pi/2$) and choosing the best fit to the signal array by minimisation of the fitting error. This gives the phase estimation by also allowing the beat frequency to be refined. These give the initial boundary conditions by which to fit Eq [4.12] to the full ringdown. Two minimisation routines are performed, the first where $\tau_{i,1} = \tau_{i,2}$ and the second where $\tau_{i,1} \neq \tau_{i,2}$ as defects on the substrate or coating can lead to differing mechanical loss values for mode pairs [24]. The residuals (deviation of fit from the data) in each case are considered and the case where they are minimised is used. From this the additional parameters are calculated and outputted to a file. Figure [4.13] shows the fit and residuals for the 2.9 kHz mode of a 50 mm diameter 0.5 mm thick disk.

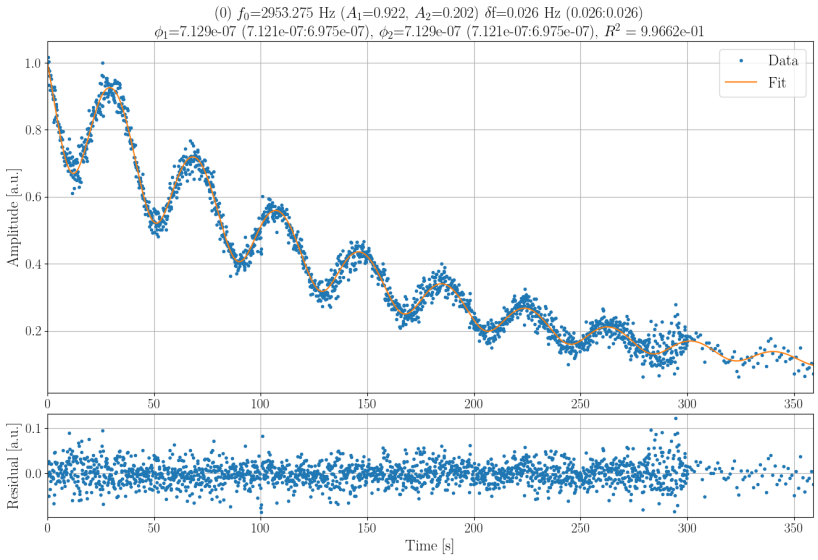

Figure 4.13: Plot of ringdown fitting to the 2.9 kHz mode of a 50 mm diameter 0.5 mm thick disk. The top plot shows the original data with the degenerate mode function overlaid, the lower plot shows the residuals of the fit function.

Measurements were taken on a 50 mm diameter 0.5 mm thick Corning 7980 grade fused silica disk to commission the system and assess repeatability over three separate suspensions, shown in Figure [4.14]. A suspension is defined here as the raising and

lowering of the disk onto the nodal support. The data points shown are the average mechanical loss of three repeated runs per suspension with error bars as the standard deviation of the three repeats.

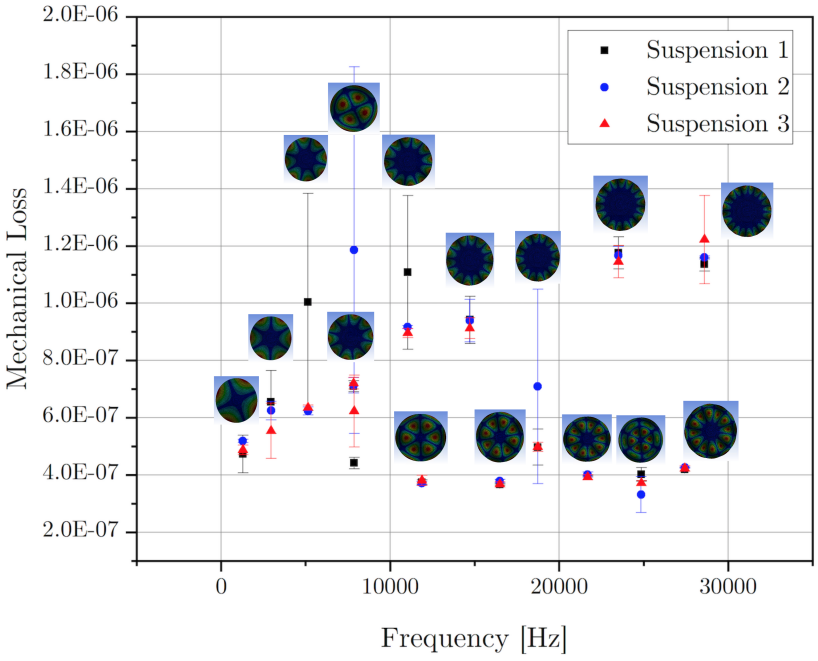

Figure 4.14: Measurements of a 50 mm diameter 0.5 mm thick Corning 7980 fused silica disk over three separate suspensions to access GeNS repeatability. Resonant mode shapes are shown pictorially adjacent to data points.

Over 3 suspensions the mechanical loss of the GeNS system is consistently within the error bars of measurements for each mode. The error bars for the 7 kHz mode are however higher than other measurements due to anti-nodes being closer to the suspension point than other mode shapes. This could be due to mechanical energy coupling to the lens support and artificially increasing the measured mechanical loss. The 5 kHz and 11 kHz mode additionally having higher error bars for suspension 1 which could be due to a chip at the edge of the disk. Fig [4.14] also shows a clear separation in mechanical loss, dependant on the mode frequency and shape. This is consistent with results shown previously for such measurements on disks [245]. The losses shown here are however higher by approximately an order of magnitude for this

material [243, 245], which is due to the aforementioned disk chip. This does however prove the validity of the measurements as the mechanical loss was consistent over the three suspensions.

Two different support lenses (Si and SiO_2) were tested in order to evaluate if a higher radius of curvature (ROC) of the lens corresponds to lower loss. Additionally the lens with the lower radius of curvature may allow resonant modes with antinodes closer to the suspension point to oscillate freely, such as the 1,1 mode (see 3863.2 Hz mode pair in Figure [4.11]). This is dependant on the surface contact radius of the disk and suspension point (r_c) defined as [228],

$$r_c = \left[\frac{3}{4}MgR\left(\frac{1-\sigma^2_{\text{sample}}}{Y_{\text{sample}}} + \frac{1-\sigma^2_{\text{sphere}}}{Y_{\text{sphere}}}\right)\right]^{1/3}, \tag{4.13}$$

where M is the mass of the disk, R is the radius of the sphere, Y_{sample}, Y_{sphere}, σ_{sample}, σ_{sphere} are the Youngs moduli and the Poissons ratios of the sample and of the sphere. Table [4.1] shows the contact radius for two lenses used for this experiment and Figure 4.15 outlines the results for 8 modes of the 50 mm diameter 0.5 mm thick Corning 7980 grade fused silica substrate annealed at 950°C for 5 hrs. The annealing step was conducted to remove any residual O-H bonded to the surface of the samples [246]. Results are presented as an average over two separate suspensions with each mode being measure three times per suspension. Error bars are taken as the standard deviation of the six results per mode.

Lens Material	ROC	Young's Modulus	Poisson's Ratio	Surface contact radius
Si	60.44 mm	156 GPa [247]	0.27 [247]	26.5 μm
SiO_2	15.50 mm	72 GPa [248]	0.17 [248]	18.8 μm

Table 4.1: Summary of surface contact radius calculation for silicon and silica lenses. Included are the material parameters used for the calculations

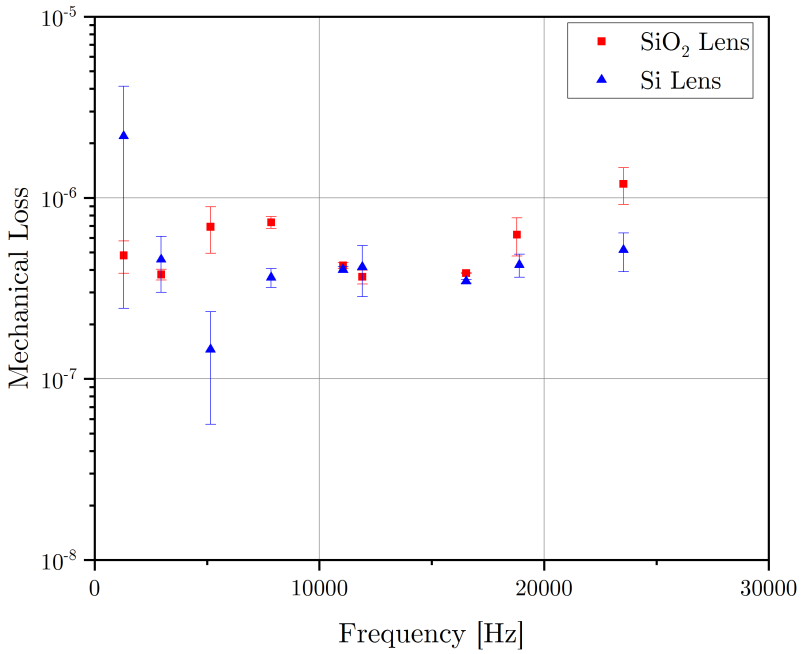

Figure 4.15: Average mechanical loss of 50 mm diameter 0.5 mm thick Corning 7980 grade fused silica disk over two suspensions using a crystalline silicon and silica lens as a nodal support. Error bars are taken as the standard deviation of the measurements.

With the exception of three modes the mechanical losses of disk suspension conducted with the SiO_2 lens are higher than the Si lens, larger than a factor of 2 for the 23 kHz mode. The three Si lens measurements which show higher losses are however within error bars, the first having the largest error bars due to erroneous signal output from the QPD.

The losses are however higher than typically seen for a Corning 7980 grade fused silica disk. This is due to a large delay between high temperature annealing (950° for 5 hours) and measurement on the order of a few weeks. The annealing step will reduce the loss of an uncoated disk as it removes any surface O-H on the disk [249].

Data is not shown for the 4 kHz 1,1 mode (Shown in Figure [4.11]) as for both lenses the mode decay was too fast for meaningful data to be collected (on the order of a few seconds). Given the results in Fig [4.15] and that the 4 kHz mode cannot be accessed with the SiO_2 lens with the lower surface contact radius, the Si lens has been

used for further measurements as it produces lower loss values.

Recent efforts have been to create a multi-modal GeNS system whereby a white noise signal is used to excite all mode simultaneously [243]. This is done by outputting white noise directly from the DAQ to the comb exciter. As all eigenfrequencies are excited a method is needed by which to de-convolute the QPD signal. Firstly an FFT is taken of the raw QPD signal is both the X and Y axis before and after white noise excitation. Subtracting the two power spectral densities shows the resonant peak frequencies and an amplitude associated with the X and Y axis. This is dependant on the mode shape as different resonant frequencies will cause a larger displacement in on axis than the other. Depending on which amplitude is larger, that particular axis will be chosen to be analysed. The raw signal is then separated into frequency bins via an FFT to compute the signal amplitude vs time data. Once this is complete the same fitting routine is applied to the data as shown in Figure [4.12].

The software to output white noise and continuously measure the QPD signal from both axis was written in Python by the author. The analysis program for deconvolution of the data was modified by the author in Python from code previously written by G.Vajente [244]. Comparison between measurements of a 50 mm diameter 0.5 mm thick Corning 7980 grade fused silica substrate using single mode and white noise excitation are shown in Fig [4.16]. Data points are taken as an average over 3 separate measurements from the same suspension.

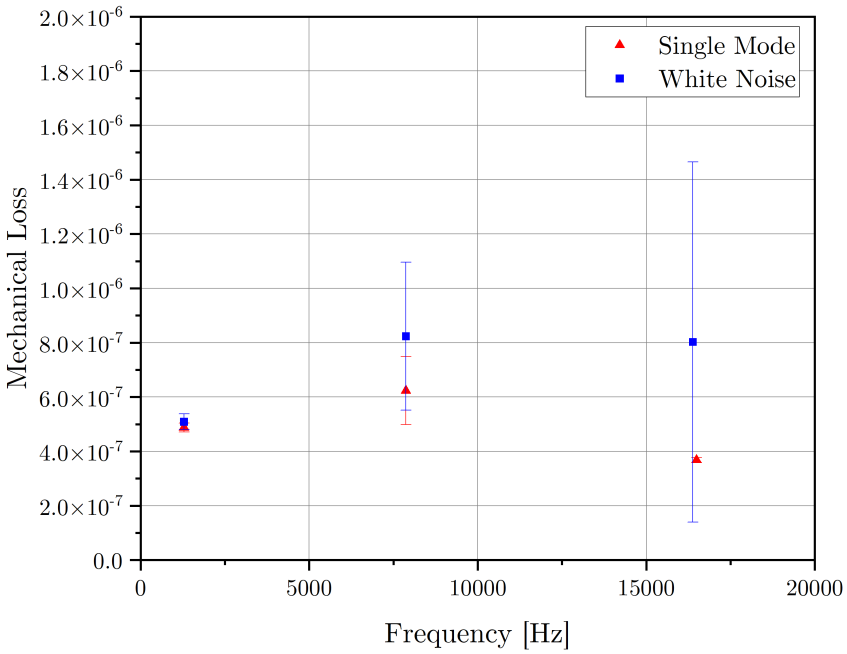

Figure 4.16: Single mode vs white noise data for 3 modes of a 50 mm diameter 0.5 mm thick Corning 7980 fused silica substrate. Error bars are shown as the standard deviation of these measurements.

The larger error bars from the white noise measurements are a result of poor excitation of the resonant modes. This is due to the signal being spread over a large frequency range and with the current capabilities of the equipment it is unable to generate band limited noise. This has additionally led to a higher loss value (a factor of 2 for the 16 kHz mode) as by barely exciting the mode the functionality of the analysis program cannot accurate fit to the degenerate mode decay. The fundamental mode excitation works well for white noise and can generate the same results as single mode excitation however the additional issues outweigh this result.

This measurement technique is however in the early stages as more equipment development is required to generate a reliable measurement system. As such single mode excitation and analysis is used for all measurements in this thesis conducted by the author.

4.8 Conclusions

In summary a variety of metrology techniques are required to evaluate coating suitability for a gravitational wave detector.

Optical, compositional and structural techniques give deeper understanding into the morphology of the coatings produced by IBSD. This is key in understanding how the properties of these films change by adjustment of the deposition parameters. Furthermore this would allow coatings to be tailored to the design specification of a gravitational wave detector.

The author has built and tested a GeNS system capable measurement of mechanical loss of disk resonators, calculating a property directly linked to the thermal noise performance of a gravitational wave detector. A full assessment was given of the repeatability of the system in addition to how changing of the nodal support can effect the loss measured.

Chapter 5

Characterisation of silicon coatings with varying IBSD process parameters

5.1 Introduction

At present the choice of coating materials used for aLIGO is alternating layers of TiO_2 doped Ta_2O_5 as the high index material and SiO_2 as the low index material in the HR stack.

Moving towards A+, as there are no plans to reduce the temperature or scale up the GWD size (laser arms or test masses) a new design is needed to permit a lower thermal noise floor (by a factor of 2 for A+). This mean the materials chosen must have at least a factor of 4 lower mechanical loss that the current HR stack design layers [250]. The materials are also required to exhibit low optical loss properties, with an absorption < 0.5 ppm and scattering < 2 ppm [251]. Beyond A+, while the temperature and scale of the GWD can be altered materials are also required which can operate in these regimes. A material which has shown to have high refractive index (meaning reduce bilayers to achieve reflectivity in HR mirrors) and a low mechanical loss (at room temperature and ~ 125K) is amorphous silicon (a-Si) [135, 252].

There has been much work on a-Si for GW research using many coating deposition

techniques, including IBSD [135, 252–256]. However none of the work concerning IBSD has specifically explored the process parameters as a function of mechanical and optical loss properties. The research described in this chapter regards a-Si films produced with varying deposition ion beam energy and current. The optical mechanical properties are measured and related to the composition and structure of the films.

This will be paramount in developing coatings for next generation GWDs, in order to push the current limits of thermal noise performance to reach detector design sensitivity.

5.2 Deposition Parameters

In order to understand the deposition process, multiple parameters were adjusted systematically. Table [5.1] shows the variation in ion beam energy and current for all runs conducted on a-Si. All deposition processes used a fix target angle ($\alpha = 60°$), with a fixed flow of Ar gas to the RF ion source and neutraliser (15 sccm and 5 sccm respectively) in accordance with the manufacturer documentation [164, 185]. This gave a working gas pressure of $(2 \rightarrow 4) \times 10^{-4}$ mbar. The beam parameters that were used created a stable plasma at this working gas pressure. Run durations between the variable beam energy and current studies were changed to avoid overheating of the Si target. The ion beam was turned on for approximately 20 minutes before every deposition process to ensure any oxidation layer form on the target was etched away. Coating thickness for each deposition is also shown in Table [5.1] which are calculated from fitting spectrophotometry interference fringes in SCOUT (more details regarding this are given in Section 5.3.2. Errors shown for the beam energy and current are represented as $\pm 1\%$ of the full power supply range [164] and for run times errors are attributed to approximate deposition times. Errors in coating thickness are calculated as the standard uncertainty of thickness calculated from two separate witness samples.

Ion Beam Energy	Ion Beam Current	Run Duration	Coating thickness
0.4(±0.02) keV	200(±20) mA	2(±0.16) hrs	207.4(±11.0) nm
0.6(±0.02) keV	200(±20) mA	2(±0.16) hrs	227.1(±20.0) nm
0.7(±0.02) keV	200(±20) mA	2(±0.16) hrs	230.6(±14.2) nm
0.8(±0.02) keV	200(±20) mA	2(±0.16) hrs	228.5(±19.4) nm
1.0(±0.02) keV	200(±20) mA	2(±0.16) hrs	178.1(±15.2) nm
1.2(±0.02) keV	200(±20) mA	2(±0.16) hrs	189.0(±14.8) nm
0.6(±0.02) keV	100(±20) mA	1(±0.16) hrs	43.3(±19.0) nm
0.6(±0.02) keV	300(±20) mA	2(±0.16) hrs	220.0(±28.4) nm
0.6(±0.02) keV	400(±20) mA	2(±0.16) hrs	205.8(±16.2) nm

Table 5.1: Deposition parameters used in study of a-Si thin film coatings.

Each process used multiple witness substrates consisting of two JGS grade fused silica and two high purity (99.999%) crystalline silicon ($\langle 100 \rangle$ orientation) substrates. Details regarding substrates for different characterisation techniques are given in Chapter 4. Each substrate was cleaned in an ultrasonic bath, using first acetone and then iso-propyl alcohol (IPA). The samples were then dried with N_2 and, if appropriate, wiped with high grade clean room optic wipes. This minimised contaminates which could interfere with the coating process and lead to coating adhesion issues. Substrates were then mounted in custom holders (see Section [3.6]) which were again mounted to a rotational stage, rotating at 3.1 rpm to ensure good uniformity across the substrate face. The typical deposition temperature was around 40°C.

5.3 Results

5.3.1 Deposition Simulation

To extract sputtering yield and particle energies in the deposition process simulation were conducted in SDTrimSP to calculate the information. More details on the simulation program are given in Section [3.5.2]. Simulations were created using beam energies between 0.4 keV - 1.2 keV with $\alpha = 60^\circ$ with the results shown in Table [5.2]. The Kr-C interaction potential [257] was used with a Lindhard-Schaff inelastic loss model [258]. This was shown in [259] to accurately model the interaction between an RF inductively coupled ion source and Si target. While the simulated energy output from SDTrimSP is angle dependant, the values shown are the average across the entire dis-

tribution, accounting for 80(±10)% of ions and particles. SDTrimSP does not have a facility to alter the beam current directly therefore the analysis shown is only for varying beam energies of the deposition process. Errors are shown for results as the standard uncertainty in data produced by 3 separate simulations.

Beam Energy	Sputtering Yield	Sputtered Si Energy	Backscattered Ar Energy
0.4 keV	1.8(±0.2) atoms/ion	29.7(±0.3) eV	97.2(±0.2) eV
0.6 keV	2.4(±0.3) atoms/ion	34.7(±0.4) eV	137.1(±0.3) eV
0.7 keV	2.6(±0.3) atoms/ion	36.8(±0.4) eV	156.0(±1.2) eV
0.8 keV	2.8(±0.4) atoms/ion	38.8(±0.6) eV	174.2(±1.3) eV
1.0 keV	3.1(±0.3) atoms/ion	42.6(±0.4) eV	211.6(±0.9) eV
1.2 keV	3.4(±0.4) atoms/ion	46.1(±0.4) eV	248.3(±1.0) eV

Table 5.2: Simulated sputtered Si yield, average sputtered Si particle energy and average backscattered Ar ion energy for varying ion beam energy of Ar on Si using SDTrimSP.

The results in Table [5.2] highlights a number of interesting features in the simulations. The first is the linear dependence of sputtering yield on ion beam energy. While this is not something from experimental depositions in this work this will be due to the beam divergence not being considered by the software. This is however a guide result which should be considered carefully in this analysis.

The second interesting result is the contrast in energy between backscattered and sputtered ions. This relates directly to the surface binding energy of the crystalline Si target however the majority of atoms sputtered have an exceeding low energy. This however could lead to a number of Ar induced defects embedded in the coatings which could effect optical and mechanical properties. This should be considered carefully when selecting deposition parameters for the coating process.

5.3.2 Optical Characterisation

Spectrophotometry

In order to optimise the deposition process, the optical properties of the thin films should be considered. These properties are essential to achieving the high performance coatings required for a GWD. To fit and characterise the refractive index, extinction coefficient and thickness of the a-Si thin films (nkd), measurements were taken of optical

transmission (T) and reflection (R) using spectrophotometry. The films were measured between 185 nm - 3000 nm using a Photon RT UV-Vis-IR spectrometer. Further details of this equipment are given in Chapter [4]. The transmission spectra from varying the beam energy and beam current are shown in Figure [5.1].

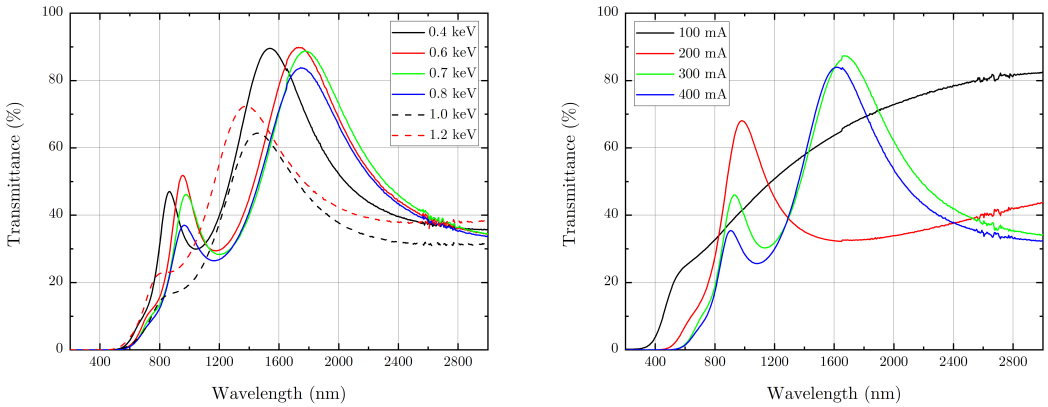

(a) Transmission curves of a-Si coatings varying ion beam energy on JGS1 and JGS3 grade silica disks.

(b) Transmission curves of a-Si coatings varying ion beam current on JGS1 and JGS3 grade silica disks.

Figure 5.1: Summary of all optical transmission curves for a-Si coatings with variation of ion beam energy (0.4 keV - 1.2 keV) and current (100 mA - 400 mA). Sharp increases in T at 1650 nm are due to changing diffraction grating on the spectrophotometer and have not effected any subsequent results.

By varying the beam energy used in the deposition process the thickness of the film changes, particularly at energies $>$ 0.8 keV. As the energy of the ions from the beam increases so does the likelihood of disassociation of residual gas molecules in the deposition chamber. This would result in a thin film of both lower thickness and index.

Increasing the beam current correlates directly to an increase in overall coating thickness. This is confirmed by the increase of interference fringes in Figure [5.1b] with a maximum thickness at 300 mA (shown in Table [5.1]). As all depositions were run for the same duration, the thickness decrease at 400 mA is due to increased beam spread due to non optimal current being used [259]. This would decrease the efficiency of sputtering material from the Si target and therefore decrease the coating thickness.

The transmittance data was then used to calculate the refractive index and extinc-

tion coefficient of the coatings using SCOUT optical fitting software. This is shown in Figures [5.2, 5.3] and [5.4, 5.5]. For the a-Si material configuration an OJL term was used in addition to a UV oscillator and constant refractive index term. A thickness averaging term was used for the coating to account for any scatter or inhomogeneity [201]. Further details about this can be found in Chapter [4]. While an oxidation layer on these films is likely the methodology used from similar studies of IBD a-Si using analogous measurement equipment does not consider this [253, 256]. This is therefore thought to be of negligible thickness for analysis. In addition as the fits produced have matched closely to the R and T spectra, surface roughness is thought to not be at a level which would highly impact these results.

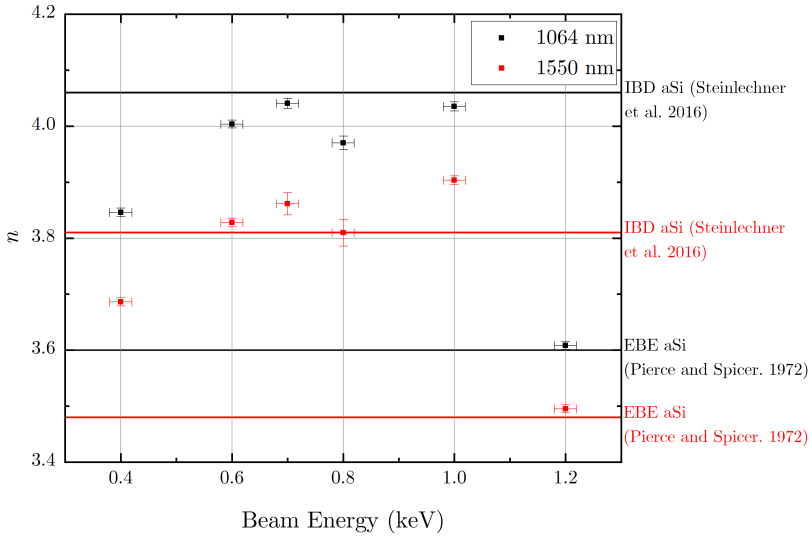

Figure 5.2: Refractive indices at 1064 nm (black) and 1550 nm (red) for a-Si films with varying beam energy (0.4 keV - 1.2 keV) on JGS1 and JGS3 grade silica substrates. Also marked are reference refractive indices for IBSD a-Si [255] in addition to EBE a-Si [260]. Error bars show the standard uncertainty in results for each deposition based on the two silica witness samples.

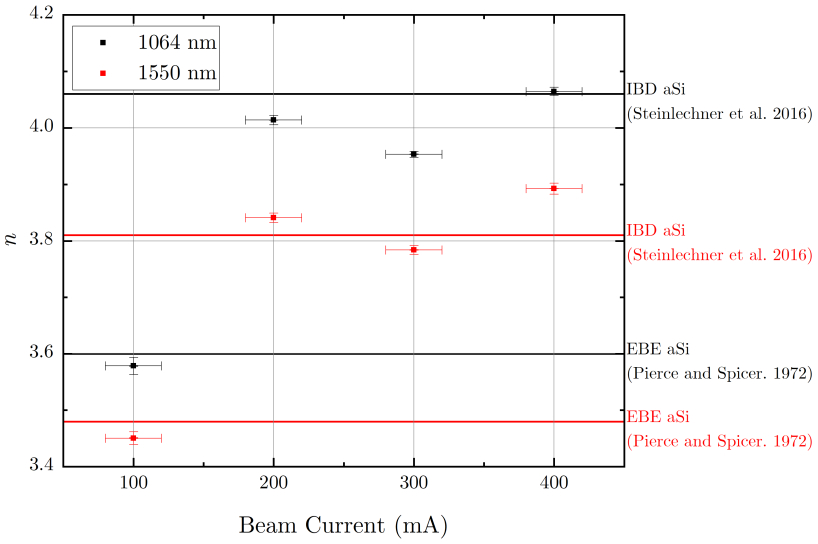

Figure 5.3: Refractive indices at 1064 nm (black) and 1550 nm (red) for a-Si films with varying beam current (100 mA - 400 mA) on JGS1 and JGS3 grade silica substrates. Also marked are reference refractive indices for IBSD a-Si [255] in addition to EBE a-Si [260]. Error bars show the standard uncertainty in results for each deposition based on the two silica witness samples.

The refractive index data shows that the film indices are, in the majority of cases, close to values previously attained for IBSD a-Si. Regarding the beam energy variation (Figure [5.2]), there is an upward trend between 0.4 - 0.7 keV, likely due to the increased film density. After this the index plateaus at 1064 nm between 3.97 - 4.04 until 1.2 keV where there is a huge decrease in n values to 3.6. At 1550 nm the refractive index increases to a maximum of 3.90 at 1.0 keV, well above what was measured in [255]. At 0.4 keV however the index is lower than [255], where $n = 3.68$ at 1550 nm, but this is still higher than the EBE a-Si films [260].

Regarding the beam current variation films have the lowest refractive index, where $n = 3.45$ at 1550 nm using 100 mA of beam current. This is mainly due to the low ion flux giving low film thickness (43.3 nm $\pm$19.0 nm) in comparison to the other a-Si coatings.

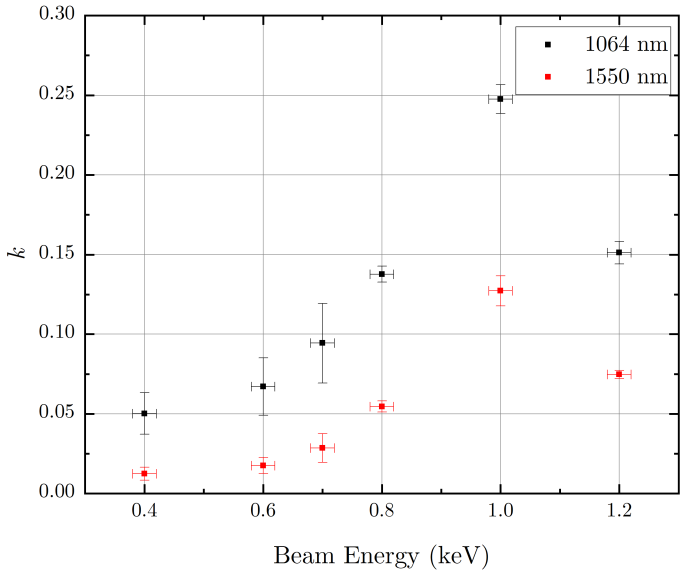

Figure 5.4: Extinction coefficient at 1064 nm (black) and 1550 nm (red) for a-Si films with varying beam energy (0.4 keV - 1.2 keV) on JGS1 and JGS3 grade silica substrates. Error bars show the standard uncertainty in results for each deposition based on the two silica witness samples.

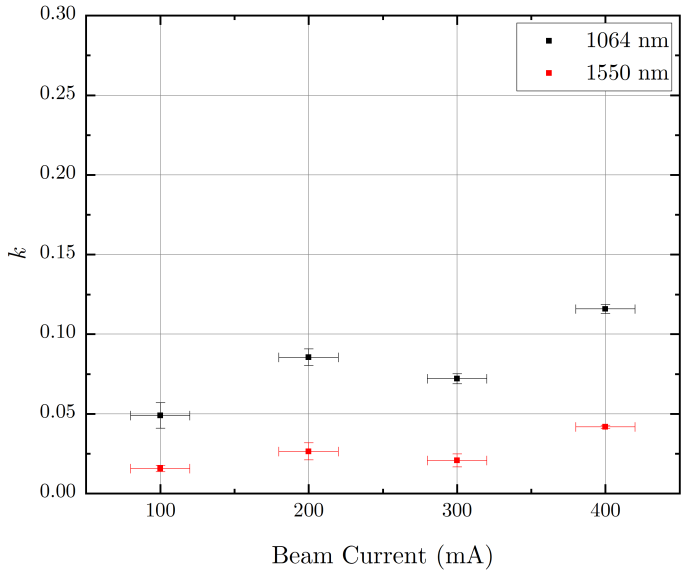

Figure 5.5: Extinction coefficient at 1064 nm (black) and 1550 nm (red) for a-Si films with varying beam current (100 mA - 400 mA) on JGS1 and JGS3 grade silica substrates. Error bars show the standard uncertainty in results for each deposition based on the two silica witness samples.

The extinction coefficient results (Figures [5.4, 5.5]) show a minimum k value of 0.01 at 1550 nm for 0.4 keV at 200 mA. At increasing values of beam energy the k value also increases showing incorporation of absorbing material into the coating. This is maximised to 0.12 at 1.0 keV, likely due to beam overspill (divergence of the ion beam spreading beyond the target area) onto the Al backing plate of the Si target. With regards to the beam current variation the minimum value of 0.01 is at 100 mA.

Annealing a-Si coatings in a high temperature environment has proven to decrease optical absorption [253, 255]. As such the coatings produced here were annealed at increasing temperatures up to 450°C, to study the effects of heat treatment on their optical properties. The temperature of 450°C was chosen as the end step in the annealing schedule due to it producing the lowest values of absorption for IBSD a-Si [255, 261]. Each annealing run consisted of a 5°C/min ramp in a Carbolite Gero 30-3000°C RHF annealing furnace (in air at 1 bar of pressure) to a set temperature point which the samples were held at for 1 hour before passively cooling to 25°C. Results of re-

fractive index and extinction coefficient fitting generated from SCOUT for varying the deposition process beam energy and current are shown in Figures [5.6, 5.7] and [5.8, 5.9].

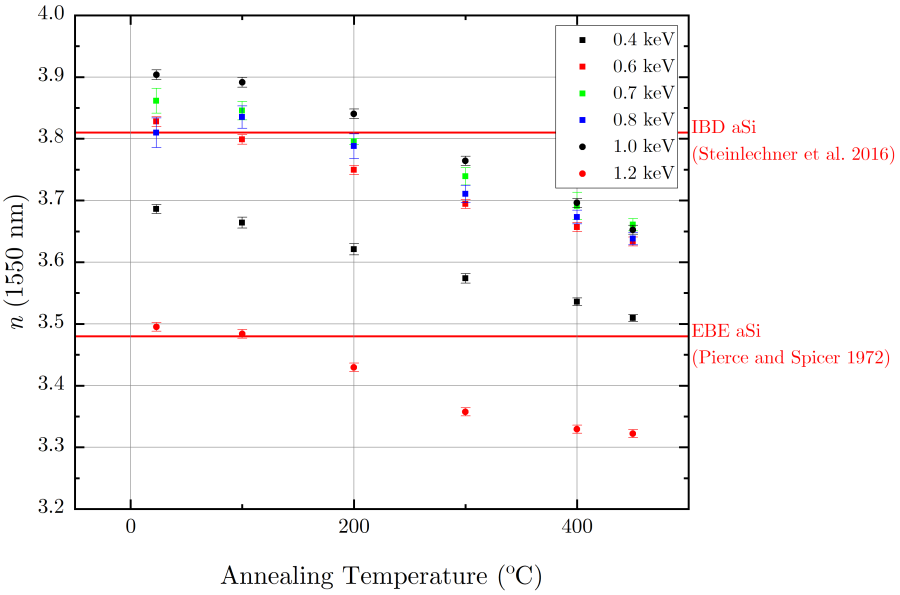

Figure 5.6: Refractive index at 1550 nm for a-Si films with varying beam energy (0.4 - 1.2 keV) annealed to 450°C on JGS1 and JGS3 grade silica substrates. Also marked are reference refractive indices for IBSD a-Si [255] in addition to EBE a-Si [260]. Error bars show the standard uncertainty in results for each deposition based on the two silica witness samples.

Annealing the samples to higher temperatures has decreased the fitted refractive index from multiple witnesses for each deposition process. Also the decrease in index is nominally invariant of the beam energy used for deposition but not the beam current. This can be seen in Figure [5.6] and [5.7]. An interesting point is the collection of samples between 0.6 keV - 1.0 keV which have similar refractive indices when annealed given n values between 3.63 - 3.66 at 450°C showing a preferential growth structure at these energies.

In particular the 100 mA sample refractive index decreases from 3.45 to 3.23 before rising after being annealed to 450°C to 3.27. As this is the thinnest coating produced in this study in addition to the only sample to exhibit this behaviour however this is still

within the error bars of the measurement. In order to produce a high refractive index for the film a high beam current is required as can be seen in the 400 mA sample which has produced the highest annealed n value at 1550 nm of 3.68. While the refractive index is not as high as reported in [255] this is still compatible with a HR mirror stack design at 1550 nm due to the contrast in refractive index between this material and a low index material such as SiO_2 ($n = \approx 1.47$ [262]).

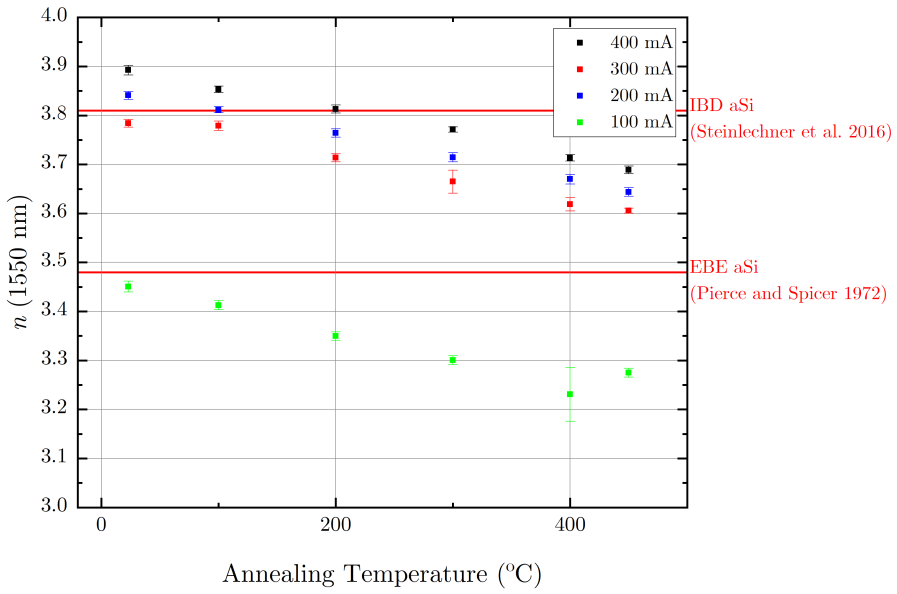

Figure 5.7: Refractive index at 1550 nm for a-Si films with varying beam current (100 mA - 400 mA) annealed to 450°C on JGS1 and JGS3 grade silica substrates. Also marked are reference refractive indices for IBSD a-Si [255] in addition to EBE a-Si [260]. Error bars show the standard uncertainty in results for each deposition based on the two silica witness samples.

The k value of these samples is equally important, to ensure low optical absorption (and therefore optical loss) at the intended wavelength of future GWDs. This has been shown to decrease with increasing annealing temperature [253, 255] which was conducted on the samples is shown in Figures [5.8, 5.9].

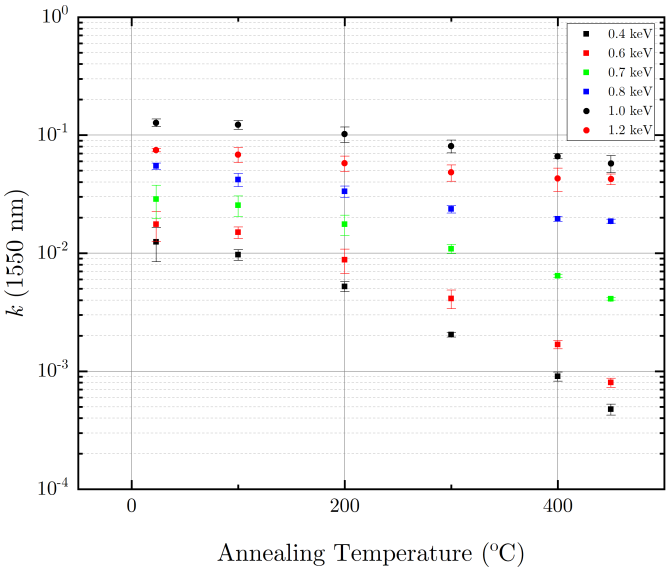

Figure 5.8: Extinction coefficient at 1550 nm for a-Si films with varying beam energy (0.4 - 1.2 keV) annealed to 450°C on JGS1 and JGS3 grade silica substrates. Error bars show the standard uncertainty in results for each deposition based on the two silica witness samples.

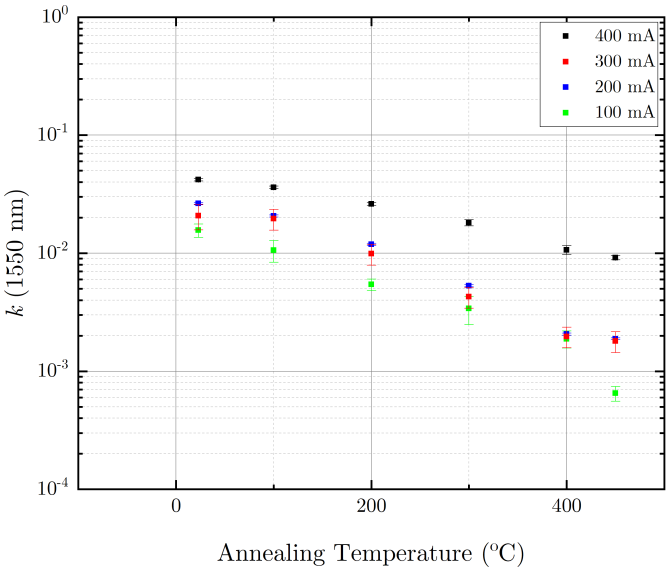

Figure 5.9: Extinction coefficient at 1550 nm for a-Si films with varying beam current (100 mA - 400 mA) annealed to 450°C on JGS1 and JGS3 grade silica substrates. Error bars show the standard uncertainty in results for each deposition based on the two silica witness samples.

From the data it can be seen that the extinction coefficient of the 0.4 keV and 0.6 keV samples is the lowest independent of thickness variation, continued at high annealing temperatures. As the spectrophotometer reaches a limit of absorption resolution at $k = 2 \times 10^{-4}$ [192], these samples were selected for PCI measurements to determine there absolute absorption at 1064 nm and 1550 nm.

5.3.3 PCI

To fully assess the optical absorption characteristics of the a-Si samples, PCI measurements were conducted on the coatings. Scans across the coating surface are taken with two interfering laser beams. This technique can accurately assess the optical absorption at 1064nm and 1550nm by comparing the change in the phase of the transmitted light through an induced thermal lens. More details of this measurement system are given in Chapter 4. Scans were taken at $\approx$ 2 mm intervals across the surface of the samples using a 1550 nm laser on coated Corning 7979 fused silica substrates. By

taking the maximum optical absorption amplitude from the scans at a phase angle of -50° the absorption of the film can be calculated. Results of these scans are shown in Figure [5.10]. Error bars show for absorption represent the standard uncertainty in results over 3 separate measurements. Errors shown for the beam energy and current are represented as ±1% of the full power supply range [164].

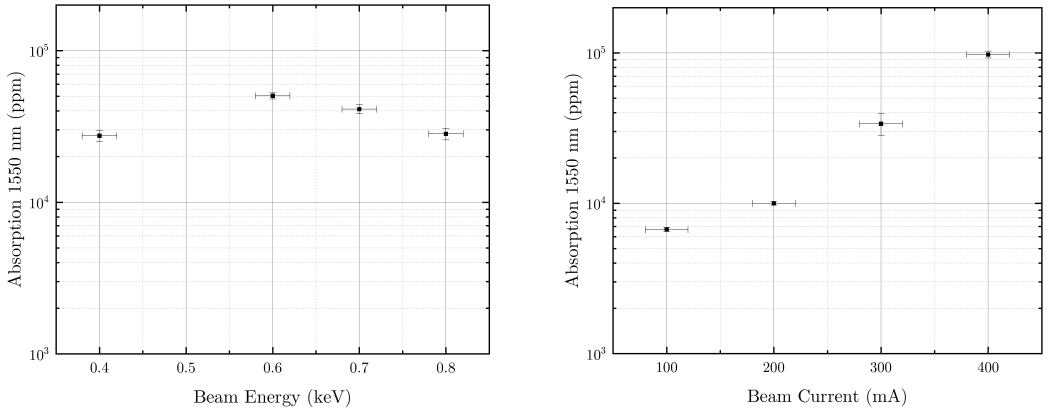

(a) PCI absorption measurements as deposited for varying deposition beam energy (0.4 keV - 0.8 keV).

(b) PCI absorption measurements as deposited for varying deposition beam current (100 mA - 400 mA).

Figure 5.10: PCI measurements at 1550 nm for as deposited a-Si thin films on Corning 7979 grade SiO_2 of varying deposition beam energy and beam current.

Figure [5.10] highlights the change in optical absorption properties of a-Si coatings when altering beam parameters of the deposition. In particular Figure [5.10a] shows that at low energy levels (0.4 keV) the absorption is reduced at 1550 ppm to $2.7(\pm 0.2) \times 10^4$ ppm. At higher energies (0.8 keV), the absorption reduces from $5.03(\pm 0.24) \times 10^4$ ppm at 0.6 keV to $2.8(\pm 0.3) \times 10^4$ ppm. Figure [5.10b] shows an exponential increase in optical absorption when using a higher beam current for deposition. This ranges from measurements for the 100 mA film, where the absorption is $6.9(\pm 0.2) \times 10^3$ ppm to 400 mA where the absorption is $9.8(\pm 0.5) \times 10^4$ ppm. This is likely due to thickness as it should be noted that the film deposited using 100 mA is approximately 1/5 the thickness of the film produced using 400 mA (205.83 nm).

Using the same methodology as described in Section 5.3.2 samples produced at 0.4 keV and 0.6 keV were annealed to assess there absorption characteristics up to

450°C. These samples were chosen as they produced lower k values when annealed and measured by spectrophotometry (see Section 5.3.2). Results of this experiment can be shown in Figure [5.11]. Error bars show the standard uncertainty in results over 3 separate measurements.

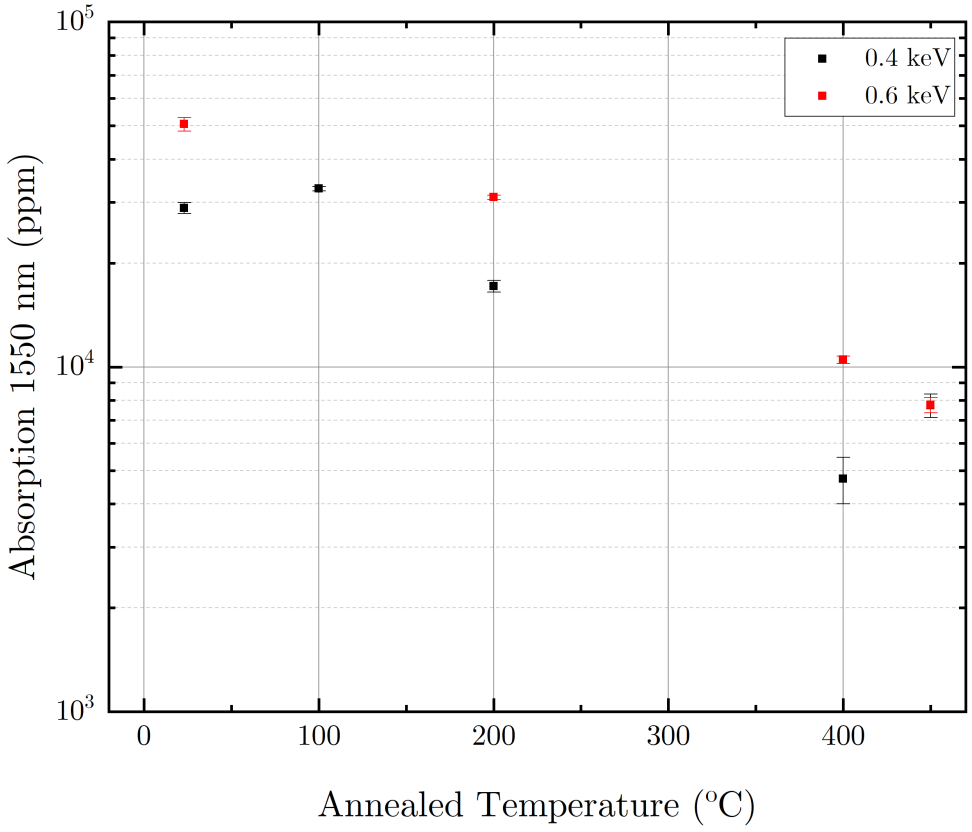

Figure 5.11: PCI measurements at 1550 nm for a-Si films produced at 0.4 keV and 0.6 keV on Corning 7979 grade SiO_2, annealed in steps to 450°C.

Figure [5.11] shows a decreasing trend in absorption with increasing annealing temperature. A feature of note of this data includes the absorption of the 0.4 keV sample at 100°C which appears to increase to $3.28(\pm 0.05) \times 10^4$ ppm. Given the k values extracted by the spectrophotometer (see Section 5.3.2) at this temperature contradict this result, the measurement here is subject to an experimental uncertainty which is undefined (such as physical change in the aligment quality of the set up). The sub-

sequent results at higher temperatures are in agreement with results in Section 5.3.2 therefore these can be taken as absolute values.

At the higher annealing temperatures both samples appear to either reduce the decreasing rate of absorption between annealing steps or show an increase in absorption. For the case of the a-Si coating using 0.6 keV, the absorption is shown to be $7.8(\pm 0.4) \times 10^3$ ppm at 450°C. This is only 2.73×10^3 ppm lower than the previous step (400°C) in contrast to the jump between 200°C and 400°C of 2.05×10^4 ppm. a-Si produced at 0.6 keV show an increase in absorption from $4.7(\pm 0.7) \times 10^3$ ppm to $7.7(\pm 0.6) \times 10^3$ ppm at 450°C.

5.3.4 Mechanical Characterisation

Coating mechanical loss measurements

To understand the effect the a-Si would have in the context of a GWD, the coating mechanical loss is required in order to calculate the expected level of coating thermal noise. This was conducted as described in Section [4.7.4] by the use of GeNS. 50 mm $\varnothing$ 1 mm thick Corning 7980 fused silica substrates were first measured in the suspension system to attain uncoated base loss values across the frequency spectrum. Each resonant mode was measured three times before the disk was re-suspended. Three suspension was conducted for each sample. The samples were then cleaned with acetone and IPA before being coated with a-Si. After deposition, the samples were remeasured in the GeNS system, giving the coated mechanical loss.

To extract the coating mechanical loss, FEA modelling of the disks is required to calculate the elastic energy ratio between the substrate and coating. Using ANSYS Workbench a model of the disk was created using the internal CAD designer and a sweep mesh method. The uncoated disk was first modelled by changing the thickness of the disk to match the eigenmodes measured in the GeNS system with the difference between the modelled and measured frequencies (Δf) being $< 1\%$. Once coated a similar process was conducted by changing the coating thickness, Young's modulus and Poisson's ratio. Base parameters for the a-Si coating mechanical properties were taken from literature values [263, 264], shown in Table [5.3].

Parameter	Value
Young's Modulus	130 GPa
Poisson's Ratio	0.28
Density	2329 kg/m^3

Table 5.3: Mechanical parameters used in ANSYS simulation for a-Si.

Once a match was found to the coated disk eigenmodes, a custom ANSYS Parametric Design Language script (see Appendix [B]) was employed to extract the energy ratio between the coating and substrate. The coating results are shown in Figure [5.12] for a-Si using 0.4 keV and 0.6 keV beam energy in the deposition process. Error bars were calculated from the standard deviation of all resonant mode measurements to show the spread in results [24].

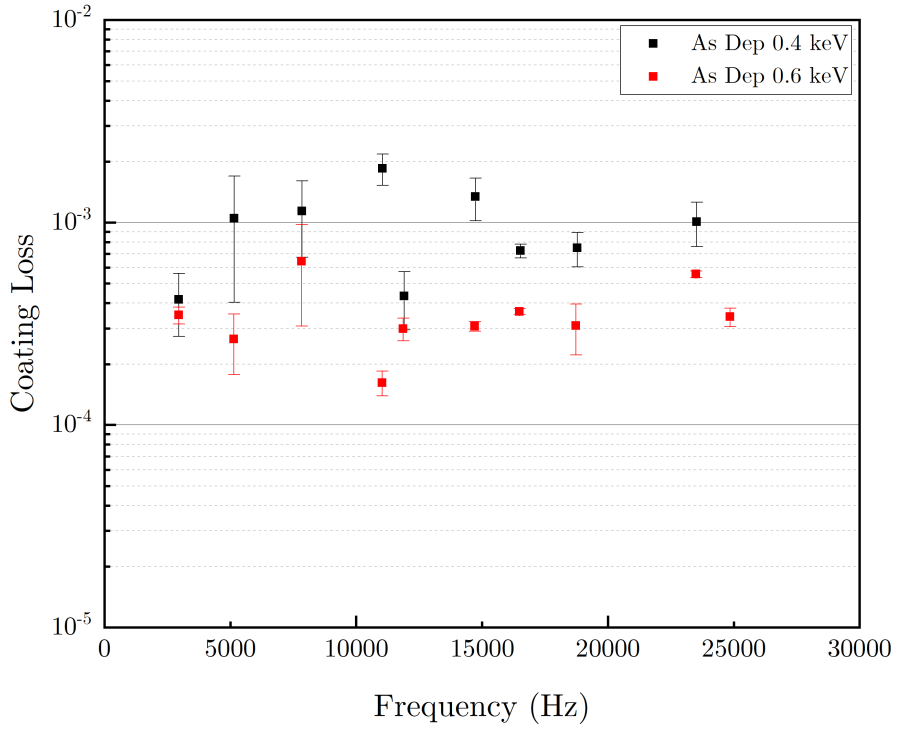

Figure 5.12: Coating loss of a-Si as deposited using 0.4 keV and 0.6 keV beam energy current during deposition. Error bars show the spread in measurements of each mode over three separate suspensions.

Figure [5.12] highlights that overall the deposition at 0.6 keV gives a coating with

lower mechanical loss than coatings at 0.4 keV. The loss values of the 0.4 keV coating is higher than has been previously reported for as deposited a-Si, $\phi \approx 4 \times 10^{-4}$ [265], being on average $\phi = 9.7(\pm 4.5) \times 10^{-4}$.

Annealing the samples at high temperature has proven to decrease the mechanical loss of a-Si [265]. The 0.4 keV and 0.6 keV samples were annealed up to 450°C in a Carbolite Gero 30-3000°C RHF annealing furnace using the same temperature profile outlined in Section [5.3.2]. The coating loss across is shown in Figure [5.13] for the 0.4 keV and 0.6 keV samples at the annealing steps up to 450°C. This is the average coating loss across multiple eigenmodes with the error bars being the standard deviation of the losses. However between measuring the 0.6 keV sample as deposited and annealing to the first temperature step of 100 °C, the disk suffered a small chip in its edge (Figure [5.14b]). Subsequently any data measured for this sample after the 100°C annealing step has not been included in the presented graph due to inconsistent beam alignment during measurements.

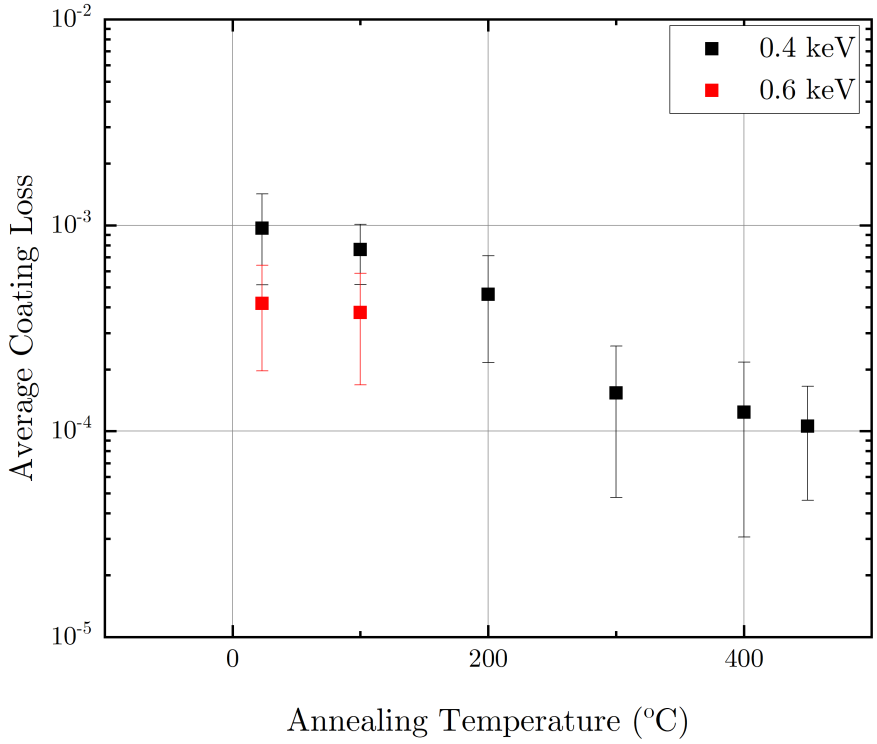

Figure 5.13: Coating loss of a-Si annealed up to 450°C using 0.4 keV and 0.6 keV beam energy 200 mA current during deposition. The 0.6 keV disk was chipped between as deposited measurements and annealing at 100°C. Error bars show the spread in measurements of each mode over three separate suspensions.

As the 0.4 keV coating has been annealed its average mechanical loss has reduced. The increase in error bar size of the 0.4 keV sample as the annealing temperature increases is thought to be due to partial delamination of the coating from the disk (see Figure [5.14a]). Even in this case the lowest loss attained for this coating was at 450°C where $\phi = 1.05 \times 10^{-4}$.

The 0.6 keV a-Si coating shows similar downward trend when annealed to that of the 0.4 keV a-Si. The lowest mechanical loss measured for this disk was $\phi = 3.77 \times 10^{-4}$ however the chip in the disk has resulted in large error bars.

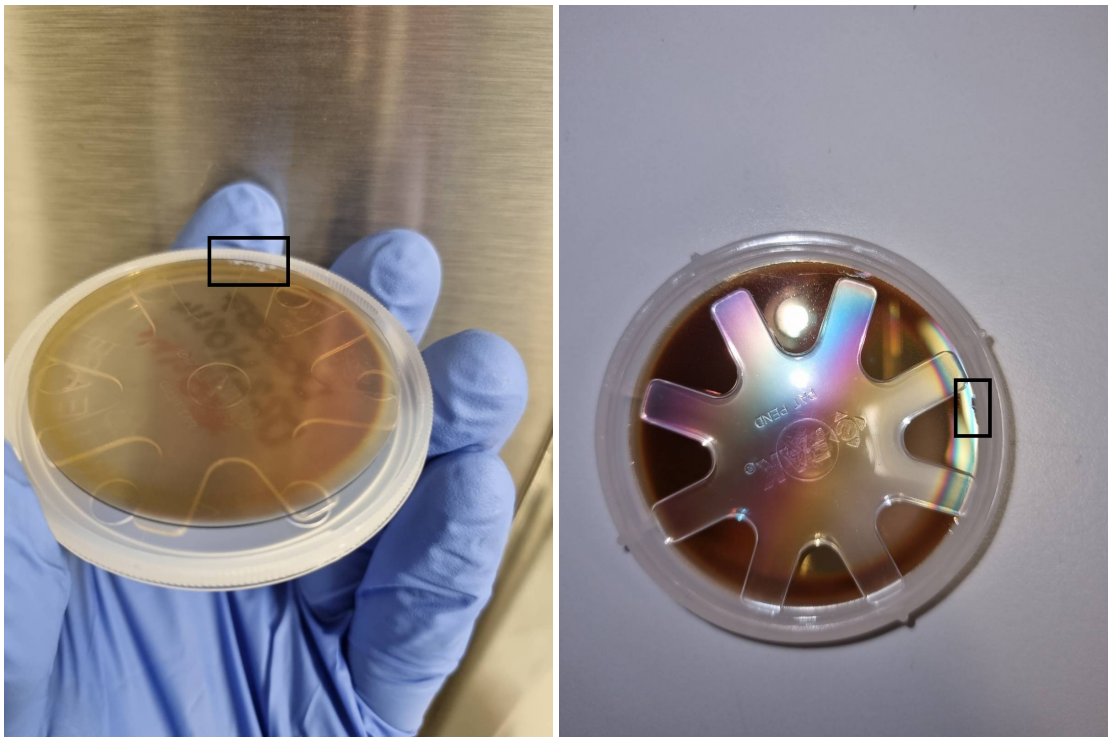

(a) Image of GeNS disk coated with a-Si, highlighting partial delamination and removal of coating at the disk's edge in black.

(b) Image of GeNS disk coated with a-Si, highlighting a small chip at the disk's edge in black.

Figure 5.14: Images of a-Si coated GeNS disks (50 mm diameter 0.5 mm thick Corning 7980 fused silica).

Thermal Noise modelling

Following on from the results in Section [5.3.4] the thermal noise implications of an a-Si coating design were investigated using a modified version of pyGWINC [29]. This Python code base has the capability to simulate noise sources associated with a GWD, including Brownian coating thermal noise (CTN), by inputting relevant material parameters (refractive index, Young's modulus, mechanical loss, *etc.*) into the code base and using the approach by Yam *et al.* [266] and Hong *et al.* [110]. The multilayer mirror design used here is comprises of a-Si and SiO_2 layers. Due to the high optical absorption of the films produced they would not likely be fully compatible by themselves as a GWD mirror coatings, however could be used as part of a multimaterial

(MM) stack design [136, 267]. This multimaterial design utilises lower absorption materials in the front layers of the stack to decrease the electric field intensity of the laser light before reaching the lower layers of the coating. This allows lower mechanical loss materials with higher absorption such as a-Si to be utilised without larger absorption effects causing reflectivity issues with the coating [268, 269]. In this case the "lower stack" shown in Tait *et al.* [24, 136] would be modified to include the a-Si coating properties at 0.4 keV annealed to 450°C as part of a full MM coating design with < 0.5 ppm transmission at 1550 nm. This consists of 5 bilayers of a-Si and SiO_2 with a thickness of $\lambda/4$ at 1550 nm with 5 bilayers of Ta_2O_5 and SiO_2 with a thickness of $\lambda/4$ at 1550 nm on top. This design is shown graphically in Figure [5.15] with the parameters used in Table [5.4]. The wavelength of 1550 nm was chosen for this design due to lower absorption levels a-Si, as the optical band edge of Si occurs at ≈ 1 μm [270].

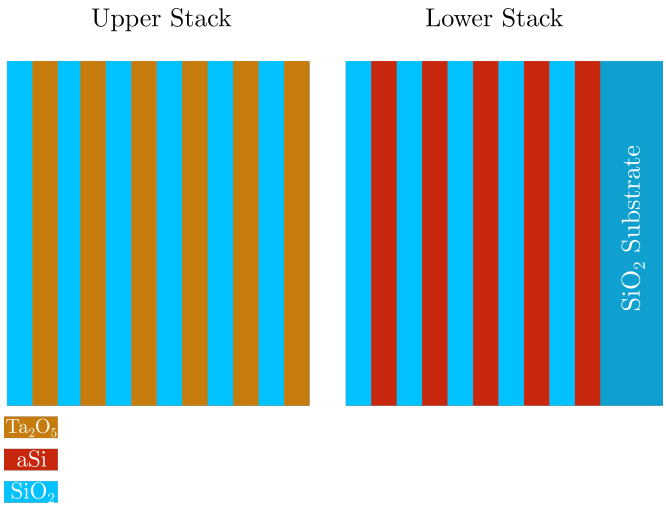

Figure 5.15: Schematic of the multimaterial coating: The full stack is composed of the upper stack (SiO_2 and Ta_2O_5) and the lower stack (a-Si and SiO_2). Each layer has an optical thickness = $\lambda/4$ [136].

Parameter	a-Si	SiO_2	Ta_2O_5
n (1064 nm/1550 nm)	N/A / 3.50	1.44 / 1.44	2.07 / 2.05
Young's Modulus (Y)	130 GPa	92.9 GPa	99.5 GPa
Poisson's ratio(σ)	0.28	0.17	0.23
Mechanical loss (ϕ)	1.06×10^{-4}	2.3×10^{-5}	3.6×10^{-4}

Table 5.4: Refractive index, Young's modulus, Poisson's ratio and mechanical loss of materials used for thermal noise modelling. Parameters for materials not studied in this research are taken from [24, 235, 262]

Results are shown in Figure [5.16] for modelled Brownian CTN for an ETM using a MM coating with a-Si from this work compared to both the MM design in [24] at 1550 nm and the current aLIGO coating at 1064 nm.

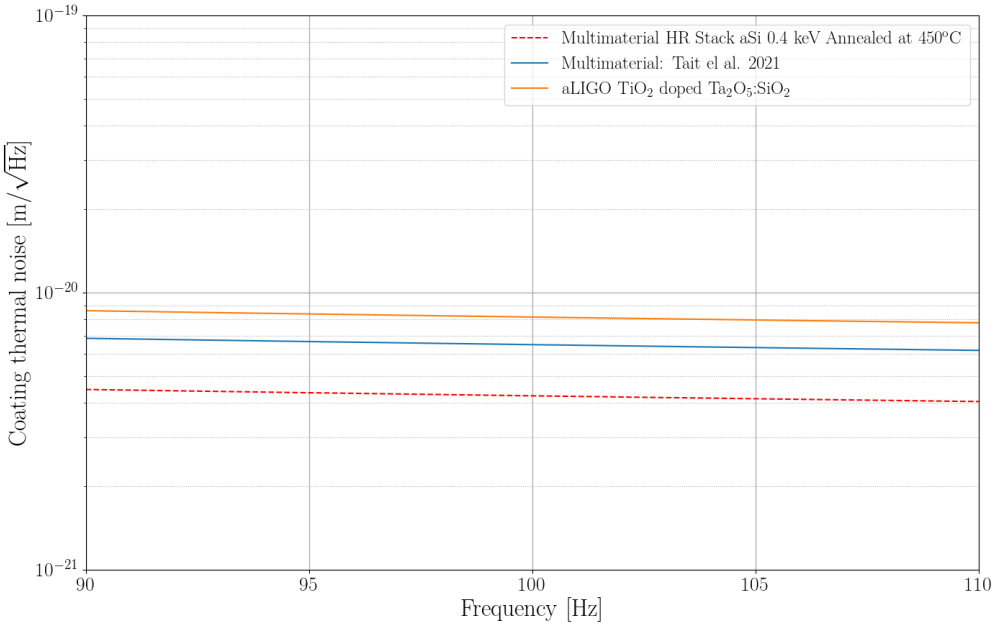

Figure 5.16: Coating thermal noise simulations of current aLIGO coating design at 1064 nm, multimaterial design as deposited from [24] and multimaterial design at 1550 nm using a-Si from RF IBSD system with a beam energy = 0.4 keV.

Figure [5.16] shows that both MM designs give a lower thermal noise contribution than the current aLIGO coatings. Using the 0.4 keV a-Si coatings in this design reduces the CTN to 4.24×10^{-21} m/$\sqrt{\text{Hz}}$ at 100 Hz. This is $\approx$ 35% lower compared to the

coating design in [24] (6.48×10^{-21} m/$\sqrt{\text{Hz}}$ at 100 Hz) and $\approx 49\%$ lower compared to that of the current aLIGO coating (8.16×10^{-21} m/$\sqrt{\text{Hz}}$ at 100 Hz) however this is calculated for an aLIGO ETM only.

5.3.5 Compositional Characterisation

EDS

Measurements of composition were conducted with EDS to analyse any potential heavy metal contaminants introduced during the process. As described in Section [4.4] measurements of the a-Si coatings depositions were conducted on Si witness samples. Each sample was measured compositionally 3 times across there surface at 15 kV of electron voltage in order to ensure penetration into the coating without visibly damaging the thin film. An average was calculated from the 3 measurements and error bars were taken as the standard uncertainty of these measurements. Typical relative uncertainty in EDS measurements are $< \pm 5\%$ [271]. Results are shown in Table [5.5] for heavy metal composition and in Table [5.6] for lighter elements (Atomic number ≤ 4).

Beam Energy	Beam Current	Silicon (%)	Aluminium (%)	Molybdenum (%)
0.4(±0.02) keV	200(±20) mA	89.81 ± 0.01	0.16 ± 0.01	0
0.6(±0.02) keV	200(±20) mA	90.43 ± 0.13	0.14 ± 0.01	0
0.7(±0.02) keV	200(±20) mA	90.23 ± 0.32	0.15 ± 0.02	0
0.8(±0.02) keV	200(±20) mA	90.68 ± 0.14	0.18 ± 0.01	0
1.0(±0.02) keV	200(±20) mA	88.69 ± 0.06	0.18 ± 0.02	0.64 ± 0.14
1.2(±0.02) keV	200(±20) mA	86.93 ± 0.23	0.25 ± 0.02	0.87 ± 0.13
0.6(±0.02) keV	100(±20) mA	91.10 ± 0.27	0.02 ± 0.03	0
0.6(±0.02) keV	200(±20) mA	91.40 ± 0.23	0.02 ± 0.03	0
0.6(±0.02) keV	300(±20) mA	90.58 ± 0.40	0.06 ± 0.04	0
0.6(±0.02) keV	400(±20) mA	91.02 ± 0.17	0.08 ± 0.02	0

Table 5.5: As deposited heavy element compositional results of a-Si coatings, determined by EDS analysis. Each percentage is determined by an average of 3 separate measurements of one sample. Errors are calculated as the standard uncertainty of the measurements.

Beam Energy	Beam Current	Carbon (%)	Oxygen (%)	Nitrogen (%)	Argon (%)
0.4 keV	200 mA	6.96 ± 0.16	2.09 ± 0.03	0	0.98 ± 0.01
0.6 keV	200 mA	7.33 ± 0.17	0.14 ± 0.01	0	2.09 ± 0.03
0.7 keV	200 mA	7.20 ± 0.19	0.93 ± 0.05	0	1.41 ± 0.05
0.8 keV	200 mA	7.00 ± 0.11	1.08 ± 0.09	0	1.05 ± 0.01
1.0 keV	200 mA	6.93 ± 0.19	0.81 ± 0.03	1.82 ± 0.10	0.91 ± 0.03
1.2 keV	200 mA	5.55 ± 0.23	3.46 ± 0.02	1.69 ± 0.06	1.19 ± 0.01
0.6 keV	100 mA	7.05 ± 0.18	1.56 ± 0.08	0	0.26 ± 0.01
0.6 keV	200 mA	7.19 ± 0.24	0.76 ± 0.13	0	0.62 ± 0.12
0.6 keV	300 mA	7.96 ± 0.83	0.91 ± 0.022	0	0.50 ± 0.35
0.6 keV	400 mA	7.41 ± 0.08	0.73 ± 0.07	0	0.76 ± 0.11

Table 5.6: As deposited light element (Atomic number ≤ 4) compositional results of a-Si coatings, determined by EDS analysis. Each percentage is determined by an average of 3 separate measurements of one sample. Errors are calculated as the standard uncertainty of the measurements.

The compositional data in Table [5.5] highlights a number of features associated with the films. The first is the higher Al content of the films (0.16 % - 0.25 %) with changing beam energy. This is thought to be associated with changing beam dimensions which can induce visible "clipping" of both the Si target backing plate, made of Al, and the target stage during the process. This will result in higher concentrations of material in the films.

The 0.6 keV 200 mA coatings show large variation in Al content when repeated. While possibly related to uncertainty during measurement, this could be a result of oxidation of the etched Al backing plate from multiple depositions creating a partial oxide layer which is harder to sputter than Al due to higher surface binding energy .

At deposition beam energies $\geq$ 1.0 keV incorporation of Mo is seen in the films. This is due to the high energy being sufficient to sputter grid material from the RF source, made from Mo. This is likely the reason for higher absorption coefficients (k) in these films. The Al content in these films does not seem to play a significant role in absorption characteristics, due to the low levels seen by EDS ($\ll 1\%$).

Regarding the lighter elements the role of O_2 in the films plays an important role in determining refractive index and absorption as can be seen from the 0.4 keV and 1.2 keV films with O concentration $> 2\%$. The 0.6 keV and 0.7 keV films have a higher Ar percentage ($\approx 2\%$) than the other films produced.

5.3.6 Structural Characterisation

XRD

The amorphous nature of the coatings at varied annealing temperatures were investigated through the use of a Bruker D8 Advance XRD system. Using both coupled theta and GIXRD measurements. Scans were taken between $25° - 60°$ in order to capture the strong Si crystalline peaks ($\langle 111 \rangle$ at 28°, $\langle 220 \rangle$ at 47° and $\langle 311 \rangle$ at 56° [272]). Figure [5.17] shows the scan results for a-Si at 0.4 keV beam energy as deposited and annealed to 400°C and 450°C. The as deposited sample scan was measured in coupled theta mode while the annealed scans were measured at 0.5° grazing incidence. This was in part to test the validity of the measurements taken, further details of which can be found in Appendix [A].

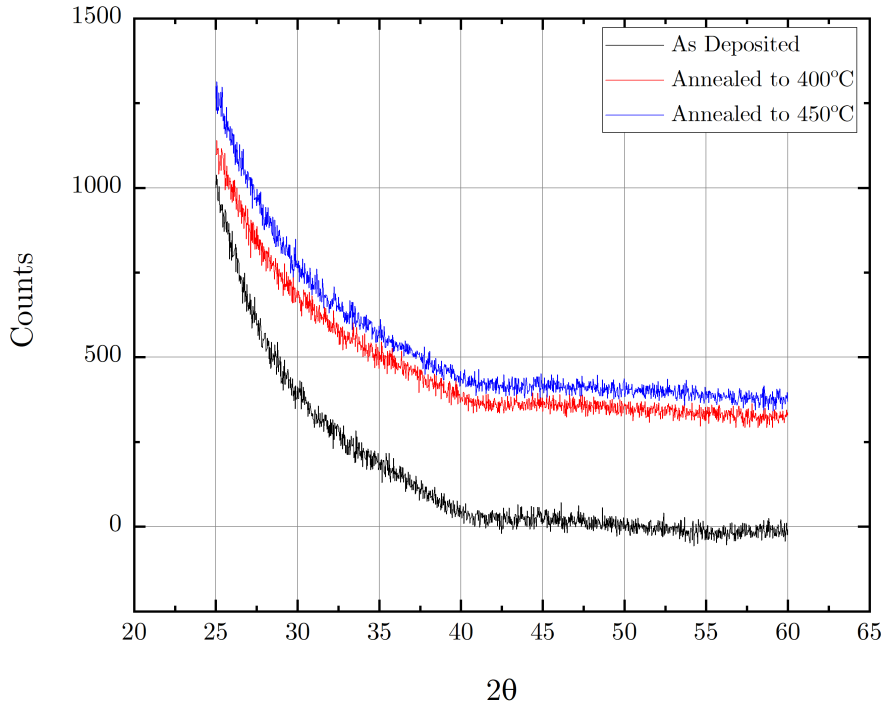

Figure 5.17: XRD scans for a-Si coating on SiO_2 at 0.4 keV beam energy and 200 mA beam current. Data is offset on y-axis to highlight each scan separately. As deposited scan were done in coupled 2θ configuration while annealed samples were measured at grazing incidence of 0.5°.

Figure [5.17] shows that annealing the a-Si sample up to 450°C does not induce a crystalline phase detectable by GIXRD. The trailing edge of the scan from 25° - 45° is a result of the JGS grade SiO_2 substrate. It can therefore be concluded that this sample is indeed amorphous. All other samples were scanned with the same method and showed similar results to this sample as none produced crystalline peaks at 450°C between 25° - 60°. Given the crystallisation temperature of a-Si is $\approx$ 550°C [273] these samples should be fully amorphous up to the last annealing step of 450°C unless deposited as a polycrystalline film, which is not the case.

5.4 Discussion

The results shown in Section [5.3] highlight a number of interesting phenomena that have occurred within the a-Si films. The reduction in film thickness at 1.0 keV and 1.2 keV in comparison to other films with varying beam energy is due to the higher percentage of N_2 contaminants in the deposition process. Non-stoichiometric silicon nitride (SiN_x) has a lower growth rate than Si, resulting in lower film thickness [274]. These results are not reflected in the simulations shown in Section [5.3.1] highlighting a limitation of the software to introduce contaminant gases into the process.

This is also reflected in the 0.4 keV a-Si films where large concentrations of O are present resulting in both a slightly lower film thickness in addition to a lower refractive index. This is due to both the lower energy of the beam leading to a reduced sputtering yield [275] and the more SiO_2 nature of the coating (n = 1.44 at 1550 nm) [276], which has a lower growth rate than pure Si [274]. Varying the beam energy will also change its size and shape, which can influence the film thickness, due to direction of beamlets which can effect the sputtering process [277]. Even in this case however the film index is greater than that of EBE, due to the IBSD process being able to attain higher film mass density [161].

O_2 incorporation into the films can be a result from excess water molecules introduced to the process through the ion source and neutraliser gas feeds [278]. This was minimised as much as possible with steel piping and leak checking however this plus

residual O_2 in the chamber has lead to contamination in particular depositions.

The lower absorption in the a-Si films with varying beam current in comparison to varying ion energy can be related to the structure of the a-Si films. Varying beam current will lead to more ion flux towards the target and therefore will directly correlate to an increase in film thickness, however deposition beam energy will also contribute significantly to the film structure of a-Si films [279]. It has been shown that a-Si grown with a lower deposition rate reduces the number of uncoordinated Si atoms in the film structure [253]. This correlates with the 100 mA a-Si sample which had the lowest measured absorption ($k = 1 \times 10^{-2}$) whilst also having the lowest deposition rate of all samples grown (0.01 nm/s).

The PCI results give a number of interesting observations regarding the optical behaviour of the a-Si films in an as deposited state and when annealed. As deposited results revealed that both 0.4 keV and 0.8 keV are preferential energies for lower absorption in a-Si coatings, independent of thickness. By analysing the composition of these films it is revealed that at these energies the coatings have higher O_2 content which has been known to reduce absorption in this material by increasing the band gap energy [280]. This contributes to the decrease in absorption at higher annealing temperatures where more O_2 is diffused into the a-Si matrix.

The 0.6 keV film absorption behaves much like the films produced in [255] at 450°C where it seems to flatten out. This is juxtapose by the 0.4 keV coating which increases in absorption at this temperature from 400°C. The differing characteristics between these two coatings is likely due to structural reorganisation leading to differing absorption effects however Raman spectroscopy or transmission electron microscopy (TEM) would be required to understand this further.

It has been shown that the absorption levels in a-Si coatings are related to the concentration of unpaired electrons or "dangling bonds" in the film [253, 256]. This is one of two key absorption mechanisms in a-Si, the other being interband transitions [261]. As the films are annealed, it has been shown that the concentration of these bonds decreases due to structural relaxation from short range diffusion [281], resulting in lower photon absorption.

The annealing process has also been known to reduce the number of two level systems (TLS) in the material associated with mechanical loss [282]. These are double well potential states which exist within the material, the product of which is high internal friction in the material, which will subsequently lead to a high Brownian thermal noise contribution. While the reduction of these states can be achieved by hydrogenating the a-Si [135], current research also points to high deposition or post deposition annealing temperatures reducing these states [253, 283]. This is shown in the 0.4 keV a-Si sample where the loss was reduced from $(9.7 \pm 4.5) \times 10^{-4}$ to $(1.05 \pm 0.59) \times 10^{-4}$ by high temperature annealing. Optimised deposition parameters contribute to the reduction of these states [135] which can be seen by the difference in mechanical loss between films grown at 0.4 keV and 0.6 keV.

In the case of the research conducted here no annealing steps were undertaken at temperatures higher than 450°C both due to previous published results from IBSD a-Si [255] and the mechanical loss samples forming larger defects (coating delamination and substrate cracking) as the temperature increased. Without being able to correlate both the optical and mechanical properties of the films at all temperature steps to the composition and structure a full understanding of the films cannot be gained.

5.5 Conclusions and Future Work

Thin film a-Si coatings were created with IBSD using varying ion beam energy and current in order to optimise the process. What has been shown is there is indeed an optimised set of deposition parameters for this material in the RF IBSD system used.

Optically, the best results are for 0.6 keV of beam energy and 200 mA of beam current, giving a high n value of 3.76 after being annealed to 450°C while maintaining a low k value of 7.32×10^{-3} with PCI absorption of $7.8(\pm 0.4) \times 10^3$ ppm at 1550 nm. Unfortunately due to experimental issues the 0.6 keV mechanical loss sample was unable to be resolved at an annealing temperature of 450°C but given both the loss trend and results at 0.4 keV it could be inferred the coating loss will be $\phi < (1.1 \pm 0.6) \times 10^{-4}$. Using the a-Si measured here as part of a multimaterial HR coating design for a GWD gives a CTN contribution at 100 Hz of 4.24×10^{-21} m/$\sqrt{\text{Hz}}$, $\approx 38\%$ lower than the

current aLIGO coatings.

Future work into this subject matter would include the repeated deposition and measurement of mechanical loss with 0.6 keV films at higher annealing temperatures post deposition to fully assess the impact to coating thermal noise of a GWD. Additional structural measurements such as Raman spectroscopy or TEM could bring further understanding to structural changes in the a-Si at different annealing temperatures. Using hydrogen in the process would reduce the number of silicon dangling bonds in the final coatings, known to create higher levels of absorption in the material.

Finally conducting a separate study to optimise the parameters used in the deposition process using a higher energy IBSD source such as ECR could prove useful in determining both the optimum process variables for deposition but also the correct IBSD process necessary to maintain low optical and mechanical loss while maintaining a high refractive index.

This will be key to develop coatings with low optical and mechanical loss a-Si for future GWD projects, especially those projects which choose to operate at a longer laser wavelength than the current $\lambda_{\mathrm{aLIGO}} = 1064$ nm.

Chapter 6

Characterisation of non-stoichiometric silicon nitride coatings with varying IBSD process parameters

6.1 Introduction

In addition to amorphous silicon being shown as a promising high index layer material for next generation GWDs, silicon nitride (Si_3N_4) has also been proposed and studied as another candidate. This material has also been proven to give excellent optical performance and coating adhesion in applications including anti-reflection coatings for solar cells [284] and biomedical implants [285] respectively. Si_3N_4 boasts a refractive index ≈ 2, giving a suitable index contrast for a GWD HR mirror stack with a low index material such as SiO_2 at both 1064 nm and 1550 nm. Non-stoichiometric silicon nitride (SiN_x) has been shown to exhibit low absorption at 1064 nm and 1550 nm and provide an increase in refractive index [73, 286]. Recent studies have also shown this material has a low mechanical loss [73, 123, 262], a property thought to be associated with its atomic coordination and extremely high temperature annealing capabilities (up to 900°C [73]).

The research in this chapter explores the relationship between the process parameters of ion beam deposition and the optical and mechanical properties of SiN_x. Furthermore the atomic composition is measured in order to identify lighter elements in the material as annealing temperature increases. The method of delivery for the reactive gas, including gas pressure, is investigated.

6.2 Deposition Parameters

Using similar methodology to Chapter 5 process parameters of the deposition, in particular the ion beam voltage and current, were adjusted to assess the role this has on film properties. However, the reactive gas pressure (in this case N_2) was adjusted to assess which parameters gave improved optical and mechanical properties. The deposition parameters used are shown in Table [6.1] alongside partial pressure of N_2 used and coating thickness. The thickness was calculated from fitting spectrophotometry interference fringes in SCOUT (more details are given in Section 6.3.2) for two separate samples. Errors shown for the beam energy and current are represented as ±1% of the full power supply range [164]. Errors for the partial pressure of gas is taken from the pressure gauge reading error. Errors in coating thickness are calculated as the standard uncertainty of thickness fittings.

Ion Beam Energy	Ion Beam Current	Partial pressure of N_2	Coating thickness
0.6(±0.02) keV	200(±20) mA	60(±5)%	258.63(±16.6) nm
0.6(±0.02) keV	200(±20) mA	70(±5)%	553.77(±30.47) nm
0.6(±0.02) keV	200(±20) mA	80(±5)%	422.40(±25.59) nm
0.4(±0.02) keV	200(±20) mA	80(±5)%	177.72(±21.9) nm
0.6(±0.02) keV	200(±20) mA	80(±5)%	193.29(±12.21) nm
0.7(±0.02) keV	200(±20) mA	80(±5)%	134.15(±13.61) nm
0.8(±0.02) keV	200(±20) mA	80(±5)%	124.25(±17.08) nm
1.0(±0.02) keV	200(±20) mA	80(±5)%	157.15(±18.84) nm
1.2(±0.02) keV	200(±20) mA	80(±5)%	157.21(±11.48) nm
0.6(±0.02) keV	100(±20) mA	80(±5)%	95.37(±18.93) nm
0.6(±0.02) keV	300(±20) mA	80(±5)%	313.52(±19.24) nm

Table 6.1: Deposition parameters for silicon nitride coatings. Shown is the run number, beam energy, current and partial pressure of N_2 used through the ion source.

Each deposition process shown in Table [6.1] contained two substrates of both JGS

grade fused silica and two high purity (99.999%) crystalline silicon ($\langle 100 \rangle$ orientation) substrates for characterisation as shown in Chapter 4. Additional 75 mm diameter 1 mm thick Corning 7980 fused silica substrates were included for mechanical loss studies which were conducted at the California Institute of Technology. As discussed in Chapter 5, all substrates were cleaned in an ultrasonic bath, firstly using acetone and then iso-propyl alcohol (IPA). The samples were then dried with nitrogen gas and, if appropriate, wiped with high grade clean room optic wipes. This minimised contaminates which could interfere with the coating process and potentially lead to coating adhesion issues. Substrates were then mounted in custom holders (see Section [3.6]) which were again mounted to a rotational stage, rotating at 3.1 rpm to ensure good uniformity across the substrate face. The typical deposition temperature was around 40°C.

6.3 Results

6.3.1 Deposition Simulation

To understand the sputtering of SiN_x further and extract sputtering yield and relevant ion energies simulations of the process were conducted in SDTrimSP with a similar approach to that detailed in Chapter 5. The difference with in the simulations is associated with using N_2 as an active gas species in the sputtering process. Using N_2 as 80% of the gas mixture and varying beam energies between 0.4 keV and 1.2 keV and $\alpha = 60°$, results shown in Table [6.2] were obtained. As detailed in Chapter 5 the Kr-C interaction potential [257] was used with a Lindhard-Schaff inelastic loss model [258]. While the simulated energy output from SDTrimSP is angle dependant, the values shown are the average across the entire distribution, accounting for 80($\pm$10)% of ions and particles. Errors are shown for results as the standard uncertainty in data produced by 3 separate simulations.

Beam Energy	Sputtering Yield	Sputtered SiN_x Energy	Backscattered Ar/N Energy
0.4 keV	1.4(±0.2) atoms/ion	27.0(±0.4) eV	98.0(±0.3)/155.7(±0.3) eV
0.6 keV	1.8(±0.2) atoms/ion	31.7(±0.5) eV	133.3(±0.4)/225.9(±0.5) eV
0.7 keV	1.9(±0.4) atoms/ion	33.9(±0.2) eV	156.9(±0.6)/258.9(±0.4) eV
0.8 keV	2.0(±0.2) atoms/ion	35.9(±0.4) eV	174.5(±0.5)/294.8(±0.2) eV
1.0 keV	2.2(±0.4) atoms/ion	39.5(±0.7) eV	213.5(±0.7)/364.0(±0.5) eV
1.2 keV	2.3(±0.6) atoms/ion	43.1(±0.8) eV	246.4(±0.3)/434.0(±0.7) eV

Table 6.2: Simulated sputtered Si yield, average sputtered Si particle energy and average backscattered Ar and N ion energy for varying ion beam energy of Ar on Si using SDTrimSP.

Tab [6.2] highlights some features of the SiN_x deposition process which differ from the sputtering of a-Si using Ar. The first is the sputtering yield being lower for the SiN_x deposition which is consistent given the introduction of a second ion species with less mass that Ar (N = 14.00 amu, Ar = 39.95 [287]) and the removal of Ar ion percentage in the process.

The second interesting observation from the simulations is the energy of backscattered N ions. In all cases the energy of the backscattered N ion is at least 58% greater than that of the Ar ions. This could lead to more reactive processes occurring after the target where the reactive N ions can fully disassociate additional molecules, like residual O_2 (diatomic bond energy = 6.33 eV [288]). The energetic ions could also bombard the substrate leading to interstitial sites of N forming within the coating. Much like in Chapter 5 careful consideration of deposition parameters including target angle α is necessary to both maximise sputtering yield whilst also reducing backscattered bombardment of substrates.

6.3.2 Optical Characterisation

Spectrophotometry: Gas Partial Pressure

In order to deposit SiN_x thin films, nitrogen (N_2) has to be introduced as a reactive gas. A vital step in optimising the coating process is understanding how the partial pressure of this gas introduced into the deposition effects the optical properties of the films. The optimum partial pressure of reactive gas was first investigated by mixing 60%, 70% and 80% of N_2 with Ar in the RF ion source to analyse the effects this has

on refractive index (n) and extinction coefficient (k) values. These values were fitted from spectrophotometry measurements of three coated JGS grade fused silica samples per deposition. The scans were carried out on a Photon RT spectrophotometer using SCOUT optical software (see Chapter 5 for more details). The terms used in the fitting process were an OJL model with a constant refractive index term and UV oscillator to account for absorption effects in the fused SiO_2. A thickness averaging term was used for the coating to account for any scatter or inhomogeneity [201]. More details about these terms can be found in Chapter 4. While an oxidation layer on these films is likely the methodology used from studies of SiN_x using similar measurement equipment does not consider this [123]. This is therefore thought to be of negligible thickness for analysis. In addition as the fits produced have matched closely to the R and T spectra, surface roughness is thought to not be at a level which would highly impact these results. All deposition runs had both the same ion source beam parameters (600 keV beam energy, 200 mA beam current) and total gas pressure with the only variation being the percentage of N_2 used. Results of the fits can be seen in Figure [6.1]. Error bars for n and k are calculated from the standard uncertainty of separate measurements of 3 witnesses. Errors for the partial pressure of gas is taken from the pressure gauge reading error.

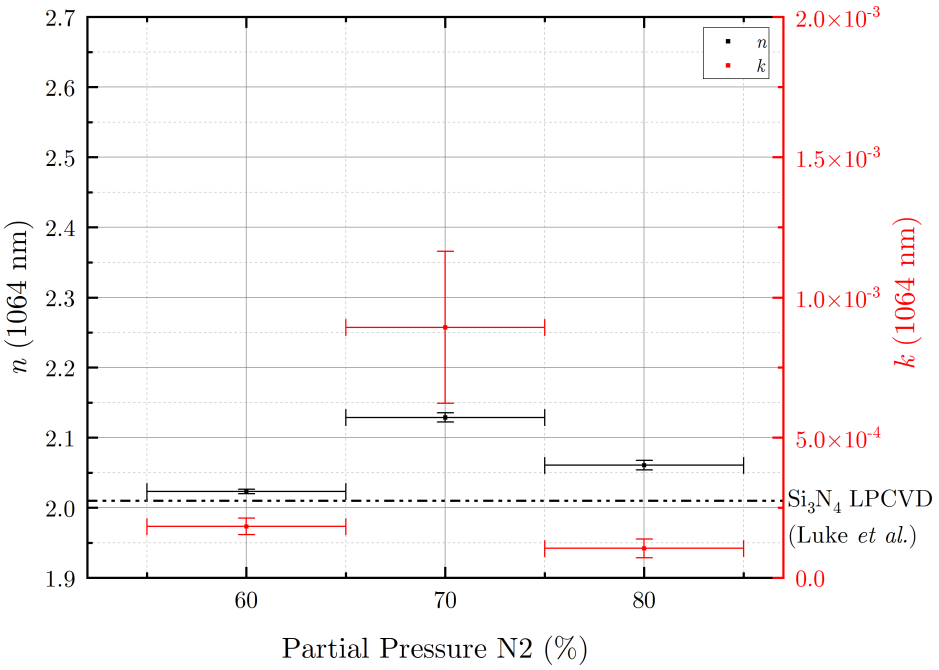

Figure 6.1: Summary of refractive indices and extinction coefficients for SiN_x coatings with variation of gas partial pressure in chamber. Also shown is a reference value of refractive index for Si_3N_4 taken from [289]. Error bars are calculated from the standard uncertainty calculated for three separate silica witness samples.

As shown in Figure [6.1], in order to achieve a refractive index close to Si_3N_4, while minimising the absorption, 80% partial pressure of N_2 should be used in this particular process. While the k values calculated for 60% and 80% are below the resolution limit of the spectrophotometer ($k = 2.0 \times 10^{-4}$), there is still a large indication that at 80% PP of N_2 the absorption is lower than 60%. The high levels of absorption at 70% can be attributed to the increasingly silicon-like nature of the coating ($n = 2.13$). Without optimisation of beam parameters, it is likely that the coating atomic structure could be highly uncoordinated and therefore highly absorbing in comparison to 60% and 80% [290].

In addition to the composition, the method in which the reactive gas is delivered to the process chamber can also play an important role in affecting the thin film properties. Using a circular pipe surrounding the ion beam, or "showerhead", a comparative

experiment was conducted between delivering reactive N_2 as backfill gas through the showerhead or feeding this gas directly through the ion source. The reactive index and extinction coefficient were used to measure which method is more effective at creating SiN_x coatings with a refractive index close to Si_3N_4 while maintaining low absorption. The results of this experiment is shown in Figure [6.2]

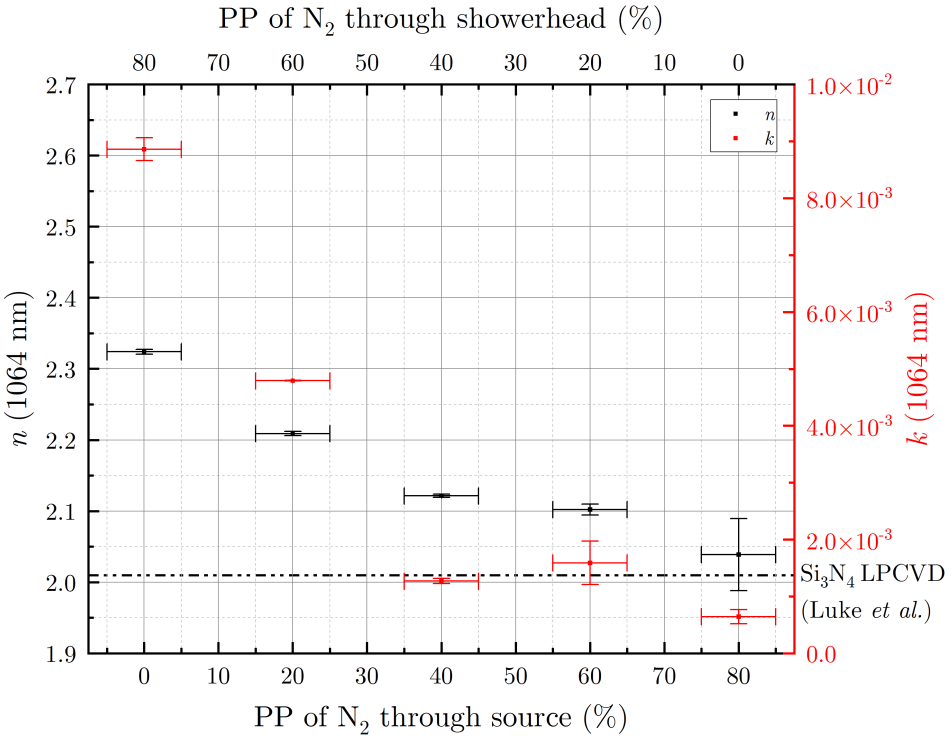

Figure 6.2: Summary of refractive indices and extinction coefficients for SiN_x coatings with variation of gas percentage through source and showerhead configuration at 80% partial pressure. Also shown is a reference value of refractive index for Si_3N_4 taken from [289]. Error bars are calculated from the standard uncertainty calculated for three separate silica witness samples.

The data in Figure [6.2] shows that by increasing the concentration of N_2 through the ion source, the refractive index is closer to that of Si_3N_4 ($n = 2.04$) in addition to attaining a lower extinction coefficient ($k = 6.43 \times 10^{-4}$). The reasoning behind the showerhead being less effective in generating coatings with suitable refractive index partially lies in the energy required to break the diatomic bond in N_2. As the bond

energy is 9.7 eV for N_2 [291], a large amount of energy is needed to break this and create reactive atomic nitrogen. Using the showerhead to backfill the chamber with gas relies on the energy of Ar ions from the source being sufficient enough to both break the N_2 molecule efficiently and scatter towards the Si target. This would seem plausible however from the results presented here it is not practically feasible. By discharging the N_2 within the quartz chamber of the ion source as part of the gas feed mixture, the atomic nitrogen created has sufficient kinetic energy to react on the Si target creating SiN_x.

Spectrophotometry: Beam Energy and Current

Using the same approach as in 5 to fit, and characterise, the refractive index, extinction coefficient and thickness of the SiN_x thin films (nkd) for varying beam energy and current, measurements were taken of optical transmission (T) and reflection (R) using spectrophotometry. The films were measured between 185 nm - 2000 nm using a Photon RT UV-Vis-IR spectrometer. Further details of this equipment are given in Chapter [4]. The transmission spectra from varying the beam energy and beam current are shown in Figure [6.3].

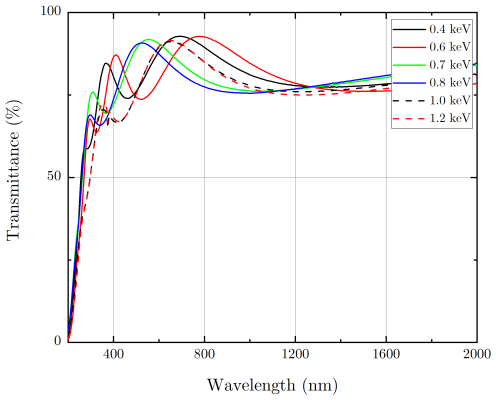

(a) Transmission curves of SiN_x coatings varying ion beam energy on JGS1 and JGS3 grade SiO_2 disks.

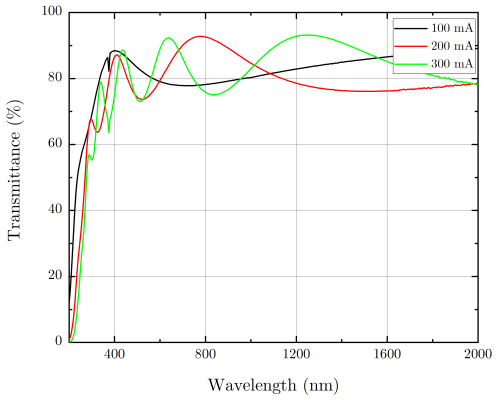

(b) Transmission curves of SiN_x coatings varying ion beam current on JGS1 and JGS3 grade SiO_2 disks.

Figure 6.3: Summary of optical transmission spectra for SiN_x coatings with varying ion beam parameters.

From the results shown in Figure [6.3a] it is clear that varying the beam energy of the ion source influences both the thickness and band edge of the coatings fabricated. The band gap of Si_3N_4 has been reported as high as 5.3 eV [292], making it difficult to ascertain band gap properties visually from all the transmittance spectra. It can be seen however that the 1.0 keV and 1.2 keV depositions have a lower band gap than the other grouping due to the extended transmittance tail into the UV region of measurement. This is a good indication that these samples may have higher absorption characteristics than the other coatings from this study.

Another observation is the differing thickness between coating runs. Although show in Table 6.1 this is shown by the increase of interference fringes present in the transmittance spectra. This is more apparent in Figure [6.3b] where the differing beam current have resulted in a drastic change in film thickness. It should be noted that the dip in reflectance of the 100 mA spectra is an experimental error resulting from a diffraction grating in the spectrophotometer [192].

By fitting the transmittance data, the refractive index of the coatings could be calculated using SCOUT software. The terms used in the fittings were previously discussed in Section 6.3.2, with further details in Chapter 4. The indices from coatings with varying ion source beam energy and current are presented in Figure [6.4] and Figure [6.5].

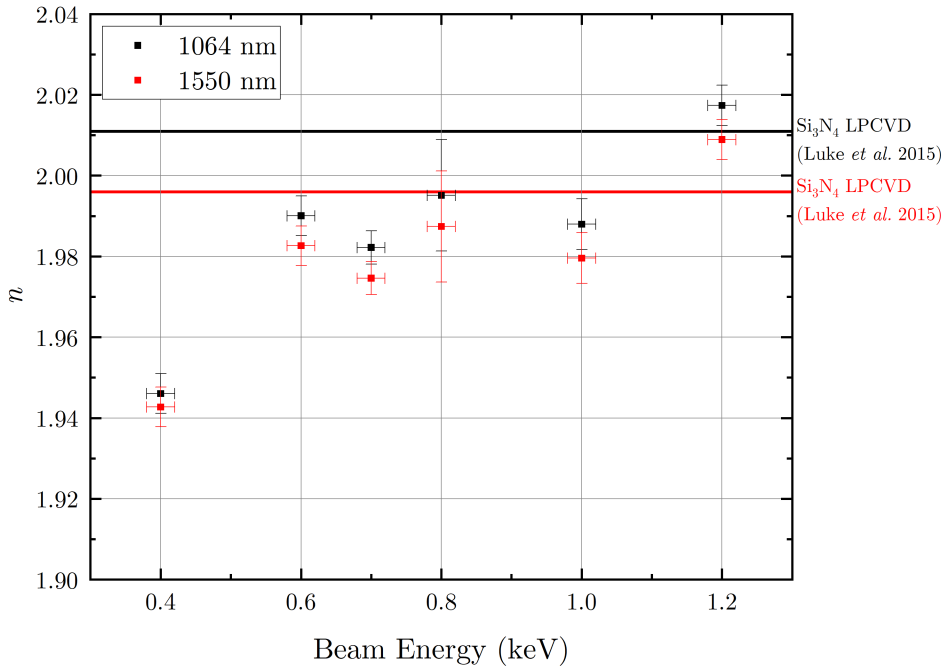

Figure 6.4: Refractive indices at 1064 nm (black) and 1550 nm (red) for SiN_x films with varying beam energy (0.4 keV - 1.2 keV) on JGS1 and JGS3 grade SiO_2 glass. Also marked are reference refractive indices for LPCVD Si_3N_4 [289]. Error bars are calculated from the standard uncertainty calculated for two separate silica witness samples.

The results in Figure [6.4] show there is an increase in refractive index of the films as the ion energy is increased. The highest refractive index attained was at 1.2 keV where $n = 2.017$ at 1064 nm. Regarding beam energy, this is the closest index to Si_3N_4 achieved. The "dips" in the upward trending refractive index are highly correlated with the O_2 and N_2 content of the films, associated with residual O-H in the deposition chamber and possible leaks from the source gas lines, as shown in Section 6.3.4.

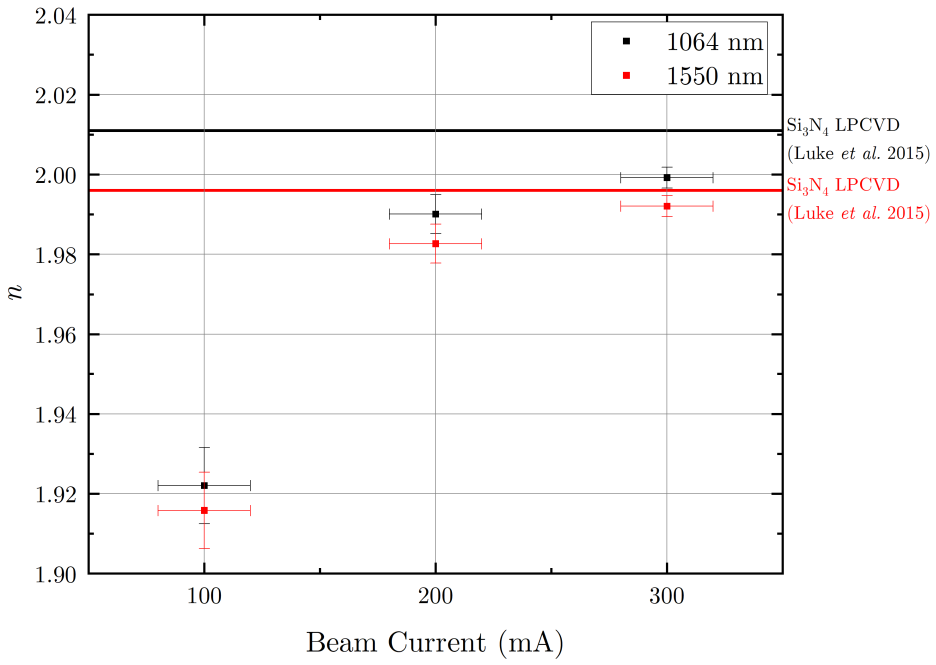

Figure 6.5: Refractive indices at 1064 nm (black) and 1550 nm (red) for SiN_x films with varying beam current (100 mA - 300 mA) on JGS1 and JGS3 grade SiO_2 glass. Also marked are reference refractive indices for LPCVD Si_3N_4 [289]. Error bars are calculated from the standard uncertainty calculated for two separate silica witness samples.

The data shown in Figure [6.5] highlights a logarithmic increase in refractive index as the beam energy increases. The index which is closer to Si_3N_4 was 1.99 at 1064 nm using 300 mA beam current. This current suggests the higher ion flux will lead to a logarithmic increase of the film index. Additional insight into the increase of the film index is giving from the stoichiometry in Section 6.3.4.

Also calculated from the SCOUT fittings of spectrophotometry data is the extinction coefficient (k). The results of this parameter fitting is shown in Figure [6.6] and Figure [6.7].

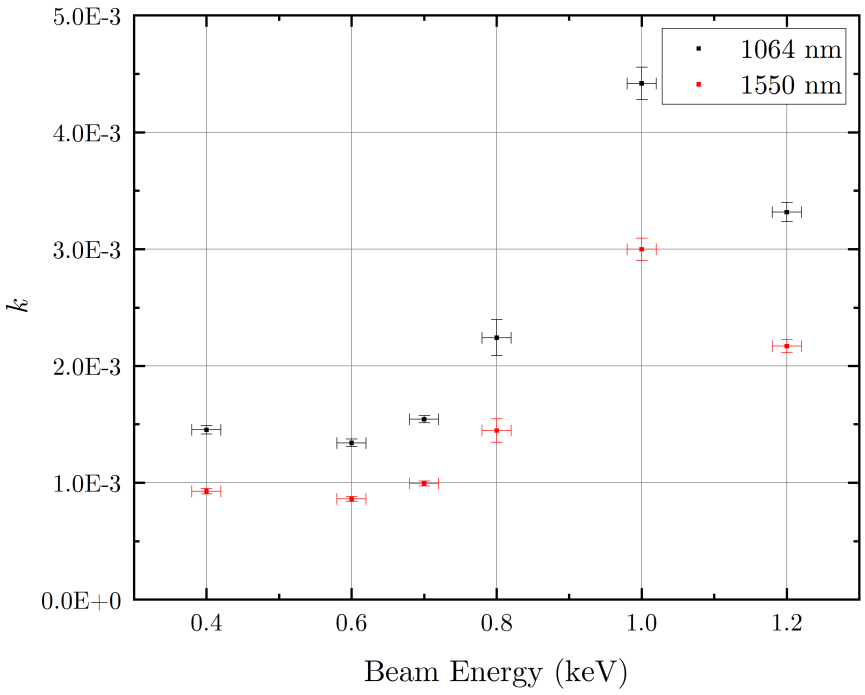

Figure 6.6: Extinction coefficients at 1064 nm (black) and 1550 nm (red) for SiN_x films with varying beam energy (0.4 keV - 1.2 keV) on JGS1 and JGS3 grade SiO_2 glass. Error bars are calculated from the standard uncertainty calculated for two separate silica witness samples.

Figure [6.6] shows how both the value of k increases and the dispersion in the indices between 1064 nm and 1550 nm increases between 0.4 keV - 1.0 keV. The highest value for the extinction coefficients are exhibited in the 1.0 keV beam energy coatings where $k = 4.4 \times 10^{-3}$ and 3×10^{-3} at 1064 nm and 1550 nm respectively. The lowest levels of k are observed in SiN_x deposited with 0.6 keV beam energy where $k = 1.3 \times 10^{-3}$ and 8.6×10^{-4} at 1064 nm and 1550 nm respectively. The exponential increase between 0.6 keV - 1.0 keV highlights a correlation between changing lighter element composition ($Z < 4$) and extinction coefficient. These results are shown in Section 6.3.4.

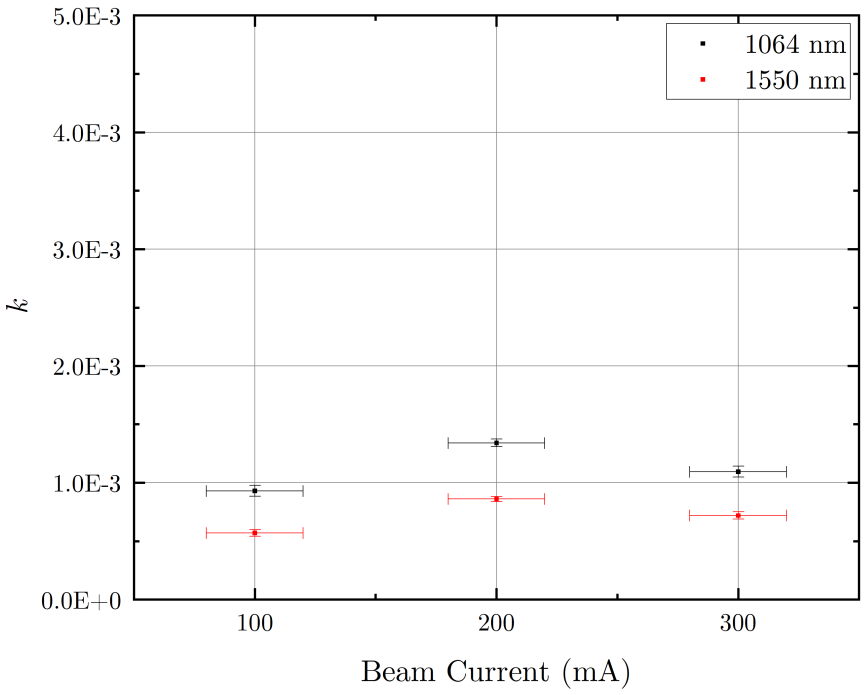

Figure 6.7: Extinction coefficients at 1064 nm (black) and 1550 nm (red) for SiN_x films with varying beam current (100 mA - 300 mA) on JGS1 and JGS3 grade SiO_2 glass. Error bars are calculated from the standard uncertainty calculated for two separate silica witness samples.

Results shown in Figure [6.7] show an increase in the extinction coefficient when using a higher beam current during SiN_x deposition. The highest value of which is at 200 mA, where $k = 1.3 \times 10^{-3}$ and 8.6×10^{-4} at 1064 nm and 1550 nm respectively. This coating also exhibits higher dispersion properties in comparison to coatings at 100 mA and 300 mA due to the slightly larger separation between k values at 1064 nm and 1550 nm. The low extinction coefficient at 300 mA ($k = 1.1 \times 10^{-3}$ and 7.2×10^{-4} at 1064 nm and 1550 nm respectively) is an interesting result given the higher thickness of the coating (313.52 nm) in comparison to the coating at 100 mA (95.37 nm), therefore these coatings are further studied using PCI.

Annealing SiN_x has been shown to improve the optical performance of SiN_x thin films [262, 293]. The coatings were annealed in steps from 500°C - 900°C in a Carbolite

Gero 30-3000°C RHF annealing furnace (in air at 1 bar of pressure). Each annealing run consisted of a 5°C/min ramp in temperature to a set point which the samples were held at for 1 hour before passively cooling (at ≈ 0.9°C/min) to 25°C. The upper limit of 900°C was imposed due it being close to the crystallisation temperature of IBSD SiO_2 coating (T_c = 1000°C [262]) which would be used in a GWD HR coating design as the low index material. The annealed coatings refractive index results are shown in Figure [6.8] and Figure [6.9].

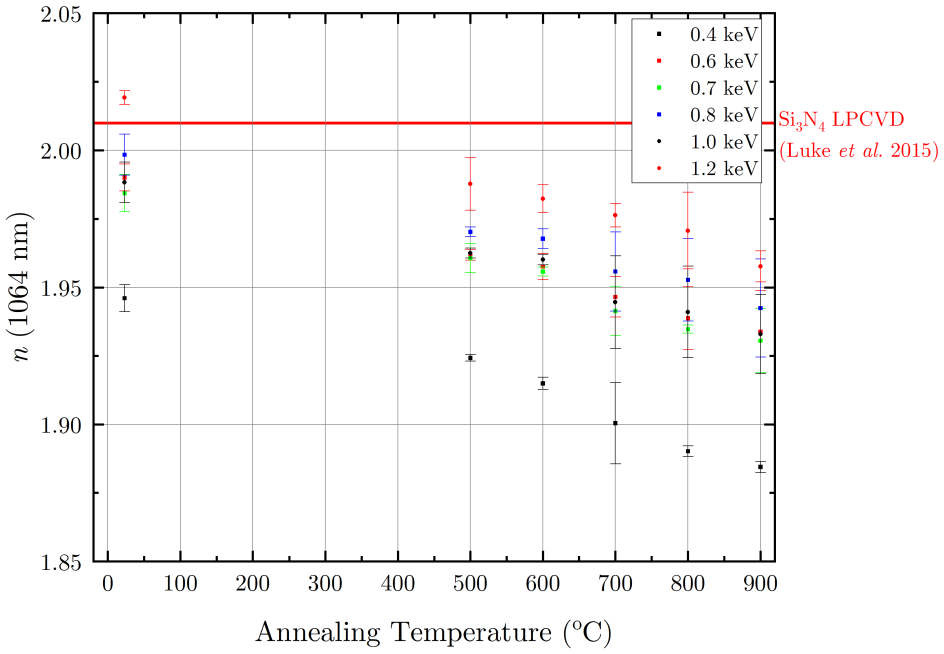

Figure 6.8: Refractive indices at 1064 nm (black) for SiN_x films with varying beam energy (0.4 keV - 1.2 keV) annealed in steps between 500°C - 900°C on JGS1 and JGS3 grade SiO_2 glass. Also marked is a reference refractive index for LPCVD Si_3N_4 [289]. Error bars are calculated from the standard uncertainty calculated for two separate silica witness samples per deposition.

The results in Figure [6.8] show a decreasing trend in refractive index when annealed in steps to 900°C. The lowest index shown is for the SiN_x coating deposited at 0.4 keV where n = 1.88 at 900°C annealing temperature. This would not be compatible with a GWD HR stack composed of this particular SiN_x and SiO_2 as they would not have a sufficient index contrast to lower transmission and achieve a reflectivity of 99.999

%. The highest index shown when annealed is that of the SiN_x coating deposited at 1.2 keV, where $n = 1.95$ at 900°C annealing temperature. This could work as part of a SiN_x:SiO_2 GWD HR stack however more layers would be required than the current Ti doped Ta_2O_5:SiO_2 stack, which could incur a greater coating thermal noise contribution, depending on the mechanical loss of the SiN_x layers.

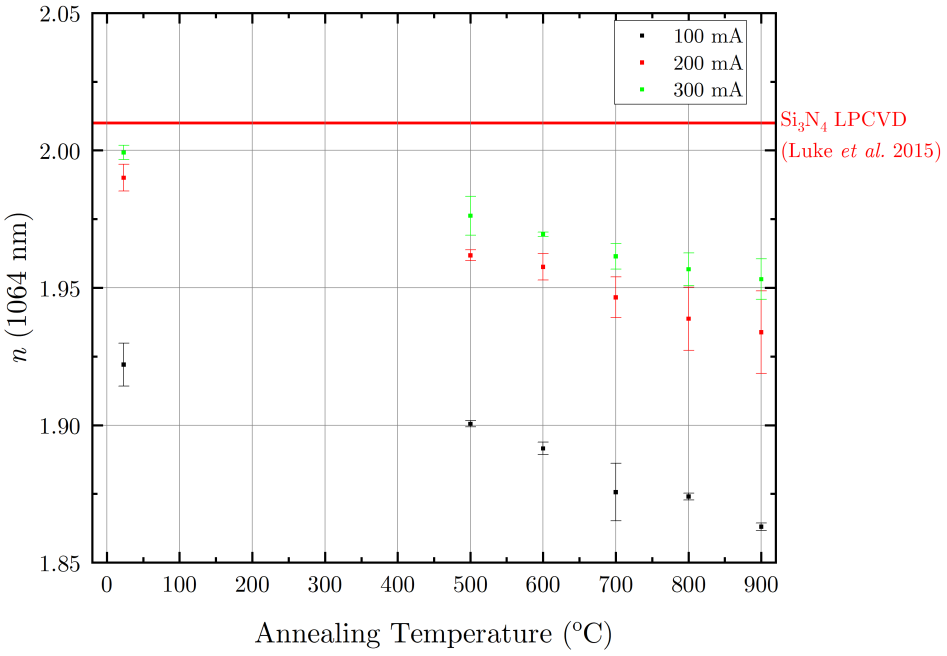

Figure 6.9: Refractive indices at 1064 nm (black) for SiN_x films with varying beam current (100 mA - 300 mA) annealed in steps between 500°C - 900°C on JGS1 and JGS3 grade SiO_2 glass. Also marked is a reference refractive index for LPCVD Si_3N_4 [289]. Error bars are calculated from the standard uncertainty calculated for two separate silica witness samples per deposition.

Figure [6.9] highlights a similar trend to [6.8], where coating refractive index decreases with increasing annealing temperature. The indices of some films at 900°C are compatible with a GWD HR stack centered at 1064 nm such as the 200 mA and 300 mA beam current depositions ($n = 1.93$ and 1.95 respectively). However, as mentioned previously, at 100 mA beam current the index is sufficiently low ($n = 1.86$) that to incorporate this material into a GWD coating design would require a high number of coating layers and could increase the coating thermal noise contribution depending on

mechanical properties of the film. It is clear that increasing the ion flux towards the Si target has improved both the refractive index as deposited and when the coatings are annealed.

The annealed values of k for these films have not been included in the discussion here due to both experimental issues while measuring the transmittance spectra (partial covering of aperture and diffraction grating issues) and the low absorption characteristics of the films when annealed. While this has not effected the n values extracted from these fits the k values have a far greater uncertainty than the measured value. The absorption values of the coatings with the best optical and mechanical performance have been measured by PCI and are included in Section 6.3.2.

PCI

To more precisely assess the optical absorption characteristics of the SiN_x samples, PCI measurements were conducted. Scans across the coating surface are taken with two interfering laser beams. This technique can accurately asses the optical absorption at 1064nm and 1550nm by comparing the change in the phase of the transmitted light through an induced thermal lens. More details of this measurement system are given in Chapter 4. Scans were taken at ≈ 2 mm intervals across the surface of the samples using a 1064 nm laser on coated Corning 7979 silica substrates. By taking the maximum optical absorption amplitude from the scans at a phase angle of -50^o the absorption of the film can be calculated. Samples that were measured had either low absorption characteristics measured by spectrophotometry (see Section 6.3.2) or low mechanical loss properties measured by GeNS (See Section 6.3.3). The samples were annealed after measurement in steps up to 900^{o}C for 1 hour using the same methodology as described in Section 6.3.2. Results of these scans are shown in Figure [6.10].

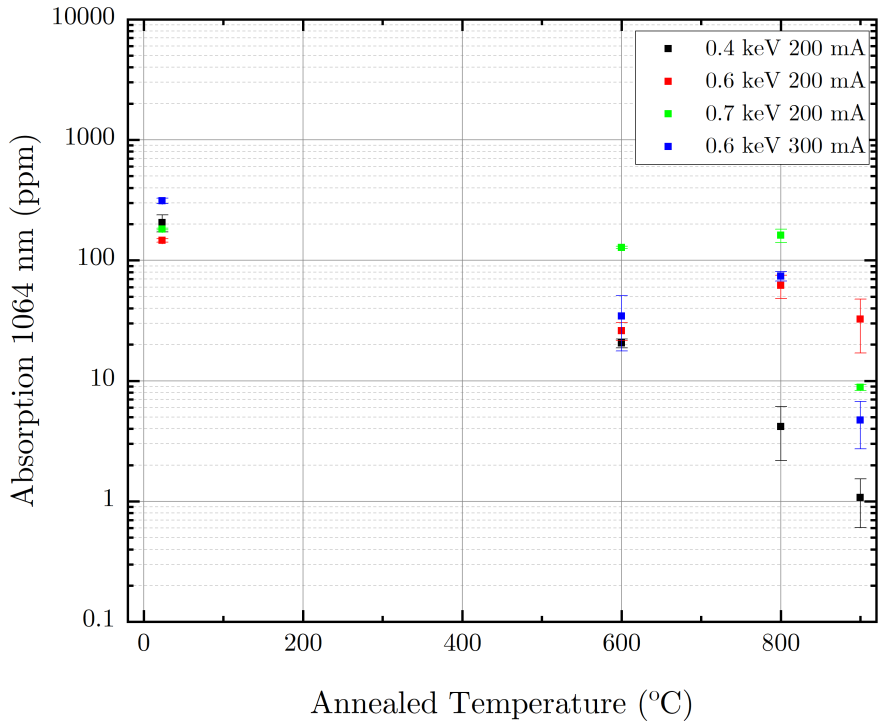

Figure 6.10: PCI measurements at 1064 nm for SiNx films on Corning 7979 grade fused silica substrates, annealed in steps to 900°C. Error bars are shown as the standard uncertainty of three separate measurements of the samples.

Figure [6.10] highlights a number of interesting features of these annealed SiN_x coatings. The first is that the as deposited trend of absorption levels for the 0.4 keV - 0.7 keV coatings matches the calculated k values from Section 6.3.2. The second is the decreasing trend in absorption at increased annealing temperature where the lowest value achieved is using 0.4 keV ion beam energy (annealed to 900°C) to give an absorption at 1064 nm of 1.1($\pm$0.5) ppm.

6.3.3 Mechanical Characterisation

Coating mechanical loss measurements

To assess the mechanical characteristics of the SiN_x coatings GeNS measurements were conducted by Dr Gabriele Vajente at the California Institute of Technology. These

measurements differ from those conducted in Chapter 5 as white noise is used as the input signal waveform to resonate all modes of a disk sample simultaneously. More details about this can be found in Chapter 4. Samples were measured before and after coating repeatedly 8 times over 3 separate suspensions to gauge statistical significance of results. Before coating the samples were then cleaned with Acetone and IPA to ensure minimal contamination to the coating surface before deposition, maximising coating adhesion.

Calculating the elastic energy ratios for the coating used a different approach than that used in Chapter 5. In brief, COMSOL [235] FEA simulations were done prior to this study in a random parameter space with varied Young's modulus, Poisson's ratio, coating density and thickness to give a distribution of solutions which are tracked against the shift in resonant frequency from uncoated to coated disk. By fitting a 3rd order polynomial to this data, any possible coating mechanical properties can be extracted by simply fixing the thickness and density of the coating and using the measured shift in resonant frequency. More details on this method can be found in [294, 295]. For these simulations the density was fixed at 3200 kg/m^3 [296] and the coating thickness was taken from measured witness samples as described in Section [6.3.2]. The coating loss, averaged across all modes measured, for varying beam energy and current is shown in Figure [6.11] and [6.12].

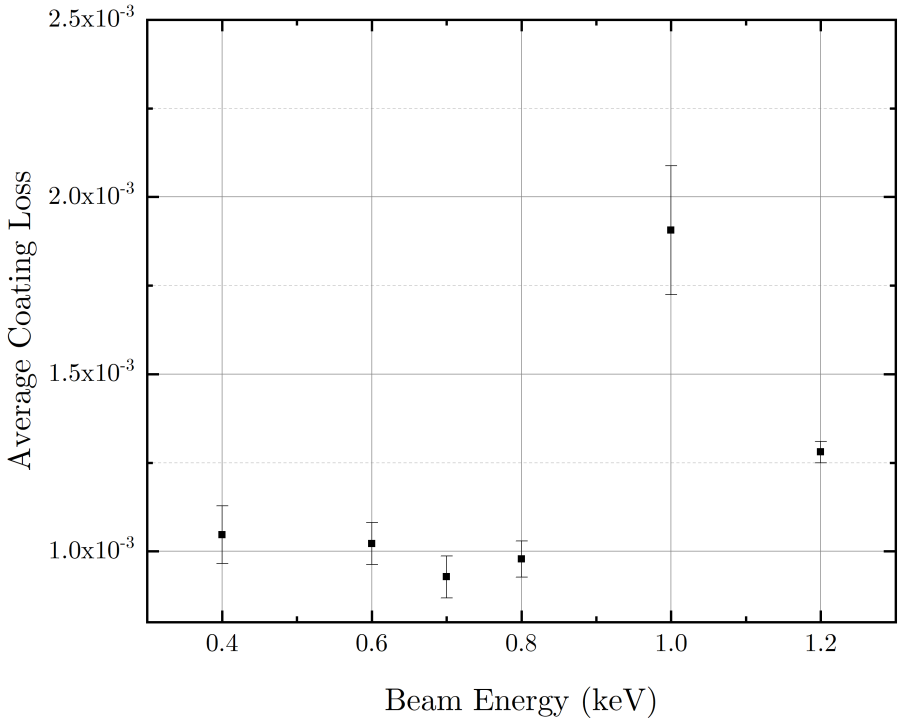

Figure 6.11: As deposited coating loss as a function of beam energy. Data points are an average of coating loss across multiple resonant modes. Error bars are shown as the spread of all measurements.

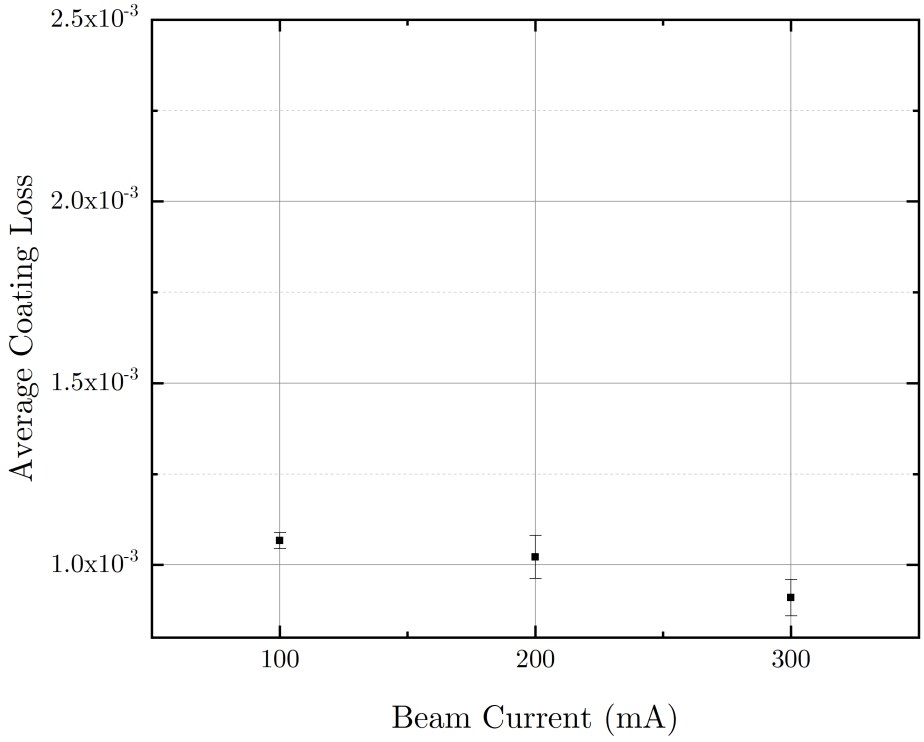

Figure 6.12: As deposited coating loss as a function of beam current. Data points are an average of coating loss across multiple resonant modes. Error bars are shown as the spread of all measurements.

Figure [6.11] shows a similar trend to as deposited refractive index of the varying beam energy samples, with a peak in coating loss at 1.0 keV ($\phi = 1.9(\pm 0.8) \times 10^{-3}$). This can be attributed to contamination from the Mo grids (see Section 6.3.4) in the ion source at high energy (> 1.0 keV), leading to both a higher refractive index ($n = 4.69$ at 1064 nm [297]) and a higher coating loss [298]. The lowest loss value from the process ion beam energy variation is at 0.7 keV ($\phi = 9.3(\pm 0.6) \times 10^{-4}$). While this is not as low as reported in [299] ($\phi \approx 6 \times 10^{-4}$) this is however lower than what was witnessed in as deposited IBSD TiO_2:Ta_2O_5 ($\phi = 7.6 \times 10^{-4}$ [262]). This is likely due to both the higher nitrogen content in the sample at this energy, leading to higher coordination within the atomic structure of the film, in addition to the sample having no measurable contaminants.

Figure [6.12] shows a decreasing trend in loss when using a higher beam current with the lowest loss value at 300 mA being $\phi = 9.1(\pm 0.5) \times 10^{-4}$. As mentioned in Chapter 5, at higher beam currents the sputtered material flux of the film increases, reflected also in the thickness of the films and refractive index in Figure [6.5]. The higher ion flux leads to more nitrogen ions in the process, giving a higher nitrogen content in the film (see Figure [6.20]) and a lower mechanical loss.

SiN_x films have been shown to have improved mechanical performance when annealed to 900°C [73, 262]. Results of the annealed coatings average mechanical loss across multiple resonant modes are shown in Figure [6.13] and Figure [6.14] for beam energy and current respectively.

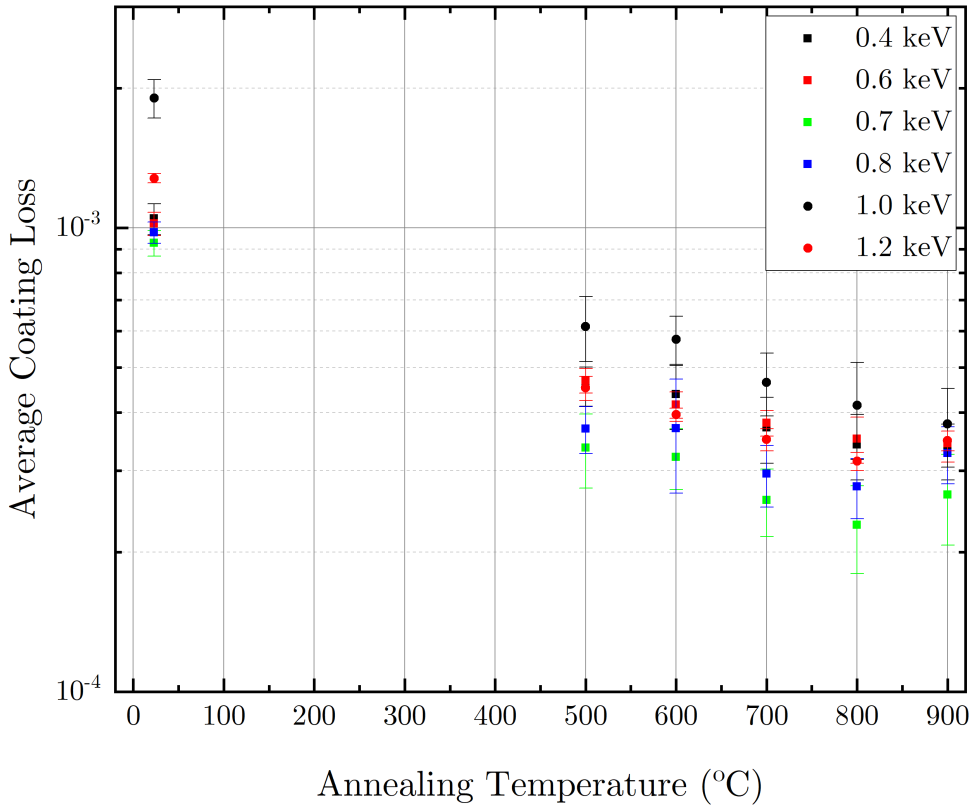

Figure 6.13: Coating loss of SiN_x annealed up to 900°C using 0.4 - 1.2 keV keV beam energy 200 mA current during deposition. Data points are an average of coating loss across multiple resonant modes. Error bars are shown as the spread of all measurements.

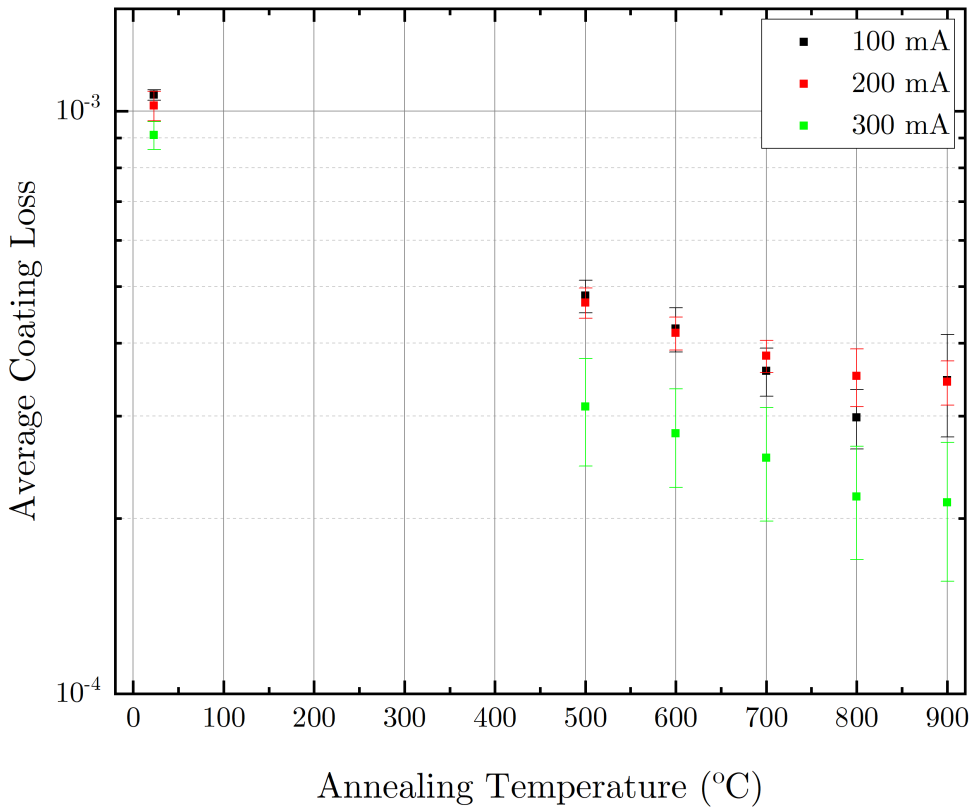

Figure 6.14: Coating loss of SiN_x annealed up to 900°C using 0.6 keV beam energy, 100 - 300 mA current during deposition. Data points are an average of coating loss across multiple resonant modes. Error bars are shown as the spread of all measurements.

Figure [6.13] and Figure [6.14] shows a decrease in mechanical loss at higher annealing temperatures up to 900°C, with the lowest recorded loss at 300 mA where $\phi = 2.1(\pm 0.6) \times 10^{-4}$. The decrease in loss appears linear in trend until 800°C, with the rate of mechanical loss decrease being the same within error bars. After 800°C all but 3 samples increase in mechanical loss with others having similar losses within error bars. This is not thought to be a structural change brought on by partial crystallisation of the sample (see Section 6.3.5) but linked to change of the SiN_x stoichiometry due to lighter elements ($Z < 4$). This has been seen before by Hockett, who observed the concentration of N_2 in Si change dramatically at temperatures > 800°C [300].

Thermal Noise Modelling

To estimate the thermal noise impact of using SiN_x coatings in a GWD, computer simulations were conducted using Python (specifically a modified pyGWINC program [29] as described in Chapter 5). Optical modelling software (TFCalc) [301] was utilised to design an HR stack which would meet the requirements for a GWD coating (99.999% reflectivity at 1064 nm, $<$ 0.5ppm transmission and optimised for CTN performance). Using TFCalc to model an HR stack of SiN_x and SiO_2, a design was calculated which meets these requirements and is shown visually in Figure [6.15].

Parameter	SiN_x	SiO_2	Ta_2O_5
n (1064 nm)	1.95	1.44	2.07
Young's Modulus (Y)	243 GPa	92.9 GPa	99.5 GPa
Poisson's ratio(σ)	0.24	0.17	0.23
Mechanical loss (ϕ)	2.1×10^{-4}	2.3×10^{-5}	3.6×10^{-4}

Table 6.3: Refractive index, Young's modulus, Poisson's ratio and mechanical loss of materials used for thermal noise modelling in this study. Parameters for materials not directly measured are taken from [24, 235, 262]

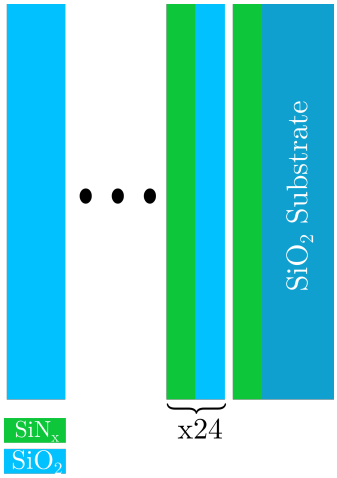

Figure 6.15: Schematic of HR stack design: The full stack is composed of the layers of SiO_2 and SiN_x (300 mA beam current, annealed to 900°C) with an optical thickness = $\lambda/4$ and a cap layer of SiO_2 with optical thickness = $\lambda/2$.

From this design the coating thermal noise can be calculated using the Python scripts. The SiN_x optical and mechanical parameters used were that of the 0.6 keV beam energy, 300 mA beam current deposition annealed to 900°C. The SiO_2 parameters

used were that of LMA SiO_2 used in the current aLIGO coating [235, 262]. These are shown in Table [6.3]. Results of the thermal noise modelling are shown in Figure [6.16], compared to the current aLIGO HR stack CTN.

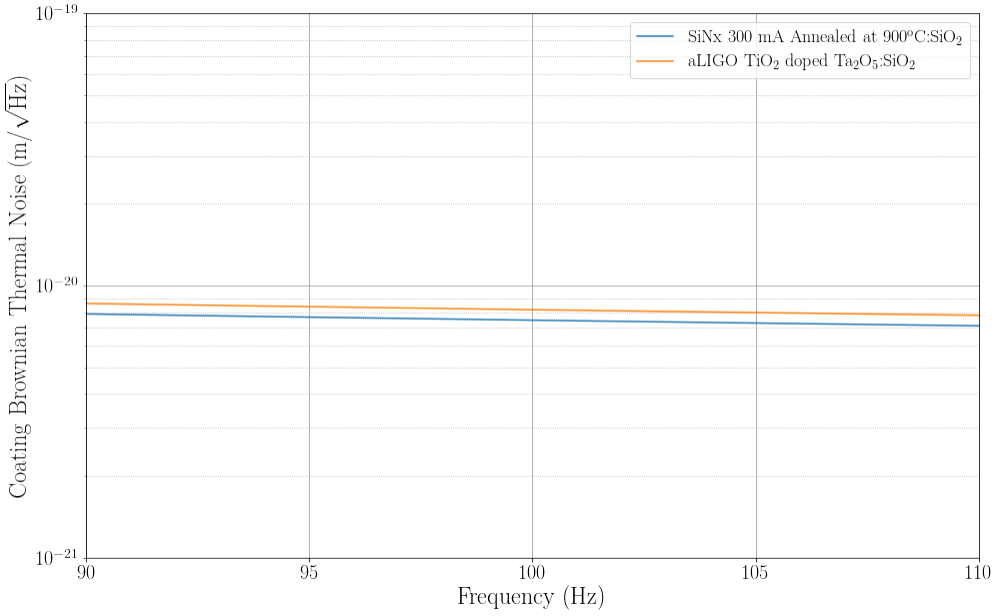

Figure 6.16: Coating thermal noise simulations of current aLIGO coating design at 1064 nm and a HR stack design at 1064 nm using SiN_x from RF IBSD system with a beam current of 300 mA (annealed at 900°C) and SiO_2.

Figure [6.16] shows that SiN_x HR stack produces lower CTN than the current aLIGO design. Specifically at 100 Hz, the region of the detector where CTN limits sensitivity the greatest, the CTN $= 7.47 \times 10^{-21}$ m/$\sqrt{\text{Hz}}$. This is 9% lower than the CTN of the current aLIGO coating, which while only a small improvement is potentially a gateway to additional coating possibilities for a GWD. This also presents a 9% improvement in astrophysical reach for a GWD, giving $\approx 27\%$ increase in event rate.

One of these possibilities is to use a multimaterial (MM) design. As discussed in Chapter 5, this consists of low mechanical loss materials for the lower portion of the HR stack (closest to the substrate) to maintain low CTN while in this case the upper portion uses materials with higher mechanical loss but lower absorption where the

electric field intensity (EFI) of the laser is at its largest. Similarly to the SiN_x SiO_2 HR stack, TFCalc was utilised to ensure the design created met the requirements for a GWD. Parameters for the SiN_x were again taken from the results of the 0.6 keV beam energy, 300 mA beam current deposition coating and the SiO_2 and Ta_2O_5 were taken from [262]. These are shown in Table [6.3] and the resultant design is shown in Figure [6.17].

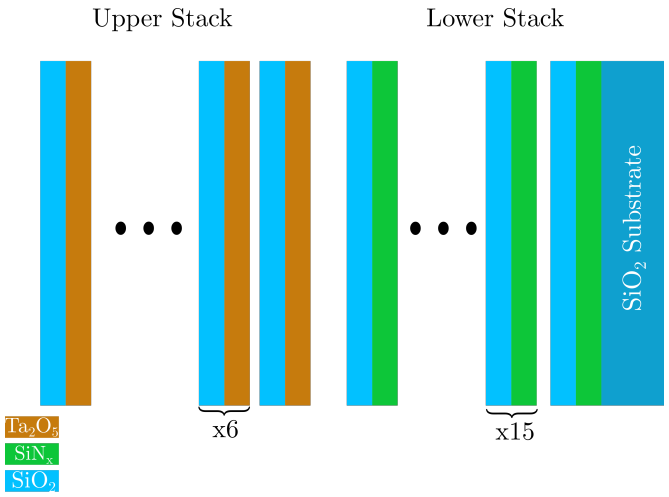

Figure 6.17: Schematic of the multimaterial coating: The full stack is composed of the upper stack (SiO_2 and Ta_2O_5) and the lower stack (SiN_x and SiO_2). Each layer has an optical thickness = $\lambda/4$.

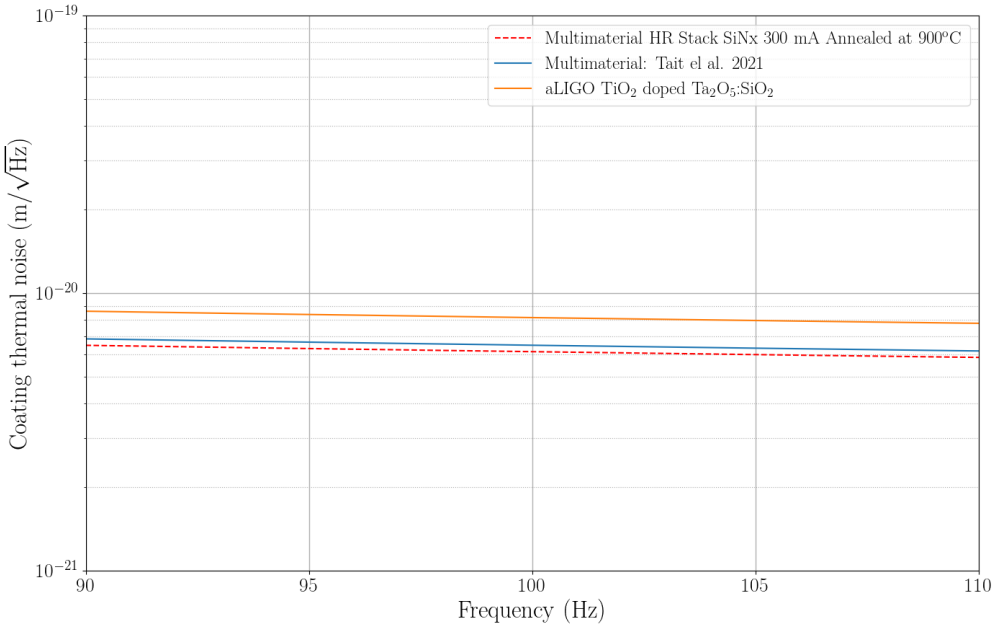

Figure 6.18: Coating thermal noise simulations of current aLIGO coating design at 1064 nm, multimaterial design at 1064 nm using SiN_x from RF IBSD system with a beam current of 300 mA (annealed at 900°C). and multimaterial design as deposited from [24] (Credit to S. Tait for the reference data) at 1550 nm.

Figure [6.16] shows that a MM SiN_x HR stack produces lower CTN than the current aLIGO design. Specifically at 100 Hz, the region of the detector where CTN limits sensitivity the greatest, the CTN $= 6.15 \times 10^{-21}$ m/$\sqrt{\text{Hz}}$. This is 25% lower than the CTN of the current aLIGO coating and 6% lower than the design shown in [24].

6.3.4 Compositional Characterisation

To characterise the material content in the SiN_x coatings and understand the effects this has on optical and mechanical properties two separate methods were employed. The first was x-ray photoelectron spectroscopy (XPS), used in order to accurately assess the lighter element (Atomic number (Z) < 4) content of the films. This was used in conjunction with energy dispersive x-ray spectroscopy (EDS) to give a baseline from which to measure lighter elements after the samples had been annealed in steps up to

900°C. EDS was also used to measure the samples for heavy elements ($Z > 4$) which have resulted from process contamination.

XPS

XPS was conducted on coated Si witness samples using the carbon 1s peak to calibrate all additional peaks found. Wide survey scans were conducted to analyse all peaks between 0 keV - 600 keV. Once elemental peaks were found, finer scans across the peaks were taken to increase data resolution. The data was then inputted into CasaXPS software to fit these peaks and assess the stoichiometry of the films. O 1s, N 1s and Si 2s peaks were fitted using this software, the resultant film stoichiometry calculated are shown in Table [6.4].

Ion Beam Energy	Ion Beam Current	Stoichiometry
0.4(±0.02) keV	200(±20) mA	$SiN_{0.83}O_{0.37}$
0.6(±0.02) keV	200(±20) mA	$SiN_{0.72}O_{0.28}$
0.7(±0.02) keV	200(±20) mA	$SiN_{0.73}O_{0.32}$
0.8(±0.02) keV	200(±20) mA	$SiN_{0.70}O_{0.30}$
1.0(±0.02) keV	200(±20) mA	$SiN_{0.82}O_{0.41}$
1.2(±0.02) keV	200(±20) mA	$SiN_{0.80}O_{0.41}$
0.6(±0.02) keV	100(±20) mA	$SiN_{0.76}O_{0.38}$
0.6(±0.02) keV	300(±20) mA	$SiN_{0.71}O_{0.26}$

Table 6.4: As deposited nitrogen and oxygen based stoichiometry results of SiNx coatings, determined by XPS analysis.

The results in Table [6.4] show there is a large O_2 content within the SiNx films. The reasoning for this lies around the nature of the sputtering process. Possible leaks within the source gas line in addition to residual O-H content within the vacuum chamber can result in O_2 contamination of films [302, 303]. The content within these films is however comparable to other SiN_x work [304] and is not sufficient enough to label these films as silicon oxy-nitride coatings (SiO_yN_x) [305].

EDS

As described in Section [4.4] and Chapter 5, measurements of the SiN_x coatings depositions were conducted on Si witness samples. Each sample was measured compositionally

3 times across there surface at 15 kV of electron voltage in order to ensure penetration into the coating. An average was calculated from the 3 measurements and error bars were taken as the measurement standard uncertainty. Typical relative uncertainty in EDS measurements are $< \pm 5\%$ [271]. Results are shown in Table [5.5] for heavy metal composition ($Z > 4$).

Ion Beam Energy	Ion Beam Current	Silicon (%)	Aluminium (%)	Molybdenum (%)
0.4($\pm$0.02) keV	200($\pm$20) mA	69.2 ± 1.4	0.2 ± 0.1	0
0.6($\pm$0.02) keV	200($\pm$20) mA	68.3 ± 0.3	0.07 ± 0.03	0
0.7($\pm$0.02) keV	200($\pm$20) mA	74.3 ± 0.2	0	0
0.8($\pm$0.02) keV	200($\pm$20) mA	73.3 ± 1.1	0.2 ± 0.1	0.7 ± 0.3
1.0($\pm$0.02) keV	200($\pm$20) mA	71.4 ± 0.2	0.22 ± 0.01	0.8 ± 0.5
1.2($\pm$0.02) keV	200($\pm$20) mA	70.3 ± 0.5	0.23 ± 0.02	0.7 ± 0.2
0.6($\pm$0.02) keV	100($\pm$20) mA	79.2 ± 0.6	0	0
0.6($\pm$0.02) keV	300($\pm$20) mA	60.2 ± 1.4	0.25 ± 0.01	0

Table 6.5: As deposited heavy element ($Z > 4$) compositional results of SiNx coatings, determined by EDS analysis. Each percentage is determined by an average of 3 separate measurements of one sample. Data points are an average of three separate measurements with error bars as the standard uncertainty of these measurements.

Table [6.5] highlights the importance of ion beam parameters on mitigating contaminants within the IBSD process. In particular at beam energies > 0.7 keV, Mo grid material starts to be incorporated into the thin films. Al is present in all films except those using 0.7 keV beam energy, 200 mA beam current and 0.6 keV beam energy, 100 mA beam current. The percentage of Al content is small however for all additional films ($\leq 0.25\%$).

Annealed samples

The SiN_x coated Si witness samples were also measured by EDS after annealing in steps between 500°C - 900°C using the same method as in Section 6.3.4. This was to assess the light element ($Z < 4$) composition at higher annealing temperatures. The initial values were offset using the XPS results to attain as accurate a compositional value as possible. The results of these scans for N_2 composition are shown in Figure [6.19] and Figure [6.20] for beam energy and current respectively. the results for O_2 composition are shown in Figure [6.21] and Figure [6.22] for beam energy and current respectively.

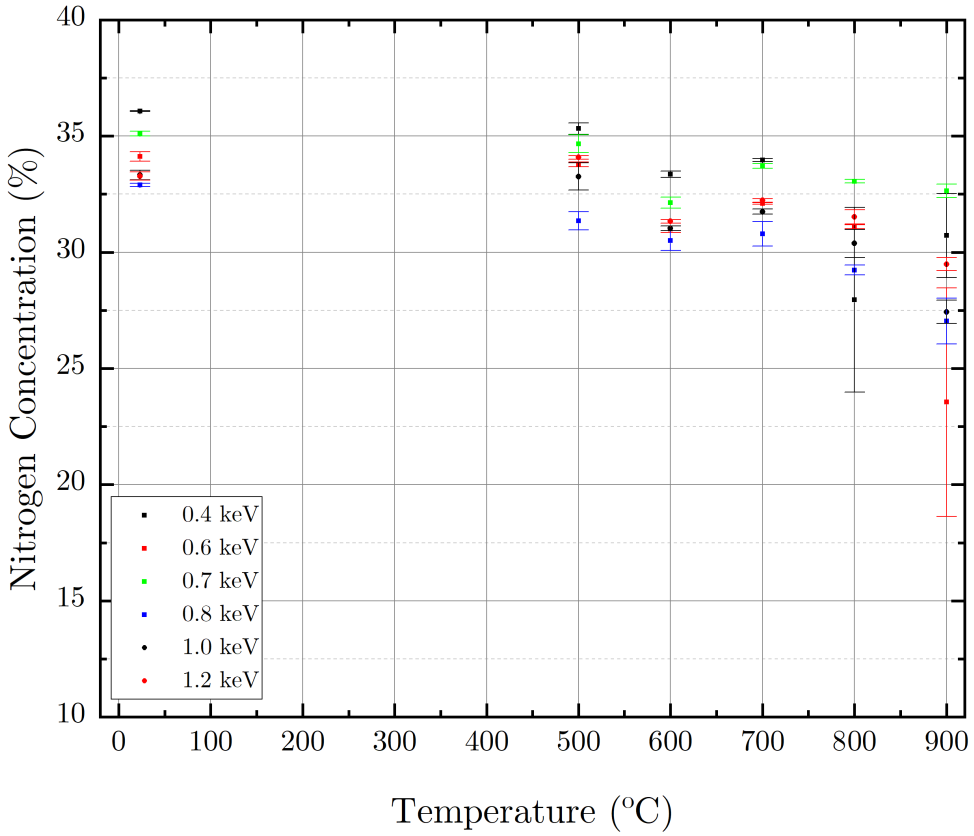

Figure 6.19: Nitrogen concentration in SiN_x coatings produced by varying beam energy (0.4 keV - 1.2 keV) as a function of annealing temperature up to 900°C, measured by EDS. Atomic concentration is normalised to XPS measurements. Data points are an average of three separate measurements with error bars as the standard uncertainty of these measurements.

Figure [6.19] shows a general decrease in N_2 content as the annealing temperature increases. Data points with large error bars occur from the random error of the EDS measurement technique. As the coating is measured at varying points across the face, the lighter element content in the coating can vary largely from center to edge. The coating able to attain the highest N_2 content until the final annealing temperature of 900°C was using 0.7 keV beam energy with an atomic concentration of 32.6 (±0.5)%. This gives an insight into why this coating has both the lowest as deposited and annealed mechanical loss, as the atomic structure is more coordinated than other coatings with

varying beam energy.

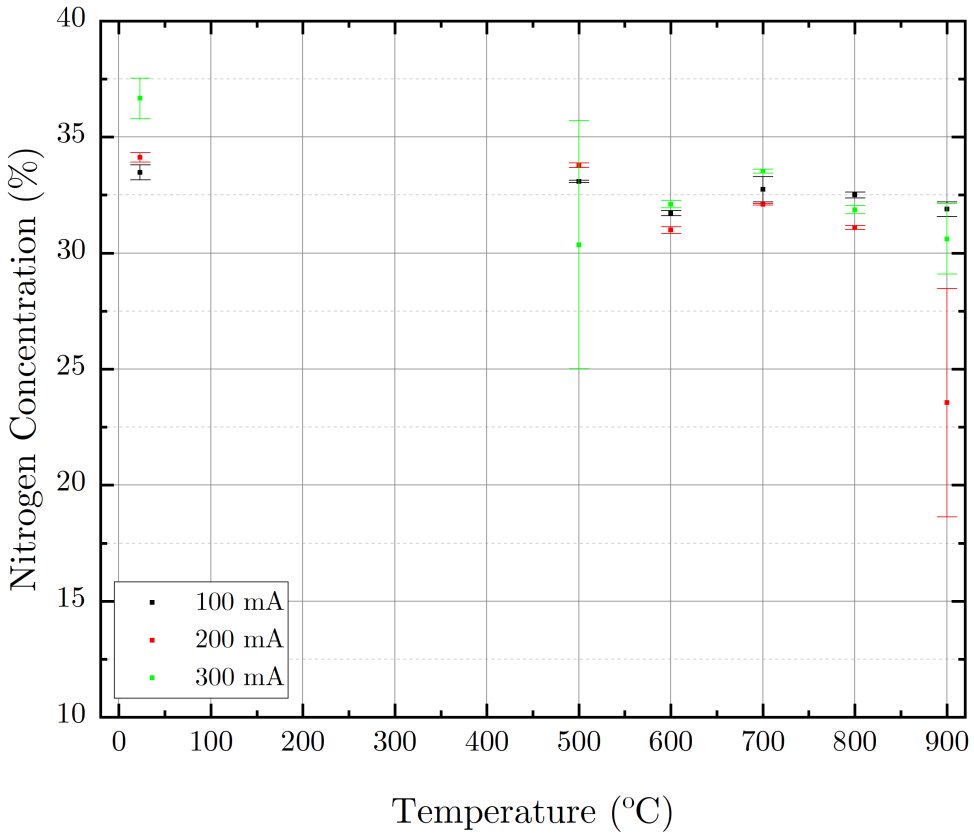

Figure 6.20: Nitrogen concentration in SiN_x coatings produced by varying beam current (100 mA - 300 mA) as a function of annealing temperature up to 900°C measured by EDS. Atomic concentration is normalised to XPS measurements. Data points are an average of three separate measurements with error bars as the standard uncertainty of these measurements.

Figure [6.20] also highlights a similar trend, for varying beam current of SiN_x coatings as varying beam energy, that the N_2 content of the films decreases with increasing annealing temperature. Again there are data points with high uncertainty resulting from the measurement technique however a downward trend can still be surmised as plausible given the results from Figure [6.19]. At an annealing temperature of 900°C all three of the samples have a similar N_2 content within error bars ($\approx 31\%$). Because of experimental random error it is therefore difficult to accurately determine the exact

concentration of N_2 at this temperature.

While N_2 concentration plays an important role in the optical and mechnical properties of the coatings O_2 should also be considered equally important. O_2 can greatly effect optical and mechanical properties of thin films, with annealing in air changing the O_2 composition in the coating through atomic restructuring [306, 307]. Figure [6.21] and Figure [6.22] show the effect annealing the SiN_x coatings has on the O_2 concentration in the films for vary beam energy and beam current respectively.

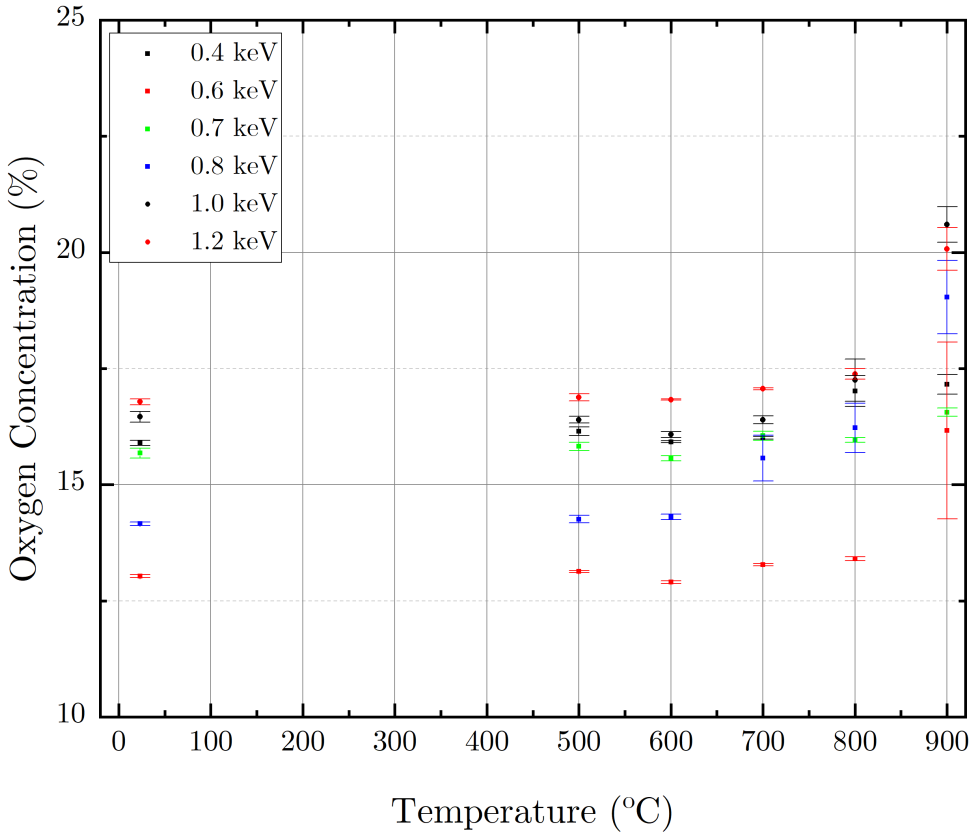

Figure 6.21: Oxygen concentration in SiN_x coatings produced by varying beam energy (0.4 keV - 1.2 keV) as a function of annealing temperature up to 900°C measured by EDS. Atomic concentration is normalised to XPS measurements. Data points are an average of three separate measurements with error bars as the standard uncertainty of these measurements.

It can be seen from Figure [6.21] that as the annealing temperature increased for the

SiN_x films the O_2 also increased. The greatest increase in this concentration occured after 800°C where coating produced using 1.0 and 1.2 keV beam energy experience a sudden "jump" of $> 2\%$ O_2 concentration. The highest O_2 content is that of the 1.2 keV beam energy coating with an average atomic concentration of 20.6 ($\pm$0.8) %. The sample with the lowest O_2 concentration when annealed to 900°C was the SiN_x produced at 0.6 keV, with an average atomic concentration of 16.2 ($\pm$3.3) %.

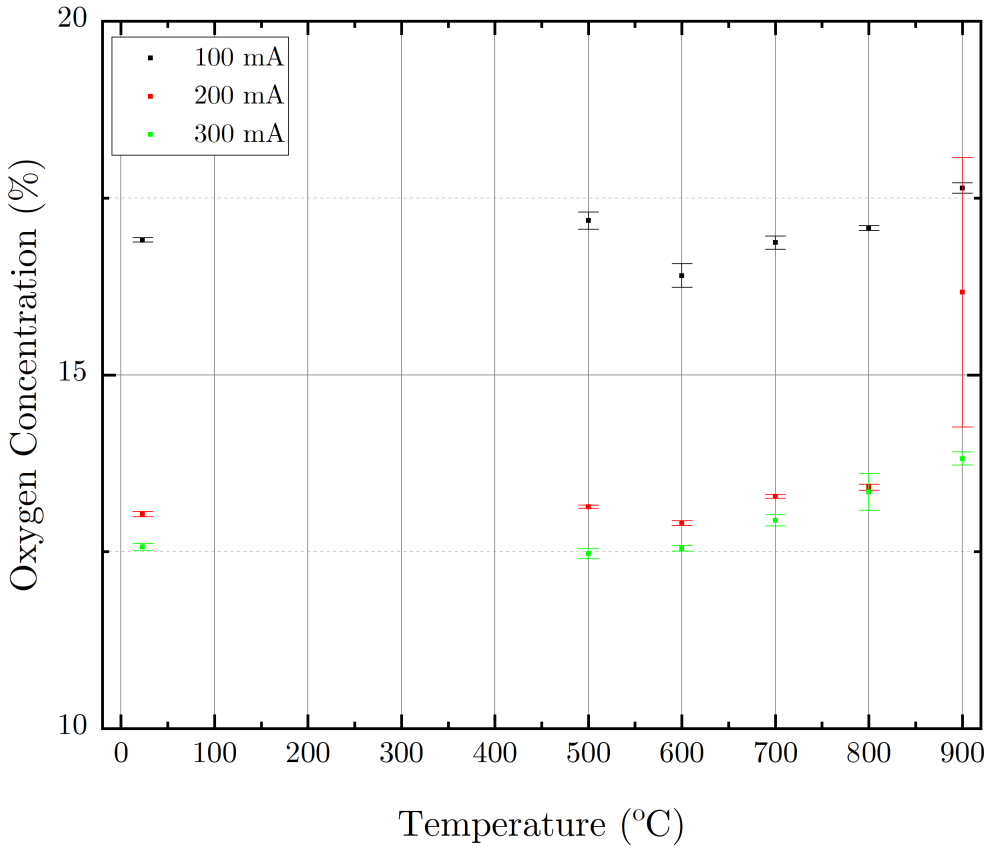

Figure 6.22: Oxygen concentration in SiN_x coatings produced by varying beam current (100 mA - 300 mA) as a function of annealing temperature up to 900°C measured by EDS. Atomic concentration is normalised to XPS measurements. Data points are an average of three separate measurements with error bars as the standard uncertainty of these measurements.

Figure [6.22] shows a similar trend to Figure [6.21], where O_2 concentration increases within the SiN_x coatings at higher annealing temperatures. The highest concentration

of O_2 is found in the 100 mA beam current coating, with a atomic concentration of 17.6 ($\pm$0.1) % at 900°C. The rate at which the O_2 concentration increases follows a similar trend for all coatings shown. The large error bars from the measurement at 900°C from the 200 mA coating is from random error associated with measured EDS site on the coating surface (center, edge *etc.*). The lowest concentration of O_2 is found in the 300 mA beam current coating, with a atomic concentration of 13.82 ($\pm$0.2) % at 900°C.

6.3.5 Structural Characterisation

XRD

The amorphous nature of the coatings across the various annealing temperatures was investigated through the use of a Bruker D8 Advance XRD system. Using both coupled theta and GIXRD measurements, scans were taken between $25° - 60°$ in order to capture the strong Si_3N_4 crystalline peaks [308, 309]. Figure [6.23] shows the scan results for SiN_x at 1.2 keV beam energy as deposited and annealed to 600°C and 900°C. The as deposited sample scan was measured at 0.5° grazing incidence.

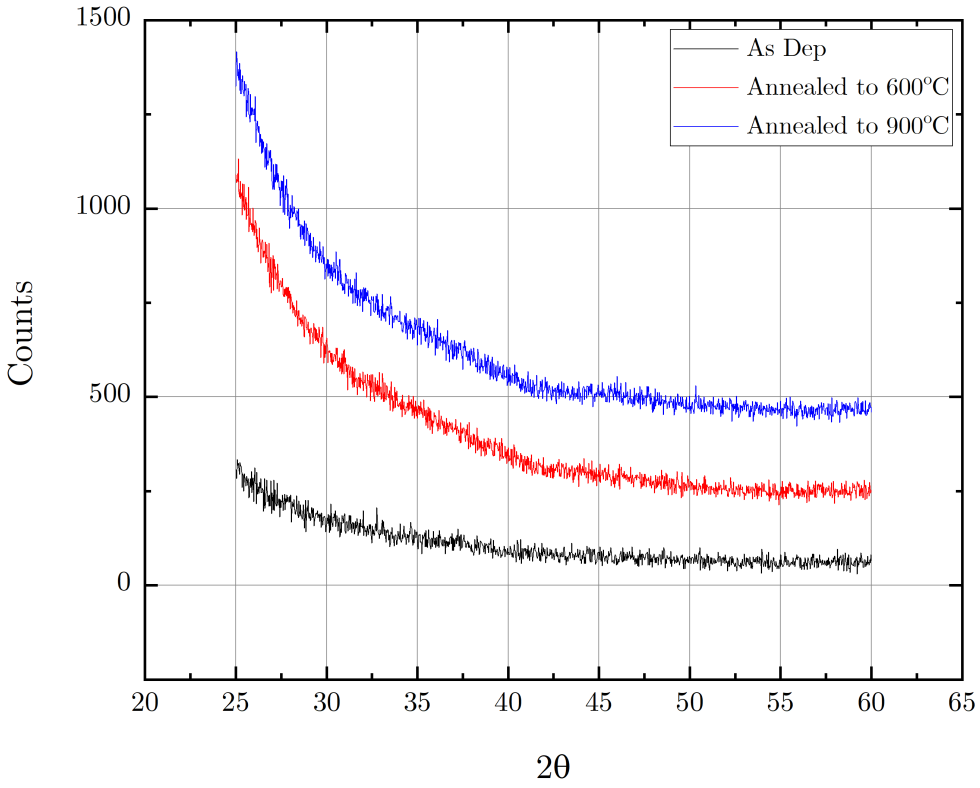

Figure 6.23: XRD scans for SiN_x coating on SiO_2 at 1.2 keV beam energy and 200 mA beam current. Data is offset on y-axis to highlight each scan separately. All scans were done using grazing incidence at an angle of 0.5°.

Figure [6.23] shows that annealing the SiN_x sample up to 900°C does not induce a crystalline phase detectable by GIXRD. The trailing edge of the scan from 25° - 45° is a result of the JGS grade SiO_2 substrate. As no sharp crystal peaks are witnessed it can therefore be concluded that this sample is amorphous. All other samples were scanned with the same method and showed similar results to this sample as none produced crystalline peaks at 900°C between 25° - 60°. Given the crystallisation temperature of Si_3N_4 is $\approx$ 1300°C [309] these samples should be fully amorphous up to the last annealing step of 900°C unless deposited as a polycrystalline film, which is not the case.

6.4 Discussion

The results show in Section 6.3 highlights some interesting properties of IBSD SiN_x coatings. The first is the dependence of the film stoichiometry and by extension optical properties on partial pressure of N_2 used in the process. The method by which the gas is introduced into the deposition process has proven paramount in creating a thin film with the correct refractive index as Si_3N_4 with low absorption characteristics. The reasoning behind this lies in the interaction between N ions and the Si target. As Si does not chemisorb molecular N_2 [310] and moreover will only adsorb atomic N [311], SiN_x is produced as a surface layer on the Si target which is then sputtered to form the thin film [312]. Given this fact it is understandable the SiN_x coatings with the best optical properties and a refractive index that is closest to Si_3N_4 (n = 2.04) are using the highest N_2 partial pressure and highest percentage of gas delivered to the ion source. It must be mentioned however that at 70% partial pressure the absorption was uncharacteristically high in comparison to the other SiN_x films ($k = 8.93 \times 10^{-4}$). While theoretically plausible that this was caused by the partial pressure of gas used it is more practically plausible that this run incorporated more heavy contaminants (Al, Mo, *etc.*) into these films. As these films were not measured by XPS or EDS this can only hypothesised.

The PCI results revealed that SiN_x can exhibit low absorption properties when the process beam parameters are taken into consideration. The lowest value of absorption measured at 1064 nm was from SiN_x at 0.4 keV beam energy, annealed to 900°C (1.1($\pm$0.5) ppm). Even with the lower refractive index of this film ($n = 1.88$) in comparison to other SiN_x coatings, this could still be used as part of a GWD design. In its current state however the absorption measured would be too high when considered as a full HR stack. Another interesting result from the measurements is at 900°C using 300 mA beam current where the absorption was 4.7($\pm$2.0) ppm. Given the higher thickness of this film (313.52) and refractive index ($n = 1.95$) this could be compatible with a GWD HR stack design. The increase in absorption at 800°C in all but one sample (0.4 keV) is likely due to higher oxygen levels in the other samples however no additional

evidence supports any structural changes occurring at this specific temperature.

As the beam current was increased between depositions both the film thickness and optical properties of the SiN_x films improved. This is thought to be linked to the decrease in O_2 content in these films. Using higher beam current in an IBSD deposition process increases the ion flux impingent on the target, in this case Si, which at 300 mA is preferential for decreasing the dissociation of O_2. It is clear that the ratio between O_2 and N_2 in the coatings is paramount in determining there optical and also mechanical properties. This has been shown by Gibson *et al.* [313] where the decreasing ratio between O_2 and N_2 led to an increase in refractive index of silicon oxynitride films.

The mechanical properties of the films produced with varying beam energy follow a similar trend to that of the optical properties. This can be related by both the contaminant, O_2 and N_2 content of the films. The film with the highest mechanical loss and, by extension, optical extinction coefficient, were the coatings produced at 1.0 keV. The SiN_x films also have the highest Mo content, a material known for its high absorption properties [297, 314] and low coordination in a SiN_x matrix leading to high mechanical loss [314].

The lowest loss produced was at 300 mA where $\phi = 2.1 \times 10^{-4}$ when annealed to 900°C. This is higher in comparison to [262] ($\phi \approx 1.8 \times 10^{-4}$ when annealed to 900°C) and [123] ($\phi = 1.3 \times 10^{-5}$). The higher losses in the 300 mA coating are a result of Al content in the film, decreasing atomic coordination in the thin films, which if reduced would likely lower the mechanical loss of this coating as deposited and when annealed to high temperatures. The high nitrogen content in both this film and the SiN_x coating using 0.7 keV highlights that nitrogen bonding is preferential for reducing coating mechanical loss in this material.

When annealed the SiN_x coatings optical and mechanical properties drastically improved. While the nitrogen content in the films decreased the oxygen content increased. This has been shown to improve both optical and mechanical properties due to structural reordering and diffusion of O_2 into the coating which increases at higher temperatures [305, 315] as the films move from being more SiO_2 like than Si_3N_4 like. Grabowski *et al.* have shown that at temperatures around 1200°C, crystallisation and

blisters can form in ion assisted SiN_x deposition [316]. As these temperatures were not reached in this study due to the sought out application this has posed no issues for these films.

The thermal noise performance of the SiN_x was shown to be improved over the current aLIGO coating. However the caveat to this this as mentioned in [262] is the Young's modulus mismatch between the SiN_x layers (Y = 245 GPa for 300 mA beam current annealed to 900°C) and SiO_2 (Y = 92.9 GPa) could limit the CTN performance at room temperature. This is however a positive step to attaining the CTN performance required for the aLIGO + upgrade.

6.5 Conclusions and Future Work

It is possible to optimise the optical and mechanical properties of IBSD non-stoichiometric amorphous silicon nitride by varying the ion source beam energy and current. This work the best performing coating was at 0.6 keV beam energy and 300 mA of beam current. This gave an as deposited refractive index of 1.99 at 1064 nm and a mechanical loss value of $\phi = 9.14 \times 10^{-4}$. PCI measurements of this film revealed this film to have an absorption of 311.8(±15.5) ppm as deposited and 4.7(±2.0) ppm, when annealed to 900°C.

Annealing to 900°C also further improved its mechanical properties to $\phi = 2.13 \times 10^{-4}$ but however lowered the refractive index to 1.95 at 1064 nm. This is however still compatible with a GWD HR stack design which in its current state gives a thermal noise performance of 7.47×10^{-21} m/$\sqrt{\text{Hz}}$ at 100 Hz. Using this coating as part of a multimaterial design gave a coating thermal noise performance at 100 Hz of 6.15×10^{-21} m/$\sqrt{\text{Hz}}$. This is 25% lower than the CTN of the current aLIGO coating. The relationship between nitrogen and oxygen content, particularly when the samples are annealed plays a key role in determining there optical and mechanical characteristics.

Future work would look to further optimise the parameter space and conduct a deposition at 0.7 keV beam energy using 300 mA of beam current and specific testing of thermal annealing duration, shown to be effective at reducing mechanical loss [64].

Going by current understanding this could further improve the optical and mechanical performance of the coatings. Furthermore measuring the mechanical loss of the coating at cryogenic temperatures would assess how SiN_x would perform in a future cryogenic GWD such as LIGO Voyager. The creation of a multilayer stack of SiN_x and SiO_2 using this optimisation would allow direct thermal noise evaluation [224] and give a more accurate understanding of how this design would perform in a GWD.

These results have shown that SiN_x could be a promising candidate for next generation gravitational wave detectors and could help further push the thermal noise limits, and astrophysical reach, of the current technologies employed in aLIGO.

Chapter 7

Conclusion

Following on the first confirmed gravitational wave signal detection in 2015, there are currently around 90 candidate detections confirmed including black hole and neutron star mergers. The gravitational wave detector network, comprised of multinational experimental facilities monitor the position of test masses to detect displacements $< 10^{-18}$ m both at room temperature (aLIGO, aVIRGO *etc*,) and cryogenic temperatures (KAGRA). The next generation of detectors hope to peer further into the Universe by observing more exotic cosmic phenomena, such as supernovae and pulsars, by upgrading current technologies to overcome limiting noise factors. One of these noise sources is Brownian coating thermal noise, associated with random thermal fluctuations in the material structure of the highly reflective coatings used to operate the detectors at 1064 nm and 1550 nm, which cuts across the most sensitive region of detector operation ($\sim$ 50 Hz - 150 Hz).

The research shown in this thesis used ion beam deposition to create amorphous silicon and non-stoichiometric silicon nitride coatings to monitor their optical and mechanical properties when the ion beam parameters (beam energy and current) were varied. This will be crucial in creating the next generation of optical coatings for gravitational wave detectors in order to understand how the coating process can be further optimised.

An overview was given of the 16 cm RF ion source deposition system, built and operated by the author, used to produce the coatings in this thesis in addition to

encapsulating both the fundamental theory and simulation of the IBD process. The measurement techniques utilised in this work were outlined with particular attention given to the mechanical loss measurement system (GeNS) built and operated by the author. The optimisation of this quantity is paramount in improving the coating thermal noise performance of next generation GWD detectors.

The amorphous silicon coatings produced by RF IBD proved empirically to have optimised optical and mechanical properties using 0.4 keV beam energy and 200 mA beam current. This coating was shown to have an optical absorption using PCI of $7.74(\pm 0.60) \times 10^3$ ppm with $n = 3.51$ at 1550 nm when annealed to 400°C. The mechanical properties of this film at this temperature also proved interesting where $\phi = 1.1(\pm 0.6) \times 10^{-4}$, while higher than recorded previously for IBD aSi still showed optimisation of the process is possible. Using the mechanical properties of this film as part of a multimaterial HR coating design (layers of Ti:Ta_2O_5, SiO_2 and SiN_x) gave a coating thermal noise performance at 100 Hz of 4.24×10^{-21} m/$\sqrt{\text{Hz}}$, $\approx 38\%$ lower than the current aLIGO design. It was shown that the relationship between oxygen content in the films, which increases at higher annealing temperatures, contributed to the improvement in optical and mechanical properties in the a-Si films.

The SiN_x coatings proved to show optimised optical performance when using 80% partial pressure of N_2, in particular when this is fed through the ion source as opposed to filling the deposition chamber with the gas ($n = 2.03$, $k < 2.0 \times 10^{-4}$ at 1064 nm). This coupled with optimisation of the beam energy and current gave $n = 1.95$ and a PCI absorption measurement of $4.7(\pm 2.0)$ ppm at 1064 nm using 0.6 keV and 300 mA beam energy and current, annealed to 900°C. The mechanical properties were also optimised using these deposition parameters where $\phi = 2.13 \times 10^{-4}$ when the film was annealed to 900°C. Using this as part of a full HR stack (SiN_x and SiO_2 layers) meeting the design requirements of 99.999% reflectivity and 0.5% transmission, the thermal noise performance at 100 Hz would be 6.15×10^{-21} m/$\sqrt{\text{Hz}}$, 25% lower than the CTN of the current aLIGO coating. The determination of the oxygen, nitrogen percentage relationship when annealing is key in determining the optical and mechanical properties of the SiN_x films.

Further investigation into these materials would involve using the data presented here to further optimisation of the parameter space in addition to minimising foreign contaminant material entering the coating process. Additionally cryogenic absorption and mechanical loss measurements of both the aSi and SiN_x coatings would give evaluation of the optical and thermal noise performance in future GWDs operating at low temperature, e.g., $\sim$ 18K and $\sim$ 125K and allow the creation of an optimal HR stack design.

The coating material optimisation conducted here presents enhanced insight into the IBD process. This will be necessary when further developing the next generation of GWD as IBD is currently the chosen method by which the HR coating stacks are produced. Further knowledge of this process will aid in enhancement of the materials mentioned here (aSi and SiN_x) which will also play a key role when developing coatings and moreover detectors at 1064 nm and 1550 nm both at room and cryogenic temperatures. This is the stepping stone by which next generation detectors can peer even further back in time to witness large cosmic events never before observed by humanity and gain an empirical understanding of the Universe which builds on Einstein's century old theory.

List of Publications

Stated below are key publications the author has contributed to or key LIGO collaboration papers published during the duration of study.

1. R. Abbott et al. “Search for Gravitational Waves Associated with Gamma-Ray Bursts Detected by Fermi and Swift during the LIGOVirgo Run O3a”. In: *The Astrophysical Journal* 915.2 (2021), p. 86. ISSN: 0004-637X. DOI: 10.3847/1538-4357/ABEE15. arXiv: 2010.14550

2. D. Davis et al. *LIGO detector characterization in the second and third observing runs*. 2021. DOI: 10.1088/1361-6382/abfd85. arXiv: 2101.11673. URL: https://iopscience.iop.org/article/10.1088/1361-6382/abfd85https://iopscience.iop.org/article/10.1088/1361-6382/abfd85/meta

3. R. X. Adhikari et al. “A cryogenic silicon interferometer for gravitational-wave detection”. In: *Classical and Quantum Gravity* 37.16 (2020). ISSN: 13616382. DOI: 10.1088/1361-6382/ab9143. arXiv: 2001.11173

4. Carlos Garcia Nuñez et al. “Study of Amorphous Dielectric Optical Coatings Deposited by Plasma Ion Assisted Electron Beam Evaporation for Gravitational Wave Detectors”. In: *Optics InfoBase Conference Papers*. Washington, D.C.: Optica Publishing Group, 2022, WB.4. ISBN: 9781557528209. DOI: 10.1364/ao.477186. URL: https://opg.optica.org/abstract.cfm?uri=OIC-2022-WB.4

5. Shigeng Song et al. “Tantalum Oxide and Silica Mixture Coatings Deposited

Using Microwave Plasma Assisted Co-sputtering for Optical Mirror Coatings in Gravitational Wave Detectors". In: *Optics InfoBase Conference Papers*. Washington, D.C.: Optica Publishing Group, 2022, WB.2. ISBN: 9781557528209. DOI: 10.1364/ao.477211. URL: https://opg.optica.org/abstract.cfm?uri=OIC-2022-WB.2

Appendix A

XRD Scan Method Comparison

During the course of measuring both aSi and SiN_x coatings using X-Ray Diffraction (XRD) it was observed that samples exhibited an amorphous structure both being measured using the conventional Bragg-Brentano method in addition to at grazing incidence (GIXRD). The following appendix shows additional scans taken for SiN_x coatings, deemed not relevant to the main body of the thesis but interesting to highlight the validity of the methodology used by the author in this research. No peaks (except signal noise) are observed in these scans which warrant differing scanning techniques to be utilised for these films.

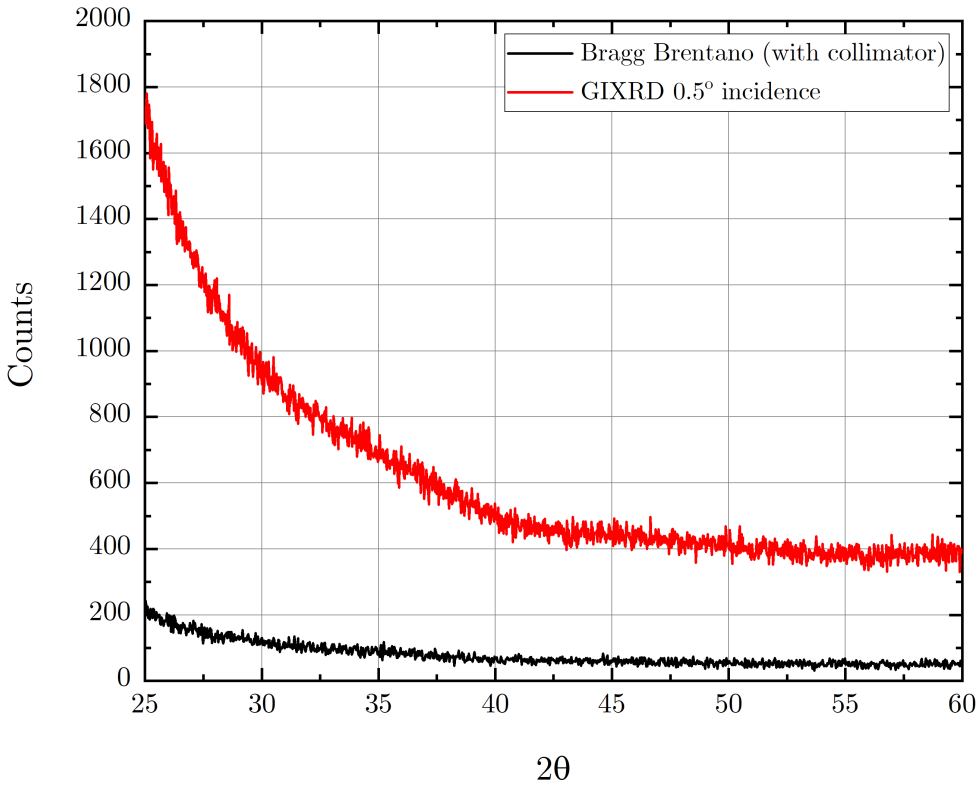

Figure A.1: XRD scans of SiN_x coating using coupled theta or Bragg Brentano measurement with a collimator with 0.025° steps lasting 1.5 s per step and GIXRD at 0.5° with 0.03° steps lasting 1 s per step. In this case the collimator reduced the number of counts present in the scan but has not effected the overall result.

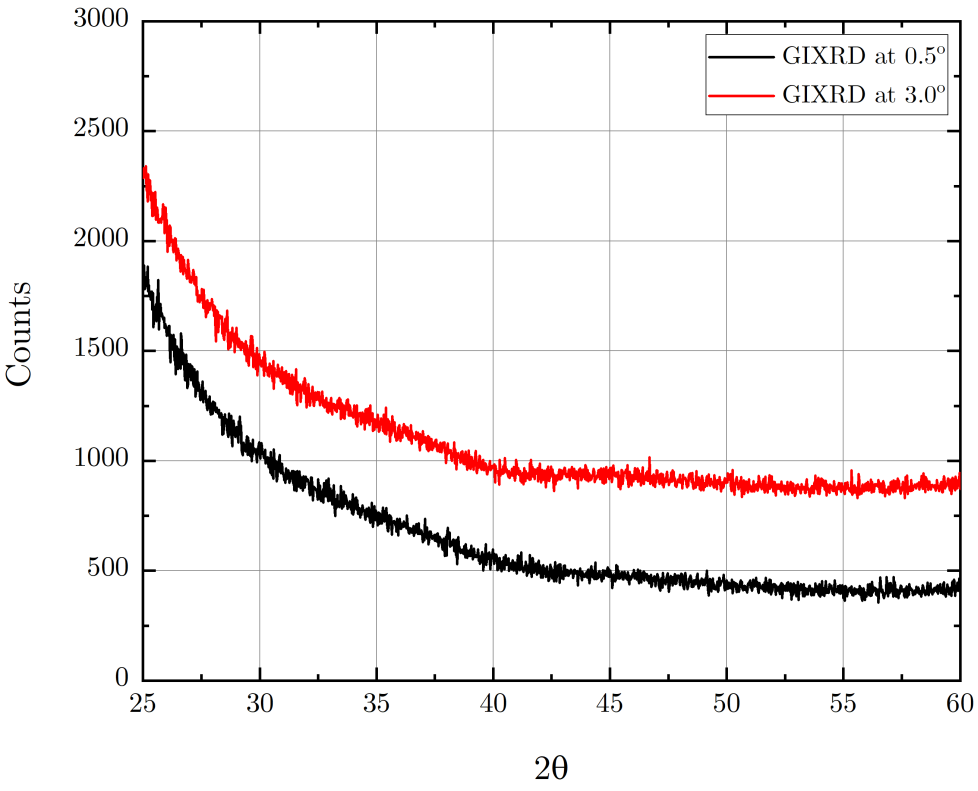

Figure A.2: XRD scans of SiN_x coating both using GIXRD measurement at 0.5° with 0.025° steps lasting 1.5 s the other at 3.0° with 0.015° steps lasting 10 s per step.

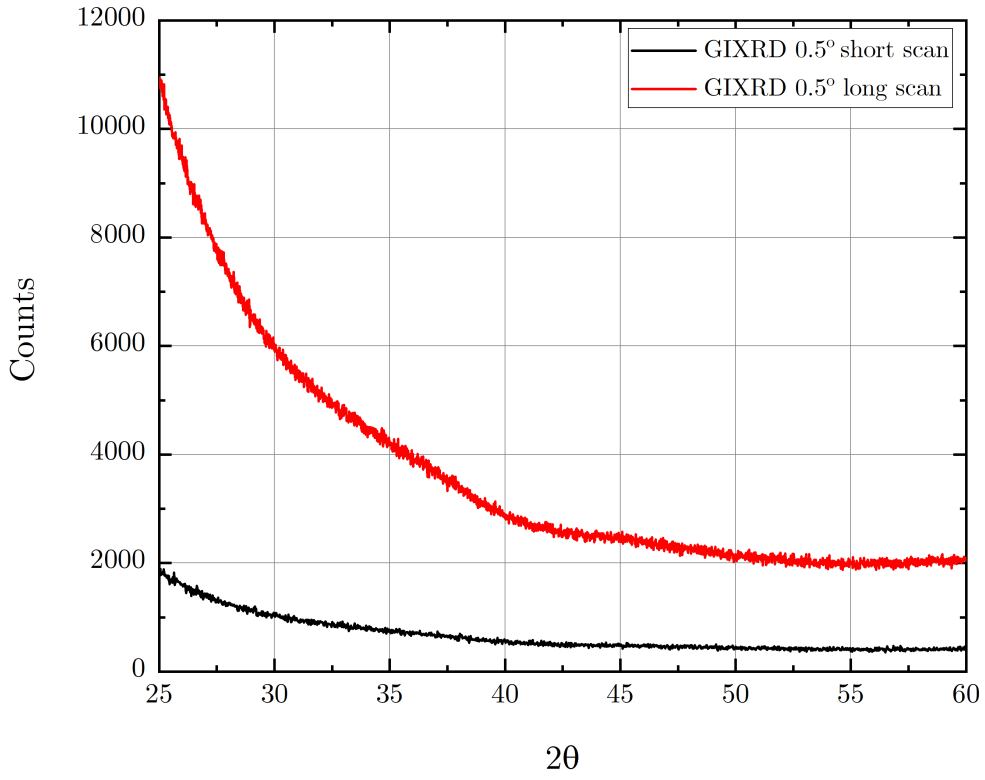

Figure A.3: XRD scans of SiN_x coating both using GIXRD measurement at 0.5 ° with 0.025° steps lasting 1.5 s and the other with 0.015° steps lasting 10 s per step.

Appendix B

ANSYS APDL Energy Ratio Extraction Code

```
!Command to calculate energy ratios of a coated disk and output
results to a .txt file !Author G.Wallace UoS 06/2019
   !!!!!!!!!!!!!!!!!!Create text file and set headings!!!!!!!!!!!!!!!
   *CFOPEN,ENERGY_RATIOS,txt !Open txt file, in place of ENERGY_RATIOS
can put direct file path or change txt to any file format
   *VWRITE,'Mode','Freq','ERatio','Coat','Sub','Total' !Title of
document
   (A,A,A,A,A,A) !FORTRAN format for string
   !!!!!!!!!!!!!!!!!!Create modal loop for extraction of energy ratios!!!!
   *DO,Step,1,100,1 !Set for a model of 100 modes, this can be changed
   SET,1,Step
   !!!!!!!!!!!!!!!!!!Calculate elastic strain energy of geometries
from mesh elements!!!!!!!!!
   CMSEL,s,Substrate !Select Substrate (defined in model named selection)
   ETABLE,Substrate_1,sene !Generate table of elastic strain energy
for each element in selection
   AVPRIN,1
   ALLSEL
```

```
   cmsel,s,Coating !Select Coating (defined in model named selection)
   etable,coat_1,sene
   avprin,1
   allsel
   CMSEL,s,Total !Select all of model
   ETABLE,Total_1,sene
   AVPRIN,1
   ALLSEL
   SSUM !Integrate over named selections
   !!!!!!!!!!!!!!!!!Retrieve variables created and output to file!!!!!!!!
   *GET,my_Coating_1,ssum, ,item,coat_1 !Retrieve Coating elastic
strain energy
   *GET,my_Total_1,ssum, ,item,Total_1 !Retrieve Total elastic strain
energy of system (depending on formula used for loss calc)
   *GET,my_Sub_1,ssum, ,item,Substrate_1 !Retrieve Coating elastic
strain energy
   *GET,my_Freq_1,active, ,set,freq !Retrieve Modal frequency from
model
   Coating_ER = my_Substrate_1/my_Coating_1 !Calculate Energy Ratio
of coating
   *VWRITE,Step,my_Freq_1,Coating_ER,my_Coating_1,my_Sub_1,my_Total_1
!Write to file
   (F4.0,F12.4,E16.8,E16.8,E16.8,E16.8)
   !First Step requires etable deletion - L.Cunningham via S.Tait,
University of Glasgow
   *IF,Step,EQ,1,THEN
   ETABLE,erase
   ALLSEL
   *ENDIF
   *ENDDO
```

```
,*CFCLOS !Close file
```

Appendix C

Mechanical loss of e-beam evaporated HfO_2, Sc_2O_3 and MgF_2

Alongside IBD, e-beam evaporation is being considered to produce coatings for the next generation of GWD. Although not considered by the author in this work, they have contributed to mechanical loss measurements shown in [321, 322], where the formal motivation behind the research is detailed.

In order to calculate coating mechanical loss, as outlined in Chapter 4, both the mechanical loss before and after coating is required in addition to the elastic energy ratios between the coating and substrate for each resonant mode measured. For this process ANSYS Workbench [234] and by extension ANSYS Mechanical FEA software with modal analysis [236] was utilised . As the GeNS disk for this study had a flat machined onto the edge consideration of the impact on resonant frequency had to be taken into account. By meshing the disk face and sweeping through the body structure mechanical parameters could be assigned (shown in Figure [C.1]).

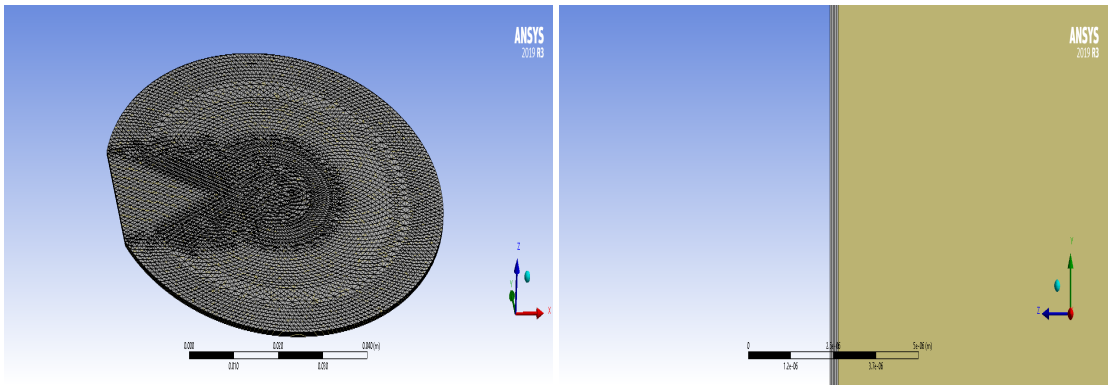

(a) Screenshot from ANSYS FEA software showing meshing structure on surface of GeNS disk.

(b) Screenshot from ANSYS FEA software showing mesh layer structure between coating and substrate.

Figure C.1: Screenshots from ANSYS FEA showing meshing of GeNS disk used to measure mechanical loss of coatings in [321].

Setting the machined flat length, disk thickness, Young's modulus and Poisson's ratio as variables and using ANSYS Mechanical FEA in built optimisation routine a match to the uncoated resonant frequencies was acquired. Following on from this the coating was added on top and the same process undergone for the coating to match to the coated disk eigenfrequencies (varying thickness, Young's modulus *etc*) using initial parameter estimations from literature [323–327]. Extraction of the energy ratios once the eigenfrequencies were matched was then conducted via a custom script written by the author (see Appendix B) which integrates the elastic strain energy elements over a specified components (*i.e* coating or substrate) and divides these components to output E_s/E_c. Both the material parameters calculated and the energy ratios extracted are shown in Table [C.1] and Table [C.2].

Parameter	HfO_2	Sc_2O_3	MgF_2
Young's Modulus (Y)	164.9 GPa	195 GPa	144.2 GPa
Poisson's Ratio (σ)	0.27	0.2	0.273
Density (ρ)	9680 kg/m^3	3860 kg/m^3	3150 kg/m^3

Table C.1: Mechanical parameters calculated from ANSYS FEA simulation of measured GeNS eigenfrequencies.

From this step to extract coating loss the coated mechanical loss was required to be measured, conducted as described in Chapter 4. All data except ϕ_{uncoated} was produced

by the author but is included for completeness and shown in Table [C.2].

Sample	Frequency (Hz)	ϕ_{uncoated} ($\times 10^{-6}$)	ϕ_{coated} ($\times 10^{-6}$)	E_s/E_c	ϕ_{coating} ($\times 10^{-4}$)
Sc_2O_3	556	1.82 ± 0.02	4.96 ± 0.06	169.41	5.0 ± 0.1
	1277	2.15 ± 0.04	6.52 ± 0.02	170.39	6.27 ± 0.1
	3387	1.83 ± 0.05	7.2 ± 0.1	163.60	7.7 ± 0.1
HfO_2	513	1.01 ± 0.05	4.2 ± 0.2	314.29	10.3 ± 0.7
	1189	1.95 ± 0.04	5.2 ± 0.3	308.68	9.92 ± 0.8
	2076	2.72 ± 0.03	7.0 ± 0.6	304.85	13.2 ± 1.7
MgF_2	549	1.73 ± 0.03	7.6 ± 0.5	275.65	16.1 ± 1.2
	1266	1.41 ± 0.03	9.35 ± 0.71	280.79	22.3 ± 2.0

Table C.2: Summary of measured and calculated mechanical losses published in [321] for HfO_2, Sc_2O_3 and MgF_2 ion beam assisted e-beam evaporated thin film materials.

Bibliography

[1] A. Einstein. "Über die von der molekularkinetischen Theorie der Wärme geforderte Bewegung von in ruhenden Flüssigkeiten suspendierten Teilchen". In: *Annalen der Physik* 322.8 (1905), pp. 549–560. ISSN: 15213889. DOI: 10.1002/andp.19053220806. URL: https://onlinelibrary.wiley.com/doi/full/10.1002/andp.19053220806.

[2] R. A. Hulse and J. H. Taylor. "Discovery of a pulsar in a binary system". In: *The Astrophysical Journal* 195 (1975), p. L51. ISSN: 0004-637X. DOI: 10.1086/181708. URL: https://ui.adsabs.harvard.edu/abs/1975ApJ...195L..51H/abstract.

[3] J. H. Taylor and J. M. Weisberg. "A new test of general relativity - Gravitational radiation and the binary pulsar PSR 1913+16". In: *The Astrophysical Journal* 253 (1982), p. 908. ISSN: 0004-637X. DOI: 10.1086/159690. URL: https://ui.adsabs.harvard.edu/abs/1982ApJ...253..908T/abstract.

[4] B. P. Abbott et al. "Observation of gravitational waves from a binary black hole merger". In: *Physical Review Letters* 116.6 (2016), p. 061102. ISSN: 10797114. DOI: 10.1103/PHYSREVLETT.116.061102/FIGURES/4/MEDIUM. arXiv: 1602.03837. URL: https://journals.aps.org/prl/abstract/10.1103/PhysRevLett.116.061102.

[5] Peter R Saulson. *Fundamentals of Interferometric Gravitational Wave Detectors*. World Scientific Publishing Co. Pte. Ltd., 1994. DOI: 10.1142/2410.

[6] Alexandre Le Tiec and Jérôme Novak. "Theory of gravitational waves". In: *Overview of Gravitational Waves: Theory, Sources and Detection*. World Sci-

entific Publishing Co. Pte. Ltd., 2017, pp. 1–42. ISBN: 9789813141766. DOI: 10.1142/9789813141766_0001. arXiv: 1607.04202. URL: http://arxiv.org/abs/1607.04202.

[7] Einstein Telescope Collaboration. "ET Design Study". In: (2011), pp. 299–452. URL: http://www.et-gw.eu/.

[8] Pablo Cerda-Duran and Nancy Elias-Rosa. "Neutron Stars Formation and Core Collapse Supernovae". In: 2018, pp. 1–56. DOI: 10.1007/978-3-319-97616-7_1. arXiv: 1806.07267.

[9] A. Hewish et al. "Observation of a rapidly pulsating radio source". In: *Nature* 217.5130 (1968), pp. 709–713. ISSN: 00280836. DOI: 10.1038/217709a0. URL: https://www.nature.com/articles/217709a0.

[10] Magdalena Sieniawska and Michał Bejger. "Continuous Gravitational Waves from Neutron Stars: Current Status and Prospects". In: *Universe* 5.11 (2019), p. 217. ISSN: 2218-1997. DOI: 10.3390/universe5110217. arXiv: 1909.12600. URL: https://www.mdpi.com/2218-1997/5/11/217.

[11] Reinhard Prix. *Gravitational Waves from Spinning Neutron Stars Reinhard Prix 1 for the LIGO Scientific Collaboration.* Tech. rep. URL: https://link.springer.com/chapter/10.1007/978-3-540-76965-1{_}24.

[12] R. Abbott et al. "Search for Gravitational Waves Associated with Gamma-Ray Bursts Detected by Fermi and Swift during the LIGOVirgo Run O3a". In: *The Astrophysical Journal* 915.2 (2021), p. 86. ISSN: 0004-637X. DOI: 10.3847/1538-4357/ABEE15. arXiv: 2010.14550.

[13] B. S. Sathyaprakash and Bernard F. Schutz. *Physics, astrophysics and cosmology with gravitational waves.* 2009. DOI: 10.12942/lrr-2009-2. arXiv: 0903.0338. URL: http://dx.doi.org/10.12942/lrr-2009-2.

[14] Nelson Christensen. *Stochastic gravitational wave backgrounds.* 2019. DOI: 10.1088/1361-6633/aae6b5. arXiv: 1811.08797.

[15] Md Riajul Haque et al. “Decoding the phases of early and late time reheating through imprints on primordial gravitational waves”. In: *Physical Review D* 104.6 (2021). ISSN: 24700029. DOI: 10.1103/PhysRevD.104.063513.

[16] The LIGO Scientific Collaboration et al. “GWTC-3: Compact Binary Coalescences Observed by LIGO and Virgo During the Second Part of the Third Observing Run”. In: *arXiv* (2021), arXiv:2111.03606. arXiv: 2111.03606. URL: https://ui.adsabs.harvard.edu/abs/2021arXiv211103606T/abstract.

[17] J. Weber. “Detection and generation of gravitational waves”. In: *Physical Review* 117.1 (1960), pp. 306–313. ISSN: 0031899X. DOI: 10.1103/PhysRev.117.306.

[18] J. Weber. “Evidence for Discovery of Gravitational Radiation”. In: *Physical Review Letters* 22.24 (1969), pp. 1320–1324. ISSN: 00319007. DOI: 10.1103/PhysRevLett.22.1320.

[19] James L. Levine and Richard L. Garwin. “Absence of gravity-wave signals in a bar at 1695 Hz”. In: *Physical Review Letters* 31.3 (1973), pp. 173–176. ISSN: 00319007. DOI: 10.1103/PhysRevLett.31.173.

[20] L. Ju, D. G. Blair, and C. Zhao. *Detection of gravitational waves*. 2000. DOI: 10.1088/0034-4885/63/9/201. URL: https://iopscience.iop.org/article/10.1088/0034-4885/63/9/201https://iopscience.iop.org/article/10.1088/0034-4885/63/9/201/meta.

[21] Odylio Denys Aguiar. *Past, present and future of the Resonant-mass gravitational wave detectors*. 2011. DOI: 10.1088/1674-4527/11/1/001. arXiv: 1009.1138v1. URL: http://arxiv.org/abs/1009.1138.

[22] M. E. Gertsenshten et al. “On the Detection of Low-Frequency Gravitational Waves”. In: *JETP* 16 (1963), p. 433. ISSN: 1063-7761. URL: https://ui.adsabs.harvard.edu/abs/1963JETP...16..433G/abstract.

[23] A. A. Michelson and E. W. Morley. “On the relative motion of the Earth and the luminiferous ether”. In: *American Journal of Science* s3-34.203 (1887), pp. 333–345. ISSN: 0002-9599. DOI: 10.2475/ajs.s3-34.203.333.

[24] Simon Tait. "Studies of mechanical and optical properties of thin film coatings for future gravitational wave detectors". PhD thesis. Glasgow: University of Glasgow, 2021, p. 109. URL: https://theses.gla.ac.uk/82514/.

[25] Robert L. Forward. "Wideband laser-interferometer graviational-radiation experiment". In: *Physical Review D* 17.2 (1978), pp. 379–390. ISSN: 05562821. DOI: 10.1103/PhysRevD.17.379.

[26] H. Ward et al. "Laser Interferometric Sensing Techniques for Very Small DisplacementsWith Applications to Gravitational Radiation Detectors". In: *IEEE Transactions on Instrumentation and Measurement* 34.2 (1985), pp. 261–265. ISSN: 15579662. DOI: 10.1109/TIM.1985.4315319. URL: https://www.infona.pl//resource/bwmeta1.element.ieee-art-000004315319.

[27] R. L. Ward et al. "DC readout experiment at the Caltech 40m prototype interferometer". In: *Classical and Quantum Gravity*. Vol. 25. 11. 2008. DOI: 10.1088/0264-9381/25/11/114030.

[28] The LIGO Scientific Collaboration. *gwinc · GitLab*. 2022. URL: https://git.ligo.org/gwinc.

[29] The LIGO Scientific Collaboration. *gwinc / pygwinc · GitLab*. 2022. URL: https://git.ligo.org/gwinc/pygwinc.

[30] Matthew Pitkin et al. *Gravitational wave detection by Interferometry (Ground and Space)*. 2011. DOI: 10.12942/lrr-2011-5. arXiv: 1102.3355.

[31] E. J. Daw et al. "Long-term study of the seismic environment at LIGO". In: *Classical and Quantum Gravity* 21.9 (2004), pp. 2255–2273. ISSN: 02649381. DOI: 10.1088/0264-9381/21/9/003. arXiv: 0403046 [gr-qc]. URL: https://iopscience.iop.org/article/10.1088/0264-9381/21/9/003.

[32] F Matichard et al. *Seismic isolation of Advanced LIGO: Review of strategy, instrumentation and performance*. 2015. DOI: 10.1088/0264-9381/32/18/185003. arXiv: 1502.06300.

[33] Stefan Hild. "A Basic Introduction to Quantum Noise and Quantum-Non-Demolition Techniques". In: 2014, pp. 291–314. DOI: 10.1007/978-3-319-03792-9_11.

[34] J. Aasi et al. "Advanced LIGO". In: *Classical and Quantum Gravity* 32.7 (2015), p. 074001. ISSN: 0264-9381. DOI: 10.1088/0264-9381/32/7/074001. arXiv: 1411.4547. URL: https://iopscience.iop.org/article/10.1088/0264-9381/32/7/074001.

[35] Sheila Dwyer. "Squeezing quantum noise". In: *Physics Today* 67.11 (2014), pp. 72–73. ISSN: 00319228. DOI: 10.1063/PT.3.2596.

[36] Peter R. Saulson. "Terrestrial gravitational noise on a gravitational wave antenna". In: *Physical Review D* 30.4 (1984), pp. 732–736. ISSN: 05562821. DOI: 10.1103/PhysRevD.30.732. URL: https://journals.aps.org/prd/abstract/10.1103/PhysRevD.30.732.

[37] Jan Harms et al. "Gravity-Gradient Subtraction in 3rd Generation Underground Gravitational-Wave Detectors in Homogeneous Media". In: (2009). DOI: 10.48550/arxiv.0910.2774. arXiv: 0910.2774. URL: https://arxiv.org/abs/0910.2774v1.

[38] Gabriela González. "Suspensions thermal noise in the LIGO gravitational wave detector". In: *Classical and Quantum Gravity* 17.21 (2000), pp. 4409–4435. ISSN: 02649381. DOI: 10.1088/0264-9381/17/21/305. arXiv: 0006053 [gr-qc]. URL: http://arxiv.org/abs/gr-qc/0006053.

[39] P. Amico et al. "Fused silica suspension for the VIRGO optics: Status and perspectives". In: *Classical and Quantum Gravity*. Vol. 19. 7. IOP Publishing, 2002, pp. 1669–1674. DOI: 10.1088/0264-9381/19/7/359. URL: https://iopscience.iop.org/article/10.1088/0264-9381/19/7/359.

[40] G. Cagnoli and P. A. Willems. "Effećts of nonlinear thermoelastić damping in highly stressed fibers". In: *Physical Review B - Condensed Matter and Materials Physics* 65.17 (2002), pp. 1–9. ISSN: 1550235X. DOI: 10.1103/PhysRevB.65.

174111. URL: https://journals.aps.org/prb/abstract/10.1103/PhysRevB.65.174111.

[41] Charlotte Bond et al. *Interferometer techniques for gravitational-wave detection.* 2016. DOI: 10.1007/s41114-016-0002-8.

[42] Brian J. Meers. "Recycling in laser-interferometric gravitational-wave detectors". In: *Physical Review D* 38.8 (1988), pp. 2317–2326. ISSN: 05562821. DOI: 10.1103/PhysRevD.38.2317.

[43] H. Billing et al. "An argon laser interferometer for the detection of gravitational radiation". In: *Journal of Physics E: Scientific Instruments* 12.11 (1979), pp. 1043–1050. ISSN: 00223735. DOI: 10.1088/0022-3735/12/11/010. URL: https://iopscience.iop.org/article/10.1088/0022-3735/12/11/010.

[44] H Lück et al. "The upgrade of GEO 600". In: *Journal of Physics: Conference Series.* Vol. 228. 2010. DOI: 10.1088/1742-6596/228/1/012012. arXiv: 1004.0339.

[45] R Drever. "Interferometric detectors for gravitational radiation". In: *in Gravitational Radiation, Les Houches 1982 eds. N. Deruelle and T. Piran (North-Holland, Amsterdam)* (1983), p. 321.

[46] Diego Bersanetti. "Lock acquisition & commissioning of the advanced virgo detector". In: *Proceedings of Science.* Sissa Medialab Srl, 2017. DOI: 10.22323/1.307.0070.

[47] Patrick Brady, Giovanni Losurdo, and Hisaaki Shinkai. "LIGO, VIRGO, and KAGRA as the International Gravitational Wave Network". In: *Handbook of Gravitational Wave Astronomy.* 2021, pp. 1–21. ISBN: 10.1007/9789811. DOI: 10.1007/978-981-15-4702-7_51-1. URL: https://doi.org/10.1007/978-981-15-4702-7{_}51-1.

[48] R. W. P. Drever et al. "Gravitational Wave Detectors Using Laser Interferometers and Optical Cavities: Ideas, Principles and Prospects". In: *Quantum Optics, Experimental Gravity, and Measurement Theory.* Springer, Boston, MA, 1983,

pp. 503–514. DOI: 10.1007/978-1-4613-3712-6_21. URL: https://link.springer.com/chapter/10.1007/978-1-4613-3712-6{_}21.

[49] H. Billing et al. "The Munich Gravitational Wave Detector Using Laser Interferometry". In: *Quantum Optics, Experimental Gravity, and Measurement Theory*. Springer, Boston, MA, 1983, pp. 525–566. DOI: 10.1007/978-1-4613-3712-6_23. URL: https://link.springer.com/chapter/10.1007/978-1-4613-3712-6{_}23.

[50] Brian J. Meers. "Recycling in laser-interferometric gravitational-wave detectors". In: *Physical Review D* 38.8 (1988), pp. 2317–2326. ISSN: 05562821. DOI: 10.1103/PhysRevD.38.2317. URL: https://journals.aps.org/prd/abstract/10.1103/PhysRevD.38.2317.

[51] R. Loudon and P. L. Knight. "Squeezed light". In: *Journal of Modern Optics* 34.6-7 (1987), pp. 709–759. ISSN: 13623044. DOI: 10.1080/09500348714550721.

[52] J. Aasi et al. "Enhanced sensitivity of the LIGO gravitational wave detector by using squeezed states of light". In: *Nature Photonics* 7.8 (2013), pp. 613–619. ISSN: 17494885. DOI: 10.1038/NPHOTON.2013.177. arXiv: 1310.0383.

[53] B. P. Abbott et al. "Prospects for observing and localizing gravitational-wave transients with Advanced LIGO, Advanced Virgo and KAGRA". In: *Living Reviews in Relativity* 23.1 (2020). ISSN: 14338351. DOI: 10.1007/S41114-020-00026-9. arXiv: 1304.0670.

[54] Rosa Poggiani. "Multi-messenger observations of a binary neutron star merger". In: *Proceedings of Science*. Vol. 362. Sissa Medialab Srl, 2019. DOI: 10.3847/2041-8213/aa91c9. arXiv: 1710.05833.

[55] B. P. Abbott et al. "GW170817: Observation of Gravitational Waves from a Binary Neutron Star Inspiral". In: *Physical Review Letters* 119.16 (2017). ISSN: 10797114. DOI: 10.1103/PHYSREVLETT.119.161101.

[56] R. Abbott et al. "Observation of Gravitational Waves from Two Neutron Star-Black Hole Coalescences". In: *The Astrophysical Journal Letters* 915.1 (2021), p. L5. ISSN: 2041-8205. DOI: 10.3847/2041-8213/AC082E. arXiv: 2106.15163. URL: https://iopscience.iop.org/article/10.3847/2041-8213/ac082e.

[57] J. Veitch et al. "Estimating parameters of coalescing compact binaries with proposed advanced detector networks". In: *Physical Review D - Particles, Fields, Gravitation and Cosmology* 85.10 (2012), p. 104045. ISSN: 15507998. DOI: 10.1103/PhysRevD.85.104045. URL: https://journals.aps.org/prd/abstract/10.1103/PhysRevD.85.104045.

[58] California Institute of Technology. *Image — Gravitational-Wave Observatories Across the Globe — LIGO Lab — Caltech.* URL: https://www.ligo.caltech.edu/image/ligo20160211c (visited on 09/16/2022).

[59] Keith Riles. *Gravitational waves: Sources, detectors and searches.* 2013. DOI: 10.1016/j.ppnp.2012.08.001. arXiv: 1209.0667. URL: http://arxiv.org/abs/1209.0667.

[60] Kip S. Thorne and Rainer Weiss. *A Brief History of LIGO.* 2016. URL: https://www.caltech.edu/about/news/brief-history-ligo (visited on 09/21/2022).

[61] LIGO. *News — LIGO Laboratory's Response to COVID-19 — LIGO Lab — Caltech.* URL: https://www.ligo.caltech.edu/news/ligo20200317 (visited on 09/13/2022).

[62] L. McCuller et al. "Frequency-Dependent Squeezing for Advanced LIGO". In: *Physical Review Letters* 124.17 (2020). ISSN: 10797114. DOI: 10.1103/PhysRevLett.124.171102. arXiv: 2003.13443.

[63] Kyung Ha Lee et al. "Improved fused silica fibres for the advanced LIGO monolithic suspensions". In: *Classical and Quantum Gravity* 36.18 (2019), p. 185018. ISSN: 13616382. DOI: 10.1088/1361-6382/ab28bd. URL: https://iopscience.iop.org/article/10.1088/1361-6382/ab28bd.

[64] Gabriele Vajente et al. “Low Mechanical Loss TiO2:GeO2 Coatings for Reduced Thermal Noise in Gravitational Wave Interferometers”. In: *Physical Review Letters* 127.7 (2021). ISSN: 10797114. DOI: 10.1103/PhysRevLett.127.071101. arXiv: 2108.04954v2. URL: http://arxiv.org/abs/2108.04954.

[65] Gabriele Vajente. *LIGO-G2102042-v1: Advanced LIGO+ and Advanced Virgo+ coatings down selection: TiO2:GeO2 / SiO2*. Tech. rep. 2021. URL: https://dcc.ligo.org/LIGO-G2102042.

[66] Sheila Rowan et al. *LIGO-M2100169-v2: Panel Report LIGO A+ and Virgo AdV+ coating selection for O5*. Tech. rep. 2021. URL: https://dcc.ligo.org/LIGO-M2100169.

[67] Virgo. *Virgo History Virgo*. 2021. URL: https://www.virgo-gw.eu/about/virgo-history/ (visited on 09/22/2022).

[68] L. Van Der Schaaf et al. “Advanced Virgo phase cameras”. In: *Journal of Physics: Conference Series*. Vol. 718. 7. IOP Publishing, 2016, p. 072008. DOI: 10.1088/1742-6596/718/7/072008. URL: https://iopscience.iop.org/article/10.1088/1742-6596/718/7/072008.

[69] F. Acernese et al. “Advanced Virgo: A second-generation interferometric gravitational wave detector”. In: *Classical and Quantum Gravity* 32.2 (2015), p. 024001. ISSN: 13616382. DOI: 10.1088/0264-9381/32/2/024001. arXiv: 1408.3978. URL: https://iopscience.iop.org/article/10.1088/0264-9381/32/2/024001.

[70] Raffaele Flaminio. “Status and plans of the Virgo gravitational wave detector”. In: *SPIE*. Vol. 11445. SPIE-Intl Soc Optical Eng, 2020, p. 31. ISBN: 9781510636774. DOI: 10.1117/12.2565418. URL: https://ui.adsabs.harvard.edu/abs/2020SPIE11445E..11F/abstract.

[71] American Physical Society. *Virgo Joins LIGO in Detection of Gravitational Waves*. URL: https://www.aps.org/publications/apsnews/updates/ligo-virgo.cfm (visited on 09/12/2022).

[72] S. Di Pace. "Status of Advanced Virgo and upgrades before next observing runs". In: *Physica Scripta* 96.12 (2021), p. 124054. ISSN: 14024896. DOI: 10.1088/1402-4896/ac2efc. URL: https://iopscience.iop.org/article/10.1088/1402-4896/ac2efc.

[73] Massimo Granata. *LIGO-G2101459-v1: Status of r&d activity on IBS SiNx coatings at LMA*. Tech. rep. 2021. URL: https://dcc.ligo.org/LIGO-G2101459.

[74] T. Akutsu et al. *Overview of KAGRA: Detector design and construction history*. 2021. DOI: 10.1093/ptep/ptaa125. arXiv: 2005.05574. URL: https://academic.oup.com/ptep/article/2021/5/05A101/5893487.

[75] T. Akutsu et al. *Overview of KAGRA: Calibration, detector characterization, physical environmental monitors, and the geophysics interferometer*. 2021. DOI: 10.1093/ptep/ptab018. arXiv: 2009.09305. URL: https://academic.oup.com/ptep/article/2021/5/05A102/6146420.

[76] M. E. Fine, H. Van Duyne, and Nancy T. Kenney. "Low-temperature internal friction and elasticity effects in vitreous silica". In: *Journal of Applied Physics* 25.3 (1954), pp. 402–405. ISSN: 00218979. DOI: 10.1063/1.1721649. URL: https://aip.scitation.org/doi/abs/10.1063/1.1721649.

[77] O. L. ANDERSON and H. E. BÖMMEL. "Ultrasonic Absorption in Fused Silica at Low Temperatures and High Frequencies". In: *Journal of the American Ceramic Society* 38.4 (1955), pp. 125–131. ISSN: 15512916. DOI: 10.1111/j.1151-2916.1955.tb14914.x. URL: https://onlinelibrary.wiley.com/doi/full/10.1111/j.1151-2916.1955.tb14914.xhttps://onlinelibrary.wiley.com/doi/abs/10.1111/j.1151-2916.1955.tb14914.xhttps://ceramics.onlinelibrary.wiley.com/doi/10.1111/j.1151-2916.1955.tb14914.x.

[78] H. J. McSkimin. "Measurement of elastic constants at low temperatures by means of ultrasonic waves-data for silicon and germanium single crystals, and for fused silica". In: *Journal of Applied Physics* 24.8 (1953), pp. 988–997. ISSN:

00218979. DOI: 10.1063/1.1721449. URL: https://aip.scitation.org/doi/abs/10.1063/1.1721449.

[79] Eiichi Hirose et al. "Characterization of Core Optics in Gravitational-Wave Detectors: Case Study of KAGRA Sapphire Mirrors". In: *Physical Review Applied* 14.1 (2020), p. 014021. ISSN: 23317019. DOI: 10.1103/PhysRevApplied.14.014021. URL: https://journals.aps.org/prapplied/abstract/10.1103/PhysRevApplied.14.014021.

[80] R X Adhikari et al. *A cryogenic silicon interferometer for gravitational-wave detection*. 2020. arXiv: 2001.11173.

[81] M. Punturo et al. "The Einstein Telescope: A third-generation gravitational wave observatory". In: *Classical and Quantum Gravity* 27.19 (2010), p. 194002. ISSN: 13616382. DOI: 10.1088/0264-9381/27/19/194002. URL: https://iopscience.iop.org/article/10.1088/0264-9381/27/19/194002.

[82] KAGRA. *Image — An illustration of the underground KAGRA gravitational-wave detector — LIGO Lab — Caltech*. URL: https://www.ligo.caltech.edu/image/ligo20191004b (visited on 09/12/2022).

[83] B. Willke et al. "The GEO 600 gravitational wave detector". In: *Classical and Quantum Gravity*. Vol. 19. 7. IOP Publishing, 2002, pp. 1377–1387. DOI: 10.1088/0264-9381/19/7/321. URL: https://iopscience.iop.org/article/10.1088/0264-9381/19/7/321.

[84] H Grote. "The GEO 600 status". In: *Classical and Quantum Gravity* 27.8 (2010), p. 084003. ISSN: 02649381. DOI: 10.1088/0264-9381/27/8/084003. URL: https://iopscience.iop.org/article/10.1088/0264-9381/27/8/084003.

[85] David Reitze et al. "Cosmic Explorer: The U.S. Contribution to Gravitational-Wave Astronomy beyond LIGO". In: (2019). DOI: 10.48550/arxiv.1907.04833. arXiv: 1907.04833. URL: https://arxiv.org/abs/1907.04833v1.

[86] Authors Matthew Evans et al. *Design Stage R&D for Cosmic Explorer: a Review of Critical Technologies*. Tech. rep. 2021, p. 13.

[87] ET Steering Committee Editorial Team. "Design Report Update 2020 for the Einstein Telescope". In: September (2020). URL: https://apps.et-gw.eu/tds/ql/?c=15418.

[88] Jessica Steinlechner. *LIGO-G2201614-v1: ET Sensitivity*. Tech. rep. 2022. URL: https://dcc.ligo.org/LIGO-G2201614.

[89] K. Ackley et al. "Neutron Star Extreme Matter Observatory: A kilohertz-band gravitational-wave detector in the global network". In: *Publications of the Astronomical Society of Australia* (2020). ISSN: 14486083. DOI: 10.1017/pasa.2020.39. arXiv: 2007.03128. URL: http://arxiv.org/abs/2007.03128.

[90] Stefano Vitale. "Space-borne gravitational wave observatories". In: *General Relativity and Gravitation* 46.5 (2014), pp. 1–19. ISSN: 15729532. DOI: 10.1007/s10714-014-1730-2. arXiv: 1404.3136. URL: https://link.springer.com/article/10.1007/s10714-014-1730-2.

[91] Pau Amaro-Seoane et al. "eLISA: Astrophysics and cosmology in the millihertz regime". In: (2012). DOI: 10.48550/arxiv.1201.3621. arXiv: 1201.3621. URL: https://arxiv.org/abs/1201.3621v1.

[92] M. Armano et al. "Sub-Femto- g Free Fall for Space-Based Gravitational Wave Observatories: LISA Pathfinder Results". In: *Physical Review Letters* 116.23 (2016), p. 231101. ISSN: 10797114. DOI: 10.1103/PhysRevLett.116.231101. URL: https://journals.aps.org/prl/abstract/10.1103/PhysRevLett.116.231101.

[93] Davide Castelvecchi. "Astrophysicists unveil glut of gravitational-wave detections". In: *Nature* (2021). ISSN: 0028-0836. DOI: 10.1038/d41586-021-03089-y.

[94] Robert Brown. "XXVII. A brief account of microscopical observations made in the months of June, July and August 1827, on the particles contained in the pollen of plants; and on the general existence of active molecules in organic and inorganic bodies". In: *The Philosophical Magazine* 4.21 (1828), pp. 161–173. ISSN: 1941-5850. DOI: 10.1080/14786442808674769.

[95] J. B. Johnson. "Thermal agitation of electricity in conductors". In: *Physical Review* 32.1 (1928), pp. 97–109. ISSN: 0031899X. DOI: 10.1103/PhysRev.32.97. URL: https://journals.aps.org/pr/abstract/10.1103/PhysRev.32.97.

[96] H. Nyquist. "Thermal agitation of electric charge in conductors". In: *Physical Review* 32.1 (1928), pp. 110–113. ISSN: 0031899X. DOI: 10.1103/PhysRev.32.110. URL: https://journals.aps.org/pr/abstract/10.1103/PhysRev.32.110.

[97] Herbert B. Callen and Theodore A. Welton. "Irreversibility and generalized noise". In: *Physical Review* 83.1 (1951), pp. 34–40. ISSN: 0031899X. DOI: 10.1103/PHYSREV.83.34.

[98] Herbert B. Callen and Richard F. Greene. "On a theorem of irreversible thermodynamics". In: *Physical Review* 86.5 (1952), pp. 702–710. ISSN: 0031899X. DOI: 10.1103/PHYSREV.86.702.

[99] LIGO Lab. *Ultra-High Vacuum — LIGO Lab — Caltech*. URL: https://www.ligo.caltech.edu/page/vacuum (visited on 02/06/2022).

[100] Clarence M. Zener and Sidney Siegel. "Elasticity and Anelasticity of Metals." In: *The Journal of Physical and Colloid Chemistry* 53.9 (1949), pp. 1468–1468. ISSN: 0092-7023. DOI: 10.1021/j150474a017. URL: https://pubs.acs.org/doi/abs/10.1021/j150474a017.

[101] A. V. Cumming et al. "Design and development of the advanced LIGO monolithic fused silica suspension". In: *Classical and Quantum Gravity* 29.3 (2012). ISSN: 02649381. DOI: 10.1088/0264-9381/29/3/035003.

[102] A. Gillespie and F. Raab. "Thermally excited vibrations of the mirrors of laser interferometer gravitational-wave detectors". In: *Physical Review D* 52.2 (1995), pp. 577–585. ISSN: 05562821. DOI: 10.1103/PhysRevD.52.577. URL: https://journals.aps.org/prd/abstract/10.1103/PhysRevD.52.577.

[103] M. Granata et al. "Amorphous optical coatings of present gravitational-wave interferometers". In: *Classical and Quantum Gravity* 37.9 (2020). ISSN: 13616382. DOI: 10.1088/1361-6382/ab77e9.

[104] Gregory M Harry et al. "Titania-doped tantala/silica coatings for gravitational-wave detection". In: *Classical and Quantum Gravity* 24.2 (2007), pp. 405–415. ISSN: 02649381. DOI: 10.1088/0264-9381/24/2/008. arXiv: 0610004 [gr-qc].

[105] Levin Yu. "Internal thermal noise in the LIGO test masses: A direct approach". In: *Physical Review D - Particles, Fields, Gravitation and Cosmology* 57.2 (1998), pp. 1–4. DOI: 10.1103/PhysRevE.67.046106. URL: https://journals-aps-org.libproxy.mit.edu/prd/pdf/10.1103/PhysRevD.57.659{\%}0Ahttps://journals.aps.org/prd/pdf/10.1103/PhysRevD.57.659.

[106] N. Nakagawa et al. "Estimation of thermal noise in the mirrors of laser interferometric gravitational wave detectors: Two point correlation function". In: *Review of Scientific Instruments* 68.9 (1997), pp. 3553–3556. ISSN: 00346748. DOI: 10.1063/1.1148321.

[107] S. Rowan, J. Hough, and D. R.M. Crooks. "Thermal noise and material issues for gravitational wave detectors". In: *Physics Letters, Section A: General, Atomic and Solid State Physics* 347.1-3 (2005), pp. 25–32. ISSN: 03759601. DOI: 10.1016/J.PHYSLETA.2005.06.055.

[108] N. Nakagawa et al. "Thermal noise in half-infinite mirrors with nonuniform loss: A slab of excess loss in a half-infinite mirror". In: *Physical Review D* 65.10 (2002), p. 102001. ISSN: 05562821. DOI: 10.1103/PhysRevD.65.102001. URL:

https://journals.aps.org/prd/abstract/10.1103/PhysRevD.65.102001.

[109] Gregory M. Harry et al. "Thermal noise from optical coatings in gravitational wave detectors". In: *Applied Optics* 45.7 (2006), pp. 1569–1574. ISSN: 15394522. DOI: 10.1364/AO.45.001569. URL: https://opg.optica.org/viewmedia.cfm?uri=ao-45-7-1569{\&}seq=0{\&}html=true.

[110] Ting Hong et al. "Brownian thermal noise in multilayer coated mirrors". In: *Physical Review D - Particles, Fields, Gravitation and Cosmology* 87.8 (2013). ISSN: 15507998. DOI: 10.1103/PHYSREVD.87.082001. arXiv: 1207.6145.

[111] Gabriele Vajente et al. "Method for the experimental measurement of bulk and shear loss angles in amorphous thin films". In: *Physical Review D* 101.4 (2020). ISSN: 2470-0010. DOI: 10.1103/physrevd.101.042004. arXiv: 1911.12277. URL: http://arxiv.org/abs/1911.12277.

[112] V. B. Braginsky, M. L. Gorodetsky, and S. P. Vyatchanin. "Thermodynamical fluctuations and photo-thermal shot noise in gravitational wave antennae". In: *Physics Letters, Section A: General, Atomic and Solid State Physics* 264.1 (1999), pp. 1–10. ISSN: 03759601. DOI: 10.1016/S0375-9601(99)00785-9. arXiv: 9912139 [cond-mat]. URL: http://arxiv.org/abs/cond-mat/9912139.

[113] M. M. Fejer et al. "Thermoelastic dissipation in inhomogeneous media: Loss measurements and displacement noise in coated test masses for interferometric gravitational wave detectors". In: *Physical Review D - Particles, Fields, Gravitation and Cosmology* 70.8 (2004). ISSN: 15502368. DOI: 10.1103/PHYSREVD.70.082003. arXiv: 0402034 [gr-qc]. URL: http://arxiv.org/abs/gr-qc/0402034.

[114] Clarence Zener. "Internal friction in solids. I. Theory of internal friction in reeds". In: *Physical Review* 52.3 (1937), pp. 230–235. ISSN: 0031899X. DOI: 10.1103/PhysRev.52.230. URL: https://journals.aps.org/pr/abstract/10.1103/PhysRev.52.230.

[115] Clarence Zener. "Internal friction in solids II. General theory of thermoelastic internal friction". In: *Physical Review* 53.1 (1938), pp. 90–99. ISSN: 0031899X. DOI: 10.1103/PhysRev.53.90. URL: https://journals.aps.org/pr/abstract/10.1103/PhysRev.53.90.

[116] A.S.Nowic and B.S.Berry. *Anelastic Relaxation in Crystalline Solids*. New York: Academic Press, 1972.

[117] V. B. Braginsky, M. L. Gorodetsky, and S. P. Vyatchanin. "Thermo-refractive noise in gravitational wave antennae". In: *Physics Letters, Section A: General, Atomic and Solid State Physics* 271.5-6 (2000), pp. 303–307. ISSN: 03759601. DOI: 10.1016/S0375-9601(00)00389-3. arXiv: 0008109 [cond-mat].

[118] M. Evans et al. "Thermo-optic noise in coated mirrors for high-precision optical measurements". In: *Physical Review D - Particles, Fields, Gravitation and Cosmology* 78.10 (2008), p. 102003. ISSN: 15507998. DOI: 10.1103/PHYSREVD.78.102003. arXiv: 0807.4774. URL: https://journals.aps.org/prd/abstract/10.1103/PhysRevD.78.102003.

[119] Krishna Seshan. "Handbook of Thin Film Deposition Techniques Principles, Methods, Equipment and Applications, Second Editon". In: *Handbook of Thin Film Deposition Techniques Principles, Methods, Equipment and Applications, Second Editon* (2002). DOI: 10.1201/9781482269680. URL: https://www.taylorfrancis.com/books/mono/10.1201/9781482269680/handbook-thin-film-deposition-techniques-principles-methods-equipment-applications-second-editon-krishna-seshan.

[120] Akitoshi Ueda et al. "Ultra-high quality cavity with 1.5 ppm loss at 1064 nm". In: *Optical Review* 3.5 (1996), pp. 369–372. ISSN: 13406000. DOI: 10.1007/s10043-996-0369-y. URL: https://link.springer.com/article/10.1007/s10043-996-0369-y.

[121] The LIGO Scientific Collaboration. "Instrument Science White Paper". In: *LIGO Technical Note* 225 (2021).

[122] M. Granata et al. “Progress in the measurement and reduction of thermal noise in optical coatings for gravitational-wave detectors”. In: *Applied Optics* 59.5 (2020), A229. ISSN: 1559-128X. DOI: 10.1364/ao.377293. arXiv: 1912.11394.

[123] Huang Wei Pan et al. “Silicon nitride films fabricated by a plasma-enhanced chemical vapor deposition method for coatings of the laser interferometer gravitational wave detector”. In: *Physical Review D* 97.2 (2018), p. 022004. ISSN: 24700029. DOI: 10.1103/PhysRevD.97.022004. URL: https://journals.aps.org/prd/abstract/10.1103/PhysRevD.97.022004.

[124] Huang-wei Pan et al. “Stress effect on mechanical loss of SiN X and α -Si film deposited by PECVD method on silicon cantilever”. In: vol. 15. 2005. 2014, p. 1500195.

[125] Huang-wei Pan et al. “Mechanical loss of silica film on silicon cantilever deposited by PECVD method”. In: *LIGO-G1500194*. 2006. 2013, p. 1500194.

[126] Donald M. Mattox. *Handbook of Physical Vapor Deposition (PVD) Processing*. Elsevier Inc., 2007, pp. 1–945. ISBN: 9780815517634. DOI: 10.1016/c2009-0-18800-1.

[127] K.G. Swift and J.D. Booker. “Surface Engineering Processes”. In: *Manufacturing Process Selection Handbook*. Butterworth-Heinemann, 2013, pp. 243–280. ISBN: 978-0-08-099360-7. DOI: 10.1016/b978-0-08-099360-7.00009-4.

[128] J Kuske et al. “Deposition Conditions for Large Area PECVD of Amorphous Silicon”. In: *MRS Online Proceedings Library* 467.1 (1997), pp. 591–595. ISSN: 1946-4274. DOI: 10.1557/PROC-467-591. URL: https://doi.org/10.1557/PROC-467-591.

[129] Matthew Robert Abernathy, Xiao Liu, and Thomas H. Metcalf. “An Overview of Research into Low Internal Friction Optical Coatings by the Gravitational Wave Detection Community”. In: *Materials Research* 21.suppl 2 (2018). ISSN: 1980-5373. DOI: 10.1590/1980-5373-mr-2017-0863.

[130] M. Abernathy et al. “Exploration of co-sputtered Ta2O5-ZrO2 thin films for gravitational-wave detectors”. In: *Classical and Quantum Gravity* 38.19 (2021). ISSN: 13616382. DOI: 10.1088/1361-6382/ac1b06. arXiv: 2103.14140.

[131] P. J. Kelly and R. D. Arnell. “Magnetron sputtering: A review of recent developments and applications”. In: *Vacuum* 56.3 (2000), pp. 159–172. ISSN: 0042207X. DOI: 10.1016/S0042-207X(99)00189-X.

[132] Angstrom Engineering. *Magnetron Sputtering: Overview*. 2021. URL: https://angstromengineering.com/tech/magnetron-sputtering/ (visited on 04/11/2022).

[133] ALCATechnologyS.R.L. *Magnetron Sputtering: Types of coating processes and Advantages*. URL: https://www.alcatechnology.com/en/blog/magnetron-sputtering/ (visited on 03/28/2022).

[134] Yasaman Hamedani et al. “Plasma-Enhanced Chemical Vapor Deposition: Where we are and the Outlook for the Future”. In: *Chemical Vapor Deposition - Recent Advances and Applications in Optical, Solar Cells and Solid State Devices*. INC, 2016, pp. 51–87. ISBN: 9780128189085. DOI: 10.5772/64654. URL: http://dx.doi.org/10.1016/B978-0-12-818908-5.00003-2.

[135] Xiao Liu et al. “Hydrogen-free amorphous silicon with no tunneling states”. In: *Physical Review Letters* 113.2 (2014), p. 025503. ISSN: 10797114. DOI: 10.1103/PhysRevLett.113.025503. URL: https://journals.aps.org/prl/abstract/10.1103/PhysRevLett.113.025503.

[136] Simon C. Tait et al. “Demonstration of the Multimaterial Coating Concept to Reduce Thermal Noise in Gravitational-Wave Detectors”. In: *Physical Review Letters* 125.1 (2020), p. 011102. ISSN: 10797114. DOI: 10.1103/PhysRevLett.125.011102. URL: https://journals.aps.org/prl/abstract/10.1103/PhysRevLett.125.011102.

[137] J. Steinlechner et al. “Silicon-Based Optical Mirror Coatings for Ultrahigh Precision Metrology and Sensing”. In: *Physical Review Letters* 120.26 (2018), p. 263602. ISSN: 10797114. DOI: 10.1103/PhysRevLett.120.263602. URL: https:

//journals.aps.org/prl/abstract/10.1103/PhysRevLett.120.263602.

[138] G. I. Abzalova, R. S. Sabirov, and A. V. Mikhailov. "Depositing uniform-thickness coatings on large surfaces by means of electron-beam evaporation in vacuum". In: *Journal of Optical Technology* 72.10 (2005), p. 799. ISSN: 1070-9762. DOI: 10.1364/jot.72.000799. URL: https://opg.optica.org/abstract.cfm?uri=jot-72-10-799.

[139] James B. Oliver and David Talbot. "Optimization of deposition uniformity for large-aperture National Ignition Facility substrates in a planetary rotation system". In: *Applied Optics* 45.13 (2006), pp. 3097–3105. ISSN: 15394522. DOI: 10.1364/AO.45.003097. URL: https://opg.optica.org/viewmedia.cfm?uri=ao-45-13-3097{\&}seq=0{\&}html=true.

[140] B. A. Joyce. *Molecular beam epitaxy.* 1985. DOI: 10.1088/0034-4885/48/12/002.

[141] Steven D. Penn et al. "Assessing substrate-transferred GaAs/AlGaAs coatings for gravitational-wave detectors". In: *Optics InfoBase Conference Papers.* Vol. Part F162-. Optica Publishing Group, 2019, FA.3. ISBN: 9781943580583. DOI: 10.1364/OIC.2019.FA.3. URL: https://opg.optica.org/abstract.cfm?uri=OIC-2019-FA.3.

[142] A. V. Cumming et al. "Measurement of the mechanical loss of prototype GaP/AlGaP crystalline coatings for future gravitational wave detectors". In: *Classical and Quantum Gravity* 32.3 (2015). ISSN: 13616382. DOI: 10.1088/0264-9381/32/3/035002.

[143] John Orton and Tom Foxon. *Molecular Beam Epitaxy A Short History.* Vol. 53. 9. 2013, pp. 1689–1699. ISBN: 9788578110796. arXiv: arXiv:1011.1669v3.

[144] Steven D. Penn. *Crystalline Coatings : Plan B (LIGO-DCC-G2200560).* 2022.

[145] P. Koch et al. "Thickness uniformity measurements and damage threshold tests of large-area GaAs/AlGaAs crystalline coatings for precision interferometry".

In: *Optics Express* 27.25 (2019), p. 36731. ISSN: 10944087. DOI: 10.1364/OE.27.036731.

[146] Angie C. Lin et al. "Epitaxial growth of GaP/AlGaP mirrors on Si for low thermal noise optical coatings". In: *Optical Materials Express* 5.8 (2015), p. 1890. ISSN: 21593930. DOI: 10.1364/ome.5.001890.

[147] Dung-Sheng Tsai et al. "Amorphous silicon nitride deposited by an NH3-free plasma enhanced chemical vapor deposition method for the coatings of the next generation laser interferometer gravitational waves detector". In: *Classical and Quantum Gravity* (2022). ISSN: 0264-9381. DOI: 10.1088/1361-6382/ac79f6.

[148] R. T. Galyautdinov, N. F. Kasparov, and G. S. Luchkin. "Technology of sputtering high-reflection coatings on ABS-plastic articles". In: *Inzhenerno-Fizicheskii Zhurnal* 75.5 (2002), pp. 170–173. ISSN: 00210285. DOI: 10.1023/A:1021192330461. URL: https://link.springer.com/article/10.1023/A:1021192330461.

[149] Najwa Sidqi et al. "Comparative study of dielectric coating materials for microcavity applications". In: *Optical Materials Express* 9.8 (2019), p. 3452. ISSN: 21593930. DOI: 10.1364/ome.9.003452. URL: https://doi.org/10.1364/OME.9.003452.

[150] Manuel Marchiò et al. "Optical performance of large-area crystalline coatings". In: *Optics Express* 26.5 (2018), p. 6114. ISSN: 10944087. DOI: 10.1364/oe.26.006114. URL: https://doi.org/10.1364/OE.26.006114.

[151] L. Pinard et al. "Mirrors used in the LIGO interferometers for first detection of gravitational waves". In: *Applied Optics* 56.4 (2017), p. C11. ISSN: 0003-6935. DOI: 10.1364/ao.56.000c11.

[152] Y. Chen et al. "Comparison of magnetron sputtering and ion beam sputtering on dispersive mirrors". In: *Applied Physics B: Lasers and Optics* 126.5 (2020). ISSN: 09462171. DOI: 10.1007/s00340-020-07431-6.

[153] D R Gibson et al. "Low Loss High Performance Optical Coatings Deposited Using Closed Field Magnetron Sputtering". In: (2007), pp. 361–364.

[154] M. Liehr and M. Dieguez-Campo. "Microwave PECVD for large area coating". In: *Surface and Coatings Technology* 200.1-4 SPEC. ISS. (2005), pp. 21–25. ISSN: 02578972. DOI: 10.1016/j.surfcoat.2005.02.061.

[155] Xiao Liu and R. Pohl. "Low-energy excitations in amorphous films of silicon and germanium". In: *Physical Review B - Condensed Matter and Materials Physics* 58.14 (1998), pp. 9067–9081. ISSN: 1550235X. DOI: 10.1103/PhysRevB.58.9067.

[156] LaserOptik. *IBS*. URL: https://www.laseroptik.com/en/coating-guide/production-methods/ibs (visited on 03/27/2022).

[157] Bernhard Wolf. *Handbook of ion sources*. CRC Press, 2017, pp. 1–544. ISBN: 9781351838382. DOI: 10.1201/9781315214054.

[158] Xing Jin et al. "Study on the Influence of RF Power on Inductively Coupled Plasma Ion Source Injector Gas". In: *Chinese Control Conference, CCC*. Vol. 2018-July. IEEE Computer Society, 2018, pp. 8507–8511. ISBN: 9789881563941. DOI: 10.23919/ChiCC.2018.8483212.

[159] R Scrivens. "Classification of Ion Sources". In: *CERN Yellow Report CERN-2013-007* (2014), pp. 9–26.

[160] David J. Griffiths. *Introduction to Electrodynamics*. Cambridge University Press, 2017. ISBN: 9781108333511. DOI: 10.1017/9781108333511.

[161] Carsten Bundesmann and Horst Neumann. "Tutorial: The systematics of ion beam sputtering for deposition of thin films with tailored properties". In: *Journal of Applied Physics* 124.23 (2018). ISSN: 10897550. DOI: 10.1063/1.5054046.

[162] W Kraus. "RF ion sources". In: *Materials Today* 5.5 (2002), p. 43. ISSN: 13697021. DOI: 10.1016/s1369-7021(02)05539-6.

[163] Brett Buchholtz. "Physics of Ion Beam Sources". In: (), pp. 1–7.

[164] Veeco Instruments Inc. *16cm RF Source Technical Manual*. 2002, pp. 3–5.

[165] R Geller. *Highly charged ECR ion sources: Summary and comments (invited).* 1990. DOI: 10.1063/1.1141898. URL: https://doi.org/10.1063/1.1141898.

[166] Polygon. *Ion beam sputter deposition - POLYGON PHYSICS.* URL: https://polygonphysics.com/applications/ion-beam-sputter-deposition/ (visited on 03/27/2022).

[167] C. Bundesmann et al. "Ion beam sputter deposition of Ge films: Influence of process parameters on film properties". In: *Thin Solid Films* 589 (2015), pp. 487–492. ISSN: 00406090. DOI: 10.1016/j.tsf.2015.06.017.

[168] R. Scrivens. "Requirements for Ion Sources". In: (2014). DOI: 10.5170/CERN-2013-007.1. arXiv: 1404.0914. URL: http://arxiv.org/abs/1404.0914http://dx.doi.org/10.5170/CERN-2013-007.1.

[169] Roger Smith, Steven D. Kenny, and Deerajen Ramasawmy. "Molecular-dynamics simulations of sputtering". In: *Philosophical Transactions of the Royal Society A: Mathematical, Physical and Engineering Sciences* 362.1814 (2004), pp. 157–176. ISSN: 1364503X. DOI: 10.1098/rsta.2003.1308. URL: https://royalsocietypublishing.org/.

[170] J F Ziegler, J P Biersack, and M D Ziegler. *SRIM, the stopping and range of ions in matter.* 2008. ISBN: 9780965420716. URL: http://books.google.com/books?id=JSN63qxPG5MC.

[171] Mutzke A et al. *SDTrimSP.* Garching, 2011.

[172] So Hee Kang et al. "Angular Distribution of Sputtered Particles in Shave-off Section Processing with SDTrimSP". In: *Journal of Surface Analysis* 25.3 (2019), pp. 165–171. ISSN: 1341-1756. DOI: 10.1384/jsa.25.165. URL: https://doi.org/10.1384/jsa.25.165.

[173] James Ziegler. *James Ziegler - SRIM & TRIM.* 2008. URL: http://www.srim.org/.

[174] J.P. Biersack and L.G. Haggmark. “A Monte Carlo computer program for the transport of energetic ions in amorphous targets”. In: *Nuclear Instruments and Methods* 174.1-2 (1980), pp. 257–269. ISSN: 0029554X. DOI: 10.1016/0029-554x(80)90440-1.

[175] D. J. O’Connor and J. P. Biersack. “Comparison of theoretical and empirical interatomic potentials”. In: *Nuclear Inst. and Methods in Physics Research, B* 15.1-6 (1986), pp. 14–19. ISSN: 0168583X. DOI: 10.1016/0168-583X(86)90243-0.

[176] H. Hofsäss, K. Zhang, and A. Mutzke. “Simulation of ion beam sputtering with SDTrimSP, TRIDYN and SRIM”. In: *Applied Surface Science* 310 (2014), pp. 134–141. ISSN: 01694332. DOI: 10.1016/j.apsusc.2014.03.152.

[177] A.G. Mutzke et al. “SDTrimSP Version 6.00”. In: *(IPP 2019-02). Garching: Max-Planck-Institut für Plasmaphysi* (2019). DOI: 10.17617/2.3026474.

[178] Wolfgang. Eckstein. “Computer Simulation of Ion-Solid Interactions”. In: (1991), p. 296. URL: https://books.google.com/books/about/Computer{_}Simulation{_}of{_}Ion{_}Solid{_}Interac.html?id=4h3rCAAAQBAJ.

[179] T. M. R. Ellis, Ivor R. Philips, and Thomas M. Lahey. *Fortran 90 Programming*. 1994, p. 842. ISBN: 0201544466. arXiv: 9809069v1 [arXiv:gr-qc]. URL: https://books.google.com/books/about/Fortran{_}90{_}Programming.html?id=ud01ngEACAAJ.

[180] P. S. Szabo et al. “Graphical user interface for SDTrimSP to simulate sputtering, ion implantation and the dynamic effects of ion irradiation”. In: *Nuclear Instruments and Methods in Physics Research, Section B: Beam Interactions with Materials and Atoms* 522 (2022), pp. 47–53. ISSN: 0168583X. DOI: 10.1016/j.nimb.2022.04.008.

[181] Guido. Van Rossum and Fred L. Drake. *Python 3 Reference Manual*. Scotts Valley, CA: CreateSpace, 2009.

[182] C. Verdeil et al. “Angular distribution of sputtered matter under Cs + bombardment with oblique incidence”. In: *Applied Surface Science* 255.4 (2008), pp. 870–873. ISSN: 01694332. DOI: 10.1016/j.apsusc.2008.05.231.

[183] *Laboratoire des Matériaux Avancés*. URL: http://lma.in2p3.fr/ (visited on 07/18/2022).

[184] Stuart Reid. *(Private Communication)*. 2022.

[185] Veeco Instruments Inc. *RFN-300 RF Neutraliser Manual*. 2002, pp. 3–4.

[186] Bruce Hansen. *(Private Communication)*. 2019.

[187] Royal Society of Chemistry. *Indium - Element information, properties and uses — Periodic Table*. URL: https://www.rsc.org/periodic-table/element/49/indium (visited on 05/19/2022).

[188] Honggang Hao, Ao Zhou, and Min Rao. “Study on the absorption uniformity of optical thin films based on the photothermal detuning technique”. In: *Applied Optics* 51.28 (2012), pp. 6844–6847. ISSN: 15394522. DOI: 10.1364/AO.51.006844. URL: https://opg.optica.org/viewmedia.cfm?uri=ao-51-28-6844{\&}seq=0{\&}html=true.

[189] P. Drude. “Ueber Oberflächenschichten. I. Theil”. In: *Annalen der Physik* 272.2 (1889), pp. 532–560. ISSN: 15213889. DOI: 10.1002/andp.18892720214.

[190] Harland G. Tompkins and Eugene A. Irene. *Handbook of Ellipsometry*. Elsevier, 2005, pp. 1–870. ISBN: 9780815517474. DOI: 10.1515/arh-2005-0022. URL: http://www.sciencedirect.com/science/article/pii/B9780815514992500083.

[191] S Jena et al. “Characterization of Optical Thin Films by Spectrophotometry and Atomic Force Microscopy”. In: *SMC Bulletin* 6.1 (2015), pp. 1–9.

[192] Lambda Photonics Ltd. *PHOTON RT UV-VIS-NIR*. URL: https://www.lambdaphoto.co.uk/essentoptics-photon-rt-uv-vis-nir-spectrophotometer.html (visited on 05/26/2022).

[193] Day Optics. *Optical Glass - JGS3 Datasheet – Dayoptics, Inc. — Engineering360*. URL: https://datasheets.globalspec.com/ps/3050/Dayoptics/655DE86D-9BB5-4AF1-A458-11F83D723DFF (visited on 05/26/2022).

[194] Day Optics. *Optical Glass - JGS1 Datasheet – Dayoptics, Inc. — Engineering360*. URL: https://datasheets.globalspec.com/ps/3050/Dayoptics/97EBC971-CF58-4C00-9FBD-017E286E86E2 (visited on 05/26/2022).

[195] Corning Inc. "Corning HPFS 7979, 7980, 8652, 8655 Fused Silica Optical Materials Product Information". In: (2014), pp. 1–8.

[196] Wolfgang Theiss. *SCOUT Software*. 2019. URL: http://www.wtheiss.com/..

[197] Stephen K. O'Leary, S. R. Johnson, and P. K. Lim. "The relationship between the distribution of electronic states and the optical absorption spectrum of an amorphous semiconductor: An empirical analysis". In: *Journal of Applied Physics* 82.7 (1997), pp. 3334–3340. ISSN: 00218979. DOI: 10.1063/1.365643. URL: https://aip.scitation.org/doi/abs/10.1063/1.365643.

[198] Wolfgang Theiss. *Optical constants — WTheiss Hardware and Software*. URL: https://wtheiss.com/wordpress/?cat=10 (visited on 08/05/2022).

[199] Franz Urbach. *The long-wavelength edge of photographic sensitivity and of the electronic Absorption of Solids [8]*. 1953. DOI: 10.1103/PhysRev.92.1324.

[200] Wolfgang Theiss. *The OJL model*. URL: http://www.mtheiss.com/ojlmodel.htm (visited on 05/25/2022).

[201] Wolfgang Theiss. "Technical manual for SCOUT". In: 49 (2012), p. 62. URL: https://www.mtheiss.com/help/final/pdf/scout3.pdf.

[202] P. Drude. "Zur Elektronentheorie der Metalle; II. Teil. Galvanomagnetische und thermomagnetische Effecte". In: *Annalen der Physik* 308.11 (1900), pp. 369–402. ISSN: 15213889. DOI: 10.1002/andp.19003081102.

[203] J. A. Dobrowolski, F. C. Ho, and A. Waldorf. "Determination of optical constants of thin film coating materials based on inverse synthesis". In: *Applied Optics* 22.20 (1983), p. 3191. ISSN: 0003-6935. DOI: 10.1364/ao.22.003191. URL: https://opg.optica.org/viewmedia.cfm?uri=ao-22-20-3191{\&}seq=0{\&}html=true.

[204] A. Alexandrovski et al. "Photothermal common-path interferometry (PCI): new developments". In: *Solid State Lasers XVIII: Technology and Devices*. Vol. 7193. SPIE, 2009, p. 71930D. ISBN: 9780819474391. DOI: 10.1117/12.814813. URL: https://www.spiedigitallibrary.org/conference-proceedings-of-spie/7193/71930D/Photothermal-common-path-interferometry-PCI-new-developments/10.1117/12.814813.full.

[205] G Billingsley. *Advanced LIGO End Test Mass (ETM)*. Tech. rep., pp. 3–6.

[206] The University of Iowa. *Scanning Electron Microscopy — Central Microscopy Research Facility*. URL: https://cmrf.research.uiowa.edu/scanning-electron-microscopy.

[207] Károly Havancsák. *TECHNOORG - LINDA*. 2017. URL: https://www.technoorg.hu/news-and-events/articles/high-resolution-scanning-electron-microscopy-1/ (visited on 05/27/2022).

[208] Hitachi High-Technologies Corporation. *New Scanning Electron Microscope Model S-3700N is released-Achieved 300mm diameter large specimen accommodation-Remark 1: EDX: Energy Dispersive X-ray Spectrometry WDX: Wavelength Dispersive X-ray spectrometry EBSP: Electron Backscattering Pattern Remark*. Tech. rep. 2006.

[209] Oxford Instruments. *The Business of Science ® X-Max The largest area SDD SIZE IT MATTERS 20mm 2 50mm 2 80mm 2*. Tech. rep.

[210] Hitachi High-Technologies Corporation. *New Scanning Electron Microscope Model S-3700N is released-Achieved 300mm diameter large specimen accommodation-Remark 1: EDX: Energy Dispersive X-ray Spectrometry WDX: Wavelength Dis-*

persive X-ray spectrometry EBSP: Electron Backscattering Pattern Remark. Tech. rep. 2006.

[211] University of California Riverside. "Introduction to Energy Dispersive X-ray Spectrometry (EDS)". In: (2013), pp. 1–11. URL: http://micron.ucr.edu/public/manuals/EDS-intro.pdf.

[212] Nicole M. Pirozzi, Jeroen Kuipers, and Ben N.G. Giepmans. "Sample preparation for energy dispersive X-ray imaging of biological tissues". In: *Methods in Cell Biology*. Vol. 162. Academic Press Inc., 2021, pp. 89–114. ISBN: 9780128220580. DOI: 10.1016/bs.mcb.2020.10.023.

[213] Joseph I. Goldstein et al. "Coating and Conductivity Techniques for SEM and Microanalysis". In: *Scanning Electron Microscopy and X-Ray Microanalysis*. Springer, Boston, MA, 1992, pp. 671–740. DOI: 10.1007/978-1-4613-0491-3_13. URL: https://link.springer.com/chapter/10.1007/978-1-4613-0491-3{_}13.

[214] George F. Harrington and José Santiso. "Back-to-Basics tutorial: X-ray diffraction of thin films". In: *Journal of Electroceramics* (2021). ISSN: 15738663. DOI: 10.1007/s10832-021-00263-6.

[215] Ron Jenkins. *Introduction to X-ray powder diffractometry / Ron Jenkins, Robert L. Snyder*. 1996.

[216] A. R. Lang. "X-ray Detectors". In: *Characterization of Crystal Growth Defects by X-Ray Methods*. 1980, pp. 320–332. DOI: 10.1007/978-1-4757-1126-4_12. URL: http://pd.chem.ucl.ac.uk/pdnn/inst1/detects.htm.

[217] Bruker. *D8 ADVANCE — Bruker*. 2022. URL: https://www.bruker.com/en/products-and-solutions/diffractometers-and-x-ray-microscopes/x-ray-diffractometers/d8-advance-family/d8-advance.htmlhttps://www.bruker.com/en/products-and-solutions/diffractometers-and-scattering-systems/x-ray-diffractometers/d8 (visited on 05/26/2023).

[218] Paul van der Heide. *X-Ray Photoelectron Spectroscopy: An Introduction to Principles and Practices*. Wiley-Blackwell, 2011. ISBN: 9781118062531. DOI: 10.1002/9781118162897.

[219] J F Moulder et al. "Handbook of X-Ray Photoelectron Spectroscopy (Perkin-Elmer, Eden Prairie, MN, 1992)". In: *Google Scholar* (2002), p. 128. URL: https://books.google.com/books/about/Handbook{_}of{_}X{_}ray{_}Photoelectron{_}Spectros.html?id=A{_}XGQgAACAAJ.

[220] S E E Profile. "In-operando hard X-ray photoelectron spectroscopy study on the resistive switching physics of HfO 2 -based RRAM". In: June 2014 (2019).

[221] Scienta Omicron. *ESCA+ - Scienta Omicron - PDF Catalogs — Technical Documentation — Brochure*. URL: https://pdf.directindustry.com/pdf/scienta-omicron/esca/20757-631038.html (visited on 05/26/2023).

[222] R. Hesse et al. "Error estimation in peak-shape analysis of XFS core-level spectra using UNIFIT 2003: How significant are the results of peak fits?" In: *Surface and Interface Analysis* 36.10 (2004), pp. 1373–1383. ISSN: 01422421. DOI: 10.1002/sia.1925.

[223] Casa Software Ltd. *Casa XPS Software*. 2005. URL: http://www.casaxps.com/.

[224] S. Gras and M. Evans. "Direct measurement of coating thermal noise in optical resonators". In: *Physical Review D* 98.12 (2018). ISSN: 24700029. DOI: 10.1103/PhysRevD.98.122001. arXiv: 1802.05372.

[225] B. S. Berry and W. C. Pritchet. "VIBRATING REED INTERNAL FRICTION APPARATUS FOR FILMS AND FOILS." In: *IBM Journal of Research and Development* 19.4 (1975), pp. 334–343. ISSN: 00188646. DOI: 10.1147/rd.194.0334.

[226] A. V. Cumming. "Aspects of mirrors and suspensions for advanced gravitational wave detectors". PhD thesis. University of Glasgow, 2008.

[227] Kazuhiro Yamamoto et al. “Measurement of the mechanical loss of a cooled reflective coating for gravitational wave detection”. In: *Physical Review D - Particles, Fields, Gravitation and Cosmology* 74.2 (2006). ISSN: 15507998. DOI: 10.1103/PhysRevD.74.022002.

[228] E. Cesarini et al. “A ”gentle” nodal suspension for measurements of the acoustic attenuation in materials”. In: *Review of Scientific Instruments* 80.5 (2009). ISSN: 00346748. DOI: 10.1063/1.3124800.

[229] K. Prasai et al. “High Precision Detection of Change in Intermediate Range Order of Amorphous Zirconia-Doped Tantala Thin Films Due to Annealing”. In: *Physical Review Letters* 123.4 (2019), p. 45501. ISSN: 10797114. DOI: 10.1103/PhysRevLett.123.045501. URL: https://doi.org/10.1103/PhysRevLett.123.045501.

[230] P. Fedders and D. Drabold. “Molecular-dynamics investigations of conformational fluctuations and low-energy vibrational excitations in a-Si:H”. In: *Physical Review B - Condensed Matter and Materials Physics* 53.7 (1996), pp. 3841–3845. ISSN: 1550235X. DOI: 10.1103/PhysRevB.53.3841.

[231] Jonathan P. Trinastic et al. “Molecular dynamics modeling of mechanical loss in amorphous tantala and titania-doped tantala”. In: *Physical Review B* 93.1 (2016), p. 014105. ISSN: 24699969. DOI: 10.1103/PhysRevB.93.014105. URL: https://journals.aps.org/prb/abstract/10.1103/PhysRevB.93.014105.

[232] Singiresu S. Rao. *Vibration of Continuous Systems*. John Wiley and Sons, 2007, pp. 1–720. ISBN: 0471771716. DOI: 10.1002/9780470117866. URL: https://onlinelibrary.wiley.com/doi/book/10.1002/9780470117866.

[233] Gabriele Vajente. *Notes on measuring coatings with a nodal suspension*. Tech. rep. 225. California Insitute of Technology, 2019.

[234] ANSYS. *ANSYS Mechanical*. 2020. URL: https://www.ansys.com/products/structures.

[235] COMSOL AB. *COMSOL Multiphysics*. Stockholm, Sweden. URL: www.comsol.com.

[236] ANSYS Inc. *Modal Analysis - ANSYS Innovation Courses (Lecture 2))*. 2022. URL: https://courses.ansys.com/index.php/courses/modal-analysis/.

[237] Svetoslava Angelova. "Characterisation of ion-beam deposited thin-film coating materials for use in future gravitational wave observatories". PhD thesis. University of Strathclyde, 2021.

[238] Kenji Numata et al. "Measurement of the intrinsic mechanical loss of low-loss samples using a nodal support". In: *Physics Letters, Section A: General, Atomic and Solid State Physics* 276.1-4 (2000), pp. 37–46. ISSN: 03759601. DOI: 10.1016/S0375-9601(00)00646-0.

[239] Newport Corporation. *SMC100 Single-Axis DC or Stepper Motion Controller*. URL: https://www.newport.com/f/smc100-single-axis-dc-or-stepper-motion-controller (visited on 07/20/2022).

[240] A. Cadez and A. Abramovici. "Measuring high mechanical quality factors of bodies made of bare insulating materials". In: *Journal of Physics E: Scientific Instruments* 21.5 (1988), pp. 453–456. ISSN: 00223735. DOI: 10.1088/0022-3735/21/5/007.

[241] Kieran Craig. "Studies of the mechanical dissipation of thin films for mirrors in interferometric gravitational wave detectors". PhD thesis. Glasgow: University of Glasgow, 2015, p. 210. URL: https://theses.gla.ac.uk/6582/.

[242] National Instruments. *LabVIEW*.

[243] G. Vajente et al. "A high throughput instrument to measure mechanical losses in thin film coatings". In: *Review of Scientific Instruments* 88.7 (2017). ISSN: 10897623. DOI: 10.1063/1.4990036.

[244] Gabriele Vajente. *Gabriele Vajente / pycrime · GitLab*. URL: https://git.ligo.org/gabriele-vajente/pycrime (visited on 07/27/2022).

[245] G. Cagnoli et al. “Mode-dependent mechanical losses in disc resonators”. In: *Physics Letters, Section A: General, Atomic and Solid State Physics* 382.33 (2018), pp. 2165–2173. ISSN: 03759601. DOI: 10.1016/j.physleta.2017.05.065.

[246] Mohammed J Ahamed, Doruk Senkal, and Andrei M Shkel. “Effect of annealing on mechanical quality factor of fused quartz hemispherical resonator”. In: *1st IEEE International Symposium on Inertial Sensors and Systems, ISISS 2014 - Proceedings*. 2014. ISBN: 9781479909162. DOI: 10.1109/ISISS.2014.6782512.

[247] L. G. Prokhorov et al. “Upper limits on the mechanical loss of silicate bonds in a silicon tuning fork oscillator”. In: *Physics Letters, Section A: General, Atomic and Solid State Physics* 382.33 (2018), pp. 2186–2191. ISSN: 03759601. DOI: 10.1016/j.physleta.2017.07.007.

[248] Solomon. Musikant. *OPTICAL MATERIALS: AN INTRODUCTION TO SELECTION AND APPLICATION*. Dekker, 1985, p. 257. ISBN: 0824773098. URL: https://www.routledge.com/Optical-Materials-An-Introduction-to-Selection-and-Application/Musikant/p/book/9780824773090.

[249] Gabriele Vajente. *(Private Communication)*. 2021.

[250] Lisa Barsotti et al. *LIGO-T1800042-v5: The A+ design curve*. Tech. rep. 2018. URL: https://dcc.ligo.org/cgi-bin/private/DocDB/ShowDocument?.submit=Number{\&}docid=T1800042{\&}version=.

[251] Stuart Reid and Iain Martin. “Development of Mirror Coatings for Gravitational Wave Detectors”. In: *Coatings* 6.4 (2016), p. 61. ISSN: 2079-6412. DOI: 10.3390/coatings6040061. URL: https://www.mdpi.com/2079-6412/6/4/61/htm.

[252] Peter G Murray et al. “Ion-beam sputtered amorphous silicon films for cryogenic precision measurement systems”. In: *Physical Review D - Particles, Fields, Gravitation and Cosmology* 92.6 (2015). ISSN: 15502368. DOI: 10.1103/PhysRevD.92.062001.

[253] R. Birney et al. “Amorphous Silicon with Extremely Low Absorption: Beating Thermal Noise in Gravitational Astronomy”. In: *Physical Review Letters* 121.19 (2018), p. 191101. ISSN: 10797114. DOI: 10.1103/PhysRevLett.121.191101. URL: https://journals.aps.org/prl/abstract/10.1103/PhysRevLett.121.191101.

[254] Xiao Liu et al. “Comparing amorphous silicon prepared by electron-beam evaporation and sputtering toward eliminating atomic tunneling states”. In: *Journal of Alloys and Compounds* 855 (2021), p. 157431. ISSN: 09258388. DOI: 10.1016/j.jallcom.2020.157431. URL: https://linkinghub.elsevier.com/retrieve/pii/S0925838820337956.

[255] Jessica Steinlechner et al. “Optical absorption of ion-beam sputtered amorphous silicon coatings”. In: *Physical Review D* 93.6 (2016), p. 62005. ISSN: 24700029. DOI: 10.1103/PhysRevD.93.062005. URL: http://eprints.gla.ac.uk/134436/http://eprints.gla.ac.uk.

[256] Lukas Terkowski et al. “Influence of deposition parameters on the optical absorption of amorphous silicon thin films”. In: *Physical Review Research* 2.3 (2020), p. 033308. ISSN: 26431564. DOI: 10.1103/PhysRevResearch.2.033308. URL: https://journals.aps.org/prresearch/abstract/10.1103/PhysRevResearch.2.033308.

[257] W. D. Wilson, L. G. Haggmark, and J. P. Biersack. “Calculations of nuclear stopping, ranges, and straggling in the low-energy region”. In: *Physical Review B* 15.5 (1977), pp. 2458–2468. ISSN: 01631829. DOI: 10.1103/PhysRevB.15.2458. URL: https://journals.aps.org/prb/abstract/10.1103/PhysRevB.15.2458.

[258] J. Lindhard and M. Scharff. “Energy dissipation by ions in the kev region”. In: *Physical Review* 124.1 (1961), pp. 128–130. ISSN: 0031899X. DOI: 10.1103/PhysRev.124.128. URL: https://journals.aps.org/pr/abstract/10.1103/PhysRev.124.128.

[259] Erik Rohkamm et al. “Characterization of an RF excited broad beam ion source operating with inert gases”. In: *Journal of Applied Physics* 129.22 (2021), p. 223305. ISSN: 10897550. DOI: 10.1063/5.0052758. URL: https://aip.scitation.org/doi/abs/10.1063/5.0052758.

[260] D. T. Pierce and W. E. Spicer. “Electronic structure of amorphous Si from photoemission and optical studies”. In: *Physical Review B* 5.8 (1972), pp. 3017–3029. ISSN: 01631829. DOI: 10.1103/PhysRevB.5.3017. URL: https://journals.aps.org/prb/abstract/10.1103/PhysRevB.5.3017.

[261] Lukas Terkowski. “Silicon Based Mirror Coatings For Gravitational Wave Detectors”. PhD thesis. University of Hamburg, 2022.

[262] Alex Amato. “Low Thermal Noise Coating for New Generation Gravitational-Wave Detectors”. PhD thesis. University of Lyon, 2020. URL: https://dcc.ligo.org/LIGO-P2000051.

[263] Matthew A Hopcroft, William D Nix, and Thomas W Kenny. “What is the Young’s modulus of silicon?” In: *Journal of Microelectromechanical Systems* 19.2 (2010), pp. 229–238. ISSN: 10577157. DOI: 10.1109/JMEMS.2009.2039697.

[264] IOFFE Inst. *NSM Archive - Physical Properties of Semiconductors*. 2003. URL: http://matprop.ru/.

[265] Peter G. Murray et al. “Ion-beam sputtered amorphous silicon films for cryogenic precision measurement systems”. In: *Physical Review D - Particles, Fields, Gravitation and Cosmology* 92.6 (2015), p. 062001. ISSN: 15502368. DOI: 10.1103/PhysRevD.92.062001. URL: https://journals.aps.org/prd/abstract/10.1103/PhysRevD.92.062001.

[266] William Yam, Slawek Gras, and Matthew Evans. “Multimaterial coatings with reduced thermal noise”. In: *Physical Review D - Particles, Fields, Gravitation and Cosmology* 91.4 (2015). ISSN: 15502368. DOI: 10.1103/PHYSREVD.91.042002.

[267] Jessica Steinlechner and Iain W. Martin. "How can amorphous silicon improve current gravitational-wave detectors?" In: *Physical Review D* 103.4 (2021), p. 042001. ISSN: 24700029. DOI: 10.1103/PhysRevD.103.042001. URL: https://journals.aps.org/prd/abstract/10.1103/PhysRevD.103.042001.

[268] Jessica Steinlechner et al. "Thermal noise reduction and absorption optimization via multimaterial coatings". In: *Physical Review D - Particles, Fields, Gravitation and Cosmology* 91.4 (2015), p. 042001. ISSN: 15502368. DOI: 10.1103/PhysRevD.91.042001. arXiv: 1411.3150. URL: https://journals.aps.org/prd/abstract/10.1103/PhysRevD.91.042001.

[269] William Yam, Slawek Gras, and Matthew Evans. "Multimaterial coatings with reduced thermal noise". In: *Physical Review D - Particles, Fields, Gravitation and Cosmology* 91.4 (2015), p. 042002. ISSN: 15502368. DOI: 10.1103/PhysRevD.91.042002. URL: https://journals.aps.org/prd/abstract/10.1103/PhysRevD.91.042002.

[270] Richard Corkish and Martin A. Green. "Band edge optical absorption in intrinsic silicon: Assessment of the indirect transition and disorder models". In: *Journal of Applied Physics* 73.8 (1993), pp. 3988–3996. ISSN: 00218979. DOI: 10.1063/1.352864. URL: https://aip.scitation.org/doi/abs/10.1063/1.352864.

[271] Robert A. Carlton, Charles E. Lyman, and James E. Roberts. "Accuracy and precision of quantitative energy-dispersive X-ray spectrometry in the environmental scanning electron microscope". In: *Scanning* 26.4 (2004), pp. 167–174. ISSN: 01610457. DOI: 10.1002/sca.4950260404.

[272] J. M. Westra et al. "Formation of thin-film crystalline silicon on glass observed by in-situ XRD". In: *Energy Procedia*. Vol. 2. 1. Elsevier, 2010, pp. 235–241. DOI: 10.1016/j.egypro.2010.07.034.

[273] R. Kakkad et al. "Crystallized Si films by low-temperature rapid thermal annealing of amorphous silicon". In: *Journal of Applied Physics* 65.5 (1989), pp. 2069–

2072. ISSN: 00218979. DOI: 10.1063/1.342851. URL: https://aip.scitation.org/doi/abs/10.1063/1.342851.

[274] Suzanne Paradis and Keptsu Jean-Baptiste. *Characterization and optimization of SiO2 and Si3N4 thin films : for a smart uncooled IR sensor / Suzanne Paradis, DRDC Valcartier ; Jean-Baptiste A. Keptsu, Plasmionique Inc.:D68-6/270-2013E-PDF - Government of Canada Publications - Canada.ca.* Tech. rep. Defence R&D Canada, 2013. URL: https://publications.gc.ca/site/eng/9.879914/publication.html.

[275] P. C. Zalm. "Energy dependence of the sputtering yield of silicon bombarded with neon, argon, krypton, and xenon ions". In: *Journal of Applied Physics* 54.5 (1983), pp. 2660–2666. ISSN: 00218979. DOI: 10.1063/1.332340. URL: https://aip.scitation.org/doi/abs/10.1063/1.332340.

[276] I. H. Malitson. "Interspecimen Comparison of the Refractive Index of Fused Silica*,". In: *Journal of the Optical Society of America* 55.10 (1965), p. 1205. ISSN: 0030-3941. DOI: 10.1364/josa.55.001205.

[277] Wjatscheslaw Sakiew et al. "Influence of ion beam parameters onto two-dimensional optical thin film thickness distributions deposited by ion beam sputtering". In: *Thin Solid Films* 682 (2019), pp. 109–120. ISSN: 00406090. DOI: 10.1016/j.tsf.2019.05.027.

[278] Grégoire R.N. Defoort-Levkov, Alan Bahm, and Patrick Philipp. "Influence of water contamination on the sputtering of silicon with low-energy argon ions investigated by molecular dynamics simulations". In: *Beilstein Journal of Nanotechnology* 13.1 (2022), pp. 986–1003. ISSN: 21904286. DOI: 10.3762/bjnano.13.86. URL: https://www.beilstein-journals.org/bjnano/articles/13/86.

[279] M. S. Mikhailenko et al. "Influence of ion-beam etching by Ar ions with an energy of 2001000 eV on the roughness and sputtering yield of a single-crystal silicon surface". In: *Applied Optics* 61.10 (2022), p. 2825. ISSN: 1559-128X. DOI: 10.1364/ao.455096.

[280] Hong Ping Ma et al. “Measurements of microstructural, chemical, optical, and electrical properties of silicon-oxygen-nitrogen films prepared by plasma-enhanced atomic layer deposition”. In: *Nanomaterials* 8.12 (2018), p. 1008. ISSN: 20794991. DOI: 10.3390/nano8121008. URL: https://www.mdpi.com/2079-4991/8/12/1008/htmhttps://www.mdpi.com/2079-4991/8/12/1008.

[281] F. Strauß et al. “Short range atomic migration in amorphous silicon”. In: *Journal of Applied Physics* 119.17 (2016), p. 175102. ISSN: 10897550. DOI: 10.1063/1.4948333. URL: https://aip.scitation.org/doi/abs/10.1063/1.4948333.

[282] Kiran Prasai et al. “Annealing-Induced Changes in the Atomic Structure of Amorphous Silica, Germania, and Tantala Using Accelerated Molecular Dynamics”. In: *Physica Status Solidi (B) Basic Research* 258.9 (2021). ISSN: 15213951. DOI: 10.1002/pssb.202000519. URL: https://onlinelibrary.wiley.com/doi/10.1002/pssb.202000519.

[283] H. C. Jacks et al. “Structural tunability and origin of two-level systems in amorphous silicon”. In: *Physical Review Materials* 6.4 (2022), p. 045604. ISSN: 24759953. DOI: 10.1103/PhysRevMaterials.6.045604. arXiv: 2111.10914.

[284] Shubham Duttagupta et al. “Optimised antireflection coatings using silicon nitride on textured silicon surfaces based on measurements and multidimensional modelling”. In: *Energy Procedia*. Vol. 15. 2012, pp. 78–83. DOI: 10.1016/j.egypro.2012.02.009.

[285] Xiaoyu Du et al. *Silicon Nitride as a Biomedical Material: An Overview*. 2022. DOI: 10.3390/ijms23126551. URL: /pmc/articles/PMC9224221/ /pmc/articles/PMC9224221/?report=abstracthttps://www.ncbi.nlm.nih.gov/pmc/articles/PMC9224221/.

[286] Dung Sheng Tsai et al. “Amorphous silicon nitride deposited by an NH3-free plasma enhanced chemical vapor deposition method for the coatings of the next

generation laser interferometer gravitational waves detector". In: *Classical and Quantum Gravity* 39.15 (2022), 15LT01. ISSN: 13616382. DOI: 10.1088/1361-6382/ac79f6. URL: https://iopscience.iop.org/article/10.1088/1361-6382/ac79f6.

[287] Kevin Boudrea. *The Parts of the Periodic Table*. URL: https://www.angelo.edu/faculty/kboudrea/periodic/structure{_}mass.htmhttps://www.angelo.edu/faculty/kboudrea/periodic/physical{_}metals.htm (visited on 01/07/2023).

[288] D. P. Stevenson. "The Strengths of Chemical Bonds". In: *Journal of the American Chemical Society* 77.8 (1955), pp. 2350–2350. ISSN: 0002-7863. DOI: 10.1021/ja01613a116. URL: https://www.worldcat.org/formats-editions/591162486.

[289] Kevin Luke et al. "Broadband mid-infrared frequency comb generation in a Si3N4 microresonator". In: *Conference on Lasers and Electro-Optics Europe - Technical Digest*. Vol. 2015-Augus. 21. Optica Publishing Group, 2015, pp. 4823–4826. ISBN: 9781557529688. DOI: 10.1364/ol.40.004823. URL: https://opg.optica.org/viewmedia.cfm?uri=ol-40-21-4823{\&}seq=0{\&}html=truehttps://opg.optica.org/abstract.cfm?uri=ol-40-21-4823https://opg.optica.org/ol/abstract.cfm?uri=ol-40-21-4823.

[290] Shih Liang Ku and Cheng Chung Lee. "Optical and structural properties of silicon nitride thin films prepared by ion-assisted deposition". In: *Optical Materials* 32.9 (2010), pp. 956–960. ISSN: 09253467. DOI: 10.1016/j.optmat.2010.01.032.

[291] D.C Frost and C.A Mcdowell. "The dissociation energy of the nitrogen molecule". In: *Proceedings of the Royal Society of London. Series A. Mathematical and Physical Sciences* 236.1205 (1956), pp. 278–284. ISSN: 0080-4630. DOI: 10.1098/rspa.1956.0135.

[292] J. Bauer. "Optical properties, band gap, and surface roughness of Si3N4". In: *physica status solidi (a)* 39.2 (1977), pp. 411–418. ISSN: 1521396X. DOI: 10.1002/pssa.2210390205. URL: https://onlinelibrary.wiley.com/doi/full/10.1002/pssa.2210390205https://onlinelibrary.wiley.com/doi/abs/10.1002/pssa.2210390205https://onlinelibrary.wiley.com/doi/10.1002/pssa.2210390205.

[293] Emilia M. Esposito et al. "Annealing effects on PECVD-grown Si rich aSiNx thin films". In: *Energy Procedia*. Vol. 2. 1. Elsevier, 2010, pp. 159–164. DOI: 10.1016/j.egypro.2010.07.022.

[294] Gabriele Vajente. *LIGO-T1900276-v2: Notes on measuring coatings with a nodal suspension*. Tech. rep. 2019. URL: https://dcc.ligo.org/cgi-bin/private/DocDB/ShowDocument?.submit=Identifier{\&}docid=T1900276{\&}version=.

[295] Gabriele Vajente. *LIGO-T1900554-v1: How the loss angle is extracted from the gentle nodal suspension measurements*. Tech. rep. LIGO Lab, 2019. URL: https://dcc.ligo.org/cgi-bin/private/DocDB/ShowDocument?.submit=Identifier{\&}docid=T1900554{\&}version=.

[296] Bing K. Yen et al. "Coverage and properties of a-SiNx hard disk overcoat". In: *Journal of Applied Physics*. Vol. 93. 10 3. 2003, pp. 8704–8706. DOI: 10.1063/1.1543136. URL: https://www.researchgate.net/publication/234868209{_}Coverage{_}and{_}properties{_}of{_}a-SiNx{_}hard{_}disk{_}overcoat.

[297] Wolfgang S.M. Werner, Kathrin Glantschnig, and Claudia Ambrosch-Draxl. "Optical constants and inelastic electron-scattering data for 17 elemental metals". In: *Journal of Physical and Chemical Reference Data* 38.4 (2009), pp. 1013–1092. ISSN: 00472689. DOI: 10.1063/1.3243762. URL: https://aip.scitation.org/doi/abs/10.1063/1.3243762.

[298] C. R. Grandini et al. "Internal friction and frequency measurements in molybdenum containing oxygen and nitrogen". In: *Journal De Physique. IV : JP*

6.8 (1996). ISSN: 11554339. DOI: 10.1051/jp4:1996823. URL: https://click.endnote.com/viewer?doi=10.1051{\%}2Fjp4{\%}3A1996823{\&}token=WzE5NjM3NiwiMTAuMTA1MS9qcDQ6MTk5NjgyMyJd.l8w6jb21EkVo7H3q5CJc-N8hJW8.

[299] Huang Wei Pan et al. "Silicon nitride films fabricated by a plasma-enhanced chemical vapor deposition method for coatings of the laser interferometer gravitational wave detector". In: *Physical Review D* 97.2 (2018), p. 022004. ISSN: 24700029. DOI: 10.1103/PhysRevD.97.022004. URL: https://journals.aps.org/prd/abstract/10.1103/PhysRevD.97.022004.

[300] R. S. Hockett. "Anomalous diffusion of nitrogen in nitrogenimplanted silicon". In: *Applied Physics Letters* 54.18 (1989), pp. 1793–1795. ISSN: 0003-6951. DOI: 10.1063/1.101266. URL: http://aip.scitation.org/doi/10.1063/1.101266.

[301] HULINKS Inc. *TFCalc (Software for Optical Thin Film) - HULINKS Inc.* URL: https://www.hulinks.co.jp/en/tfcalc-e.

[302] Yung Chin Yang et al. "Influence of high power impulse magnetron sputtering pulse parameters on the properties of aluminum nitride coatings". In: *Surface and Coatings Technology* 259.PB (2014), pp. 219–231. ISSN: 02578972. DOI: 10.1016/j.surfcoat.2014.05.028.

[303] M. A. Signore et al. "Role of oxygen contaminant on the physical properties of sputtered AlN thin films". In: *Journal of Alloys and Compounds* 649 (2015), pp. 1267–1272. ISSN: 09258388. DOI: 10.1016/j.jallcom.2015.05.289.

[304] Pierre Boher et al. "Hydrogen and oxygen content of silicon nitride films prepared by multipolar plasma-enhanced chemical vapor deposition". In: *Applied Physics Letters* 54.6 (1989), pp. 511–513. ISSN: 00036951. DOI: 10.1063/1.100915.

[305] Shiuh Chao et al. "LIGO-P2200153-v2: Silicon oxy-nitride for the low refractive index layers in the mirror coatings of the cryogenic laser interferometer gravi-

tational waves detectors". In: *Pre-print* (2022). URL: https://dcc.ligo.org/LIGO-P2200153.

[306] P. Marwoto et al. "Influence of annealing time on the morphology and oxygen content of ZnO:Ga thin films". In: *Journal of Physics: Conference Series*. Vol. 1321. 2. Institute of Physics Publishing, 2019. DOI: 10.1088/1742-6596/1321/2/022020.

[307] Martin J. Hart et al. "Medium range structural order in amorphous tantala spatially resolved with changes to atomic structure by thermal annealing". In: *Journal of Non-Crystalline Solids* 438 (2016), pp. 10–17. ISSN: 00223093. DOI: 10.1016/j.jnoncrysol.2016.02.005.

[308] K. Abbas et al. "Role of argon plasma on the structural and morphological properties of silicon nitride films by pulsed DC glow discharge". In: *2013 International Conference on Aerospace Science & Engineering (ICASE)*. IEEE, 2013, pp. 1–5. ISBN: 978-1-4799-0993-3. DOI: 10.1109/ICASE.2013.6785561. URL: http://ieeexplore.ieee.org/document/6785561/.

[309] H. Schmidt et al. "Thermal stability and crystallization kinetics of sputtered amorphous Si3N4 films". In: *Thin Solid Films* 450.2 (2004), pp. 346–351. ISSN: 00406090. DOI: 10.1016/j.tsf.2003.11.274. URL: https://linkinghub.elsevier.com/retrieve/pii/S0040609003018832.

[310] Kun-Hsien Lee et al. "SiNx optical thin films prepared by RF ion-beam sputtering and residual stress elimination technique". In: *Advances in Thin-Film Coatings for Optical Applications V*. Ed. by Jennifer D. T. Kruschwitz and Michael J. Ellison. Vol. 7067. SPIE, 2008, 70670K. ISBN: 9780819472878. DOI: 10.1117/12.795846. URL: http://proceedings.spiedigitallibrary.org/proceeding.aspx?doi=10.1117/12.795846.

[311] Harold F. Winters and Eric Kay. "Influence of surface absorption characteristics on reactively sputtered films grown in the biased and unbiased modes". In: *Journal of Applied Physics* 43.3 (1972), pp. 794–799. ISSN: 00218979. DOI: 10.

1063/1.1661282. URL: https://aip.scitation.org/doi/abs/10.1063/1.1661282.

[312] D. Bouchier et al. "Low Temperature Deposition of Silicon Nitride by Reactive IonBeam Sputtering". In: *Journal of The Electrochemical Society* 130.3 (1983), pp. 638–644. ISSN: 0013-4651. DOI: 10.1149/1.2119772.

[313] D R Gibson et al. "Closed Field Magnetron Sputter Deposition of Carbide and Nitrides for Optical Applications". In: *51st Annual Technical Conference Proceedings* October 2014 (2008), pp. 1–6.

[314] Nanthakishore Makeswaran et al. "Structural, Optical and Mechanical Properties of Nanocrystalline Molybdenum Thin Films Deposited under Variable Substrate Temperature". In: *Materials* 15.3 (2022), p. 754. ISSN: 19961944. DOI: 10.3390/ma15030754. URL: https://www.mdpi.com/1996-1944/15/3/754/htmhttps://www.mdpi.com/1996-1944/15/3/754.

[315] A. Giannattasio et al. "Oxygen and Nitrogen Transport in Silicon Investigated by Dislocation Locking Experiments". In: *Journal of The Electrochemical Society* 152.6 (2005), G460. ISSN: 00134651. DOI: 10.1149/1.1901669. URL: https://www.researchgate.net/publication/228565344{_}Oxygen{_}and{_}Nitrogen{_}Transport{_}in{_}Silicon{_}Investigated{_}by{_}Dislocation{_}Locking{_}Experiments.

[316] K. S. Grabowski et al. "Thermal stability of silicon nitride coatings produced by ion assisted deposition". In: *Nuclear Inst. and Methods in Physics Research, B* 39.1-4 (1989), pp. 190–193. ISSN: 0168583X. DOI: 10.1016/0168-583X(89)90769-6.

[317] D. Davis et al. *LIGO detector characterization in the second and third observing runs*. 2021. DOI: 10.1088/1361-6382/abfd85. arXiv: 2101.11673. URL: https://iopscience.iop.org/article/10.1088/1361-6382/abfd85https://iopscience.iop.org/article/10.1088/1361-6382/abfd85/meta.

[318] R. X. Adhikari et al. “A cryogenic silicon interferometer for gravitational-wave detection”. In: *Classical and Quantum Gravity* 37.16 (2020). ISSN: 13616382. DOI: 10.1088/1361-6382/ab9143. arXiv: 2001.11173.

[319] Carlos Garcia Nuñez et al. “Study of Amorphous Dielectric Optical Coatings Deposited by Plasma Ion Assisted Electron Beam Evaporation for Gravitational Wave Detectors”. In: *Optics InfoBase Conference Papers*. Washington, D.C.: Optica Publishing Group, 2022, WB.4. ISBN: 9781557528209. DOI: 10.1364/ao.477186. URL: https://opg.optica.org/abstract.cfm?uri=OIC-2022-WB.4.

[320] Shigeng Song et al. “Tantalum Oxide and Silica Mixture Coatings Deposited Using Microwave Plasma Assisted Co-sputtering for Optical Mirror Coatings in Gravitational Wave Detectors”. In: *Optics InfoBase Conference Papers*. Washington, D.C.: Optica Publishing Group, 2022, WB.2. ISBN: 9781557528209. DOI: 10.1364/ao.477211. URL: https://opg.optica.org/abstract.cfm?uri=OIC-2022-WB.2.

[321] Carlos Garcia Nuñez et al. “Study of Amorphous Dielectric Optical Coatings Deposited by Plasma Ion Assisted Electron Beam Evaporation for Gravitational Wave Detectors”. In: *Optics InfoBase Conference Papers*. Washington, D.C.: Optica Publishing Group, 2022, WB.4. ISBN: 9781557528209. DOI: 10.1364/OIC.2022.WB.4.

[322] Carlos Garcia Nuñez et al. “Study of Amorphous Dielectric Optical Coatings Deposited by Plasma Ion Assisted Electron Beam Evaporation for Gravitational Wave Detectors”. In: *Optics InfoBase Conference Papers*. Washington, D.C.: Optica Publishing Group, 2022, WB.4. ISBN: 9781557528209. DOI: 10.1364/ao.477186.

[323] André Luís Marin Vargas, Fabiana De Araújo Ribeiro, and Roberto Hübler. “Changes in the Young Modulus of hafnium oxide thin films”. In: *Nuclear Instruments and Methods in Physics Research, Section B: Beam Interactions with*

Materials and Atoms 365 (2015), pp. 362–366. ISSN: 0168583X. DOI: 10.1016/j.nimb.2015.07.096.

[324] S. Barzilai, I. Halevy, and O. Yeheskel. "Bulk modulus of Sc2O3: Ab initio calculations and experimental results". In: *Journal of Applied Physics* 110.4 (2011), p. 043532. ISSN: 00218979. DOI: 10.1063/1.3626457. URL: https://aip.scitation.org/doi/abs/10.1063/1.3626457.

[325] Maria Berdova et al. "Hardness, elastic modulus, and wear resistance of hafnium oxide-based films grown by atomic layer deposition". In: *Journal of Vacuum Science & Technology A: Vacuum, Surfaces, and Films* 34.5 (2016), p. 051510. ISSN: 0734-2101. DOI: 10.1116/1.4961113. URL: https://avs.scitation.org/doi/abs/10.1116/1.4961113.

[326] Alexandr Belosludtsev et al. "Effect of Annealing on Optical, Mechanical, Electrical Properties and Structure of Scandium Oxide Films". In: *Physica Status Solidi (A) Applications and Materials Science* 216.18 (2019), p. 1900122. ISSN: 18626319. DOI: 10.1002/pssa.201900122. URL: https://onlinelibrary.wiley.com/doi/full/10.1002/pssa.201900122https://onlinelibrary.wiley.com/doi/abs/10.1002/pssa.201900122https://onlinelibrary.wiley.com/doi/10.1002/pssa.201900122.

[327] Knight Optical. *Optical Material Magnesium Fluoride*. URL: https://www.crystran.co.uk/optical-materials/magnesium-fluoride-mgf2https://www.knightoptical.com/wp-content/uploads/2020/02/IR-material-magnesium-fluoride.pdf (visited on 01/16/2023).